

UNIVERSITY OF BREMEN

CUMULATIVE DOCTORAL THESIS

Glaciological observations using
phase-sensitive radar

Author:

Ole Zeising

Supervisor:

Prof. Dr. Angelika Humbert

*A thesis submitted in partial fulfilment of the requirements
for the degree of Doctor Rerum Naturalium (Dr. rer. nat.)*

to the

Department of Geosciences

Ole Zeising

Glaciological observations using phase-sensitive radar

Cumulative Doctoral Thesis

Supervisor: Prof. Dr. Angelika Humbert

Reviewers: Prof. Dr. Angelika Humbert and Prof. Dr. Matthias Braun

Date of Submission: November 17, 2021

Date of Defence: February 15, 2022

University of Bremen

Department of Geosciences

1st Reviewer

Prof. Dr. Angelika Humbert

Alfred-Wegener-Institut Helmholtz-Zentrum für
Polar- und Meeresforschung, Bremerhaven,
Germany
Department of Geosciences, University of
Bremen, Bremen, Germany,

2nd Reviewer

Prof. Dr. Matthias Braun

Department of Geography, Friedrich-Alexander
University Erlangen-Nürnberg, Erlangen,
Germany

“I seemed to vow to myself that some day I would go to the region of ice and snow and go on and on till I came to one of the poles of the earth, the end of the axis upon which this great round ball turns.”

— **ERNEST SHACKLETON**
Polar Explorer

Abstract

The large ice sheets in Greenland and Antarctica are losing mass due to global warming. In particular, the acceleration of ice streams and thus the increased discharge into the ocean contributes significantly to global sea-level rise. The floating extensions of the ice streams counteract this, but intense basal melting can destabilise the ice shelves. The quantification of the basal melt rates as well as an enhanced understanding of the processes influencing the spatial distribution and temporal variability of basal melting is of great importance. These findings allow to assess the causes of ice shelf change, but above all they have an influence on the projections of future sea-level rise.

In this thesis, a contribution is made to determine the melt rates of two ice shelves, which are crucial for the future mass losses of the respective ice sheets. To this end, we use a phase-sensitive radar. In the north, the focus is on the Northeast Greenland Ice Stream (NEGIS) that feeds the Nioghalvfjærdsbræ (79°N Glacier), one of three remaining glaciers in Greenland with a floating tongue. My analysis of radar measurements indicates high melt rates near the onset of the ice stream and thus the presence of subglacial melt water, which is associated with the formation of the ice flow. An extensive study in my thesis, which includes measurements by airborne radar and satellite in addition to phase-sensitive radar, reveals that the 79°N Glacier has been thinned out considerably in recent years due to extreme melt rates and that large channels have been formed. The cause of the channel formation could be the runoff of subglacial water, which is significantly increased in summer and leads to higher ice flow velocities, as another study of mine shows.

Melt rates of the Filchner Ice Shelf, Antarctica, which I also determined using phase-sensitive radar measurements, are comparatively low. At some locations, however, they deviate significantly from remote sensing-derived melt rates, which I was able to attribute to inaccuracies in the used ice flow velocity field. Furthermore, I show that the use of newer velocity fields improves the determination of the melt rates from remote sensing. This improvement is important because remote sensing melt rates are used for projecting future sea-level rise. My analysis of melt rate time series in the vicinity of a channel indicates higher melt rates in the summer as well as several melt events spread over the entire measurement period. Another study to which I contributed combines measurements and numerical modelling to show that in order to preserve the channel, higher melt rates

must have occurred in the past than those that were measured. These would lead to the closure of the channel within 250 years. Thus, neither the channel itself nor the present day melt rates endanger the stability of one of the largest Antarctic ice shelves at present.

In addition to these findings, this thesis demonstrates the possibilities but also the limitations of the phase-sensitive radar used to determine the basal melt rates.

Zusammenfassung

Die großen Eisschilde in Grönland und der Antarktis verlieren durch die Klimaerwärmung an Masse. Insbesondere die Beschleunigung von Eisströmen und damit der verstärkte Abfluss in den Ozean trägt wesentlich zum globalen Meeresspiegelanstieg bei. Die schwimmenden Verlängerungen der Eisströme wirken dem entgegen, aber starkes basales Schmelzen kann die Schelfeise destabilisieren. Die Quantifizierung der basalen Schmelzraten sowie ein erweitertes Verständnis der Prozesse, welche die räumliche Verteilung und zeitliche Variabilität der Schmelzraten beeinflussen, ist von großer Wichtigkeit. Die gewonnenen Erkenntnisse erlauben es, die Ursachen der Schelfeisveränderung abzuschätzen, vor allem aber haben diese Einfluss auf die Projektionen des zukünftigen Meeresspiegelanstiegs.

Diese Arbeit liefert einen Beitrag dazu, die Schmelzraten eines Eisstroms und zweier Schelfeise zu bestimmen, die für den zukünftigen Massenverlust des zugehörigen Eisschildes entscheidend sind. Zu diesem Zweck verwenden wir ein phasen-sensitives Radar. Im Norden liegt der Fokus auf dem Nordostgrönländischen Eisstrom, der den Nioghalvfjærdsbræ (79°N Gletscher) speist, einen von drei verbliebenen Gletschern mit einer schwimmenden Eiszunge in Grönland. Meine Analyse von Radarmessungen zeigt, dass in der Nähe des Ursprungs des Eisstroms hohe Schmelzraten auftreten und somit subglaziales Schmelzwasser vorhanden ist. Dieses wird mit der Bildung des Eisstroms in Zusammenhang gebracht. Eine umfangreiche Studie in meiner Arbeit, die neben den phasen-sensitiven Messungen auch Flugradar und Satelliten-Messungen einbezieht, deckt auf, dass der 79°N Gletscher in den vergangenen Jahren durch extreme Schmelzraten stark ausgedünnt ist und sich große basale Kanäle gebildet haben. Ursache für die Entstehung der Kanäle könnte der Ausstrom von subglazialen Wasser sein, der im Sommer deutlich erhöht ist und zu höheren Fließgeschwindigkeiten führt, wie eine weitere Studie in dieser Arbeit zeigt.

Schmelzraten des Filchner-Schelfeises in der Antarktis, die ich ebenfalls mittels phasen-sensitiven Radarmessungen bestimmt habe, sind vergleichsweise niedrig. Stellenweise weichen sie jedoch signifikant von Schmelzraten aus Fernerkundungsmessungen ab, was ich auf Ungenauigkeiten des verwendeten Geschwindigkeitsfelds zurückführen konnte. Des Weiteren zeige ich, dass die Verwendung von neueren Geschwindigkeitsfeldern die Bestimmung der Schmelzraten aus der Fernerkundung verbessert. Diese Verbesserung ist wichtig, weil Fernerkundungs-

schmelzraten für die Projektionen des zukünftigen Meeresspiegelanstiegs verwendet werden. Meine Analyse von einer Schmelzraten-Zeitreihe in der Nähe eines Kanals deutet auf höhere Schmelzraten in den Sommermonaten sowie auf mehrere Schmelzereignisse verteilt über den gesamten Messzeitraum hin. Eine weitere Studie mit meiner Beteiligung, die Messungen und numerische Modellierung verbindet, zeigt, dass zur Erhaltung des Kanals in der Vergangenheit höhere Schmelzraten aufgetreten sein müssen als jene, die gemessen wurden. Diese würden innerhalb von 250 Jahren zu einer Schließung des Kanals führen. Somit gefährden derzeit weder der Kanal selbst noch die Schmelzraten die Stabilität von einem der größten Schelfeise der Antarktis.

Neben diesen Erkenntnissen zeigt diese Arbeit die Möglichkeiten, aber auch die Limitierungen des zur Bestimmung der basalen Schmelzraten verwendeten phasensensitiven Radars auf.

Contents

Abstract	v
Zusammenfassung	vii
1 Introduction	1
1.1 Mass loss of the Greenland and Antarctic ice sheets	1
1.2 Radioglaciology and other geophysical methods	3
1.3 Objectives and thesis outline	5
2 Ice dynamics	7
2.1 Introduction	7
2.2 Kinematics	8
2.3 Ice thickness evolution	10
3 Basal energy balance	13
3.1 Introduction	13
3.2 Energy balance	13
3.3 Energy balance at ice base	16
3.4 Oceanic heat flux	18
4 Phase-sensitive radio echo sounding	21
4.1 Basics of radio echo sounding on ice	21
4.2 Phase-sensitive radio echo sounding	23
4.3 Phase-sensitive FMCW radar theory	24
4.4 Data processing	28
4.5 Basal melt rates from pRES measurements	29
5 Northeast Greenland Ice Stream, Greenland	41
5.1 Introduction	41
5.2 Lubricated sliding of the Northeast Greenland Ice Stream	42
5.3 Ice–ocean interaction at 79°N Glacier	43
6 Indication of high basal melting at the EastGRIP drill site on the Northeast Greenland Ice Stream	45
6.1 Introduction	46
6.2 Data and methods	48
6.3 Results	52

6.4	Discussion	52
6.5	Conclusion	58
6.6	Appendix	59
7	Extreme melt rates at Greenland’s largest floating ice tongue	63
7.1	Introduction	64
7.2	Data and methods	65
7.3	Results	73
7.4	Discussion	77
7.5	Conclusion	81
7.6	Appendix	83
8	Filchner Ice Shelf, Antarctica	93
8.1	Introduction	93
8.2	Basal melting	94
8.3	Basal channel at Support Force Glacier	94
9	Basal melt of the southern Filchner Ice Shelf, Antarctica	97
9.1	Introduction	98
9.2	Materials and methods	100
9.3	Results	102
9.4	Comparison with remote sensing basal melt estimates	105
9.5	Conclusion	108
9.6	Appendix	109
10	On the evolution of an ice shelf melt channel at the base of Filchner Ice Shelf, from observations and viscoelastic modeling	115
10.1	Introduction	117
10.2	Observations	119
10.3	Viscoelastic modeling	129
10.4	Discussion	136
10.5	Conclusions	140
10.6	Appendix	141
11	Conclusion and outlook	153
	References	157
	Lists	175
	List of figures	175
	List of tables	177

List of abbreviations	178
List of symbols	179
Acknowledgements	183
Appendix	I
A Seasonal Observations at 79° N Glacier (Greenland) From Remote Sensing and in situ Measurements	III
A.1 Introduction	IV
A.2 Seasonal melt patterns	VI
A.3 Surface velocities	VII
A.4 Lake drainage	X
A.5 Discussion	XII
A.6 Conclusions	XVI
References	XIX
B Elastic deformation plays a non-negligible role in Greenland's outlet glacier flow	XXIII
B.1 Introduction	XXIV
B.2 Results and discussion	XXVII
B.3 Methods	XLI
References	XLIX
Versicherung an Eides Statt/Affirmation in Lieu of an Oath	LVII

Introduction

1.1 Mass loss of the Greenland and Antarctic ice sheets

Global mean sea-level rise is the most momentous effect of climate change. Between 2006 and 2015, the global mean sea-level raised by about 3.6 millimetre per year (mm a^{-1}) (IPCC, 2019). While thermal expansion of ocean water causes the sea-level to rise by 1.4 mm a^{-1} , the most dominant source of sea-level rise is the contribution from ice sheets and glaciers which add up to 1.8 mm a^{-1} (IPCC, 2019). The polar regions, in particular the Greenland Ice Sheet (GrIS), are affected by global warming. Between 2005 and 2016, the GrIS lost mass at an average rate of $278 \pm 11 \text{ Gt a}^{-1}$ and so contributed by $0.77 \pm 0.03 \text{ mm a}^{-1}$ to the mean sea-level rise (IPCC, 2019). The rate in mass loss of the Antarctic Ice Sheet (AIS) in the same period of time was $155 \pm 19 \text{ Gt a}^{-1}$ (equivalent to a sea-level rise of $0.43 \pm 0.05 \text{ mm a}^{-1}$; IPCC, 2019).

Two processes were identified to evoke the mass loss of GrIS: (1) a reduced surface mass balance and (2) increased glacier dynamical imbalance (Shepherd et al., 2020). Both result from increased temperatures of the atmosphere and of the ocean (Shepherd et al., 2020). While warmer air temperatures facilitate surface melting, warmer ocean water in the fjords leads to an increase in basal melting that thins the floating extensions of the ice sheet. As ice shelves restrain the outflow of the grounded ice, thinning reduces the buttressing effect and causes their feeding ice streams to accelerate (Dupont and Alley, 2005; Fürst et al., 2016). This dynamical mass change is the dominant cause for the mass loss of the AIS, especially due to thinning and the retreat of major outlet glaciers of the West Antarctic Ice Sheet (WAIS) (IPCC, 2019; Pattyn and Morlighem, 2020).

Projections of the future dynamics of the GrIS and AIS under changing climate conditions require a reliable quantification of the basal mass loss (Seroussi et al., 2020). Several studies tried to estimate ice shelf melting around Greenland and Antarctica using indirect observations from satellites in conjunction with ice flow models (e.g. Rignot et al., 2013; Moholdt et al., 2015; Wilson et al., 2017; Adusumilli et al., 2020). Rignot et al. (2013) found basal melting of ice shelves with $1325 \pm 235 \text{ Gt a}^{-1}$ to be the largest ablation process of Antarctic ice shelves. Although calving is dominating the ablation of the large Ross, Filchner and Ronne ice shelves, ten smaller ice shelves that drain the WAIS account for about half

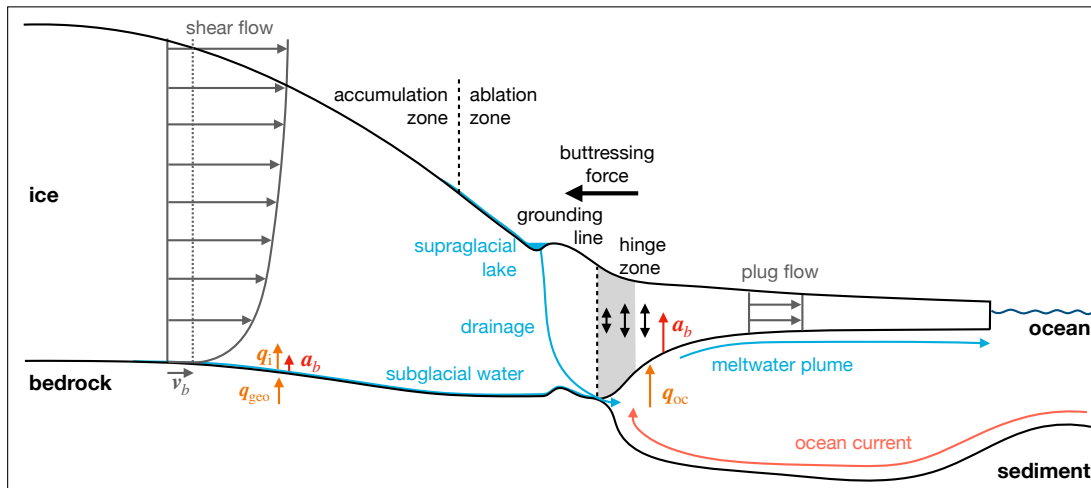


Figure 1.1: Ice sheet and ice shelf geometry with physical processes. The two ice flow types (shear flow for grounded ice and plug flow for floating ice) are marked in grey. The basal velocity is shown by v_b . Freshwater is marked in blue (supraglacial lakes, subglacial drainage, meltwater plume) and ocean currents in light red. Geothermal heat flux q_{geo} , oceanic heat flux q_{oc} and the heat flux within the ice q_i are coloured in orange. The basal melt rate a_b is shown in red with different sizes for grounded and floating ice. Dashed lines mark the position of the grounding line and the transition of the accumulation to the ablation zone. The grey shaded area marks the hinge zone and the vertical black arrows mark the tidal movement. The butressing force is shown by the black horizontal arrow.

of the mass loss as they suffer from warm ocean waters reaching their cavities (Rignot et al., 2013). While AIS is surrounded by band of ice shelves that are butressing the AIS (Fürst et al., 2016), only three glaciers with large floating extensions are left in Greenland: Nioghalvfjærdsbræ (79°N Glacier; 79NG), Ryder Glacier, and Petermann Gletscher. Wilson et al. (2017) found large basal melt rates under all three ice tongues and indications for present thinning of 79NG. Observations with satellites allow to quantify basal mass loss for wide areas, but the methods used are accompanied with considerable uncertainties and limited to freely floating parts. In situ measurements with precise ground-based radar techniques overcome these uncertainties and allow to determine spatial and temporal variability of basal melt rates (e.g. Nicholls et al., 2015; Stewart et al., 2019; Vaňková et al., 2020). These precise measurements are needed, since the accuracy of projections of future sea-level rise, such as ISMIP6 (Seroussi et al., 2020), depends greatly on the calibration of the basal melt rate parametrisation (Jourdain et al., 2020).

Figure 1.1 shows a sketch of an ice sheet with its floating extension. All relevant processes visualised in this sketch are discussed in this thesis.

1.2 Radioglaciology and other geophysical methods

The study of glaciers by using ice penetrating radar is called radioglaciology. In the course of a measurement, a pulsed radio wave, is transmitted via an antenna and penetrates the ice. The electromagnetic wave is reflected by inhomogeneities in the glacier and by the ice bed (grounded ice) or by the ice-ocean interface (floating ice). The returned signal is recorded by an antenna (Bogorodsky et al., 1985). Ice penetrating radar typically uses frequencies spanning High Frequency (HF; 3 – 30 MHz), Very High Frequency (VHF; 30 – 300 MHz) and Ultra High Frequency (UHF; 300 MHz–3 GHz; Schroeder et al., 2020). Airborne radar measurements (by mounting a radar device on an aircraft) as well as ground-based measurements (by pulling a radar behind a vehicle) enable measurements over large distances, whereas point measurements offer advantages in terms of vertical and temporal resolution.

Various properties of glaciers can be determined from radar echograms, such as the thickness and geometry of the glacier, the stratigraphy as well as englacial and subglacial properties. These include water-filled channels or basal conditions. Certain polarised measurements allow conclusions to be drawn about crystal orientation fabric due to its anisotropy (e.g. Hargreaves, 1978; Fujita et al., 2006). In addition to these properties which can be obtained from measurements at one point in time, repeated measurements allow analysing vertical displacements from which densification, vertical strain and basal melting can be analysed (e.g. Corr et al., 2002; Jenkins et al., 2006). By means of multiple repetitive measurements, e.g. by autonomous stations, changes over time can be determined, such as those caused by tides or seasonal cycles (Nicholls et al., 2015).

In addition to radioglaciology, other methods also allow the investigation of processes and properties of glaciers with corresponding advantages and disadvantages. Only their combination allows a comprehensive assessment of the properties of a glacier:

- Seismic waves from *active seismic measurements* penetrates the ice in a similar way to radar, but offer the advantage to also penetrate the bedrock or sediment and allow conclusions to be drawn about its properties. Furthermore, the seismic waves can penetrate through water and thus reveal the bathymetry of the cavity below ice shelves (e.g. Smith et al., 2020).
- *Firn* and *ice cores* enable the determination of a wide variety of properties with a very high vertical resolution. In addition to determining the stratigraphy and physical properties such as densities, temperatures and

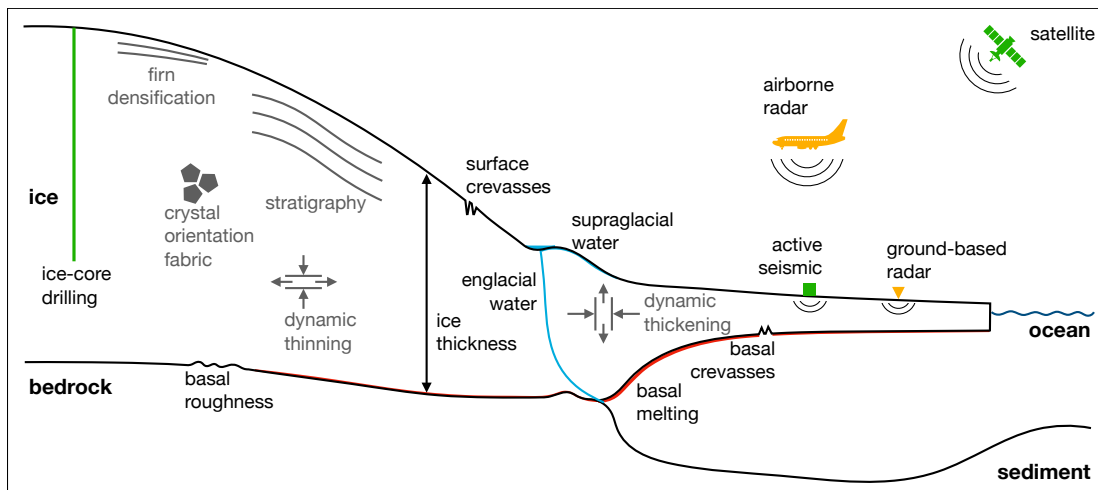


Figure 1.2: Radar and other geophysical methods and the investigated processes. Airborne and ground-based radar methods are visualised with orange symbols and other geophysical methods (ice-core drilling, active seismics and satellite remote sensing) are shown in green. The processes investigated by radar are e.g. ice thickness, firn densification, stratigraphy, crystal orientation fabric, dynamic thinning/thickening, surface/basal crevasses, supraglacial/englacial water, basal melting and basal roughness.

crystal orientation, chemical analyses can also be carried out to reconstruct the climatic history (e.g. [North Greenland Ice Core Project members, 2004](#); [Weikusat et al., 2009](#)). Due to the complex measurement, this method is very limited in its spatial coverage.

- *Satellite remote sensing* techniques offer the possibility of surveying large areas. In particular, different devices such as lasers, radar and optical sensors can be used to analyse surface and near surface properties. Digital elevation models of the ice surface allow conclusions to be drawn about the ice flow directions, changes in ice thickness and thus basal melt rates (e.g. [Howat et al., 2019](#); [Adusumilli et al., 2020](#)). Based on velocity fields, accelerations can be determined and the depth-averaged vertical strain estimated (e.g. [Alley et al., 2018](#); [Joughin et al., 2018](#); [Mouginot et al., 2019a](#)). Radar and optical sensors enable the detection of crevasses and supraglacial lakes and their drainage (e.g. [Neckel et al., 2020](#); [Schröder et al., 2020](#)).

Figure 1.2 shows processes and properties that can be determined using radar measurements on grounded glaciers and floating ice tongues. In addition to airborne and ground-based radar, other methods that are used in glaciology such as ice-core drilling, active seismics or satellite-remote sensing are also shown.

1.3 Objectives and thesis outline

The major objectives of this thesis are (1) the quantification of basal melting in key areas from phase-sensitive radar analysis and (2) combining in situ phase-sensitive measurements with other methodologies such as Global Navigation Satellite System (GNSS), remote sensing (airborne and satellite) and modelling in order to enhance understanding of processes driving changes in ice sheets and ice shelves. In addition, the assessment of limitations of detection from in situ measurements became a further objective of this work.

In the course of the project *Greenland Ice Sheet – Ocean Interaction* (GROCE) and *Filchner Ice Shelf Project* (FISP), measurements were performed with the phase-sensitive Radio Echo Sounder (pRES) on the floating tongue of 79NG, Greenland and the Filchner Ice Shelf (FIS), Antarctica, in order to quantify basal melt rates and to investigate the ice–ocean interaction in the sub-ice shelf cavities. The pRES was also used at the *East Greenland Ice-core Project* (EastGRIP) drill site to improve understanding of the ice dynamics of the Northeast Greenland Ice Stream (NEGIS), the largest ice stream in Greenland. The analysis of these measurements, in which the author was partly involved himself (at 79NG and EastGRIP), forms the basis of this thesis. However, a comprehensive analysis of basal processes requires a combination of further geophysical methods, which were either used in the course of the respective projects or other projects from the Alfred Wegener Institute (AWI), or whose data is freely accessible, and with modelling.

Previous work was done by Keith W. Nicholls who has developed the pRES (Nicholls et al., 2015) and Craig L. Stewart who wrote the original MATLAB codes for processing the pRES measurements (Stewart, 2018), which have been used as a basis of the data analysis in this thesis.

The structure of this thesis is as follows:

- Chapter 2 gives an introduction into ice dynamics and Chapter 3 into the energy balance at the ice base.
- Chapter 4 focuses on the phase-sensitive radio echo sounding and the according radar equations, processing and melt rate estimation.
- Chapter 5 introduces the Northeast Greenland Ice Stream, Greenland and includes the context of the research articles presented in Chapter 6 (*Indication of high basal melting at the EastGRIP drill site on the Northeast Greenland Ice Stream*) and Chapter 7 (*Extreme melt rates at Greenland’s largest floating ice tongue*).

- Chapter 8 introduces the Filchner Ice Shelf, Antarctica and includes the context of the research articles presented in Chapter 9 (*Basal melt of the southern Filchner Ice Shelf, Antarctica*) and Chapter 10 (*On the evolution of an ice shelf melt channel at the base of Filchner Ice Shelf, from observations and viscoelastic modeling*).
- Chapter 11 summarises the results of the publications and discusses the possibilities of the pRES device and future work.

Ice dynamics

2.1 Introduction

Ice streams of the Greenland or Antarctic Ice Sheets are large dynamic features with enhanced flow velocities, separated by shear zones from the slow moving regions of the ice sheet (Bennett, 2003). The horizontal ice flow velocities are only observed at the surface and often derived from remote sensing data (e.g., Joughin et al., 2018; Mouginot et al., 2019a).

Gravity sets up pressure gradients that cause a horizontal viscous flow of ice in the direction of the downward surface slope (see e.g. Cuffey and Paterson (2010)). When the ice is not frozen to the ground, sliding over the bed enhances the flow velocity as well as deformation of the bed, depending on whether the bed is rigid or deformable. Basal sliding generates a basal shear stress τ_b

$$\tau_b = -k^2 N \mathbf{v}_b \quad (2.1)$$

which depends on the basal drag coefficient k^2 , the effective pressure N (difference between the ice overburden pressure and the subglacial water pressure) and the basal sliding velocity \mathbf{v}_b (Cuffey and Paterson, 2010). Equation (2.1) is also known as *linear friction law* which related the basal shear stress to the sliding velocity.

However, basal sliding greatly depends on the subglacial hydrology. Liquid water, either from basal melting (e.g. due to a high geothermal heat flux) or from the drainage of supraglacial water, lubricates the base and enhances basal slip. Elevated water pressure may reduce the basal drag further (Bennett, 2003). As little is known about these basal processes, the formulation of a friction law, which is used to model basal sliding, is considered with uncertainties. These uncertainties cause inaccuracy in simulations projecting mean sea-level rise (Brondex et al., 2019). Therefore, more research must be done to determine the basal velocities of large ice streams and ice sheets. An indication of enhanced basal sliding could be obtained from the knowledge of basal melting, since a lubricated ice base facilitate sliding. The amount of basal melting of a fast moving ice stream is firstly measured at the NEGIS which results are presented in this thesis. Ice stream dynamics is also effected by the buttressing of the shelves or floating tongues (Dupont and Alley, 2005; Fürst et al., 2016). Even if the basal drag is negligible

at the ice–ocean interface of floating ice shelves, lateral shear and pinning points cause a buttressing force (e.g. [Rignot et al., 2004](#); [Scambos et al., 2004](#); [Joughin et al., 2012](#)).

Beside basal sliding, internal deformation of the viscoelastic material (so-called creep) contributes to the ice flow. Creep depends greatly on the ice temperature and the state of the mechanical anisotropy of the crystal orientation. For stresses acting parallel to the basal plane – the preferred slip direction of the ice crystal – the ice flow could be enhanced by about an order of magnitude ([Cuffey and Paterson, 2010](#)). A pronounced orientation is therefore a hint for deformation that can be assessed by ice core analysis. Due to the anisotropy of the dielectric constant of ice for radio-frequencies, radar measurements allow to infer information of the crystal orientation ([Hargreaves, 1978](#); [Fujita et al., 2006](#)) and thus of the ice dynamics ([Eisen et al., 2007](#)).

2.2 Kinematics

Kinematics are used to describe the deformation of ice based on displacements and velocities, without including the forces that cause the deformation.

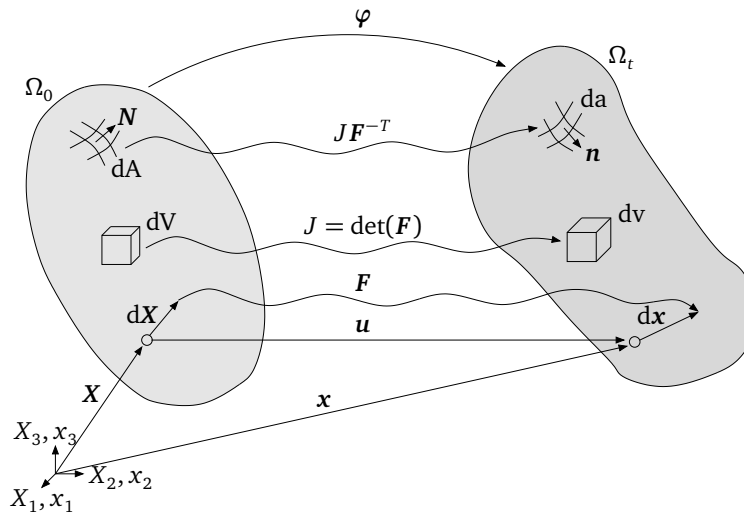


Figure 2.1: Continuum mechanics related material bodies. Material bodies in reference Ω_0 and present configuration Ω_t (from [Christmann, 2017](#)).

According to [Greve and Blatter \(2009\)](#), such a deformation transforms a body of material points, as it is usually defined in continuum mechanics, from its undeformed reference configuration into a deformed present configuration. The deformation φ (Fig. 2.1) maps the positions \mathbf{X} of the material points in the reference configuration Ω_0 to the positions \mathbf{x} in the present configuration Ω_t

$$\mathbf{x} = \varphi(\mathbf{X}, t). \quad (2.2)$$

This results in a displacement of material points from \mathbf{X} to \mathbf{x} , which is described by a displacement field \mathbf{u} :

$$\mathbf{u} = \mathbf{x} - \mathbf{X}. \quad (2.3)$$

In addition to the rigid body motion, it can also deform. The deformation gradient \mathbf{F} (tensor field of order 2) transforms line elements from the reference configuration ($d\mathbf{X}$) to the present configuration ($d\mathbf{x}$)

$$d\mathbf{x} = \mathbf{F}d\mathbf{X}, \quad (2.4)$$

and thus, it is defined as the material gradient of motion

$$\mathbf{F}(\mathbf{X}, t) = \frac{\partial \mathbf{x}}{\partial \mathbf{X}} \quad (2.5)$$

(Greve and Blatter, 2009; Christmann, 2017). Furthermore, the material time derivative of the deformation gradient $\dot{\mathbf{F}}$ is related to the velocity gradient \mathbf{l} in the present configuration

$$\mathbf{l} = \frac{\partial \mathbf{v}}{\partial \mathbf{x}} = \frac{\partial \mathbf{v}}{\partial \mathbf{X}} \frac{\partial \mathbf{X}}{\partial \mathbf{x}} = \dot{\mathbf{F}}\mathbf{F}^{-1} \quad (2.6)$$

with the velocity \mathbf{v} (Christmann, 2017).

The velocity gradient can be decomposed into a symmetric (\mathbf{d}) and an antisymmetric part (\mathbf{w})

$$\mathbf{l} = \underbrace{\frac{1}{2}(\mathbf{l} + \mathbf{l}^T)}_{\mathbf{d}} + \underbrace{\frac{1}{2}(\mathbf{l} - \mathbf{l}^T)}_{\mathbf{w}} \quad (2.7)$$

where \mathbf{d} is called *strain-rate tensor* and \mathbf{w} *spin tensor*. The strain-rate tensor \mathbf{d} is of particular importance in glaciology. For a small deformation setting in which a distinction between reference and present configuration is no longer made, the linearised strain-rate tensor is often labelled as $\dot{\boldsymbol{\epsilon}}$. Following Eq. 2.7, this symmetric strain-rate tensor is defined as

$$\dot{\boldsymbol{\epsilon}} = \dot{\epsilon}_{ij} = \frac{1}{2} \left(\frac{\partial v_i}{\partial j} + \frac{\partial v_j}{\partial i} \right) \quad (2.8)$$

with the indices i and j that stand for x , y and z and with the velocities v_x , v_y , v_z in x , y and z direction (Cuffey and Paterson, 2010). While the shear rate is described by the three independent non-diagonal components ($\dot{\epsilon}_{xy}$, $\dot{\epsilon}_{xz}$, $\dot{\epsilon}_{yz}$), the diagonal components ($\dot{\epsilon}_{xx}$, $\dot{\epsilon}_{yy}$, $\dot{\epsilon}_{zz}$) describe the extension and compression rate in normal direction. The *first invariant* of $\dot{\epsilon}_{ij}$ (the sum of the normal elements) is the divergence of the velocity field. Similar to the strain-rate tensor, the *strain*

tensor $\boldsymbol{\varepsilon}$ can be defined with the displacement \mathbf{u} instead of velocity:

$$\boldsymbol{\varepsilon} = \varepsilon_{ij} = \frac{1}{2} \left(\frac{\partial u_i}{\partial j} + \frac{\partial u_j}{\partial i} \right). \quad (2.9)$$

2.3 Ice thickness evolution

The ice thickness of ice sheets or glaciers can change due to different processes: internal deformation, surface and basal mass balance. The surface and basal mass balance are simply defined as the change in ice thickness per unit of time caused by accumulation/ablation at the surface and melting (or sometimes freezing) at the base. However, an expression for internal deformation must first be derived in order to state the ice thickness evolution equation.

Since ice is an incompressible material, the divergence of the velocity field is assumed to be zero:

$$\operatorname{div} \mathbf{v} = \frac{\partial v_x}{\partial x} + \frac{\partial v_y}{\partial y} + \frac{\partial v_z}{\partial z} = \dot{\varepsilon}_{xx} + \dot{\varepsilon}_{yy} + \dot{\varepsilon}_{zz} = 0. \quad (2.10)$$

This equation is known as the *continuity equation* (Cuffey and Paterson, 2010). Its vertical integration over the entire ice column H

$$\int_0^H \frac{\partial v_x}{\partial x} dz + \int_0^H \frac{\partial v_y}{\partial y} dz + \int_0^H \frac{\partial v_z}{\partial z} dz = 0 \quad (2.11)$$

(Greve and Blatter, 2009) leads to an expression for the divergence of the volume flux \mathbf{Q} by using Leibniz's integration rule

$$\begin{aligned} \operatorname{div} \mathbf{Q} &= \frac{\partial}{\partial x} Q_x + \frac{\partial}{\partial y} Q_y = \frac{\partial}{\partial x} \int_0^H v_x dz + \frac{\partial}{\partial y} \int_0^H v_y dz \\ &= - \int_0^H \frac{\partial v_z}{\partial z} dz = - \int_0^H \dot{\varepsilon}_{zz} dz \end{aligned} \quad (2.12)$$

with the volume flux \mathbf{Q}

$$\mathbf{Q} = \begin{pmatrix} Q_x \\ Q_y \end{pmatrix} = \begin{pmatrix} \int_0^H v_x dz \\ \int_0^H v_y dz \end{pmatrix}. \quad (2.13)$$

Thus, the divergence of the volume flux (Eq. 2.12) represents the change in ice thickness due to strain, which equals the vertically integrated vertical strain-rate.

Finally, the ice thickness evolution equation is

$$\frac{\partial H}{\partial t} = -\operatorname{div} \mathbf{Q} + a_s - a_b \quad (2.14)$$

(Greve and Blatter, 2009), with the ice thickness H , the time t , the volume flux \mathbf{Q} , the surface mass balance a_s and the basal melt rate a_b (positive for melting). As this equation is based on the continuity equation (Eq. 2.10) which is valid for bubble free ice at a density of 917 kg m^{-3} , it does not hold for firn and ice with lower densities and therefore, Eq. 2.14 does not represent densification processes.

The ice thickness evolution equation (Eq. 2.14) forms the basis for deriving basal melt rates from satellite-remote sensing and ground-based radar measurements, since all other quantities can be estimated from such measurements.

Basal energy balance

3.1 Introduction

Observations show a strong variability of the basal melt rate depending on the local conditions. Melt rates are between zero and a few decimetre per year on grounded ice (e.g. [Dahl-Jensen et al., 2003](#); [MacGregor et al., 2016](#)) and can reach by far larger values of $> 100 \text{ m a}^{-1}$ below ice shelves (e.g. [Washam et al., 2019](#); [Shean et al., 2019](#); [Adusumilli et al., 2020](#)). The reason for this are different basal processes that contribute to melting. The base of grounded ice is mainly heated by the geothermal heat flux and occasionally by supra- or subglacial melt water, which causes a heat flux of up to a few watts per square meter (e.g. [Fahnestock et al., 2001a](#); [Zeising and Humbert, 2021b](#)). Warm ocean currents, on the other hand, have the potential to cause a heat transport of hundreds of Gigawatts into the cavities below the ice shelves (e.g. [Schaffer et al., 2020](#)), which corresponds to a heat flux into the ice of $\gg 100 \text{ W m}^{-2}$.

In this chapter, the relevant equations of the energy balance and its jump condition are introduced, on the basis of which the basal melt rate can be calculated. In addition, a brief introduction to the calculation of the oceanic heat flux is provided.

3.2 Energy balance

3.2.1 Material-independent energy balance

The basis for considering the energy balance is the first law of thermodynamics. It states that the sum of the thermal and mechanical energy is conserved. By determining the energy density, the energy flux and the supply of energy density, the local energy balance can be derived, which corresponds to the first law of thermodynamics ([Greve and Blatter, 2009](#)). Each of the three components has a thermal and a mechanical part:

- Energy density:

$$g = \underbrace{\rho u}_{\text{thermal}} + \underbrace{\rho \frac{v^2}{2}}_{\text{mechanical}} \quad (3.1)$$

where the thermal part is the specific internal energy density (density ρ , specific internal energy u) and the mechanical is the kinetic energy density

(velocity \mathbf{v}).

- Energy flux density:

$$\phi = \underbrace{\mathbf{q}}_{\text{thermal}} - \underbrace{\mathbf{t} \cdot \mathbf{v}}_{\text{mechanical}} \quad (3.2)$$

where the thermal part is the heat flux and the mechanical is the negative work of surface forces (Cauchy stress tensor \mathbf{t} , velocity \mathbf{v}).

- Supply of energy density:

$$s = \underbrace{\rho r}_{\text{thermal}} + \underbrace{\mathbf{f} \cdot \mathbf{v}}_{\text{mechanical}} \quad (3.3)$$

where the thermal part is the specific radiation power density (specific radiation power r) and the mechanical is the work of the volume forces (volume force \mathbf{f}).

The resulting energy balance is

$$\rho \frac{d}{dt} \left(u + \frac{v^2}{2} \right) = -\text{div } \mathbf{q} + \text{div } (\mathbf{t} \cdot \mathbf{v}) + \rho r + \mathbf{f} \cdot \mathbf{v}. \quad (3.4)$$

This can be simplified further to

$$\rho \frac{du}{dt} = -\text{div } \mathbf{q} + \text{tr } (\mathbf{t} \mathbf{d}) + \rho r \quad (3.5)$$

with the trace (tr) of the strain-rate tensor \mathbf{d} .

3.2.2 Energy balance equation for ice

Using constitutive equations, the material-independent energy balance equation can be converted into a field equation for the temperature. Three material equations are required for this:

- (1) The caloric equation of state is the constitutive equation for internal energy and describes the relation between a change in internal energy and temperature (Greve and Blatter, 2009):

$$\frac{du}{dt} = c_i(T) \frac{dT}{dt} \quad (3.6)$$

with the temperature T in Kelvin and the temperature-dependent specific heat capacity $c_i(T)$ of ice, which is

$$c_i(T) = (146.3 + 7.253T[K]) \text{ J kg}^{-1} \text{ K}^{-1}, \quad (3.7)$$

(Ritz, 1987). For a temperature of 273.15 K (or 0 °C), the specific heat capacity of ice is $c_i(273.15 \text{ K}) = 2127.5 \text{ J kg}^{-1} \text{ K}^{-1}$.

(2) Fourier's law is the constitutive equation for heat conduction and describes that temperature differences within a homogeneous system cause heat to be transported through conduction:

$$\mathbf{q} = -\kappa_i(T) \text{grad } T \quad (3.8)$$

with the temperature-dependent heat conductivity $\kappa_i(T)$

$$\kappa_i(T) = 9.828 e^{-0.0057 T[\text{K}]} \text{ W m}^{-1} \text{ K}^{-1}, \quad (3.9)$$

(Ritz, 1987; Greve and Blatter, 2009).

(3) The constitutive equation for stress that represents strain heating is

$$\text{tr}(\mathbf{td}) = 2\eta \text{tr}\mathbf{d}^2 \quad (3.10)$$

with the shear viscosity η .

Based on these constitutive equations, the energy balance equation for ice can be derived from the material-independent energy balance (Greve and Blatter, 2009):

$$\rho c_i(T) \frac{dT}{dt} = \text{div}(\kappa(T) \text{grad } T) + 2\eta \text{tr}\mathbf{d}^2 + \rho r, \quad (3.11)$$

which is the temperature evolution equation.

3.2.3 Melting of ice

This section deals with the calculation of the amount of energy necessary to heat and melt a certain volume of ice.

The amount of energy Q_i , needed to raise the temperature T of ice of the volume V by ΔT is

$$Q_i = c_i(T) \rho_i V \Delta T \quad (3.12)$$

with the temperature-dependent specific heat capacity of ice $c_i(T)$ (Eq. 3.7).

The temperature T_m , to which the ice must be heated before melting, is pressure-dependent. The hydrostatic pressure p reduces the melting point of ice ($T_0 = 273.15 \text{ K}$ for low pressures) by a factor of $\mathcal{B} = 7.42 \times 10^{-8} \text{ K Pa}^{-1}$

$$T_m = T_0 - \mathcal{B}p, \quad (3.13)$$

(Greve and Blatter, 2009; Cuffey and Paterson, 2010). However, the Clausius-

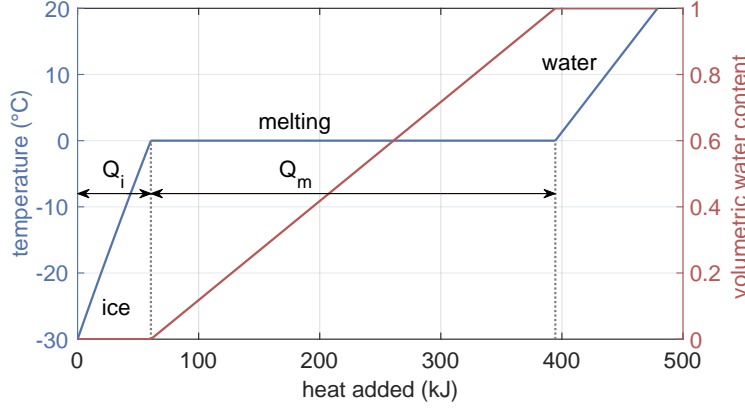


Figure 3.1: Temperature curve of ice/water and volumetric water content. Temperature curve of ice/water (blue) and volumetric water content (red) as function of added heat, starting with ice at a temperature of -30°C . Q_i marks the amount of heat necessary for heating the ice to 0°C and Q_m the amount of heat for melting.

Clapeyron constant \mathcal{B} applies for pure ice. Under realistic conditions with air-saturated ice, \mathcal{B} is $9.8 \times 10^{-8} \text{ K Pa}^{-1}$. For ice densities between 900 and 910 kg m^{-3} , the pressure melting point reduces by $8.7 \times 10^{-4} \text{ K m}^{-1}$ of ice (Greve and Blatter, 2009).

A phase change from solid to liquid requires an increase in enthalpy without a change in temperature. The amount of energy is known as the latent heat of fusion. For ice at a temperature of $T = 273.15 \text{ K}$, the latent heat of fusion L is $334,000 \text{ J kg}^{-1}$ (Cuffey and Paterson, 2010). Thus, the amount of energy Q_m needed to melt ice of the volume V is

$$Q_m = L \rho_i V. \quad (3.14)$$

Figure 3.1 shows the temperature curve as a function of added heat to 1 kg ice at a temperature of -30°C (or 243.15 K). To heat the ice by $\Delta T = 30^{\circ}\text{C}$ to the melting point, $Q_i = 60.6 \text{ kJ}$ (Eq. 3.12) is needed but more than five times as much for melting itself ($Q_m = 334 \text{ kJ}$). The volumetric water content rises when heat is added to ice at the pressure melting point.

3.3 Energy balance at ice base

From the continuum mechanical perspective, the basal melt rate can be derived from the energy balance equation at the ice base. This approach defines the jump ($[[\psi]]$) of a quantity ψ as $[[\psi]] = \psi_+ - \psi_-$, with the lithosphere/ocean as the positive side and ice as the negative side. In this way, the difference in the quantity ψ across the interface can be described (Greve and Blatter, 2009). The

jump condition of the energy at the ice base is

$$\llbracket \mathbf{q} \cdot \mathbf{n} \rrbracket - \llbracket \mathbf{v} \cdot \mathbf{t} \cdot \mathbf{n} \rrbracket + \rho_i a_b \llbracket u \rrbracket = 0 \quad (3.15)$$

with the jump of the heat flux $\llbracket \mathbf{q} \cdot \mathbf{n} \rrbracket$ (heat flux \mathbf{q} , normal vector \mathbf{n}), the jump in work of the surface force $\llbracket \mathbf{v} \cdot \mathbf{t} \cdot \mathbf{n} \rrbracket$ (velocity \mathbf{v}), the ice density ρ_i , the basal melt rate a_b and the jump of the internal energy $\llbracket u \rrbracket$ (Greve and Blatter, 2009).

The jump of the heat flux is the difference between the heat flux on the positive side q_+ and the one on the ice side q_- , which is described by Fourier's law (Eq. 3.8).

The heat flux on the positive side depends on the basal properties:

- Grounded ice with cold base: q_+ is the geothermal heat flux q_{geo}^\perp
- Grounded ice with temperate base: q_+ arises from the geothermal heat flux or from the subglacial water q_{sw}^\perp
- Floating ice: q_+ is the oceanic heat flux q_{oc}^\perp

Thus, the jump of the heat flux is

$$\llbracket \mathbf{q} \cdot \mathbf{n} \rrbracket = \underbrace{q_{\text{geo}/+\text{sw}/\text{oc}}^\perp}_{q_+} - \underbrace{\kappa_i(T) \text{grad } T \cdot \mathbf{n}}_{q_-} \quad (3.16)$$

Likewise, the jump in work of surface forces depends on the basal properties, namely the velocities of the subglacial water/ocean $\mathbf{v}_{\text{sw}/\text{oc}}$, the (sliding) velocity of the ice base \mathbf{v}_b and the Cauchy stresses on both sides $\mathbf{t}_{\text{sw}/\text{oc}}, \mathbf{t}_i$

$$\llbracket \mathbf{v} \cdot \mathbf{t} \cdot \mathbf{n} \rrbracket = \underbrace{\mathbf{v}_{\text{sw}/\text{oc}} \cdot \mathbf{t}_{\text{sw}/\text{oc}} \cdot \mathbf{n}}_{\mathbf{v}_+ \cdot \mathbf{t}_+} - \underbrace{\mathbf{v}_b \cdot \mathbf{t}_i \cdot \mathbf{n}}_{\mathbf{v}_- \cdot \mathbf{t}_-} \quad (3.17)$$

As the velocity of the bedrock is zero, $\mathbf{v}_+ \cdot \mathbf{t}_+ = 0$ and thus, the jump in this case is $\llbracket \mathbf{v} \cdot \mathbf{t} \cdot \mathbf{n} \rrbracket = -\mathbf{v}_b \cdot \mathbf{t}_i \cdot \mathbf{n}$.

The jump of the internal energy $\llbracket u \rrbracket$ is equal to the latent heat of ice melt L .

Finally, the jump condition of the energy at the ice base and solved for a_b is for the three cases:

- Grounded ice, without subglacial water:

$$a_b = \frac{q_{\text{geo}}^\perp - \kappa_i(T) \text{grad } T + \mathbf{v}_b \cdot \mathbf{t}_i \cdot \mathbf{n}}{\rho_i L} \quad (3.18)$$

- Grounded ice, with subglacial water

$$a_b = \frac{q_{\text{sw}}^\perp - \kappa_i(T) \text{grad } T - \mathbf{v}_{\text{sw}} \cdot \mathbf{t}_{\text{sw}} \cdot \mathbf{n} + \mathbf{v}_b \cdot \mathbf{t}_i \cdot \mathbf{n}}{\rho_i L} \quad (3.19)$$

- Floating ice

$$a_b = \frac{q_{oc}^\perp - \kappa_i(T) \text{grad } T - \mathbf{v}_{oc} \cdot \mathbf{t}_{oc} \cdot \mathbf{n} + \mathbf{v}_b \cdot \mathbf{t}_i \cdot \mathbf{n}}{\rho_i L} \quad (3.20)$$

3.4 Oceanic heat flux

The oceanic heat flux into a boundary layer along the ice base plays a key role for the basal mass loss of ice shelves. To compute the oceanic heat flux, models like the Finite Element Sea Ice-Ocean Model (FESOM) use a three-equation method (Timmermann et al., 2012). These three equations determine the temperature and salinity of such thin boundary layer and the basal melt rate (Hellmer and Olbers, 1989; Holland and Jenkins, 1999):

$$-\rho_i L a_b = \rho_{oc} c_{p,oc} \gamma_T (T_{oc} - T_b) + \kappa_i(T) \text{grad } T_i \quad (3.21)$$

$$-\rho_i S_b a_b = \rho_{oc} \gamma_S (S_{oc} - S_b) \quad (3.22)$$

$$T_b = 0.901 \text{ }^\circ\text{C} - 0.0575 \text{ }^\circ\text{C } S_b + 7.61 \times 10^{-4} \text{ }^\circ\text{C m}^{-1} z_b. \quad (3.23)$$

Eq. (3.21) states the heat balance of the boundary layer along the ice base with the oceanic heat flux q_{oc} derived from

$$q_{oc} = \rho_{oc} c_{p,oc} \gamma_T (T_{oc} - T_b) \quad (3.24)$$

with the density of the ocean ρ_{oc} , the specific heat capacity of ocean $c_{p,oc} = 4180 \text{ J kg}^{-1} \text{ K}^{-1}$, the turbulent heat flux γ_T and the temperatures of the ocean T_{oc} and of the boundary layer T_b . This equation assumes that the temperature of the boundary layer is at the (pressure-dependent) in situ freezing point, which is derived from Eq. (3.23), with the salinity S_b and the ice draft z_b (Jenkins, 1991). The salinity itself is governed by Eq. (3.22). The term on the left-hand side represents the salt flux from basal melting and the term from the right-hand side the turbulent transfer of salt between the ocean with salinity S_{oc} and the boundary layer with the turbulent salt flux coefficient γ_S . Following Jenkins (1991), the turbulent heat flux coefficient γ_T and the turbulent salt flux coefficient γ_S are

$$\gamma_T = \frac{u_\star}{2.12 \ln \left(u_\star \frac{L}{\nu} \right) + 12.5 \text{Pr}^{\frac{2}{3}} - 8.68} \quad (3.25)$$

$$\gamma_S = \frac{u_\star}{2.12 \ln \left(u_\star \frac{L}{\nu} \right) + 12.5 \text{Sc}^{\frac{2}{3}} - 8.68} \quad (3.26)$$

with the friction velocity $u_\star = \sqrt{2.5 \times 10^{-3} \mathbf{v}_{oc}^2}$, the flow velocity \mathbf{v}_{oc} , the kine-

matic viscosity of sea water $\nu = 1.95 \times 10^{-6} \text{ m}^2 \text{ s}^{-1}$, a characteristic length scale $\mathcal{L} = 10 \text{ m}$ and the dimensionless Prandtl number $\text{Pr} = 13.8$ and Schmidt number $\text{Sc} = 2432$ of seawater.

The temperature of the ocean and its speed have the greatest influence on the oceanic heat flux. Ocean temperatures of $+1 \text{ }^\circ\text{C}$ and flow velocities of 0.25 m s^{-1} can generate heat fluxes that exceed 1500 W m^{-2} , which causes extreme melt rates of above 100 m a^{-1} .

Phase-sensitive radio echo sounding

4

This chapter first gives a brief introduction of the basics of radio echo sounding on ice and the pRES device. Then, the signal and data processing is described in detail, followed by the method of determining the spatial and temporal variability of basal melt rates.

4.1 Basics of radio echo sounding on ice

Radio echo sounding or radio detection and ranging (Radar) is an active remote-sensing method in which electromagnetic waves are emitted by one or more antennas and the returned signal is recorded. In the meantime, the electromagnetic wave propagates through carrier media whose properties control the propagation. These properties are:

- the complex dielectric permittivity

$$\varepsilon = \varepsilon_0 \varepsilon_r = \varepsilon_0 (\varepsilon' - i\varepsilon'') \quad (4.1)$$

with the permittivity of free space $\varepsilon_0 = 8.854 \times 10^{-12} \text{ A m V}^{-1} \text{ s}^{-1}$ and the relative permittivity ε_r , that has a real ε' and an imaginary part ε'' (Bogorodsky et al., 1985). Kovacs et al. (1995) derived an equation for the real part of the relative permittivity of ice

$$\varepsilon' = (1 + 0.000845 \text{ kg } \rho)^2 \quad (4.2)$$

which depends on the ice density ρ . The imaginary part, also known as loss factor,

$$\varepsilon'' = \frac{\sigma}{\omega \varepsilon_0} \quad (4.3)$$

depends on the conductivity σ and the angular frequency ω of an external electric field (Bogorodsky et al., 1985).

- the complex magnetic permeability

$$\mu = \mu_0 \mu_r \quad (4.4)$$

with the magnetic permeability of free space $\mu_0 = 1.25710^{-6} \text{ V s A}^{-1} \text{ m}^{-1}$

and the relative magnetic permeability μ_r . Since ice is a non-magnetic material, the relative magnetic permeability is $\mu_r = 1$ (Bogorodsky et al., 1985).

Maxwell's equations connect these material properties which leads to the differential equation for the electromagnetic field

$$\Delta \mathbf{E} - \mu_0 \varepsilon_0 \varepsilon_r \frac{\partial^2 \mathbf{E}}{\partial t^2} = 0 \quad (4.5)$$

where \mathbf{E} is the electric field. A solution of the wave equation for the electromagnetic field is given by

$$\mathbf{E} = E_0 e^{i(\omega t - kz)} \quad (4.6)$$

for an electric field vector in the x-y-plane and a propagation along the z-axis (vertical axis). The wavenumber k is the magnitude of the propagation vector.

The propagation velocity of the electromagnetic wave in ice c_i is

$$c_i = \frac{c}{\sqrt{\varepsilon_r}} \quad (4.7)$$

and the wavelength is

$$\lambda = \frac{c_i}{f} \quad (4.8)$$

with the speed of light $c = 299,792,458 \text{ m s}^{-1}$ and the frequency f . The density, temperature and frequency dependent relative permittivity of ice is in the range of 3.15 – 3.18 and thus the propagation velocity is $c_i \approx 168 - 169 \times 10^6 \text{ m s}^{-1}$ (Fujita et al., 2000). Assuming a frequency of 300 MHz, the resulting wavelength in ice is roughly 0.56 m.

If a propagating electromagnetic wave reaches an interface between two media with different electrical properties, one part of the energy is reflected and another part is refracted (Fig. 4.1). For a plane wave incident on a planar interface between two homogeneous, isotropic media, the reflection coefficient is

$$R_{1,2} = \frac{E_1}{E_0} = \frac{\sqrt{\varepsilon_{r1}} - \sqrt{\varepsilon_{r2}}}{\sqrt{\varepsilon_{r1}} + \sqrt{\varepsilon_{r2}}} \quad (4.9)$$

and the transmission coefficient $T_{1,2}$

$$T_{1,2} = \frac{E_2}{E_0} = \frac{2\sqrt{\varepsilon_{r1}}}{\sqrt{\varepsilon_{r1}} + \sqrt{\varepsilon_{r2}}} \quad (4.10)$$

with the complex amplitudes of incident E_0 , reflected E_1 , and refracted wave E_2 . With Snell's law, the angle of incidence (θ_1) and refracted wave (θ_2) can be

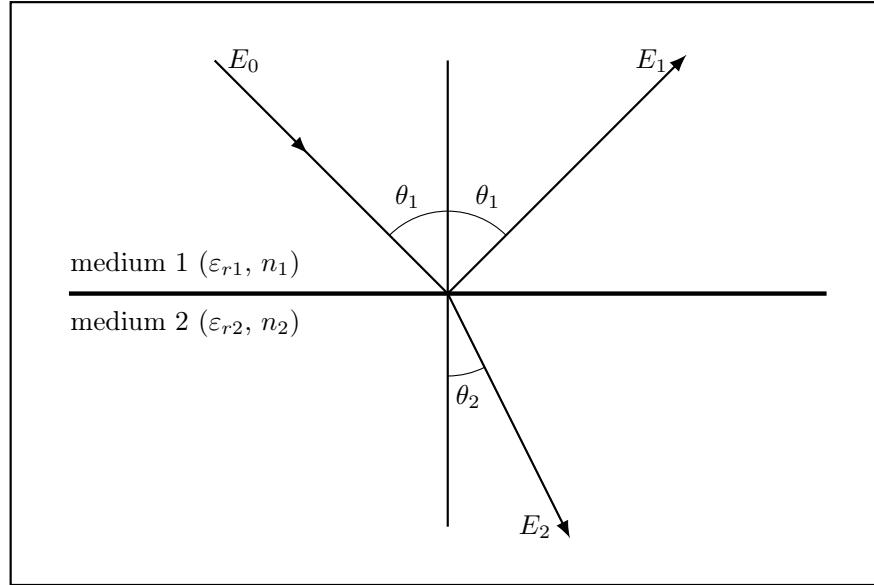


Figure 4.1: Reflection and refraction of an electromagnetic wave (Zeising, 2018). A plane wave with a complex amplitude E_0 incide with an angle of θ_1 to a planar interface between two homogeneous isotropic media. The reflected wave has a complex amplitude E_1 and an angle of θ_1 . The refracted wave has a complex amplitude E_2 and an angle of θ_2 .

calculated

$$\frac{\sin \theta_2}{\sin \theta_1} = \frac{\sqrt{\varepsilon_{r1}}}{\sqrt{\varepsilon_{r2}}} = \frac{n_1}{n_2} \quad (4.11)$$

with the refractive indexes n_1 and n_2 for the two media (Bogorodsky et al., 1985).

Assuming a propagating wave with a frequency in the VHF-range reaches the ice–ocean interface ($\varepsilon_{r1} = 3.15$ (ice), $\varepsilon_{r2} = 88$ (water at 0 °C; Andryieuski et al., 2015)), the reflection coefficient is -0.68 and the transmission coefficient 0.32 . Thus, 68% of the incident energy is reflected at the ice–ocean interface.

4.2 Phase-sensitive radio echo sounding

In order to measure changes in ice-sheet thickness, Nye et al. (1972) suggested a method to improve the sensitivity to vertical displacements by studying the phase history of the basal return. After the first phase-sensitive radio echo sounders were developed (e.g. Walford and Harper, 1981), Corr et al. (2002) advanced the theory of Nye et al. (1972) and presented a method that uses the phase information to infer basal melt rates of ice shelves.

Since the pRES – a modern phase-sensitive radio echo sounder, able to measure autonomously over longer periods of time – has been developed by Brennan et al. (2014) and Nicholls et al. (2015), many studies have used this technique to deter-

mine basal melt rates of ice shelves (e.g. Marsh et al., 2016; Stewart et al., 2019; Vaňková et al., 2020; Washam et al., 2019). The pRES is a ground-based radar, designed for measuring vertical displacements of englacial and basal reflections from repeated Lagrangian measurements (Brennan et al., 2014; Nicholls et al., 2015). Equipped with two broad band frame or bow-tie antennas, it allows the autonomous recording of time series over a longer period of time (several months to more than a year), depending on the power source and storage capacity. The pRES is a Frequency-Modulated Continuous Wave (FMCW) radar that transmits a tone sweep – called *chirp* – ranging from 200 to 400 MHz over a period of 1 s (Nicholls et al., 2015) (see Tab. 4.1 for device specifications). In order to improve the signal-to-noise ratio, several chirps (typically between 20 and 100) are transmitted within a single measurement. The ensemble of chirps is called *burst*. The returned signal is mixed with the transmitted one to obtain a de-ramped signal. The frequencies of the de-ramped signal (f_d) depend on the delay between the transmitted and received chirps and are therefore equal to the Two Way Travel Time (TWT) of the signal. After low pass filtering, the signal is digitised by the Analogue-to-Digital Converter (ADC) with sampling rate of 40 kHz (Nicholls et al., 2015). Figure 4.2 shows a pRES measurement at the 79NG.

Table 4.1: pRES specifications (Brennan et al., 2014)

Name	Symbol	Value	Unit
Bandwidth	B	200	MHz
Centre frequency	ω_c	300	MHz
Pulse duration	T	1	s
Transmitting power		100	mW
ADC Sample rate		40	kHz

4.3 Phase-sensitive FMCW radar theory

This section gives the basic equations for signal processing of phase-sensitive FMCW radar measurements like the pRES by following Brennan et al. (2014).

4.3.1 Target range

Starting with the transmitted signal as a function of time t , the instantaneous frequency $\omega_t(t)$ is

$$\omega_t(t) = \omega_c + K \left(t - \frac{T}{2} \right), \quad 0 \leq t \leq T \quad (4.12)$$

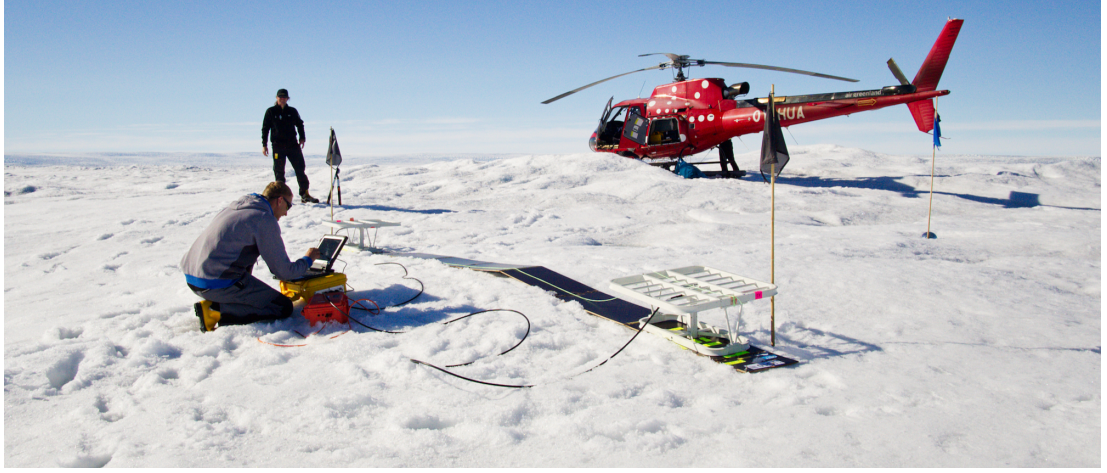


Figure 4.2: pRES measurement at 79NG. The pRES is the yellow box below the computer. Bamboos mark the location of two frame antennas. The photo was taken by *Niklas Neckel* (22 July 2018).

and the corresponding instantaneous phase $\Phi_t(t)$

$$\Phi_t(t) = \omega_c t + \frac{Kt^2}{2} - \frac{KTt}{2} + \text{const}, \quad 0 \leq t \leq T \quad (4.13)$$

with the centre frequency ω_c , the chirp duration T and the chirp gradient

$$K = \frac{2\pi B}{T},$$

that depends on the bandwidth B .

The received echo from a target at range R has the frequency $\omega_r(t)$

$$\omega_r(t) = \omega_c + K \left((t - \tau) - \frac{T}{2} \right), \quad 0 \leq t \leq T \quad (4.14)$$

and the phase $\Phi_r(t)$

$$\Phi_r(t) = \omega_c(t - \tau) + \frac{K(t - \tau)^2}{2} - \frac{KT(t - \tau)}{2} + \text{const}, \quad 0 \leq t \leq T \quad (4.15)$$

with the TWT τ

$$\tau = \frac{2R}{c_i}.$$

Next, the reflector range can be derived from the de-ramped frequency ω_d , which is the difference between the transmitted (Eq. 4.12) and received frequency (Eq. 4.14)

$$\omega_d(t) = \omega_t(t) - \omega_r(t) = K\tau = \frac{4\pi BR}{Tc_i}. \quad (4.16)$$

Solving Eq. 4.16 for the reflector range R leads to the coarse range R_c

$$R_c = \frac{\omega_d \Gamma c_i}{4\pi B} = \frac{f_d \Gamma c_i}{2B} \quad (4.17)$$

with $f_d = \omega_d(2\pi)^{-1}$.

Similar to the de-ramped frequency, the de-ramped phase Φ_d is the difference between the transmitted (Eq. 4.13) and received phase (Eq. 4.15)

$$\Phi_d(t) = \Phi_t(t) - \Phi_r(t) = \omega_c \tau + K\tau \left(t - \frac{T}{2} \right) - \frac{K\tau^2}{2}. \quad (4.18)$$

For the chirp centre ($t = \frac{T}{2}$), the de-ramped phase Φ_{dc} is

$$\Phi_{dc} = \omega_c \tau - \frac{K\tau^2}{2}. \quad (4.19)$$

Here, $\omega_c \tau$ is the crucial phase term while the second (phase offset) term $K\tau^2/2$ is negligible due to its small size (Brennan et al., 2014). Thus, Eq. 4.19 becomes

$$\Phi_{dc} \approx \omega_c \tau = \omega_c \frac{2R}{c_i} = \frac{4\pi R}{\lambda_c} \quad (4.20)$$

with the wavelength of the centre frequency λ_c which is

$$\lambda_c = \frac{2\pi c_i}{\omega_c}.$$

With that, the fine range R_f is

$$R_f = \frac{\lambda_c \Phi_{dc}}{4\pi}. \quad (4.21)$$

4.3.2 Range resolution

The resolution in the frequency space Δf_d is given by

$$\Delta f_d = \frac{1}{T}. \quad (4.22)$$

With the chirp duration of $T = 1$ s, this leads to a resolution in the frequency space of $\Delta f_d = 1$ Hz. Thus, the coarse range resolution is

$$\Delta R_c = \frac{\Delta f_d \Gamma c_i}{2B} = \frac{c_i}{2B} \quad (4.23)$$

and depends on c_i and B . With a propagation velocity in ice of $c_i = 168,914,000$ m s⁻¹, the coarse range resolution is 0.422 m.

The footprint of the antenna beamwidth is resolution-limited. It has a radius r of

$$r = \sqrt{2R\Delta R_c} \quad (4.24)$$

with the range R and the coarse range resolution ΔR_c . For a range of $R = 2000$ m, the radius of the footprint is $r = 41.09$ m.

Due to a limited resolution of the de-ramped phase $\Delta\Phi_{dc}$, the resolution of the R_f is

$$\Delta R_f = \frac{\lambda_c \Delta\Phi_{dc}}{4\pi}. \quad (4.25)$$

The resolution of the phase is about 1° (Nicholls et al., 2015). Hence, the de-ramped resolution is about $\Delta\Phi_{dc} \approx \frac{1}{180}\pi$. Using the centre wavelength of $\lambda_c = 0.563$ m, the fine range resolution is roughly 1 mm.

In order to achieve an unambiguously determined range from the phase, its variation over a range bin

$$\Delta(\omega_c\tau) = \omega_c \frac{2\Delta R_c}{c_i} = \frac{\omega_c}{B} \quad (4.26)$$

should be less than 2π (Brennan et al., 2014). For a centre frequency of $\omega_c = 2\pi \cdot 300$ MHz and the bandwidth of $B = 200$ MHz, this leads to a phase variation of $\Delta(\omega_c\tau) = 3\pi$ over one bin. This means that for the given parameters an unambiguous range measurement is not possible, as it prevents unwrapping.

However, the problem can be solved by artificially increasing the resolution in frequency space Δf_d , a method called 'zero-padding'. Zeros are added to the raw data to increase the length by a 'pad factor' p . This increases the resolution in the frequency space (after applying a Fast Fourier Transformation (FFT)) by a factor of p

$$\Delta f_d = \frac{1}{Tp} \quad (4.27)$$

and the range resolution becomes

$$\Delta R_c = \frac{c_i}{2Bp}. \quad (4.28)$$

The higher resolution is achieved by an interpolation at the FFT. The resulting phase variation over one bin after zero-padding is

$$\Delta\left(\frac{\omega_c\tau}{p}\right) = \frac{\omega_c}{Bp}. \quad (4.29)$$

Using a pad-factor of $p = 2$, the phase variation is $\Delta(\omega_c\tau 2^{-1}) = \frac{3}{2}\pi \leq 2\pi$. However a pad-factor of $p = 8$ is used for all data presented in this thesis. This

leads to a range resolution in the ice of $\Delta R_c = 0.053$ m.

4.4 Data processing

In the following, the processing of the raw data is described to obtain an amplitude-range profile. These processing steps were first described by Stewart (2018). The raw data of a measurement (burst) consists of the voltage of the de-ramped signal and the time after the beginning of transmission of every chirp (Fig. 4.3).

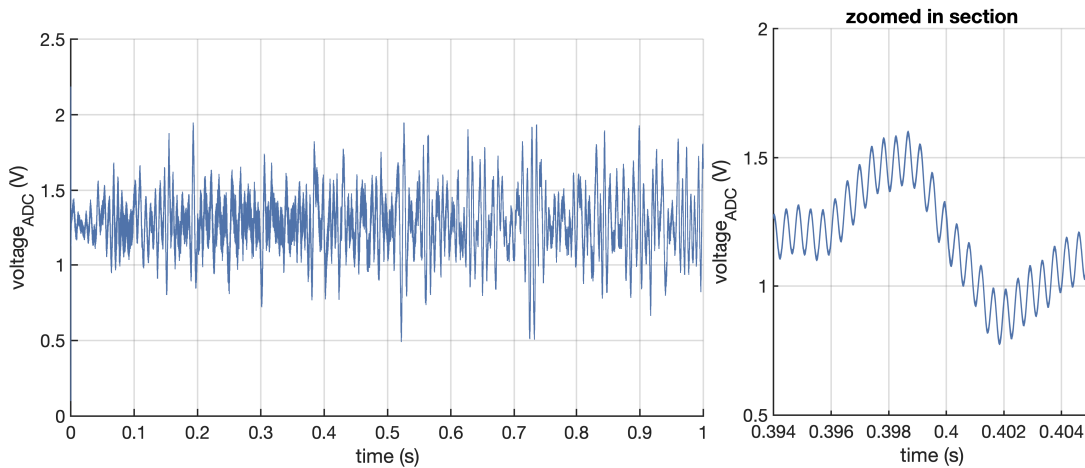


Figure 4.3: Raw data of pRES measurement. Measurement performed at FIS, Antarctica. (a) Raw data of all 100 chirps (voltage after ADC) as a function of chirp duration. (b) Zoomed in section of a part of (a).

The raw data is a function of time but the frequency contains the information of the reflector range (Eq. 4.17). Therefore, it is necessary to transform the signal into the frequency space with an FFT to obtain the time imaging. Each sample in the time space was averaged for all (accepted) chirps before calculating the FFT. The result of the FFT is a complex number Z for each de-ramped frequency. The amplitude A is the absolute value of Z given in decibel

$$A = 20 \log_{10}(|Z|).$$

The phase φ is the argument of Z , which means it is the angle between the positive real axis and the complex number

$$\varphi = \angle Z.$$

To finally obtain the TWT for the amplitude profile, the de-ramped frequency f_d is converted to TWT

$$\tau = \frac{f_d \Gamma}{B}. \quad (4.30)$$

The transformation from a time (TWT) into a range profile requires knowledge of the propagation velocity and thus of the relative permittivity (Eq. 4.7). The latter depends on various parameters like the frequency of the electromagnetic wave, the crystal orientation, the density or the temperature of the ice (Fujita et al., 2000). Here, we use a mean relative permittivity of $\varepsilon_r = 3.15$, resulting in a propagation speed of $c_i = 168.914 \times 10^6 \text{ m s}^{-1}$. The amplitude–range profile can now be obtained by using the equation

$$R = \frac{c_i \tau}{2}. \quad (4.31)$$

Figure 4.4 shows the amplitude–range profile of a pRES measurement corresponding to the raw data shown in Fig. 4.3.

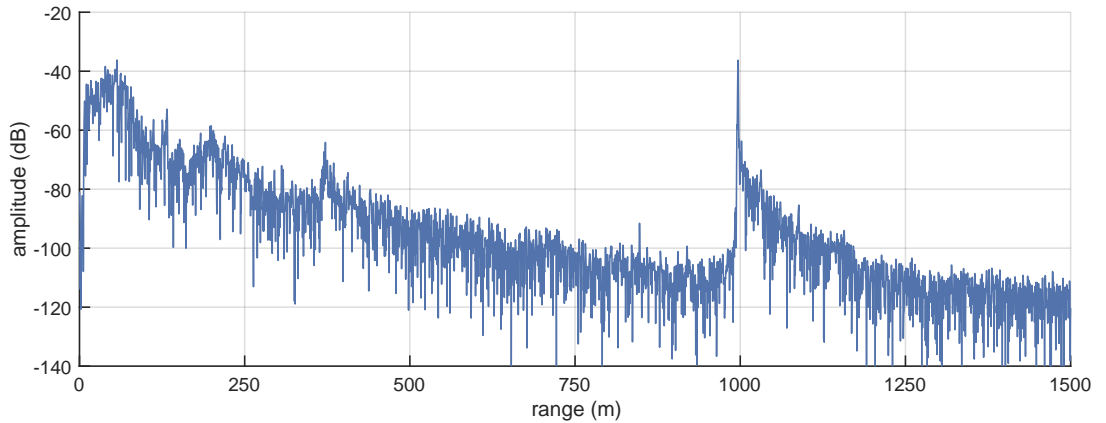


Figure 4.4: Range imaging of pRES measurement. Measurement performed at FIS, Antarctica. The basal return is characterised by a strong increase in amplitude at a range of $\sim 1000 \text{ m}$.

4.5 Basal melt rates from pRES measurements

The calculation of basal melt rates from pRES measurements is based on the ice thickness evolution equation (Eq. 2.14). This equation states that beside basal melting, the divergence of the volume flux and the surface mass balance are affecting the ice thickness. Since Eq. 2.14 is only valid for incompressible materials, it does not consider densification of firn that also affects the ice thickness change over time. The pRES system allows a precise determination of the change in ice thickness, ΔH , as well as displacements of internal layers from repeated Lagrangian measurements. From these internal displacements, the change in ice thickness due to accumulation/ablation at the surface ΔH_s , firn densification ΔH_f and vertical strain ε_{zz} can be estimated. Thus, applying the ice thickness evolution equation to the pRES measurement requires some modifications. Ac-

According to Eq. 2.12, the divergence of the volume flux can be expressed by the depth integrated vertical strain rate. However, pRES measurements allow to calculate vertical displacements u_z instead of vertical velocities v_z and thus vertical strain

$$\varepsilon_{zz} = \frac{\partial u_z}{\partial z} \quad (4.32)$$

and not a strain rate $\dot{\varepsilon}_{zz}$. To overcome this, Eq. 2.12 needs to be reformulated as

$$\int_0^H \dot{\varepsilon}_{zz} dz = \frac{1}{\Delta t} \int_0^H \varepsilon_{zz} dz = \frac{\Delta H_\varepsilon}{\Delta t} \quad (4.33)$$

with the change in ice thickness due to vertical strain ΔH_ε within the time period Δt . Finally, the modified ice thickness evolution equation can be written as (Nicholls et al., 2015):

$$\frac{\Delta H}{\Delta t} = \frac{\Delta H_s}{\Delta t} + \frac{\Delta H_f}{\Delta t} + \frac{\Delta H_\varepsilon}{\Delta t} + \frac{\Delta H_b}{\Delta t} \quad (4.34)$$

with the surface mass balance

$$a_s = \frac{\Delta H_s}{\Delta t} \quad (4.35)$$

and the basal melt rate

$$a_b = -\frac{\Delta H_b}{\Delta t}, \quad (4.36)$$

defined as the change in ice thickness at the base H_b within the time period Δt .

Phase-sensitive radar measurements allow the precise estimation of ΔH , ΔH_s , ΔH_f and ε_{zz} by tracking the relative vertical displacement of the basal and internal reflections:

- The total change in ice thickness ΔH can be determined by the vertical displacement of the basal reflector.
- Snow accumulation/ablation ΔH_s and firn densification ΔH_f cause offsets at and near the surface that can be identified by the vertical displacement of reflections below the firn. Furthermore, changes in radar hardware, e.g. cable length or antenna spacing, influence displacements in the upper layers and cannot be distinguished from the other processes.
- As the vertical strain distribution ε_{zz} is affecting the whole ice column, it needs to be determined from the internal layers within the ice to quantify the caused change in ice thickness ΔH_ε .

This analysing process was previously described by e.g. Jenkins et al. (2006), Nicholls et al. (2015), Stewart et al. (2019) and Vaňková et al. (2020).

The processing method varies slightly depending on the kind of measurement (Stewart, 2018): (1) In order to derive a spatial variability of basal melt rates, (single-) repeated measurements are performed for which the radar was placed at the same surface location after a longer period of time (Lagrangian measurement). In the meantime, the above mentioned processes can have caused vertical displacements exceeding the coarse range resolution of 0.42 m. As the analysis of phase shifts is ambiguous, shifts greater half a wavelength ($\lambda_c/2 = 0.28$ m) cannot be determined unambiguously from the phase analysis alone. Therefore, a cross-correlation of the amplitude profiles is required to avoid errors from phase wrapping.

(2) In order to derive a time series of basal melt rates, the pRES records autonomously with a short measuring interval. This type of measurement is called Autonomous phase-sensitive Radio Echo Sounder (ApRES) measurement. Thus, the vertical displacement between two consecutive measurements is always below the range resolution and the displacement can be estimated from the phase analysis alone.

Next, both processing methods are described in more detail.

4.5.1 Spatial variability of basal melt rates

The pRES allows to cover the spatial variability of basal melt rates over a wider area by performing repeated point measurements. During a survey, the pRES is transported from one measuring spot to another. At each spot, the locations of the antennas needs to be marked at the surface (often by bamboos) to allow a precise repeat measurement at the same surface spot after a certain time. The basal melt rate can be determined from the analysis of vertical displacements of internal and the basal reflection. Figure 4.5 shows the measurement setup of a pRES point measurement.

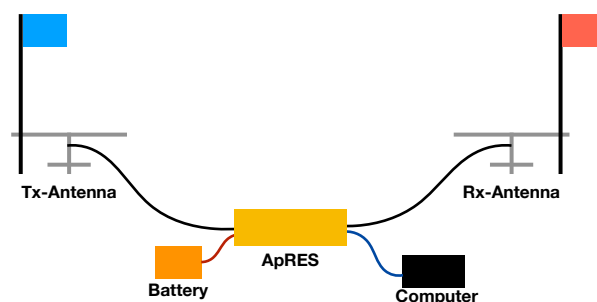


Figure 4.5: Setup of an pRES point measurement. Bamboos mark the position of the antennas. The pRES is connected with the antennas, the battery and a computer.

Following [Stewart \(2018\)](#), the estimation of vertical displacements efforts to calculate the coarse range and the fine range offsets. This is achieved by calculating a complex cross-correlation, γ , of multiple range segments of the complex profiles M_1 (first measurement, t_1) and M_2 (repeated measurement t_2):

$$\gamma(l) = \frac{\sum (M_1(n_s)^* \cdot M_2(n_s + l))}{\sqrt{\sum |M_1(n_s)|^2} \sqrt{\sum |M_2(n_s + l)|^2}} \quad (4.37)$$

where the asterisk (*) indicates the complex conjugate. Here, n_s contains the range bin indices of the range segment and the bin lag l is the integer range-bin offset. The summations are over all elements of n_s . The magnitude of γ indicates the similarity of the segments and the phase of γ represents the mean phase difference

$$\angle\gamma = \text{atan} \left(\frac{\text{imag}(\gamma)}{\text{real}(\gamma)} \right). \quad (4.38)$$

The initial profile was divided into 6 m wide range segments with a 50% overlap from a depth of 20 m below the antennas to 20 m above the ice base. A wider segment of 10 m (−9 to +1 m) was defined around the basal return, characterised by a strong increase in amplitude. In order to estimate the change in ice thickness ΔH by the vertical displacements of the basal return, the basal segment of the first measurements was cross-correlated with the repeated measurement. The lag at maximum correlation $l_m = \text{argmax}_l |\gamma(l)|$ was used to find the lag of the nearby minimum phase difference $l_p = \text{argmin}_l (\angle\gamma)$. According to [Stewart \(2018\)](#), the coarse range offset δ_c of the lag l_p is

$$\delta_c = \Delta R_c l_p \quad (4.39)$$

and the fine range displacement (derived from Eq. 4.21) is

$$\delta_f = \frac{\lambda_c \angle\gamma(l_p)}{4\pi}. \quad (4.40)$$

Finally, the average vertical displacement of the segment is

$$\delta_t = \delta_c + \delta_f. \quad (4.41)$$

Similarly, the vertical displacements of the internal layers is estimated by cross-correlating the internal segments of both measurements. However, this calculation was only carried out for the segment that shows the highest correlation coefficient in order to reduce ambiguities due to phase wrapping. As it is expected that the displacement at the nearby segment differs only slightly from δ_t , l_p of the new segment is chosen to be the nearby minimum phase difference of

the segment before. In this way, the vertical displacement is calculated for each segment. Segments at which γ is below a certain threshold are no longer considered as well as segments within the firn. Based on the vertical displacements of the remaining segments, a weighted linear regression was calculated (Menke, 2012). The gradient of this fit is the vertical strain ε_{zz} and the surface intercept is caused by snow accumulation/ablation ΔH_s , densification ΔH_f and possible hardware changes. Finally, the dynamic thinning/thickening can be derived from Eq. 4.33.

An alternative approach is to align both measurements for a segment below the firn layers (Jenkins et al., 2006). In this way, changes in ice thickness within the firn and at the surface can be neglected. The shift at the ice base is then calculated relatively to the depth of the aligned segment.

The change in ice thickness as well as the vertical displacements at the surface (ΔH_s , ΔH_f) and within the ice ΔH_ε are derived and thus the basal melt rate can be calculated from the Eq. 4.34, solved for a_b :

$$a_b = -\frac{\Delta H - (\Delta H_s + \Delta H_f + \Delta H_\varepsilon)}{\Delta t} \quad (4.42)$$

The uncertainty in the basal melt rate is affected by several factors. Errors from phase noise affects the calculated vertical displacements of the internal and basal segments and thus all derived values used to calculate a_b . Besides, uncertainties from the linear regression influence ε_{zz} and thus ΔH_s , ΔH_f and ΔH_ε . The uncertainty of H depends on the used propagation velocity, which may differ of 1% (Fujita et al., 2000). Errors from phase wrapping, which means that a false phase-minimum was selected to estimate the displacement, are of the size of half the wavelength. This effects primary ΔH_b as well as ΔH_s and ΔH_f . However, repeated measurements where this occurrence can not be excluded, have to be rejected.

Figure 4.6 shows the analysis of repeated measurement recorded on 07 January and 13 December 2016. The basal return was identified with the amplitude profiles at a depth of $H \approx 996$ m (Fig. 4.6a). The correlation of the amplitudes of both profiles and the phase shift is shown in Fig. 4.6b and c. From the highest correlation coefficients, the lag of the minimum phase difference was found and tracked from the first to the last segment above the ice base. The vertical shift of the segments obtained from the coarse and fine range estimation as well as the derived values for $\Delta H = -0.295 \pm 0.001$ m, $\Delta H_s + \Delta H_f = 0.114 \pm 0.001$ m,

$\Delta H_\varepsilon = -0.080 \pm 0.001$ m and $\Delta H_b = -0.329 \pm 0.003$ m within 340.93 days are shown in Fig. 4.6d. This results in a basal melt rate of $a_b = 0.352$ m a⁻¹. The analysis of the vertical displacement of the basal segment is shown in Fig. 4.7.

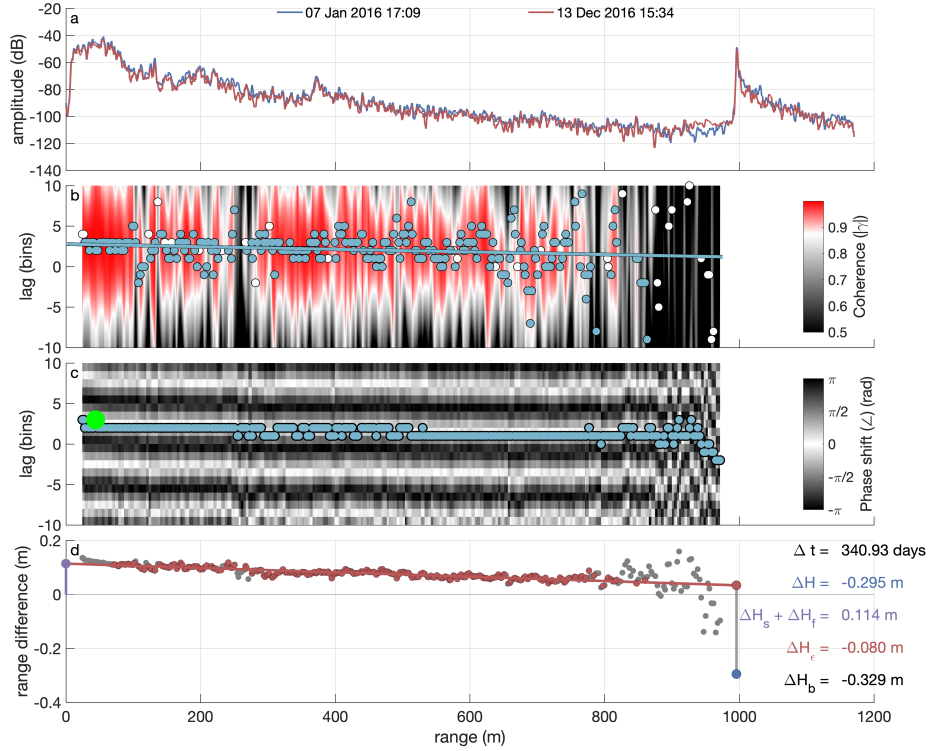


Figure 4.6: Analysis of vertical displacements of internal segments. The pRES measurement was performed at FIS, Antarctica. (a) Comparison of amplitude profiles of first (blue line) and repeated measurement (red line) as a function of range. (b) Cross-correlation ($|\gamma|$) of both measurements as a function of lag and range. White dots mark the lag of best correlation of the segment but do not meet specific criteria and have no further influence. Blue dots mark the lag of best correlation of the segment and do meet specific criteria. The blue line is the linear regression of the blue dots. (c) Phase shift as a function of lag and range. The blue dots tracked the nearest minimum phase difference of the green dot that marks the estimated lag of the segment with the highest correlation coefficient. (d) Shift of segments used for strain rate estimation (red line) are marked by red dots. Grey dots mark the shift of segments that do not meet specific criteria and have no further influence. The change in ice thickness due to snow accumulation and firn densification ($\Delta H_s + \Delta H_f$), derived from the intercept of the fitted curve (large purple dot), is 0.114 m. The ice thickness change due to dynamic thinning/thickening (difference in shift between large purple and large red dot) ΔH is -0.080 m. With the derived shift of the basal segment (large blue dot) of $\Delta H = -0.295$ m, the change in ice thickness at the base is due to melting is $\Delta H_b = -0.329$ m over the period of $\Delta t = 340.93$ days.

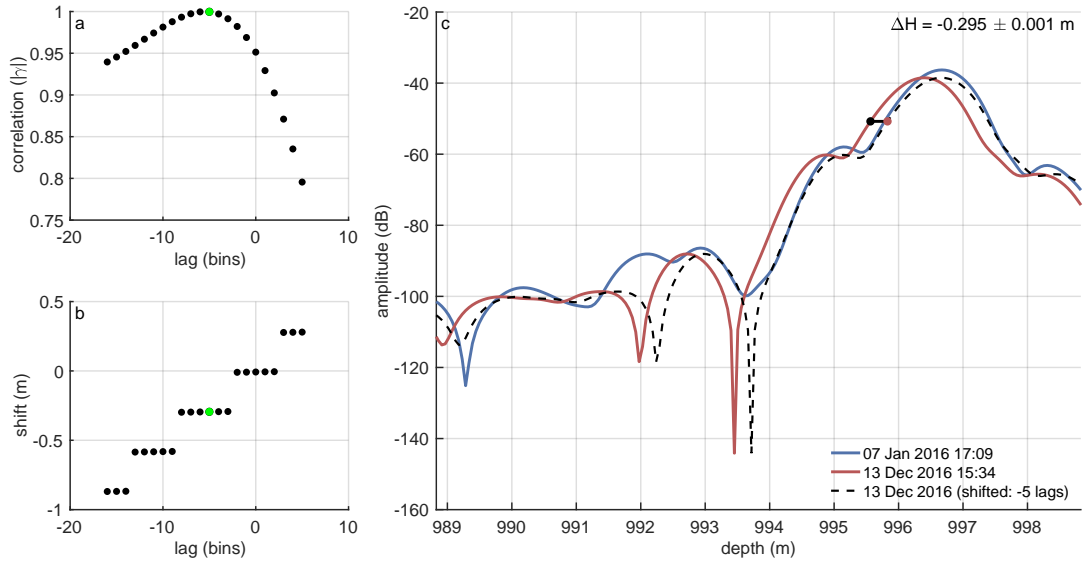


Figure 4.7: Analysis of vertical displacement of basal segment. The single-repeated pRES measurement was performed at FIS, Antarctica. (a) Correlation coefficient $|\gamma|$ for different lags (black dots) of the repeated measurement of the basal segment. The green dot marks lag with highest correlation coefficient. (b) Shifts derived from coarse plus fine range estimation for different lags (black dots). The green dot marks the shift for the lag with best correlation coefficient. (c) Amplitude profiles of first (blue line) and repeated measurement (red line) as a function of range. The dashed line shows the shifted profile of the repeated measurement for the lag with the best correlation coefficient. The change in ice thickness ΔH is $-0.295 \pm 0.001 \text{ m}$.

4.5.2 Temporal variability of basal melt rates

The autonomous operation of the pRES enables measurements to be carried out with a specific time interval over a longer period of time. The number of possible measurements and thus the duration of the measurement depends on the capacity of the battery and the storage space of the SD cards used. This enables the possibility to determine a temporal variability from the time series of vertical displacements of internal and the basal reflections and thus of the basal melt rate. Furthermore, it allows a more precise estimation of the time-averaged melt rate than a single-repeated measurement by tracking layers through the time series.

Equipped with a battery and two antennas, the ApRES can be placed on the ice surface for measurements taking place in ablation zones. In accumulation zones, the ApRES can be buried in the snow for weather protection. A GPS receiver can be used for time synchronisation and location information. An Iridium modem allows a partial data transfer and to reconfigure the instrument remotely. The Figures 4.8 and 4.9 show the measurement setup for both ApRES measurement types.

The analysis of autonomous measurements differs from the method used for single-repeated point measurements. Once the ApRES is placed on or below the surface, the measurement is independent of the accumulation and no hardware changes are made during the measurement period. Thus, an alignment for a reflection below the firm is not necessary. Furthermore, the multiple repeated measurements with short time intervals allow to derive time series of vertical displacements of the pre-processed data.

Similar to the processing described for the spatial variability, the initial profile was divided into 6 m wide range segments with a 50% overlap from a depth of 20 m below the antennas to 20 m above the ice base and a wider segment of 10 m (−9 to +1 m) around the basal return. To derive the displacement time series of each segment, a cross-correlation was calculated between the first (t_1) and each repeated measurement ($t_i, i \leq n$). As the shift of a segment between two consecutive measurements (t_{i-1} and t_i) is always $\ll \pi$ (or $\ll 0.14$ m), the lag of the correct minimum phase difference l_p at t_i , used to calculate the coarse and fine range (Eqs. 4.39 and 4.40), is the one next to the estimated l_p at t_{i-1} . For the first time interval $t_1 - t_2$, l_p is close to zero. In this way, l_p and thus the vertical displacement δt (Eq. 4.41) of a segment can be estimated for each repeated measurement.

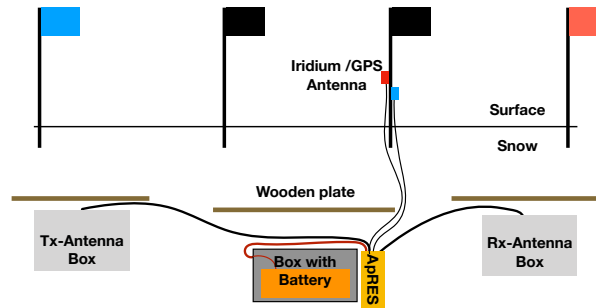


Figure 4.8: Measurement setup of an ApRES measurement in the accumulation zone. Bamboos mark the position of the buried ApRES system. The ApRES is connected with the antennas and the battery. Wooden plates cover the instruments.

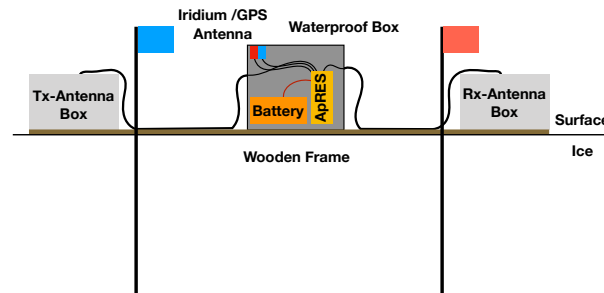


Figure 4.9: Measurement setup of an ApRES measurement in the ablation zone. Deep-drilled bamboos fix the instruments to the ice, which are placed on a wooden frame. The ApRES is connected with the antennas and the battery.

For the estimation of the vertical strain, segments in the firn as well as segments which vertical displacement was identified to be an outlier at t_n were excluded. With the remaining segments, a weighted linear regression (Menke, 2012) was calculated for each time step. The slope of this fit at the time t_i is the averaged vertical strain ε_{zz} and the surface intercept is the averaged densification ΔH_f for the period $\Delta t = t_i - t_1$. The same applies to the basal segment, which vertical displacement at t_i represents the averaged change in ice thickness. Finally, the time series is obtained from Eq. 4.42.

Figure 4.10 shows the analysis of an ApRES time series recorded at the EastGRIP drill site, consisting of 253 measurements between 19 August 2017 and 29 April 2018. The basal return was identified with the amplitude profiles at a depth of $H = 2668$ m (Fig. 4.10a). Vertical displacements of selected segments (Fig. 4.10b) were used to derive cumulative displacements of $\Delta H = -0.317 \pm 0.001$ m, $\Delta H_s + \Delta H_f = -0.053 \pm 0.001$ m, $\Delta H_\varepsilon = -0.120 \pm 0.001$ m and $\Delta H_b = -0.144 \pm 0.001$ m (Fig. 4.10c). This results in a basal melt rate of $a_b = 0.208$ m a⁻¹. Additionally, Fig. 4.10c shows the time series of the cumulative shift of the described processes. Figure 4.11 shows the time series of the vertical displacement of one internal segment at a depth of 905 – 911 m, being -0.096 ± 0.001 m. In the same period of time, the displacement of the basal segment was $\Delta H = -0.317 \pm 0.001$ m, as shown in Fig. 4.12.

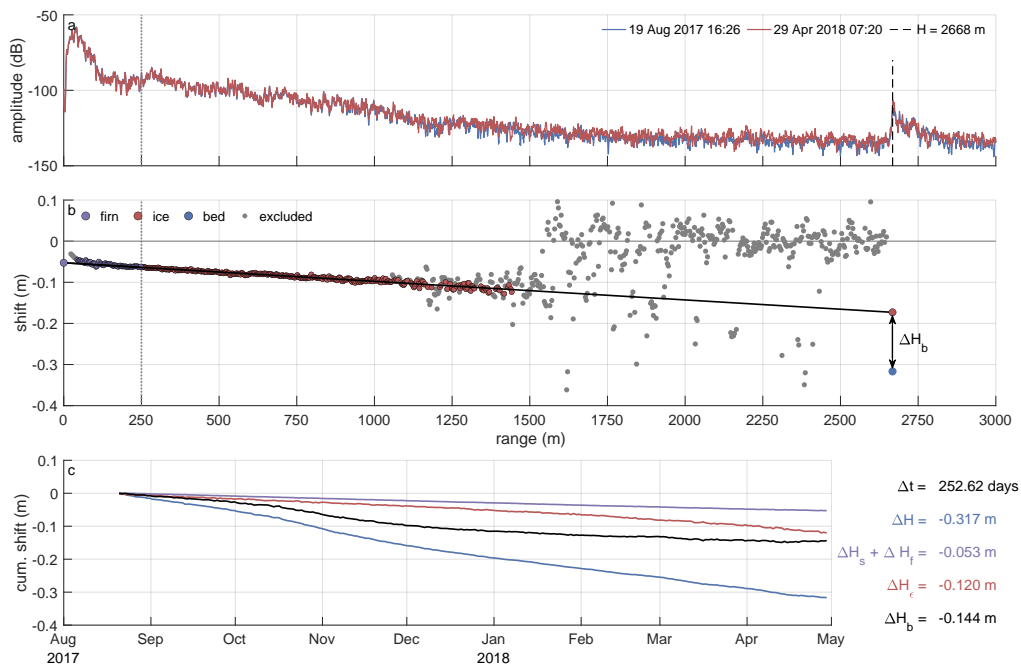


Figure 4.10: Analysis of ApRES time series. Measurement performed at EastGRIP, Greenland. (a) Amplitude profiles (after moving average filtering) of first (19 August 2017) and last measurements (29 April 2018) as function of depth. The strong increase in amplitude at a depth of 2668 m is the basal return. (b) Shift of internal segments after 252.62 days on 29 August 2018. Purple dots mark segments within the firn, red dots of accepted segments within the ice, the blue dot of the basal segment and grey dots show excluded segments. (c) Cumulative shift of ΔH , $\Delta H_s + \Delta H_f$, ΔH_ϵ and ΔH_b over the period Δt .

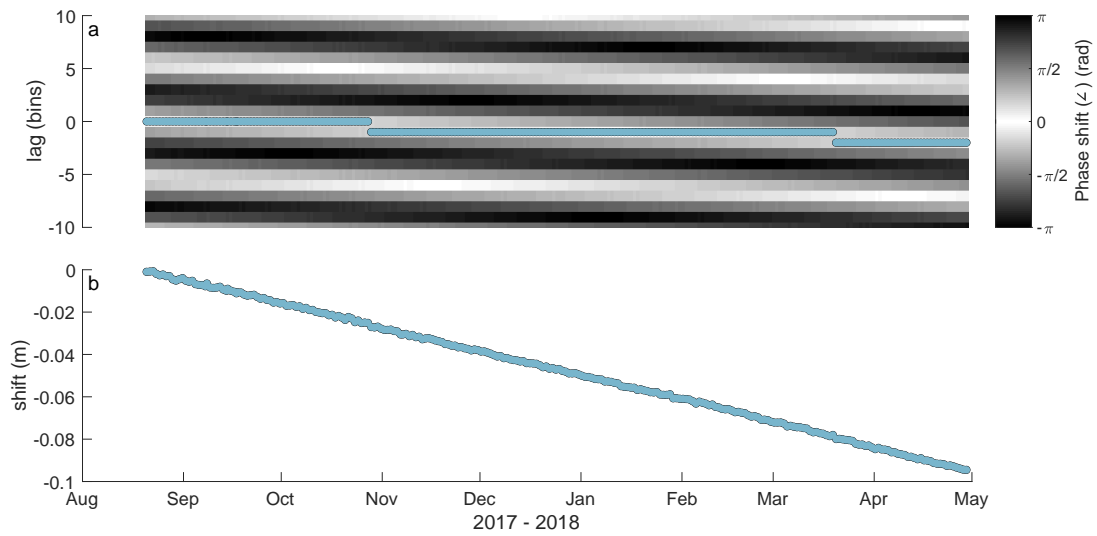


Figure 4.11: Vertical displacement time series of internal segment. Displacement analysis of internal segment (905 – 911 m) from phase analysis of ApRES time series at EastGRIP, Greenland. (a) Phase shift as function of lag and time of measurement. The selected lag of the minimum phase difference, which is used for the coarse and fine range calculation, is marked by a blue dot for each measurement. (b) Shift derived from coarse and fine range estimation for each measurement. Data were recorded from 19 August 2017 to 29 April 2018.

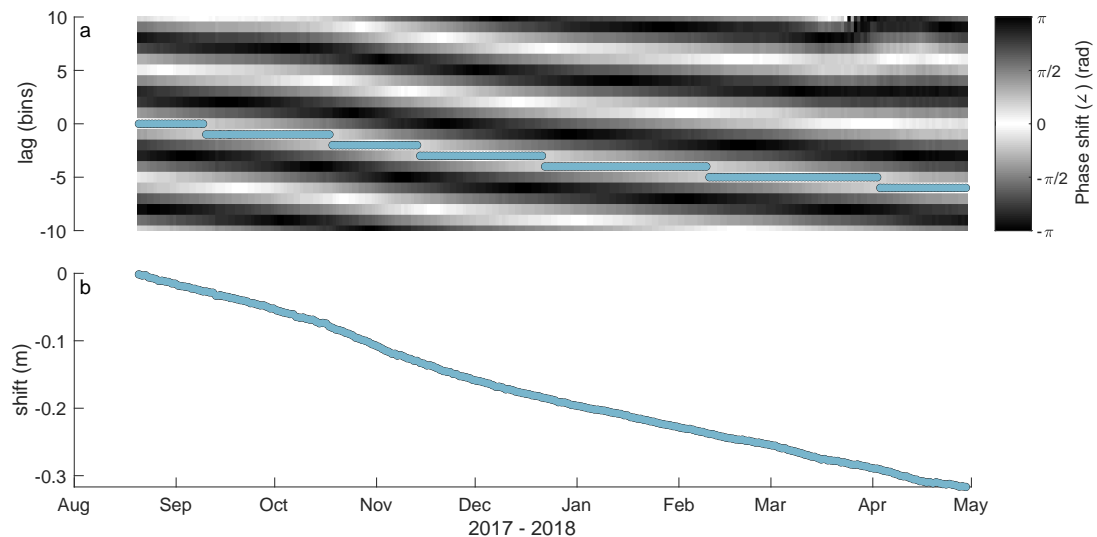


Figure 4.12: Vertical displacement time series of basal segment. Displacement analysis of basal segment from phase analysis of ApRES time series at EastGRIP, Greenland. (a) Phase shift as function of lag and time of measurement. Selected lag for each measurement is marked by a blue dot. (b) Shift derived from coarse and fine range estimation for each measurement. Data were recorded from 19 August 2017 to 29 April 2018.

Northeast Greenland Ice Stream, Greenland

5

5.1 Introduction

The Greenland Ice Sheet (GrIS) is surrounded by numerous smaller ice streams and outlet glaciers (Rignot and Mouginot, 2012). However, there is only one large ice stream that originates far in the interior of the ice sheet – the Northeast Greenland Ice Stream (NEGIS), first discovered by Fahnestock et al. (1993). The approximately 700 km long dynamic feature extends from less than 100 km from the ice divide to the coast (Fahnestock et al., 2001a). Here, it drains into its three major outlet glaciers, namely Nioghalvfjærdsbræ (79°N Glacier, 79NG), Zachariæ Isstrøm (ZI) and Storstrømmen Glacier (SG) (Fig. 5.1). The NEGIS is of particular importance for the Greenland mass loss, as the drainage basins of the three main outlet glaciers (Fig. 5.1) cover 221,048 km² (or 12.9% of the ice

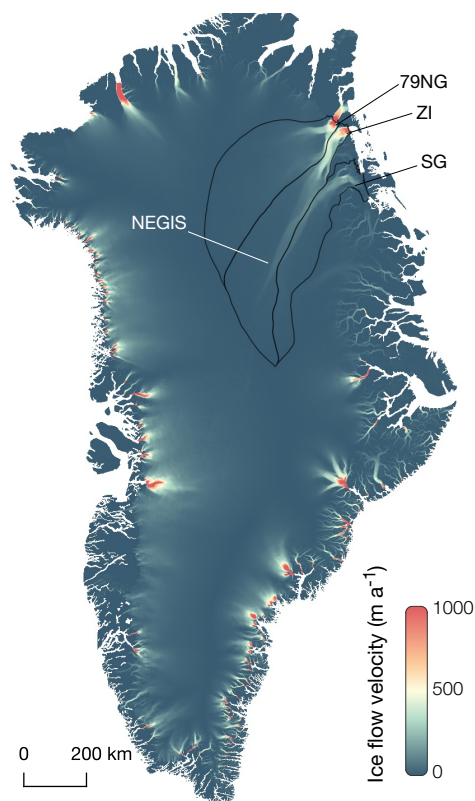


Figure 5.1: Surface ice flow velocity map of GrIS (Joughin et al., 2016, 2018). The Northeast Greenland Ice Stream (NEGIS) is marked as well as Nioghalvfjærdsbræ (79°N Glacier, 79NG), Zachariæ Isstrøm (ZI) and Storstrømmen Glacier (SG) with their drainage basins (Krieger et al., 2020a).

sheet area) and hold the potential to raise global mean sea level by 1.2 m (Krieger et al., 2020a). The NEGIS is clearly noticeable in velocity maps such as the one from Joughin et al. (2016, 2018) displayed in Fig. 5.1, as velocities of $> 50 \text{ m a}^{-1}$ are reached about 500 km and $> 500 \text{ m a}^{-1}$ about 180 km upstream the grounding lines of 79NG and ZI.

The floating ice tongue of ZI started to disintegrate in the early 2000s and with that ZI transformed into a tidewater glacier (Mouginot et al., 2015; Khan et al., 2014). The collapse was accompanied by a significant acceleration of the ice flow velocity by 50% and the ice thickness thinned by more than 2 m a^{-1} (Helm et al., 2014; Khan et al., 2014; Mouginot et al., 2015). Due to a downward-sloping bed, an ongoing rapidly retreat is projected for the upcoming decades (Mouginot et al., 2015).

5.2 Lubricated sliding of the Northeast Greenland Ice Stream

In contrast to many other ice streams of GrIS, ice sheet simulations are not able to reproduce the distinctive extent of NEGIS with sufficient accuracy unless the initial state is based on inversion (Goelzer et al., 2018) or a coupling with a subglacial hydrological model is used (Smith-Johnsen et al., 2020b). The likely reason for this could be the inadequate representation of the lubrication and thus these models underestimate sliding, which is held responsible for the high ice flow velocities. Since the ice sheet models are used to quantify the contribution of the GrIS to future sea-level rise under different climatic scenarios, inversions cannot be relied on since the basal conditions may change and influence the ice dynamics (Smith-Johnsen et al., 2020a). First estimates of basal melt rates (Fahnestock et al., 2001b; Keisling et al., 2014; MacGregor et al., 2016) and indications for deformable and water saturated sediment (Christianson et al., 2014) have been obtained from geophysical measurements. However, previous estimated basal melt rates have been derived from airborne radar data and may be prone to limited validity due to assumptions made. For this reason, we operated an ApRES on the EastGRIP drill site, from which we derived a basal melt rate based on two time-series within subsequent years. The evaluation and a new quantification of which processes at the base significantly contribute to melting were published as a research article titled *Indication of high basal melting at the EastGRIP drill site on the Northeast Greenland Ice Stream* (Chapter 6; Zeising and Humbert, 2021b) in the journal *The Cryosphere* in 2021.

5.3 Ice–ocean interaction at 79°N Glacier

In contrast to ZI, the floating tongue of 79NG still exists. With a size of roughly $20 \text{ km} \times 65 \text{ km}$, it is the largest of the three remaining glaciers with a floating ice tongue in Greenland — the others are Petermann Gletscher and Ryder Glacier. Although Mouginit et al. (2015) and Mayer et al. (2018) found substantial thinning near the grounding line, they conclude the tongue of 79NG is still remarkably stable with only minor acceleration rates (Mouginit et al., 2015). However, Mayer et al. (2018) warn that a collapse of the floating tongue could lead to a destabilisation of the entire marine-based ice sheet sector. The thinning of 79NG’s floating tongue is largely attributed to warm ($> 1^\circ \text{C}$) Atlantic Intermediate Water (AIW) that was found by means of oceanographic measurements (Straneo et al., 2012; Wilson and Straneo, 2015; Lindeman et al., 2020; Schaffer et al., 2020). The extent to which the subglacial discharge contributes to basal melting has not yet been adequately investigated. From remote sensing data and in situ GPS measurements, a seasonal acceleration ice flow velocities in summer and after a lake drainage due to a subglacial hydraulic system was found at 79NG, as revealed in the research article titled *Seasonal Observations at 79°N Glacier (Greenland) From Remote Sensing and in situ Measurements* (Appendix Chapter A; Neckel et al., 2020) published at the journal *Frontiers in Earth Science* in 2020, were the author of this thesis contributed as co-author. In order to understand the dynamics of the system, especially regarding the ice–ocean interaction, observations of the spatial distribution and temporal variability of basal melt rates of the floating tongue are a key ingredient. In the course of the GROCE project, which was funded by the German *Bundesministerium für Bildung und Forschung* (BMBF) under the grant 03F0778A and by AWI, ApRES measurements have been performed between 2016 and 2020. The derived melt rates are part of a research article titled *Extreme melt rates at Greenland’s largest floating ice tongue* (Chapter 7) that is in preparation. In addition to an expanded understanding of the system of a rapidly thinning glacier, these results can be helpful in the parametrisation of sub-ice shelf ocean conditions and thus contribute to the projections of the future contribution to sea level rise. The modelling of fast-flowing ice streams also plays a decisive role in this context, which are mostly based on viscous models. However, this neglects the elastic deformations, as they are caused by tides, but also occur near steep changes in topography or other regions with a non-steady stress field. The assessment of the contribution of elastic deformation of the 79NG is part of the research article titled *Elastic deformation plays a non-negligible role in Greenland’s outlet glacier flow* (Appendix Chapter B; Christmann et al., 2021) published in the journal *Communications Earth*

Environment in 2021. The author of this thesis contributed as co-author by analysing tidal movements using GNSS measurements, recorded in the course of the GROCE project.

Indication of high basal melting at the EastGRIP drill site on the Northeast Greenland Ice Stream

6

This chapter is published as a research article in the journal *The Cryosphere* in 2021 (Zeising and Humbert, 2021b).

Authors and affiliations

Ole Zeising^{1,2}  and Angelika Humbert^{1,2} 

¹Alfred-Wegener-Institut Helmholtz-Zentrum für Polar- und Meeresforschung, Bremerhaven, Germany

²Department of Geosciences, University of Bremen, Bremen, Germany

Contributions

O.Zeising and A.Humbert conducted part of the field study. **O.Zeising** processed the ApRES data and estimated the resulting basal melt rates. **O.Zeising** and A.Humbert discussed the basal melt rate distribution and time series. A. Humbert conducted the analysis of the energy jump condition. **O.Zeising** wrote Sect. 6.2 ("Data and methods"), 6.3 ("Results") and 6.4 ("Discussion") with the exception of Sect. 6.4.1 ("Considerations of the energy balance at the ice base") which was written by A.Humbert. To all other sections **O.Zeising** and A.Humbert contributed to the writing. Figures related to energy balance (Sect. 6.4.1) were created by A.Humbert, all other figures were created by **O.Zeising**. A.Humbert has designed the study and supervised it.

Abstract

The accelerated ice flow of ice streams that reach far into the interior of the ice sheets is associated with lubrication of the ice sheet base by basal meltwater. However, the amount of basal melting under the large ice streams – such as the Northeast Greenland Ice Stream (NEGIS) – is largely unknown. In situ measurements of basal melt rates are important from various perspectives as they indicate the heat budget, the hydrological regime and the relative importance of sliding in glacier motion. The few previous estimates of basal melt rates in the NEGIS region were 0.1 m a^{-1} and more, based on radiostratigraphy methods. These findings raised the question of the heat source, since even an increased geothermal heat flux could not deliver the necessary amount of heat. Here, we present basal melt rates at the recent deep drill site EastGRIP, located in the centre of NEGIS. Within 2 subsequent years, we found basal melt rates of $0.19 \pm 0.04 \text{ m a}^{-1}$ that are based on analysis of repeated phase-sensitive radar measurements. In order to quantify the contribution of processes that contribute to melting, we carried out an assessment of the energy balance at the interface and found the subglacial water system to play a key role in facilitating such high melt rates.

6.1 Introduction

Ice sheet models are used to quantify the contribution of the Greenland Ice Sheet to future sea-level rise under different climatic scenarios. In these simulations, the distinctive extent of Greenland’s largest ice stream – the Northeast Greenland Ice Stream (NEGIS, Fig. 6.1) – can only be reproduced well if a higher-order approximation is considered for the momentum balance and initial states are based on inversion (Goelzer et al., 2018) or involve subglacial hydrological models (Smith-Johnsen et al., 2020a). Primarily, this is due to the model’s inability to accurately represent lubrication and thus the subsequent sliding at the ice stream base that occurs.

The NEGIS is the only large ice stream in Greenland, extending from a distance of 100 km from the ice divide over a length of about 700 km towards the coast (Fahnestock et al., 1993, 2001b; Joughin et al., 2001). It drains about 12% of Greenland’s ice through three major outlet glaciers Nioghalvfjærdsbrae, Zachariæ Isstrøm and Storstrømmen Glacier (Rignot and Mouginot, 2012). Loss of the floating tongue of Zachariæ Isstrøm has already led to ice flow acceleration and increased mass loss (Mouginot et al., 2015). Consequently, it is expected and projected that NEGIS will contribute significantly to sea-level rise in the future (Khan et al., 2014), highlighting the importance of understanding the general

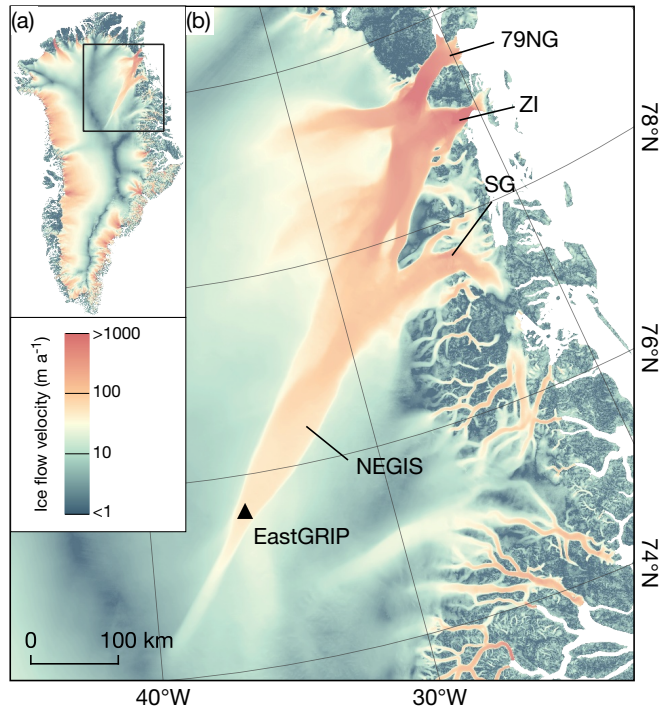


Figure 6.1: Surface ice flow velocity map of the Greenland Ice Sheet (Joughin et al., 2018). The box in the overview map (upper left corner) marks the boundaries of the main figure showing northeast Greenland and the Northeast Greenland Ice Stream (NEGIS), which drains into the three major outlet glaciers, namely Nioghalvfjærdsbrae (79°N Glacier, 79NG), Zachariæ Isstrøm (ZI) and Storstrømmen Glacier (SG). The location of the EastGRIP drill site is denoted by the black triangle.

ice-flow dynamics and its driving mechanisms.

One hypothesis for the genesis of NEGIS is locally increased basal melting at the onset area that enables and enhances basal sliding (Fahnestock et al., 2001a; Christianson et al., 2014; Franke et al., 2021) and forms a subglacial hydrological system. The coupling with basal sliding is facilitated via the water pressure, so that the sliding velocity rises with increasing water pressure (e.g. Beyer et al., 2018; Smith-Johnsen et al., 2020a). However, little is known about the amount of subglacial water below the up to ~ 3300 m thick ice sheet.

First estimates of basal melt rates by Fahnestock et al. (2001a) and later by Keisling et al. (2014) and MacGregor et al. (2016) are based on the interpretation of chronology in radiostratigraphy. All three studies found melt rates of 0.1 m a^{-1} and more – which is extremely large for inland ice. However, these estimates may be prone to limited validity given the assumptions about the flow regime and constant accumulation rate. The cause for such intensive melt was attributed to a high geothermal heat flux which possibly originates from the passage of Greenland over the Icelandic hot spot (Fahnestock et al., 2001a; Rogozhina et al., 2016; Martos et al., 2018; Alley et al., 2019).

In order to directly observe, among other things, flow regimes and basal condi-

tions of ice streams, an ice core is being drilled as part of the East Greenland Ice-Core Project (EastGRIP) near the onset of the NEGIS. Here, surface velocities reach about 57 m a^{-1} (Hvidberg et al., 2020) and the NEGIS widens (Fig. 6.1). Smith-Johnsen et al. (2020a) forced an ice model with a locally increased heat flux below the EastGRIP drill site. They found that a heat flux of 0.97 W m^{-2} (corresponding to a basal melt rate of 0.1 m a^{-1} ; (Fahnestock et al., 2001a)) is necessary to reasonably reproduce the velocities of NEGIS. By utilising a coupled subglacial hydrology and ice sheet model, Smith-Johnsen et al. (2020b) demonstrated the large impact of an uncertainty in geothermal heat flux on the flow of NEGIS arising from the subglacial hydrological system and hence from basal melting and water pressure, as well as from friction.

However, measurements with an adequate accuracy are still required to narrow down the basal melt rates further. Here, we present the first estimates of basal melt rates from repeated in situ phase-sensitive radar measurements from the EastGRIP drill site and consider the contribution of different heat sources at the ice base.

6.2 Data and methods

6.2.1 Instrument, data acquisition and processing

The autonomous phase-sensitive radio-echo sounder (ApRES; Brennan et al., 2014; Nicholls et al., 2015) is a low-power, ground-based radar that allows measurements to be carried out autonomously with a selected interval over long periods of time. By analysing the phase shifts of the return signals, the vertical displacements of internal reflections and of the base can be precisely determined in millimetre range. Thus, the ApRES is often used to determine Lagrangian basal melt rates and their temporal variability of ice shelves (e.g. Stewart et al., 2019; Washam et al., 2019; Vaňková et al., 2020). In order to derive an annual mean basal melt rate at the EastGRIP drill site, we deployed an ApRES within a near-surface trench (Fig. 6.1). The ApRES performed a measurement once a day during winter from 08/2017 – 04/2018 and 08/2018 – 05/2019.

In the following, we shortly describe the theory of operation of the ApRES and the signal processing, whereas a more detailed description is given by Brennan et al. (2014), Nicholls et al. (2015) and Stewart et al. (2019). Within a single measurement, the ApRES transmits a sequence of 100 chirps, each with a duration of 1 s in which the frequency of the transmitted electromagnetic wave is increased from 200 to 400 MHz. After reflection, the received signal is mixed with a replica of the transmitted signal and sampled with 40 kHz (Nicholls et al., 2015). Since

the frequencies of the resulting deramped signal are related to the two-way travel time, a spectral analysis needs to be done in the processing to obtain depth profiles of the amplitude and phase. For the conversion from travel time to depth, we used a vertical propagation velocity of $168,914 \text{ km s}^{-1}$ according to the relative permittivity of $\varepsilon_r = 3.15$ (Fujita et al., 2000). Prior to the spectral analysis, the performed chirps were averaged to increase the signal-to-noise ratio. However, due to weak reflections in the lower part of the ice, the signal-to-noise ratio is reduced. As a consequence, no reliable analysis of the data is possible below the noise level depth limit of $\sim 1450 \text{ m}$, with the exception of the basal return. Next, we present how we derive basal melt rates from the radar data.

6.2.2 Ice thickness evolution

The method we use to derive a basal melt rate is based on the ice thickness evolution equation that is valid in both, the Eulerian and Lagrangian reference systems:

$$\frac{\partial H}{\partial t} = -\text{div } \mathbf{Q} + a_s - a_b \quad (6.1)$$

with the ice thickness H , the time t , the volume flux \mathbf{Q} , the surface mass balance a_s and the basal melt rate a_b (positive for melting) (e.g. Greve and Blatter, 2009). Equation (6.1) states that a temporal change in ice thickness is caused by a changing volume flux arising from deformation and accumulation or ablation at the ice surface and base. It is worth noting that a basal melt rate larger than the accumulation rate only leads to thinning of the glacier, if the volume flux cannot supply sufficient ice to balance this out. The volume flux \mathbf{Q} is defined as the vertically integrated horizontal velocities $v_x, v_y(x, y, z, t)$:

$$\mathbf{Q} = \begin{pmatrix} Q_x \\ Q_y \end{pmatrix} = \begin{pmatrix} \int_0^H v_x \, dz \\ \int_0^H v_y \, dz \end{pmatrix}, \quad (6.2)$$

(Greve and Blatter, 2009), and it represents the ice thickness change due to deformation and sliding and thus stretching or compression in the horizontal direction. This may, for example, be due to changes in basal velocities or ice creeping across a bedrock undulation. Using the continuity equation for incompressible materials, $\text{div } \mathbf{v} = 0$, and Leibniz's integral rule, we can rewrite $\text{div } \mathbf{Q}$ as

$$\begin{aligned} \text{div } \mathbf{Q} &= \frac{\partial}{\partial x} \int_0^H v_x \, dz + \frac{\partial}{\partial y} \int_0^H v_y \, dz = \int_0^H \frac{\partial v_x}{\partial x} + \frac{\partial v_y}{\partial y} \, dz \\ &= \int_0^H \frac{\partial v_z}{\partial z} \, dz = \int_0^H \dot{\varepsilon}_{zz} \, dz \end{aligned} \quad (6.3)$$

with $\dot{\varepsilon}_{zz}$ the vertical strain rate $\dot{\varepsilon}_{zz} = \partial v_z / \partial z$.

The recorded ApRES time series allows for a precise estimation of changes in ice thickness ΔH from the vertical displacement of the basal reflector and of internal layers from consecutive measurements. However, applying the ice thickness evolution equation (Eq. 6.1) to the ApRES measurements requires some modifications. Since the ApRES is located within a trench below the surface, the 'measured ice thickness' H is defined as the range between the ApRES and the ice base. The total ice thickness – the range from the surface to the ice base – is about 7 to 8 m thicker and includes the upper firn and snow layers. Thus, ΔH is independent of the surface mass balance, $a_s = 0 \text{ m a}^{-1}$, but influenced by firn densification that significantly affects the vertical displacement in the upper $\sim 100 \text{ m}$. As this is not considered in Eq. (6.1), we add the term $\Delta H_f / \Delta t$ to correct for the densification process below the ApRES.

Equation (6.3) states that the divergence of the volume flux in Eq. (6.1) can be expressed by the depth-integrated vertical strain rate. However, we derive vertical displacements u_z from ApRES measurements instead of vertical velocities v_z . Thus, we can calculate strain $\varepsilon_{zz} = \partial u_z / \partial z$ for a time period of Δt . Therefore, Eq. (6.3) needs to be reformulated as

$$\int_0^H \dot{\varepsilon}_{zz} \, dz = \frac{1}{\Delta t} \int_0^H \varepsilon_{zz} \, dz = \frac{\Delta H_\varepsilon}{\Delta t} \quad (6.4)$$

with the change in ice thickness due to vertical strain ΔH_ε . Finally, the modified ice thickness evolution equation can be written as

$$\frac{\Delta H}{\Delta t} = \frac{\Delta H_f}{\Delta t} + \frac{\Delta H_\varepsilon}{\Delta t} - a_b . \quad (6.5)$$

All three quantities ΔH , ΔH_f and ΔH_ε , which are needed to derive a_b , are described by vertical displacements and hence by the radar measurement itself in a consistent manner.

6.2.3 Derivation of basal melt rates

In order to derive vertical displacements of internal layers and of the basal return from the ApRES time series, we slightly modified the processing of Vaňková et al. (2020) (details below). Both methods are based on phase differences estimated from cross-correlation of the repeated measurements.

Firstly, we divided the depth profile into 6 m segments with a 3 m overlap from a depth of 20 m below the antennas to 20 m above the ice base and a wider segment of 10 m (-9 to +1 m) around the basal return, characterised by a strong increase in amplitude. In order to derive vertical displacements, each depth segment of

the first measurement (t_1) was cross-correlated with the same segment of each repeated measurement (t_i). This is in contrast to [Vaňková et al. \(2020\)](#), who derived displacements from pairwise time-consecutive measurements ($t_{i-1} - t_i$). The lag of the minimum mean phase difference obtained from the cross-correlation gives the cumulative displacement at the given depth. The range of expected lag was limited by the estimation to the previous measurement ($t_1 - t_{i-1}$). This results in a time series of displacements for each segment individually. The vertical displacement of the basal segment is the change in the measured ice thickness ΔH .

Next, we estimate the vertical strain $\varepsilon_{zz}^{\text{obs}}$ and quantify ΔH_f as well as ΔH_ε based on a regression analysis of the vertical displacements. To avoid influences of firn densification on the determination of $\varepsilon_{zz}^{\text{obs}}$, we excluded all segments above a depth of 250 m ($\sim 9\%$ of all segments). In addition, segments below the noise-level depth limit of $h \approx 1450$ m (where noise prevents an unambiguous estimation) were excluded ($\sim 45\%$ of all segments). Furthermore, outliers were filtered out ($\sim 7\%$). We found a linear fit $u_z(z)$ of

$$u_z(z) = \varepsilon_{zz}^{\text{obs}} \cdot z + \Delta H_f, \quad 250 \text{ m} \leq z \leq h \quad (6.6)$$

that best matches the cumulative vertical displacements of the remaining ~ 400 segments within the ice. The gradient of this fit is $\varepsilon_{zz}^{\text{obs}}$, and the shift between the intercept at the depth of the ApRES and ΔH is ΔH_f . However, ε_{zz} for $z \geq h$ is unknown. Here, we used two scenarios to estimate ΔH_ε (Fig. 6.2, Appendix Fig. 6.5). First, we assumed that ε_{zz} is constant with depth:

$$\varepsilon_{zz}^{\text{const}}(z) = \varepsilon_{zz}^{\text{obs}}, \quad 0 \leq z \leq H \quad (6.7)$$

As a second scenario, we used a vertical strain distribution ($\varepsilon_{zz}^{\text{sim}}$) obtained from an ice sheet model based on inverse surface flow velocities ([Rückamp et al., 2020](#)). Here, $\varepsilon_{zz}^{\text{sim}}$ increases with depth and reaches values of roughly twice $\varepsilon_{zz}^{\text{obs}}$ at the base.

In order to be less dependent on a single measurement, we compute for each of the last 65 days (records; roughly 25% of the measurements) of a year an annual melt rate and compute from these 65 melt rate estimates a mean annual value by averaging. Finally, ΔH_ε was derived from Eq. (6.4) for the two vertical strain distributions ($\Delta H_\varepsilon^{\text{const}}$, $\Delta H_\varepsilon^{\text{sim}}$), and the basal melt rate a_b from Eq. (6.5). Given errors are based on the standard deviation of the estimates based on the considered 65 measurements and a 1% uncertainty in the signal propagation speed in ice ([Fujita et al., 2000](#)). For visualisation, we calculated the cumulative vertical displacement referenced to the ice base (Fig. 6.2).

6.3 Results

The analysis of the 2017/18 ApRES time series revealed a measured ice thickness (distance between radar and ice base) of roughly 2668 m at the EastGRIP drill site with an annual mean change of -0.471 m a^{-1} (Table 6.1, Fig. 6.2). The firn densification – the intercept (see Fig. 6.2) of the linear fit at $z = 0 \text{ m}$ (the elevation of the ApRES) – occurring below the radar is 0.074 m a^{-1} . We derived a vertical strain of $\varepsilon_{zz} = -0.068 \times 10^{-3}$ from reliable estimates of vertical displacements feasible to a depth of 1450 m. The dynamic thinning of the ice derived from the two scenarios ranges from -0.181 m a^{-1} ($\Delta H_\varepsilon^{\text{const}}$) to -0.194 m a^{-1} ($\Delta H_\varepsilon^{\text{sim}}$). This results in a basal melt rate of $0.210 \pm 0.015 \text{ m a}^{-1}$. The numbers derived from the time series recorded in 2018/19 differ slightly (Table 6.1, Appendix Fig. 6.6). The annual mean change in measured ice thickness is 27 mm (or 6%) lower and the firn densification 15 mm (or 20%) larger compared to the values derived in 2017/18. The resulting basal melt rate of $0.167 \pm 0.018 \text{ m a}^{-1}$ is $\sim 20\%$ lower than the year before. Finally, we derive an averaged melt rate over both years of $0.19 \pm 0.04 \text{ m a}^{-1}$.

Table 6.1: Results for measured ice thickness change (ΔH), firn densification (ΔH_f), vertical strain (ε_{zz}), dynamic ice thickness change obtained from a constant vertical strain ($\Delta H_\varepsilon^{\text{const}}$) and a simulation ($\Delta H_\varepsilon^{\text{sim}}$) and basal melting (a_b) for both time series projected to 365 days. Negative values contribute to the thinning of the ice column, whereas a positive melt rate represents melting.

Year	ΔH (m)	ΔH_f (m)	ε_{zz} ($\times 10^{-3}$)	$\Delta H_\varepsilon^{\text{const}}$ (m)	$\Delta H_\varepsilon^{\text{sim}}$ (m)	a_b (m a^{-1})
2017/18	-0.471 ± 0.008	-0.074 ± 0.001	-0.068 ± 0.001	-0.181 ± 0.001	-0.194 ± 0.001	0.210 ± 0.015
2018/19	-0.444 ± 0.006	-0.089 ± 0.002	-0.068 ± 0.002	-0.182 ± 0.005	-0.195 ± 0.005	0.167 ± 0.018

6.4 Discussion

We used estimated vertical displacements from the upper half of the ice column to estimate the dynamic thinning, since noise prevents an unambiguous estimation of the vertical strain for the lower half. To cover a range of variations in the dynamic thinning, we used two different scenarios for vertical strain distribution. The resulting dynamic thinning of the simulated vertical strain and the constant strain differ only slightly. However, we cannot exclude the possibility that larger strain values are reached at the base, which would lead to an overestimation of the basal melt rates. In the case of a non-existing melt rate, the dynamic thinning of the lower half of the ice column would be, on average, more than 4 times as large as the one of the upper half. However, a strong increase is not found in higher-order ice sheet simulations (Rückamp et al., 2020). A frequently used

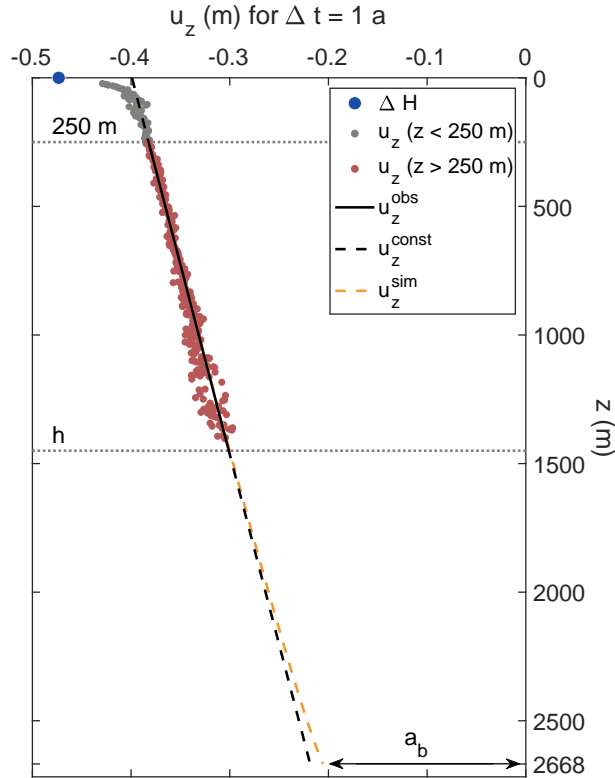


Figure 6.2: Derived vertical displacements u_z of the depth of the ApRES (ΔH ; blue dot) and of selected internal layers referenced to the ice base from the 2017/18 ApRES time series. Derived displacements used for melt rate estimations are marked by red dots and of layers within the firn by grey dots. The estimated displacements between a depth of 250 m and h are used to calculate a linear fit (solid black line), the gradient of which is the vertical strain. Extrapolations to the bottom are shown by the dashed lines. The offset at the ice base is caused by basal melting and the difference between the intercept of the linear fit at $z = 0$ m and ΔH is the firn compaction.

strain distribution (e.g. [Fahnestock et al., 2001a](#); [Keisling et al., 2014](#); [MacGregor et al., 2016](#)) that takes into account deviating strain within a shear zone is the Dansgaard–Johnsen distribution model ([Dansgaard and Johnsen, 1969](#)). As this model assumes a linearly decreasing strain in the shear zone that reaches zero at the ice base, the resulting basal melt rate at EastGRIP would be even larger. However, the Dansgaard–Johnsen model represents a no-slip boundary condition at the ice base. As this is an unrealistic assumption in an ice stream, we did not consider the Dansgaard–Johnsen model further.

The derived vertical strain is based on more than 300 vertical displacements estimated between the firn–ice transition and about 1450 m. In contrast, the estimation of the displacement of the basal return is based on the phase shift of only one segment around the basal return, slightly above the noise level. This makes the determination more prone to errors. Instead of comparing the first

measurement (t_1) with all repeated measurements (t_i), the pairwise comparison of time-consecutive measurements (t_{i-1} and t_i), as shown by [Vaňková et al. \(2020\)](#), leads to a lower thinning rate of ΔH in 2017/18 than in 2018/19 ($-0.441 \pm 0.004 \text{ m a}^{-1}$ in 2017/18, $-0.467 \pm 0.009 \text{ m a}^{-1}$ in 2018/19). Thus, the variability found is not necessarily a variability of the ice sheet system but can rather be influenced by the methodology.

A variation in the selected depth limit of densification, to exclude segments affected by densification, causes slight changes in vertical strain and thus in basal melt rate on the order of millimetres. However, we observed an increased densification rate within the considered 65 records. The increased densification can possibly be a result of increased load from the camp at the surface.

Our derived basal melt rate of $0.19 \pm 0.04 \text{ m a}^{-1}$ is above previous estimates from airborne radar measurements. [Fahnestock et al. \(2001a\)](#) and [MacGregor et al. \(2016\)](#) found melt rates on the order of 0.1 m a^{-1} in the vicinity of the EastGRIP drill site but larger melt rates of $> 0.15 \text{ m a}^{-1}$ further upstream in the onset region of NEGIS. Both studies used a constant vertical strain over depth where basal melting occurs. [Smith-Johnsen et al. \(2020a\)](#) found that basal melt rates of 0.1 m a^{-1} , derived from a heat flux of 0.97 W m^{-2} , are needed at the location of the EastGRIP drill site to reproduce the NEGIS in an ice sheet model.

6.4.1 Considerations of the energy balance at the ice base

In order to constrain the heat flux required to sustain the basal melt rates a_b derived in this study, we consider the energy balance at the ice base. As for any surface across which a physical quantity may not be continuous, a jump condition is formulated. In a typical continuum mechanical formulation, the jump ($[[\psi]]$) of a quantity ψ is defined as $[[\psi]] = \psi^+ - \psi^-$, meaning the difference in the quantity ψ across the interface ([Greve and Blatter, 2009](#)). The jump condition of the energy at the ice base reads as

$$[[\mathbf{q} \cdot \mathbf{n}]] - [[\mathbf{v} \cdot \mathbf{t} \cdot \mathbf{n}]] + [[\rho^i (u + \frac{1}{2} \mathbf{v}^2) (\mathbf{v} - \mathbf{w}) \cdot \mathbf{n}]] = [[\mathbf{q} \cdot \mathbf{n}]] - [[\mathbf{v} \cdot \mathbf{t} \cdot \mathbf{n}]] + \rho^i a_b [[u]] = 0, \quad (6.8)$$

with the heat flux \mathbf{q} , the velocity \mathbf{v} , the velocity of the singular surface \mathbf{w} , the normal vector \mathbf{n} pointing outwards from the ice body, the Cauchy stress \mathbf{t} , the ice density ρ^i and the internal energy u ([Greve and Blatter, 2009](#)). The jump of the heat flux $[[\mathbf{q} \cdot \mathbf{n}]]$ becomes $(\mathbf{q}^{\text{geo}} + \mathbf{q}^{\text{sw}}) \cdot \mathbf{n} - \kappa(T) \text{grad } T$, with \mathbf{q}^{geo} the geothermal heat flux and \mathbf{q}^{sw} the heat flux from subglacial water with a temperature above pressure melting point, T temperature and κ thermal conductivity. For the jump

in work of surface forces we find

$$\llbracket \mathbf{v} \cdot \mathbf{t} \cdot \mathbf{n} \rrbracket = \mathbf{v}^{\text{sw}} \cdot \mathbf{t}^{\text{sw}} \cdot \mathbf{n} - \mathbf{v}_b^i \cdot \mathbf{t}^i \cdot \mathbf{n}, \quad (6.9)$$

with \mathbf{t}^{sw} the Cauchy stress of the subglacial water side of the singular surface, \mathbf{v}_b^i the ice velocity and \mathbf{t}^i the stress field of the ice at the base.

We split the traction vector of the subglacial water into a normal and tangential component, with the water pressure p^{sw} and the stress in the normal direction. Following the same approach as at an ice shelf base (Greve and Blatter, 2009), we employ an empirical relation

$$\mathbf{t}^{\text{sw}} \cdot \mathbf{n} = -p^{\text{sw}} \mathbf{n} + C^{i/\text{sw}} \rho^{\text{sw}} |\mathbf{v}^{\text{sw}}|^2 \mathbf{e}_t, \quad (6.10)$$

with $\mathbf{e}_t = \mathbf{v}^{\text{sw}}/|\mathbf{v}^{\text{sw}}|$ and $\mathbf{e}_t \perp \mathbf{n}$. The drag coefficient at the underside of the ice is $C^{i/\text{sw}}$, similar to the Manning roughness is taken into account in subglacial conduits. So the part of the subglacial water becomes

$$\mathbf{v}^{\text{sw}} \cdot \mathbf{t}^{\text{sw}} \cdot \mathbf{n} = -p^{\text{sw}} \mathbf{v}^{\text{sw}} \cdot \mathbf{n} + \mathbf{v}^{\text{sw}} \cdot C^{i/\text{sw}} \rho^{\text{sw}} |\mathbf{v}^{\text{sw}}|^2 \mathbf{e}_t = -p^{\text{sw}} \mathbf{v}_\perp^{\text{sw}} + C^{i/\text{sw}} \rho^{\text{sw}} |\mathbf{v}_\parallel^{\text{sw}}|^3, \quad (6.11)$$

with $\mathbf{v}_\perp^{\text{sw}}$ and $\mathbf{v}_\parallel^{\text{sw}}$ the normal and tangential velocity of the subglacial water, respectively. This formulation is quite similar to the treatment of the jump condition at an ice shelf base. For the traction vector at the ice base, we follow the same procedure and find

$$\mathbf{t}^i \cdot \mathbf{n} = -N \mathbf{n} + \tau_b \mathbf{e}_t, \quad (6.12)$$

with N the normal component and τ_b the component in the tangential plane. For $\mathbf{v}_b^i \cdot \mathbf{t}^i \cdot \mathbf{n}$ we find

$$\mathbf{v}_b^i \cdot \mathbf{t}^i \cdot \mathbf{n} = -N \mathbf{v}_b^i \cdot \mathbf{n} + \tau_b \mathbf{v}_b^i \cdot \mathbf{e}_t. \quad (6.13)$$

With the jump of the internal energy $\llbracket u \rrbracket = L$, we can reformulate Eq. (6.8) to

$$q_\perp^{\text{geo}} + q_\perp^{\text{sw}} = \rho^i a_b L + \kappa(T) \text{grad } T + p^{\text{sw}} \mathbf{v}_\perp^{\text{sw}} - C^{i/\text{sw}} \rho^{\text{sw}} |\mathbf{v}_\parallel^{\text{sw}}|^3 - N \mathbf{v}_b^i \cdot \mathbf{n} + \tau_b \mathbf{v}_b^i \cdot \mathbf{e}_t. \quad (6.14)$$

The tangential components $C^{i/\text{sw}} \rho^{\text{sw}} |\mathbf{v}_\parallel^{\text{sw}}|^3$ and $\tau_b \mathbf{v}_b^i \cdot \mathbf{e}_t$ are frictional heating and dominate the contribution of heat arising from work of surface forces. They need to be seen as two end members of the system: either the ice is only in contact with a thick subglacial hydrological system, in which case $C^{i/\text{sw}} \rho^{\text{sw}} |\mathbf{v}_\parallel^{\text{sw}}|^3$ is active,

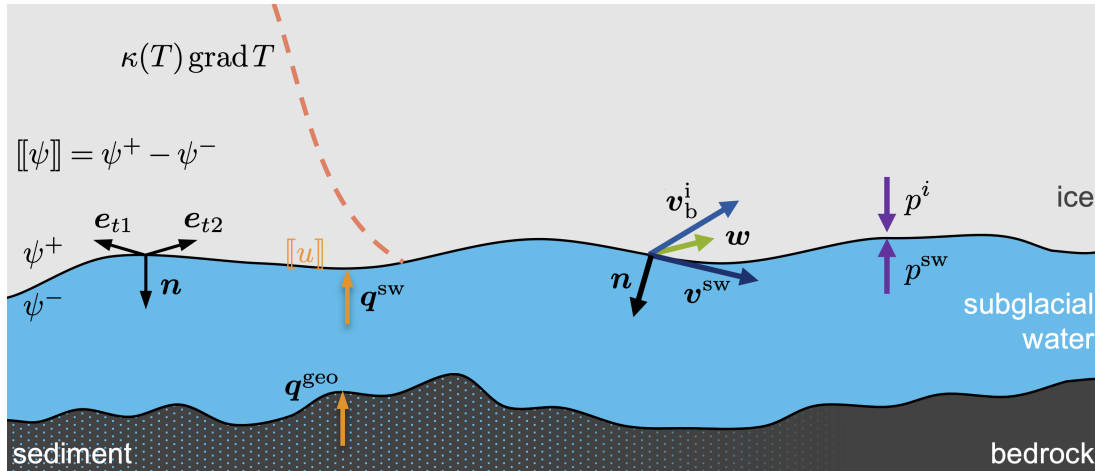


Figure 6.3: Sketch of the energy balance at the ice base. Thermal components are coloured in orange, and mechanical components are in blue-purple colour. For a detailed explanation see the main text.

or the subglacial hydrological system is permanently in contact with a lubricated base, in which case the second term $\boldsymbol{\tau}_b \mathbf{v}_b^i \cdot \mathbf{e}_t$ is governing. The components are visualised in Fig. 6.3.

Next, we aim at constraining the individual terms for which we use the following material parameters: $\rho^i = 910 \text{ kg m}^{-3}$, the latent heat of fusion, $L = 335 \text{ kJ kg}^{-1}$, and the thermal conductivity for ice at the pressure melting point of 270.81 K $\kappa(270.81 \text{ K}) = 2.10 \text{ W m}^{-1} \text{ K}^{-1}$ (Greve and Blatter, 2009).

We consider three scenarios: (i) there is only temperate ice that is melting, (ii) heat is required to warm the ice to the pressure melting point and (iii) friction at the base contributes significantly to basal melting. (i) For temperate ice and no heat arising from work of surface forces, we find a melt rate of at least 0.19 m a^{-1} to correspond to a heat flux of 1.84 W m^{-2} . (ii) Considering $\text{grad } T$ to be less than 10^{-1} K m^{-1} , this increases the required heat flux from scenario (i) by up to 0.21 W m^{-2} , as this additional heat is required to warm the ice to the pressure melting point.

(iii) Heat arising from work of the surface forces may, however, reduce the required heat flux into the ice to melt this amount of ice. To this end, we need to estimate the magnitude of the components of the stress tensors.

We assume that the normal stress component N is hydrostatic and bridging stresses to be negligible. With a mean density of ice of 910 kg m^{-3} we find $p^i = 23.8 \text{ MPa}$. The normal velocity is of the order of the basal melt rate $v_b^\perp \approx -0.2 \text{ m a}^{-1}$ by assuming the velocity of the interface (\mathbf{w}) to be zero. The normal component of the ice side is then on the order of 0.15 W m^{-2} . For the tangential components of the ice side, we consider the shear stress at the base to be $\boldsymbol{\tau}_b \approx 1$ to 100 kPa . This compares to basal shear stress found by Rückamp et al. (2020)

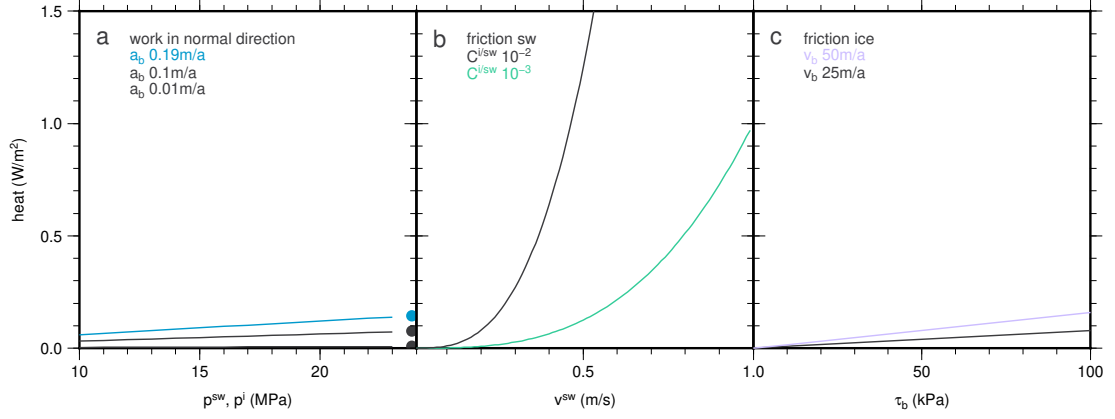


Figure 6.4: Magnitude of terms in the energy jump condition at the ice base. (a) Contribution of work of surface forces in the normal direction from water pressure (lines) and ice overburden pressure (dots). (b) Contribution of work of surface forces in the tangential direction from friction on the subglacial water. (c) Contribution of work of surface forces in the tangential direction from friction on the ice side.

of 50 kPa. To constrain the sliding velocity, we assume it to be maximum the surface velocity of 57 m a^{-1} and minimum half of the surface velocity. This leads to a tangential component on the ice side to be up to 0.15 W m^{-2} (Fig. 6.4).

Next, we constrain the normal component of the subglacial water $p^{\text{sw}} \mathbf{v}_{\perp}^{\text{sw}}$. A water pressure of 10 to 23 MPa is consistent with subglacial hydrological modelling (Beyer et al., 2018; Smith-Johnsen et al., 2020a). Assuming the normal velocity to be at most as large as the basal melt rate, we find the range of this term to be between 0.05 and 0.12 W m^{-2} (Fig. 6.4). The tangential component $C^{i/\text{sw}} \rho^{\text{w}} |\mathbf{v}_{\parallel}^{\text{sw}}|^3$ needs an assumption on the roughness $C^{i/\text{sw}}$, for which we consider a range from the roughness of the ice shelf base of 10^{-3} to a maximum roughness 10 times as large.

The motivation for this is that ice shelf roughness is governed by convection cells at the interface, whereas in the inland ice, the interaction with the bedrock may lead to a larger roughness. As nothing is known about the shape of the subglacial conduit, the range of velocity cannot be constrained well. We consider a speed similar to the one of the ocean 0.1 m s^{-1} , but as surface rivers easily reach 1.0 m s^{-1} , we take this as an upper limit (Fig. 6.4). Thus, the contribution of friction to the energy available for basal melting may account for at least $\sim 0.20 \text{ W m}^{-2}$, with the potential to be far larger based on the assumptions we made.

To summarise, the jump in the tangential component (friction) has the potential to govern the heat budget, depending on flow speeds in subglacial water and roughness of the ice base, as can be seen in Fig. 6.4. However, assuming the geothermal heat flux to be on the order of $\mathcal{O}(q^{\text{geo}}) \approx 0.25 \text{ W m}^{-2}$ makes evident

that the key player in facilitating such high melt rates is the subglacial water system, which may supply the ice base with an additional heat flux.

We have focused our consideration on the interface between a subglacial water layer and the ice, as this drives the basal melt rate. However, observations of [Christianson et al. \(2014\)](#) highlight the existence of a wet till layer beneath the ice stream. Depending on the thickness of the water layer, the velocity and pressure of the water, and the porosity of the till layer, complex interaction between the till and water may arise, too. [Kutscher et al. \(2019\)](#) present high-resolution simulations of a comparable system that highlight the importance of studying this interface as well. To date, it is unclear which vertical extent of the water layer is required to decouple the interaction of a water–till interface from the ice–water interface and thus the influence on the basal melt rate.

Large basal melting mainly affects basal sliding, as it increases the effective normal pressure. Considering sliding to be the dominant part of ice stream motion, large basal melt rates are also plausible in the respect that the subglacial hydrological system needs to be sustained over time, and hence creep closure of cavities or conduits needs to be balanced by melting.

Future measurements at EastGRIP after successful completion of the drilling to the ice base will shed more light on the sliding speed and may also provide more information on the characteristics of the subglacial hydrological system. This will enable the community to put our melt rate estimates into further context.

6.5 Conclusion

We estimated annual mean basal melt rates at the EastGRIP drill site from time series of high-precision phase-sensitive radar measurements. We derived the change in the measured ice thickness, thinning from firn densification occurring below the instrument and the vertical strain in the upper 1450 m of the roughly 2668 m thick ice. Two different scenarios for vertical strain distribution were used to quantify a plausible range of dynamic thinning. Thus, we derived an averaged melt rate of $0.19 \pm 0.04 \text{ m a}^{-1}$. We are aware that these melt rates require an extremely large amount of heat that we suggest to arise from the subglacial water system and the geothermal heat flux. However, these melt rates are based on measurements with a modern ice-penetrating radar whose penetration depth is limited due to transmitting power. Thus, no assumptions on past accumulation rates or other uncertainties in age reconstruction are involved. Our major uncertainty is the vertical strain in the lower part of the ice stream. This could be overcome if a more powerful radar with a similar vertical resolution could be operated autonomously over several months.

6.6 Appendix

6.6.1 Additional figures of ApRES processing

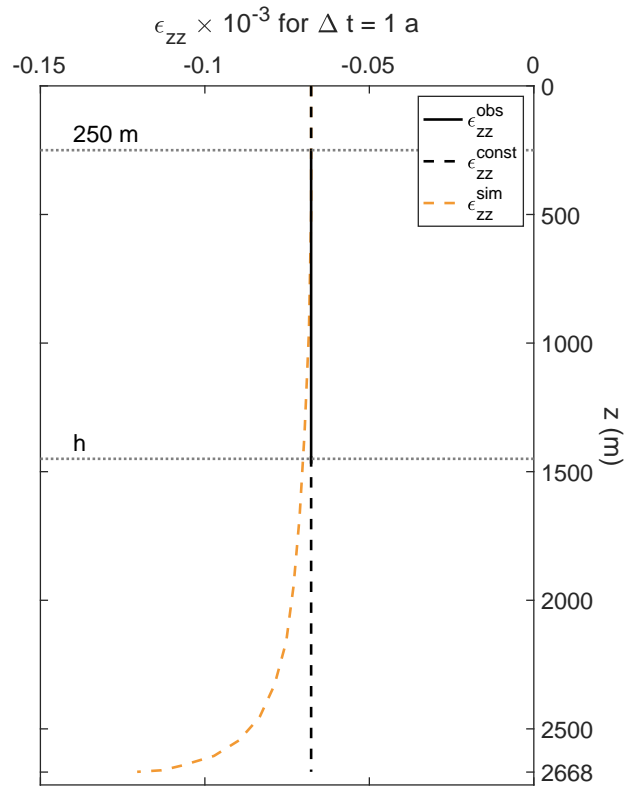


Figure 6.5: Observed vertical strain distribution (solid black line) and different extensions to the ice base (dashed lines) for two scenarios based on a constant (dashed black line), and a simulated (Rückamp et al., 2020, dashed orange line) distribution.

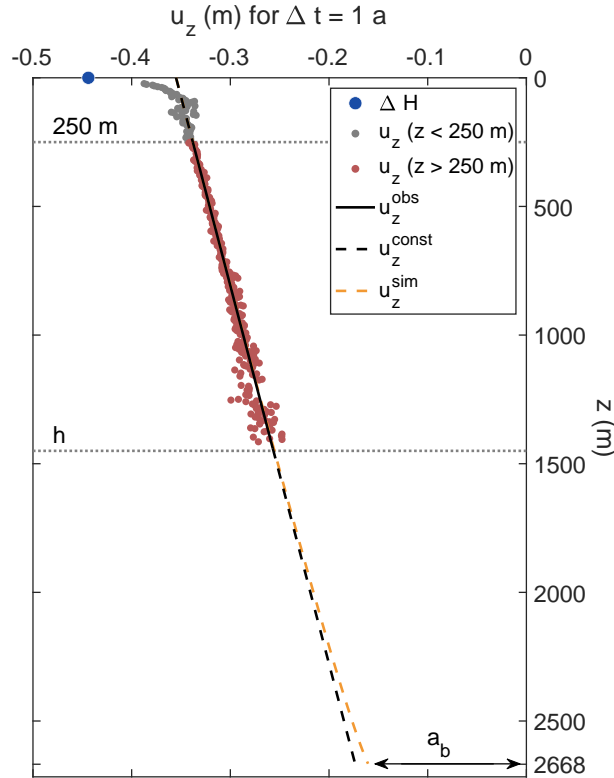


Figure 6.6: Derived vertical displacements u_z of the depth of the ApRES (ΔH ; blue dot) and of selected internal layers referenced to the ice base from 2018/19 ApRES time series. Derived displacements used for melt rate estimations are marked by red dots and for layers within the firn by grey dots. The estimated displacements between a depth of 250 m and h are used to calculate a linear fit (solid black line), the gradient of which is the vertical strain. Extrapolations to the bottom are shown by the dashed lines. The offset at the ice base is caused by basal melting, and the difference between the intercept of the linear fit at $z = 0$ m and ΔH is the firn compaction.

Data availability

Raw data of the ApRES measurements (<https://doi.org/10.1594/PANGAEA.931018>; Zeising and Humbert, 2021a) are available at the World Data Center PANGAEA.

Acknowledgements

Data were acquired at the EastGRIP camp that kindly hosted this activity as an associate project. EastGRIP is directed and organised by the Centre for Ice and Climate at the Niels Bohr Institute, University of Copenhagen. It is supported by funding agencies and institutions in Denmark (A. P. Møller Foundation, University of Copenhagen), the United States (US National Science Foundation, Office









of Polar Programs), Germany (Alfred Wegener Institute, Helmholtz Centre for Polar and Marine Research), Japan (National Institute of Polar Research and Arctic Challenge for Sustainability), Norway (University of Bergen and Trond Mohn Foundation), Switzerland (Swiss National Science Foundation), France (French Polar Institute Paul-Emile Victor, Institute for Geosciences and Environmental research), Canada (University of Manitoba) and China (Chinese Academy of Sciences and Beijing Normal University). We would like to thank Johanna Kerch, Sepp Kipfstuhl and Daniel Steinhage for their support in the deployment and the dismount of the measuring device. We are grateful for discussions with Thomas Kleiner and Martin Rückamp (AWI) and Ralf Greve (ITLS, Japan) on vertical strain rates and our results.

Extreme melt rates at Greenland's largest floating ice tongue

7

This chapter is a research article in preparation.

Authors and affiliations

Ole Zeising^{1,2}, Niklas Neckel¹, Daniel Steinhage¹, Nils Dörr^{3,4}, Thomas Kleiner¹, Martin Rückamp¹, Janin Schaffer¹, Ralph Timmermann¹, and Angelika Humbert^{1,2}

¹Alfred-Wegener-Institut Helmholtz-Zentrum für Polar- und Meeresforschung, Bremerhaven, Germany

²University of Bremen, Department of Geosciences, Germany

³Institute of Geosciences, Kiel University, Kiel, Germany

⁴Institute of Photogrammetry and Remote Sensing, Karlsruhe Institute of Technology (KIT), Karlsruhe, Germany

Contributions

O. Zeising, D. Steinhage and N. Neckel conducted the field study. A. Humbert has designed the study and planned the field expeditions and airborne campaigns. **O. Zeising** processed the pRES data, estimated and analysed the resulting basal melt rates. D. Steinhage contributed the echogram of 2015. N. Dörr processed UWB data and discovered the central channel. N. Neckel processed all satellite data and determined the elevation changes, surface melt and grounding line location. A. Humbert determined timing of lake drainage. M. Rückamp performed the ISSM simulations. R. Timmermann contributed estimated oceanic heat flux. **O. Zeising**, T. Kleiner, R. Timmermann and A. Humbert discussed the freshwater flux arising from lake drainage. **O. Zeising**, R. Timmermann, J. Schaffer and A. Humbert discussed the basal melt rate distribution and time series. **O. Zeising** wrote Sect. 7.2 ("Data and Methods") – with the exception of Sect. 7.2.2 to Sect. 7.2.4 which were written by N. Dörr, D. Steinhage and N. Neckel – Sect. 7.3 ("Results") and Sect. 7.4 ("Discussion") with contributions from A. Humbert and N. Neckel. All figures were created by **O. Zeising**.

Abstract

The 79°N Glacier (Nioghalvfjærdsbrae) is the largest of the three remaining floating ice tongues of outlet glaciers in Greenland. We conducted high-resolution in-situ observations of basal melting and found off-nadir melt rates of up to $144 \pm 2 \text{ m a}^{-1}$ right at the transition from inland to the hinge zone. Within this zone, basal melt rates declined. We found evidence for deepening of basal channels in conjunction with a surface elevation reduction near the grounding line in recent years. This can likely be linked to prominent supraglacial lakes, suggesting glacier hydrology to be an important factor for ice tongue stability in the future. Year-round time series show reduced basal melt rates from mid 2018 on, potentially attributed to a weaker inflow of AIW into the cavity below 79NG.

7.1 Introduction

Floating ice tongues are of particular importance for regulating ice-sheet discharge due to their potential buttressing effect (Joughin et al., 2004, 2008, 2014, 2020; Rückamp et al., 2019). One of the three remaining floating tongues in Greenland is the one of Nioghalvfjærdsbræ (79°N Glacier, 79NG). Together with its neighbouring Zachariæ Isstrøm (ZI) it is the main outlet glacier of the Northeast Greenland Ice Stream (Fig. 7.1a), the largest ice stream of the Greenland Ice Sheet (Fahnestock et al., 2001b). Their drainage basins cover 11% of the ice sheet area and hold the potential to raise global mean sea level by 1.1 m (Krieger et al., 2020a). After the collapse of ZI's floating tongue in 2002, the glacier has accelerated by 50% and thinned by more than 2 m a^{-1} (Helm et al., 2014; Khan et al., 2014; Mouginot et al., 2015). Although the nearby ZI has lost nearly its entire floating part, 79NG is still remarkably stable with only minor acceleration rates (Mouginot et al., 2015). Its stability is attributed to pinning points at the calving front (Thomsen et al., 1997), lateral resistance from shear margins (Mayer et al., 2000; Rathmann et al., 2017; Mayer et al., 2018) and confinement of the glacier leading to lateral compression (Fig. 7.1b). However, thinning has occurred during the last two decades (Helm et al., 2014; Mouginot et al., 2015; Mayer et al., 2018; Kjeldsen et al., 2015). Warm ocean water was found in fjords around Greenland (Holland et al., 2008; Straneo et al., 2012), giving rise to the hypothesis that it enhances basal melting, which eventually leads to disintegration and retreat of the floating ice tongues (Motyka et al., 2011). However, the supply of freshwater from glacier surface melting was found to alter circulation in fjords and basal melting of glaciers (Straneo et al., 2016). In the future, submarine melt rates are expected to increase most pronouncedly in the northeastern part of Greenland

towards the end of the 21st century (Slater et al., 2020). The role of the ocean in that is not yet fully constrained: Warm ($> 1^\circ\text{C}$) Atlantic Intermediate Water (AIW) was found to be present in the ocean cavity below 79NG’s floating tongue (Straneo et al., 2012; Wilson and Straneo, 2015; Lindeman et al., 2020). The observed oceanic heat transport into the sub-ice cavity (Schaffer et al., 2020) has been suggested to maintain intense basal melting (Mayer et al., 2018; Lindeman et al., 2020; Schaffer et al., 2020). Observations of basal melt rates are thus a key ingredient to understand the dynamics of the system.

Attempts have been made to estimate basal melt rates indirectly by using satellite observations (Rückamp et al., 2019; Moholdt et al., 2015; Schodlok et al., 2016; Wilson et al., 2017), although these methods are accompanied with considerable uncertainties and limited to freely floating parts. In the ~ 4 km wide hinge zone of 79NG between the grounding line (defined as the upper flexure limit) and the lower flexure limit, higher basal melt rates occur due to thick and temperate ice getting into contact with warm ocean waters. As the magnitude of basal melt rates as well as their variability on spatial and temporal scales, are still unknown, this is a major objective of our study. We use in-situ radar measurements to derive basal melt rates focusing on the hinge zone of 79NG. The basal geometry of floating tongues is known to be largely controlled by basal melt rates. Therefore, we first give an overview of the ice thickness distribution and its recent changes detected by radar and satellite observations.

7.2 Data and methods

We acquired airborne and ground-based radar measurements at the 79NG under the framework of the *Greenland Ice Sheet – Ocean Interaction* (GROCE) project. In order to obtain a spatial distribution of basal melt rates, we performed a repeat survey of Lagrangian phase-sensitive radar (pRES) measurements in July 2017 and 2018. The majority of the measurement locations were distributed within 8 km distance from the grounding line (Fig. 7.1b). Additionally, we operated four autonomous pRES stations (ApRES1–3) moving with the ice to derive year-round time series in Lagrangian reference. In Summer 2018, we relocated the ApRES2 to its starting position from 2016 in order to repeat the measurements on the same flowline. These stations are labelled as ApRES2a (2016–2018) and ApRES2b (2018–2019). The airborne radar measurements were performed in April 2018 with the ultra-wideband (UWB) radar in order to derive the basal geometry of the 79NG. A data set with which the UWB derived geometry is compared was recorded with the Alfred Wegener Institute’s (AWI’s) radio-echo sounding airborne system (RES) in 2015. Additionally, we generated 93 Digital

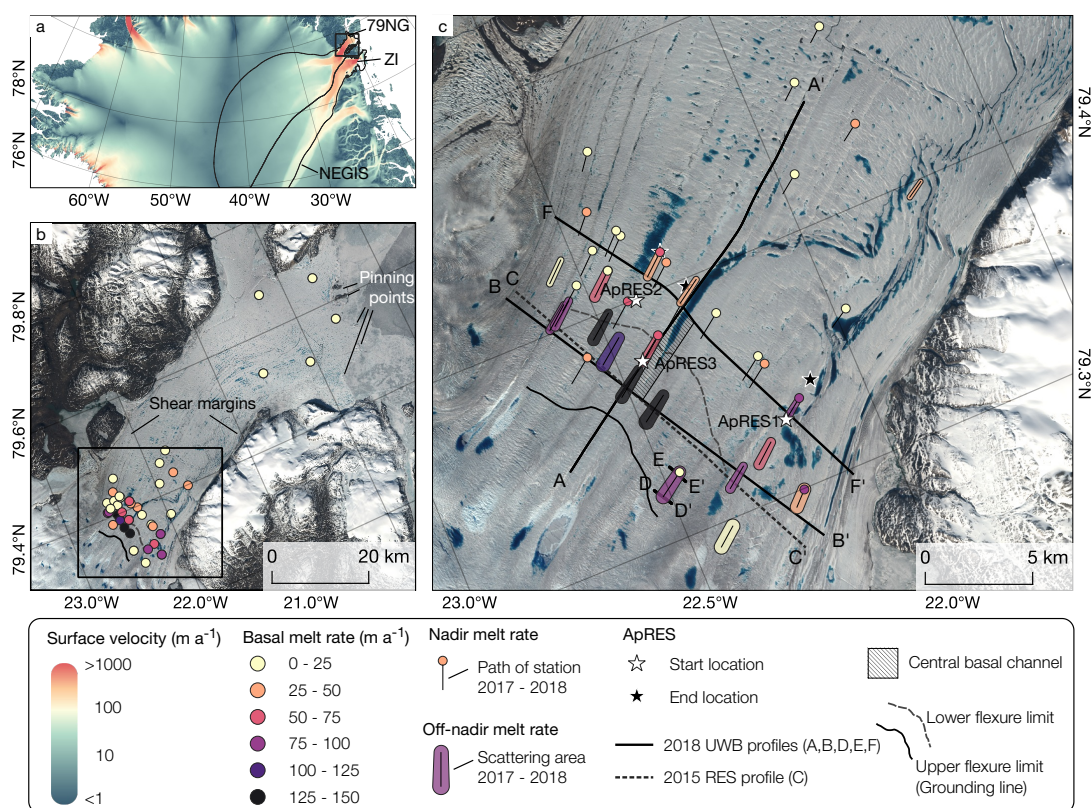


Figure 7.1: Basal melt rate distribution (2017 – 2018) and airborne radar profiles (2015 and 2018) at the floating tongue of 79NG. (a) Map of northern Greenland with drainage basins (black lines) of 79NG and Zachariæ Isstrøm (ZI) (Krieger et al., 2020a) and surface velocities (Joughin et al., 2018) showing the North-east Greenland Ice Stream (NEGIS). (b) Sentinel-2 mosaic of 79NG with basal melt rates derived from in-situ measurements in 2017 and 2018 (box in (a)). (c) Enlargement of the 79NG hinge zone (box in (b)) showing nadir and off-nadir basal melt rates with paths of Lagrangian measurement location or scattering area (off-nadir based melt rates) between July 2017 and July 2018. White stars mark the starting and black stars the ending position of ApRES stations. UWB profiles from 2018 are represented by solid black lines, the RES profile from 2015 by a dotted line.

Elevation Models (DEMs) from bistatic TanDEM-X SAR interferometry following the methods described by Neckel et al. (2013), in order to obtain a time series of surface elevations.

7.2.1 Phase-sensitive Radio Echo Sounder (pRES)

The phase-sensitive radio echo sounder (pRES), developed at the British Antarctic Survey, is a frequency-modulated continuous wave (FMCW) radar, transmitting chirps with a frequency bandwidth of 200 MHz and a centre frequency of 300 MHz (Brennan et al., 2014; Nicholls et al., 2015). Mean annual melt rate estimates are based on repeat measurements using 100 chirps. An autonomous pRES (ApRES) station consists of a pRES with two bow-tie antennas and recorded 20

chirps with a measuring interval between one and six hours. For processing the data, we calculated pairwise correlation coefficients of all chirps, rejected chirps with low correlation coefficients and stacked the remaining ones. We followed [Brennan et al. \(2014\)](#) for processing to get amplitude- and phase-depth profiles. To transform two-way travel time to depth, we used a propagation velocity for the electromagnetic wave of $168.914 \text{ m } \mu\text{s}^{-1}$ that refers to a relative permittivity of $\epsilon_r = 3.15$ for pure ice.

Figure 7.2a shows the resulting echograms of the measurements performed at ApRES2a (Appendix Figs. 7.12–7.14 show the echograms of ApRES1, ApRES2b and ApRES3). The ice base is assumed to be responsible for strong peaks in the radar signal due to a high contrast in relative permittivity between ice and sea water. In case of a flat ice base, the nadir reflection has the shortest two-way travel time (TWT) of all basal reflections in a radius defined by the antenna beamwidth. However, basal channels consist of steep basal gradients that cause off-nadir reflections which might appear before the nadir basal return. Figure 7.2a reveals such a complex base with several (off-nadir) basal returns and crossing reflections. Furthermore, it shows melt water intrusions in summer and artefacts from signal clipping.

Basal melt rates from ApRES time series

The calculation of basal melt rates follows previously described methods ([Corr et al., 2002](#); [Jenkins et al., 2006](#); [Stewart et al., 2019](#)). Several quantities cause changes to the measured ice thickness H within the time period Δt : ablation ΔH_s , vertical strain ΔH_ϵ and basal melting ΔH_b

$$\frac{\Delta H}{\Delta t} = \frac{\Delta H_s}{\Delta t} + \frac{\Delta H_\epsilon}{\Delta t} + \frac{\Delta H_b}{\Delta t} \quad (7.1)$$

(e.g. [Vaňková et al., 2020](#); [Zeising and Humbert, 2021b](#)). The basal melt rate a_b is then defined as

$$a_b = -\frac{\Delta H_b}{\Delta t}. \quad (7.2)$$

With ApRES time series, all of these quantities can be estimated in order to obtain the basal melt rate. The above stated equations give the basal melt rate from nadir changes in ice thickness. However, if off-nadir basal reflections are taken into account for the melt rate estimate, the method needs to be adjusted as [Vaňková et al. \(2021\)](#) shows.

Since the calculation is based on the detection of vertical displacement of layers, we divided the first echogram in 6 m long segments with 5 m overlap starting at a depth of 20 m. For each segment we derived displacements from complex cross-

correlation of the phase of all pairwise time-consecutive measurements (Stewart, 2018; Vaňková et al., 2020). Afterwards, we calculated the daily mean values of the displacements.

In a first step, we used the time-mean vertical displacement of internal reflectors to calculate the vertical strain profile by following Vaňková et al. (2021). Here only those segments between 20 m below the surface and 20 m above the first basal return were considered (Fig. 7.2b,c). The vertical strain is the depth derivation of the vertical displacement u_z

$$\varepsilon_{zz} = \frac{\partial u_z}{\partial z}, \quad (7.3)$$

which we derived from a linear fit that best matches the vertical displacements. Although one of the ApRES stations was located within the hinge zone in which bending might affect the strain distribution (Jenkins et al., 2006; Vaňková et al., 2021), none of the displacement distributions indicated a deviation from a linear function over depth.

The change in ice thickness is only affected by the vertical strain for a nadir basal reflection. However, the displacement of off-nadir reflectors has additionally a horizontal component. To compensate for the vertical and horizontal deformation, we use the equation

$$\Delta H_\varepsilon^\alpha = \sqrt{(x_0(1 + p\varepsilon_x))^2 + \left(z_0 + \int_0^{z_0} \varepsilon_{zz} dz\right)^2} - \sqrt{x_0^2 + z_0^2}, \quad (7.4)$$

which is slightly modified from the equation given by Vaňková et al. (2021). This equation gives the change in ice thickness due to strain $\Delta H_\varepsilon^\alpha$ for a reflector at (x_0, z_0) that is viewed at an angle α . It assumes that ice is incompressible and that the deformation takes place along the vertical (z) and only one horizontal (x) dimension, so that $\varepsilon_{zz} = -\varepsilon_{xx}$ (Vaňková et al., 2021). The factor p ranges from 0 to 1 and represents whether the reflector and the ApRES are in line with the horizontal deformation ($p = 1$) or orthogonal to it ($p = 0$). As the relative position of the basal reflectors is unknown, we estimate the maximum range of $\Delta H_\varepsilon^\alpha$ for different α . From the range of a basal reflector R , the relative location can be derived from $x_0 = \sin \alpha R$ and $z_0 = \cos \alpha R$. For a nadir return at which α is zero, we obtain

$$\Delta H_\varepsilon^0 = \int_0^{z_0} \varepsilon_{zz} dz \quad (7.5)$$

and for a maximum of $\alpha = 30^\circ$ (Brennan et al., 2014), we derived $\Delta H_\varepsilon^{30}$ from Eq. 7.4. Finally, we averaged both values to obtain ΔH_ε and consider the range of possibilities for different α within the uncertainty.

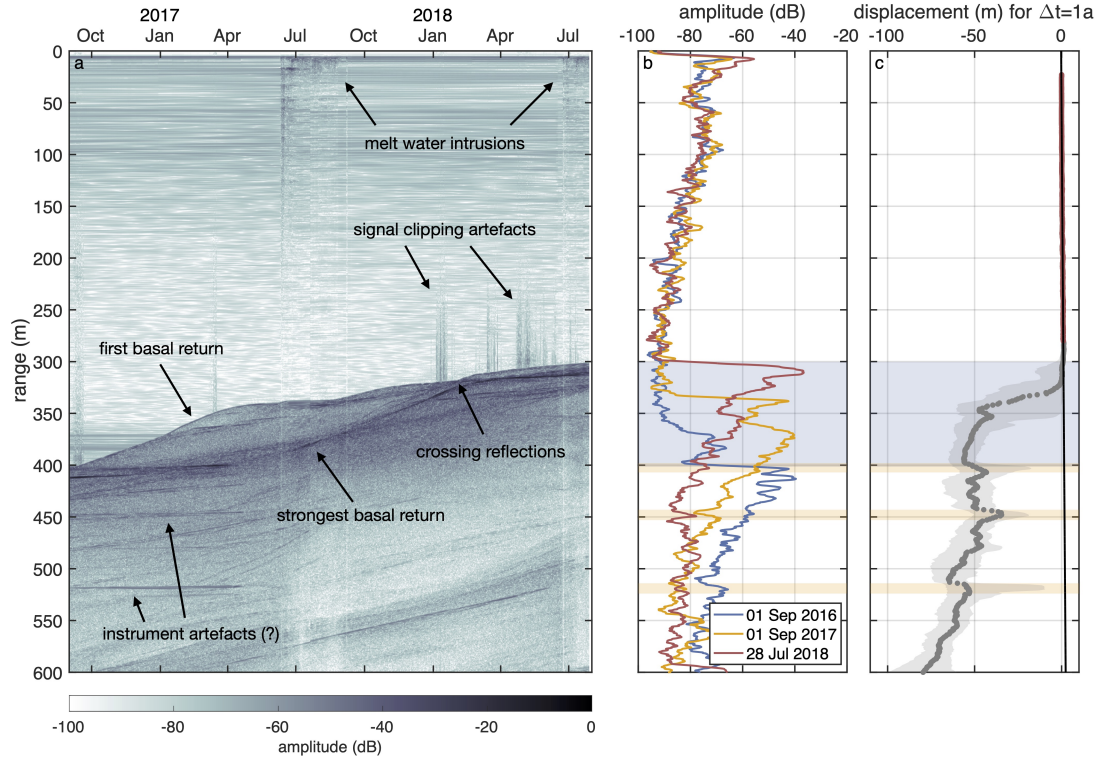


Figure 7.2: ApRES2a echograms. (a) Time-echogram of a Lagrangian measurement at ApRES2a recorded between September 2016 and July 2018. (b) Single echograms from 01 September 2016 (first measurement), 01 September 2017 and 28 July 2018 (last measurement), smoothed with a 5 m moving average filter. The blue shaded range corresponds to the displacement of the first basal return within the measurement period. Yellow shaded ranges mark depth of radar artefacts. (c) Mean vertical displacement of internal and basal segments (grey dots). The grey shaded area marks the range between the 25% and 75% quantile. Those displacements from segments between 20 m and 20 m above the first basal return at the end of the measurement period (red dots) were used to derive the change in ice thickness due to vertical strain by fitting a linear function (black line). Displacements of segments within the blue shaded range are partly from internal and partly from basal reflections.

Next, we use the displacement time series of the segment centered at a range of 100 m (u_z^{100}) to correct for ablation. Since the ice above is affected by strain thinning/thickening, we subtract this contribution from the displacement:

$$\Delta H_s = u_z^{100} - \int_0^{100} \varepsilon_{zz} dz. \quad (7.6)$$

Since melt water intrusions affect the amplitude- and phase-signals significantly, they can prevent a reliable determination of the displacements. Thus, some measurements were rejected from the melt rate analysis.

To finally derive the basal melt rate, Vaňková et al. (2021) subtracted ΔH_ε and ΔH_s from the displacement of a basal reflector and corrected for off-nadir reflec-

tions

$$a_b^\alpha = -\frac{\Delta H - \Delta H_\varepsilon - \Delta H_s}{\Delta t \cos \alpha}. \quad (7.7)$$

Here, $\cos \alpha$ is an approximation that corrects for small displacements viewed at an angle α to nadir. Since α is still unknown, we use again the range from 0° to 30° and averaged the melt rates. In this way, we calculated basal melt rates for all segments within a range of 50 m below the first basal return. This range was chosen since all strong basal reflections occurred in within 50 m. We averaged the melt rate within this range in order to derive a time series of basal melt rates. To represent the variability within a time series, we calculated the median melt rate next to the 25%, 75% and 95% quantile for each time step. Afterwards, a 7-day moving average filter was used to smooth the time series.

The largest uncertainty arises from the unknown angle α , which is roughly 7.5% of the melt rate, and from the $\sim 1\%$ inaccuracy of the signal propagation speed in ice (Fujita et al., 2000). Other contributions are comparatively small, since displacements could be derived reliably with an accuracy in millimetres range. Overall, the uncertainty is rather large with $\sim 10\%$.

Basal melt rates from single-repeated pRES measurements

The ApRES time series allow the determination of displacements of the basal return from cross-correlations. This method cannot be used for single-repeated measurements due to the high melt rates and the occurrence of off-nadir reflections. Therefore, two criteria were chosen to distinguish between nadir and off-nadir returns: (1) The ice base – ice surface – ice base multiple is assumed to be the strongest for the nadir reflection. The reflected energy from a far off-nadir reflection will be mostly reflected in the opposite direction in case of a flat ice surface. Therefore, multiples from off-nadir reflections will be weaker compared to nadir reflections. (2) Ice thickness distribution derived from UWB echograms nearby the location of the pRES observations can reveal the ice thickness and furthermore, give a hint for the origin of the recorded off-nadir reflection.

At stations where we could not distinguish reliably between a nadir and an off-nadir reflection, we used the first significant increase in amplitude for ice thickness calculation and interpret this as an off-nadir return. After identifying the basal return in the echogram of the first and repeated measurement, a cross-correlation of the amplitude and the phase of their basal segments was applied to estimate ΔH .

The estimation of vertical strain was not possible with single-repeated pRES measurements due to low correlation of the amplitude profiles. Here, we used vertical strain rates obtained from the Ice-Sheet and Sea-level System Model

(ISSM; Morlighem et al., 2010; Larour et al., 2012). The simulation is based on Rückamp et al. (2020), but uses a refined grid with ~ 100 m spacing at the grounding line and up to 3 km at the calving front of the 79NG. The model uses the MEaSURES velocity dataset (Joughin et al., 2016, 2018) and an inversion approach with a higher-order Blatter-Pattyn-type approximation (Blatter, 1995; Pattyn, 2003). In case we identified the nadir basal return in the repeated measurement, we derived ΔH_ϵ from Eq. 7.5. If an off-nadir basal return was selected within the repeated measurement, we followed the processing described for the ApRES time series and used Eq. 7.4 with α between 0° and 30° in order to derive an average of ΔH_ϵ . The surface ablation ΔH_s was derived from bamboo poles deployed at each location (Zeising et al., 2020).

In both cases we calculated the basal melt rate without an off-nadir correction (in contrast to the ApRES melt rate estimation)

$$a_b = -\frac{\Delta H - \Delta H_\epsilon - \Delta H_s}{\Delta t}. \quad (7.8)$$

In the event that an off-nadir basal return was selected (either in the first or repeat measurement), the resulting ice thickness at the origin of the reflection in the repeat measurement is overestimated and the difference in ice thickness between both measurements is underestimated. In case one of the returns has been an off-nadir return, a correction using $\cos \alpha$ is not possible anymore. Nevertheless, the derived basal melt rate underestimates the melt rate right at the location of the first basal reflector of the repeated measurement (see Appendix 7.6.1 and Figs. 7.10 and 7.11). This means that at some point in the vicinity (within a radius of x_0) of the pRES measurement, this or a higher melt rate exists. Still, no constraint on the nadir melt rate can be achieved here.

The uncertainty in melt rate at a station at which nadir basal returns were used for melt rate analysis, depends mostly on the accuracy of the ISSM derived strain rate. From the misfit of the simulated velocity to those from MEaSURES, we estimate an uncertainty of the vertical strain rate of 10%. The uncertainty of the surface ablation is on the order of 0.1 m and the one of the change in ice thickness is 0.03 m. This results in an averaged uncertainty of 6% of the nadir melt rate or 0.78 m.

The largest contribution of the uncertainty of off-nadir melt rates comes from the deviation from the mean of ΔH_ϵ^0 and ΔH_ϵ^{30} . On average, the uncertainty of the off-nadir melt rate makes about 5% or 2.36 m. In case of a misidentification of the basal return, the error could become larger. Generally, we used the first strong reflection that we referred to be reflected at the ice base to underestimate the total thinning of the glacier. Here, a large error would occur, if a weak basal

reflection was disregarded. To avoid this, we used additional information of the glacial geometry from several UWB echograms, recorded in 2018. However, if the first basal return was still unclear, we used a shallower, but more unlikely reflection to still underestimate the ice thickness or, we rejected the measurement.

7.2.2 Ultra-wideband (UWB) airborne radar

The UWB is a multichannel coherent radar depth sounder consists of an eight-element antenna array with a total transmit power of 6 kW (Hale et al., 2016), operated on board of Alfred Wegener Institutes (AWI's) research aircraft Polar6 (Alfred-Wegener-Institut, 2016). The antennas operate in the frequency band of 150 – 520 MHz, with a pulse repetition frequency of 10 kHz and a sampling frequency of 1.6 GHz. The characteristics of the transmitted waveform and the recording settings can be manually adjusted. We used alternating sequences of different transmission/recording settings (waveforms) to increase the dynamic range: short pulses ($1 \mu\text{s}$) and low receiver gain (11 – 13 dB) to image the glacier surface, and longer pulses (3 – 10 μs) with higher receiver gain (48 dB) to image internal features and the ice base. The waveforms were defined with regard to the glacier thickness at the covered profiles. Additionally, we used two different frequency bands in the survey: 180 – 210 MHz and 150 – 520 MHz. The theoretical range resolution in ice after pulse-compression for the two bandwidths is about 2.8 m and 0.23 m, respectively. Recorded traces were presumed in the hardware by a factor between 2 and 16, depending on the pulse length. In order to reduce range side lobes, the transmitted and the received signals were tapered using a Tukey window and the received signal spectrum was filtered with a Hanning window. We recorded the position of the aircraft with four NovAtel GPS receivers, which were mounted on the wings and the fuselage. They are dual-frequency trackers and operate at 20 Hz.

Post-flight processing included pulse compression in range direction, synthetic aperture radar focusing in the along-track direction and array processing in the cross-track direction to suppress off-nadir echoes. We assumed a relative permittivity of $\varepsilon_r = 3.15$ in ice for the time-to-depth conversion. No firn correction was applied, since the predominant part of the glacier is located in the ablation zone. We concatenated the echograms of the alternating waveforms to obtain the final echograms covering the glacier from the surface to the base with high dynamic range.

7.2.3 AWI's radio-echo sounding airborne (RES) radar

Another ice thickness radar system operator on board of AWI's aircraft (Alfred-Wegener-Institut, 2016) is AWI's radio-echo sounding airborne system (RES) that operates at 150 MHz and can transmit pulses of 60 ns or 600 ns. These pulses can also be transmitted alternately (toggle mode). Compared to the set-up described by Nixdorf et al. (1999), changes in the receiver hardware allow the recording of 15 radar traces per second, each internally stacked 1,024 fold. The dynamic range of the system is -105 to $+10$ dB (Humbert et al., 2018). In post-flight processing, data were differentiated, filtered and amplitudes were rescaled. The horizontal resolution in toggle mode is 75 m and the vertical resolution of the short pulse is in the order of 5 m.

7.2.4 Time series of surface elevations from TanDEM-X SAR interferometry

Interferograms were formed from co-registered Single-look Slant range Complex (CoSSC) data employing a 4×4 multi-looking step. Prior to phase unwrapping we subtracted a simulated phase from the global TanDEM-X DEM. The latter was done to reduce unwrapping errors and the simulated phase was added back afterwards. The final DEMs were geocoded and spatially adjusted to the global TanDEM-X DEM over stable bedrock following the methods described by Nuth and Kääb (2011). Surface elevation changes between 2010 and 2020 were estimated by fitting a linear trend to every pixel of the co-registered DEM stack (e.g. Berthier et al., 2016).

7.3 Results

7.3.1 Channelised basal geometry near the grounding line

The ice thickness distribution reveals a shape typical for floating ice tongues, with thicker ice at the grounding line (up to 700 m) and thinner ice towards the calving front (Fig. 7.3a). Within the first kilometre from the grounding line, the ice thickness reduces by > 100 m on average. This high thinning rate decreases afterwards. From the lower flexure limit on, where the ice thickness is about 360 m, thinning rates remain low. In across-flow direction, the airborne radar data reveal the existence of several basal channels near the grounding line (Fig. 7.3b,c) which are located downstream from supraglacial lakes (Fig. 7.4a). The largest channel with a height of 490 m in 2018 is found in the centre of the glacier with only 160 m of ice above, which is 25% of the surrounding ice thickness.

Between 2015 and 2018 we observed a massive decrease in ice thickness of 55 m a^{-1} above this channel. This is in good agreement with the lowering of the surface by $-5.9 \pm 0.1 \text{ m a}^{-1}$ derived from TanDEM-X satellite data since 2010 (Fig. 7.4b). In contrast, surface elevation change rates outside the channel are $-0.8 \pm 0.1 \text{ m a}^{-1}$. While in 2010 the surface at location l1 (Fig. 7.4c) formed a hill, it transformed to a sink in 2014 (intersection of trend lines, Fig. 7.4b). These results indicate an ongoing deepening of the central basal channel.

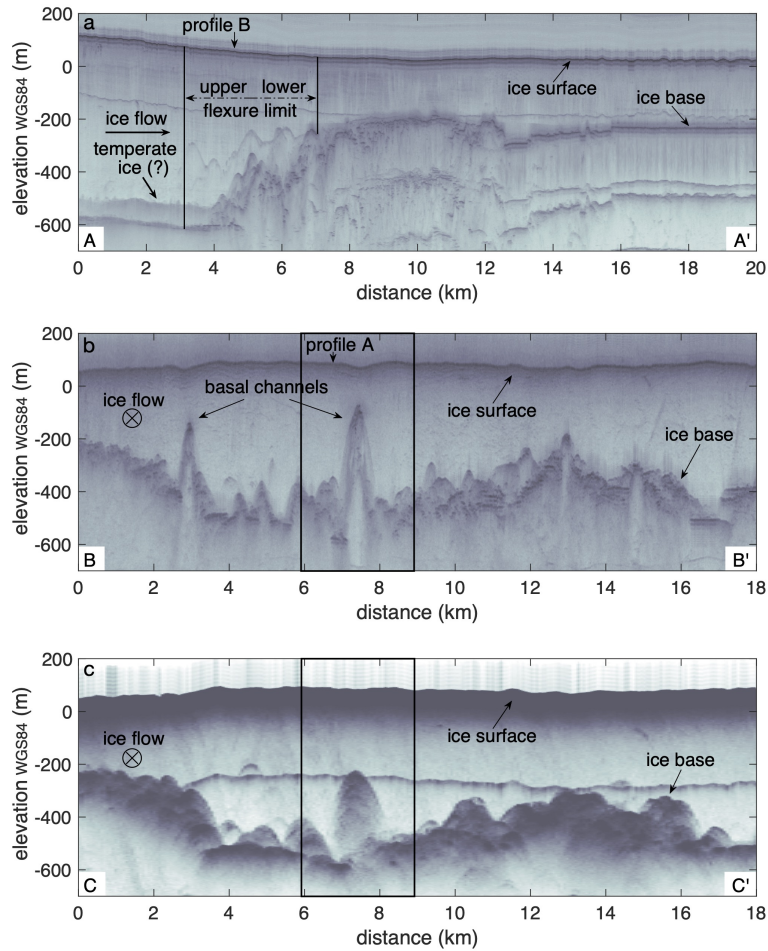


Figure 7.3: Airborne radar echograms along and across ice flow of 79NG. (a) Echogram from the along-flow profile A (location in Fig. 7.1). The ice flow direction is from left to right. Vertical lines mark the upper flexure limit (grounding line) and the lower flexure limit in 2017. (b,c) Echograms from the across-flow 2018 UWB echogram B in (b) and the 2015 RES echogram C in (c) (location in Fig. 7.1c). The ice flow direction in both cross-flow profiles is in viewing direction. The section marked by the black box around the central basal channel is displayed in detail in Fig. 7.4d to show a schematic comparison of the ice thickness. Note that the along-flow profile in (a) covers only 20% of the total length of the 79NG floating tongue.

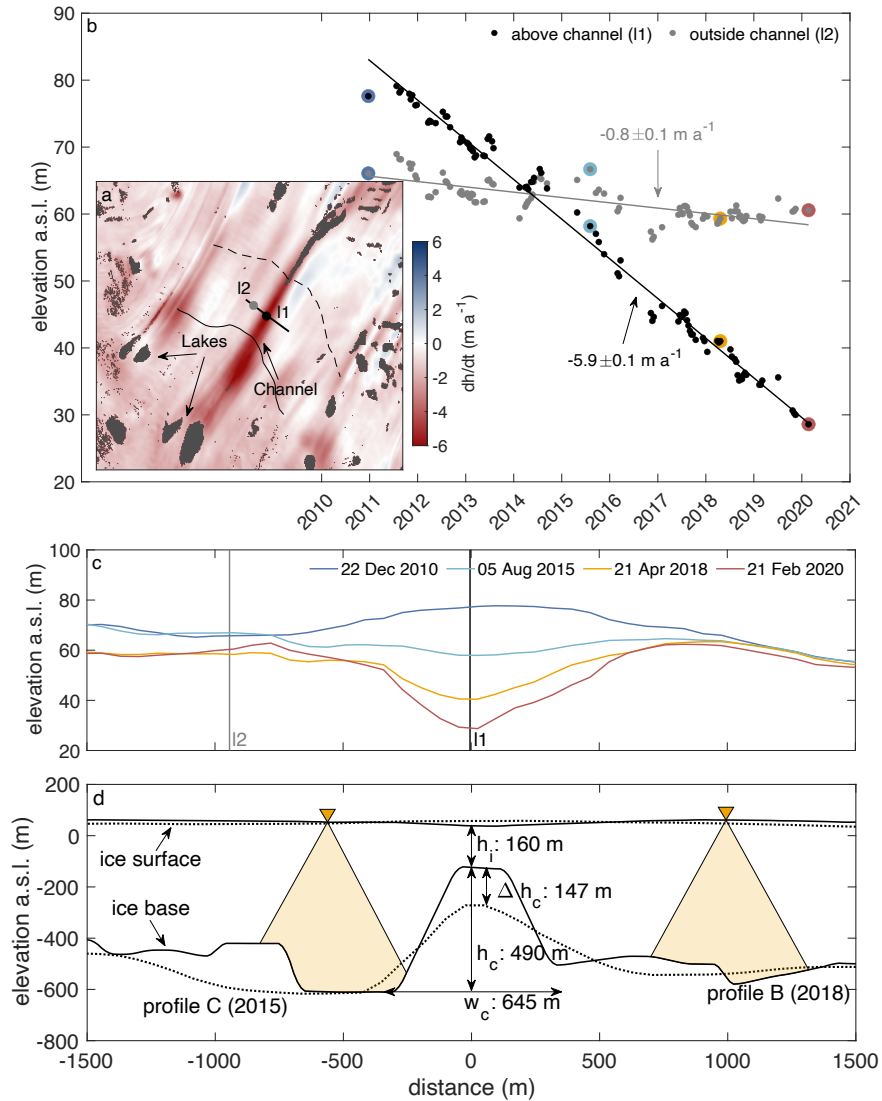


Figure 7.4: Surface lowering above central channel. (a) Surface elevation change rates (dh/dt) derived from TanDEM-X satellite data between 2010 and 2020. Grounding line and lower flexure limit are represented with solid and dashed lines, respectively. (b), Time series of surface elevation (EGM2008) derived from TanDEM-X satellite data above two locations (grey and black dots in (a)) since 2010. The numbers represent gradient of linear regression. Coloured dots mark the profiles that are shown in (c). (c) Surface elevation from 2010, 2015, 2018 and 2020 above the channel area. (d) Schematic comparison of the large central channel from airborne radar profiles B (solid line, Fig. 7.3b, 2018) and C (dotted line, Fig. 7.3c, 2015). Triangles show locations of two pRES stations and the shaded area represents their scattering area. The numbers give values for the ice thickness (h_i) above the channel and the height (h_c) and width (w_c) of the channel in 2018 (solid line). Δh_c represents the decrease in ice thickness above the channel from 2015 to 2018.

7.3.2 Extreme basal melting in the hinge zone

Mean annual basal melt rates are between 1 and $144 \pm 2 \text{ m a}^{-1}$ for the entire ice tongue of 79NG (Figs. 7.1c and 7.5). The highest (off-nadir) melt rates of 135 ± 2 and $144 \pm 2 \text{ m a}^{-1}$ were found at the most downstream bulge of the grounding line, next to the central basal channel. However, moderate melt rates of $< 27 \text{ m a}^{-1}$ were observed at similar distance to the grounding line (Fig. 7.5). Further downstream, but still within the hinge zone, we observed predominantly high melt rates of $> 50 \text{ m a}^{-1}$ spread across the entire width of the ice tongue. In general, melt rates are observed to be below 35 m a^{-1} several kilometres downstream from the grounding line, declining towards the calving front to $1.1 \pm 0.2 - 2.8 \pm 0.3 \text{ m a}^{-1}$ (Figs. 7.1 and 7.5).

Variability on small spatial scales was accessible using both nadir and off-nadir returns. UWB echograms D and E (Fig. 7.1c) reveal an example of a basal channel in the immediate vicinity of a pRES measurement (Fig. 7.6). With the additional information of the UWB echograms, we can link the origin of the off-nadir reflection to the basal channel (Fig. 7.6). Thus, we derived two estimates of basal melt rates: One is based on the repeated nadir reflection outside the channel (7 m a^{-1}) while the other is based on the 2017 nadir and the 2018 off-nadir reflection within the channel ($> 79 \text{ m a}^{-1}$).

The ApRES time series also show a strong spatial and temporal variability without a clear seasonal cycle. All three ApRES recorded high melt rates between October 2017 and July 2018 of $> 50 \text{ m a}^{-1}$ on average, which reduced to $\sim 30 \text{ m a}^{-1}$ until April 2019 and stayed low until the end of the record in July 2020 (Fig. 7.7). This change is particularly pronounced at ApRES1. Here, the melt rate dropped from 148 m a^{-1} (95% quantile) in April 2018 to only 30 m a^{-1} one year later (Fig. 7.7a). In early 2017, melt rates $> 120 \text{ m a}^{-1}$ (95% quantile) were recorded

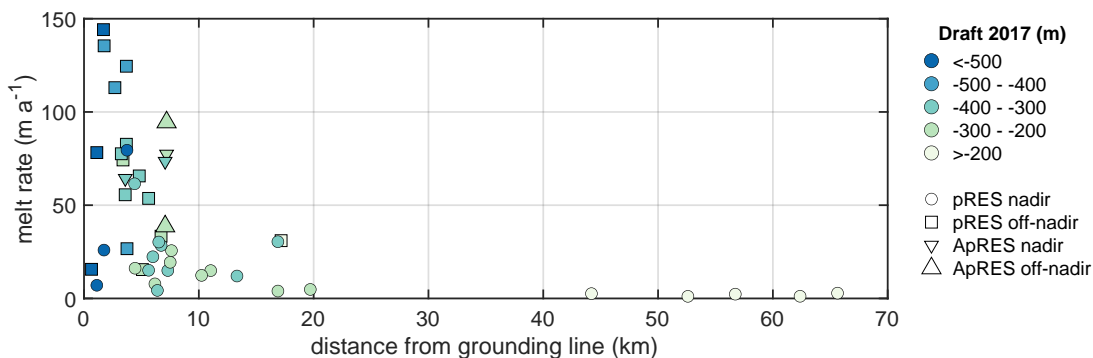


Figure 7.5: Distribution of basal melt rates as a function of distance from the grounding line. Colour-coded pRES draft of the floating tongue derived from (A)pRES measurements and separated for pRES/ApRES and nadir/off-nadir melt rates. Uncertainties are too small to visualise.

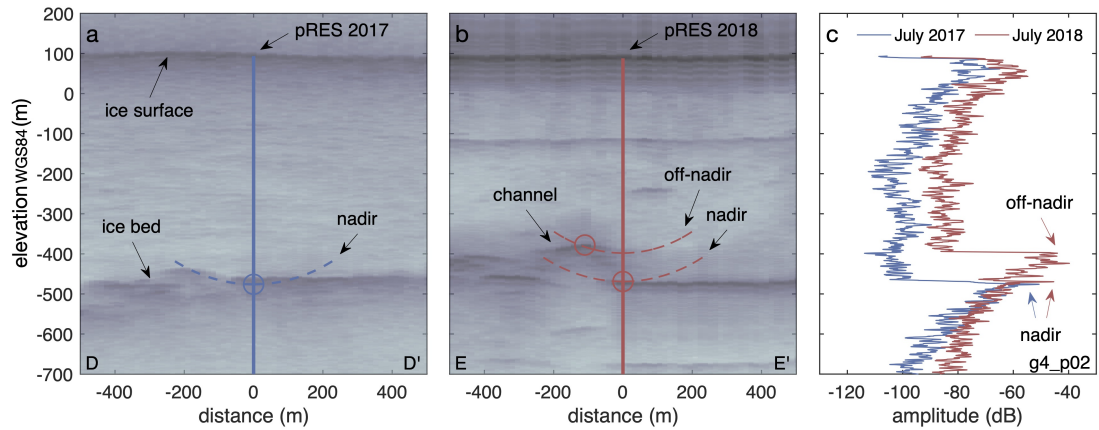


Figure 7.6: Growing basal channel from pRES and UWB echograms. (a,b) UWB echograms from the across-flow profiles D (a) and E (b) from 2018. The centre of both is the location of a Lagrangian pRES measurement in 2017 ((a), vertical blue line) and 2018 ((b), vertical red line). Possible origins of nadir and off-nadir reflections, discovered in the pRES echograms (c), are represented by dashed lines. The suggested locations at which the reflections occurred are marked by circles. (c) pRES echograms from 2017 (blue) and 2018 (red) with identified nadir and off-nadir reflections.

by ApRES2a at the first basal return, whereas at the same time the median melt rate over different α was below 60 m a^{-1} (Fig. 7.7b). After relocation in summer 2018, ApRES2b recorded a 50 m lower ice thickness and a 50% lower melt rate (95% quantile) than ApRES2a two years before. Furthermore, the spatial variability (difference between median and 95% quantile) of ApRES2b was significantly reduced. In July/August, we found reduced melt rates that recover to before July melt rates. These anomalies could be linked to subglacial discharge from supraglacial lake drainage.

7.4 Discussion

In order to analyse the evolution of 79NG geometry, we use ice thicknesses derived from reflection seismic measurements in 1998 (Mayer et al., 2000), from AWI’s RES from 2015 and from UWB measurements from 2018. Comparing 2018 and 1998 (Mayer et al., 2000) data, the geometry of the floating ice tongue has changed drastically (Fig. 7.8): thinning led to a much steeper ice base near the grounding line. In a distance of 8 km from the grounding line, we find an average ice thickness decrease rate of $11.0 \pm 5.7 \text{ m a}^{-1}$ ($221 \pm 114 \text{ m}$ or $38 \pm 18\%$ of the 1998 ice thickness) for this time period, which is in agreement with Mouginot et al. (2015). To some extent, this difference can be attributed to the fact that 2018a cuts into a large basal channel halfway to the lower flexure limit. However, there is no evidence for the existence of that channel in 1998. Nevertheless, the onset of steep basal slopes, which we associate with enhanced basal melting,

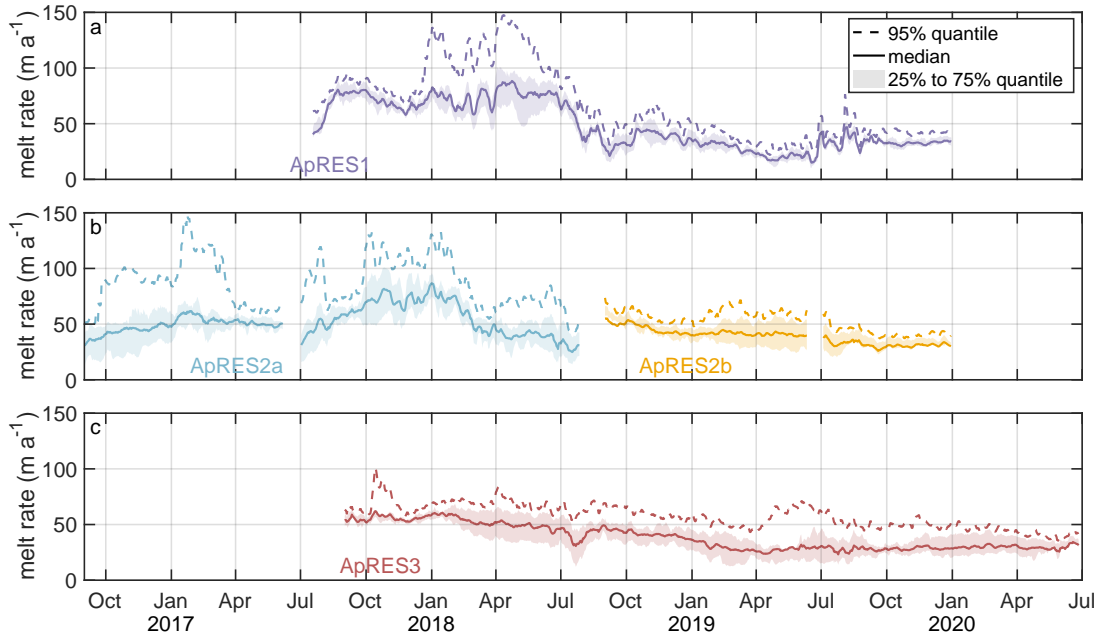


Figure 7.7: Basal melt rate time series of all ApRES measurements: (a) ApRES1, (b) ApRES2a and ApRES2b, (c) ApRES3. The dashed line shows the 95% quantile, the solid line the median and the shaded area marks the range between the 25% and 75% quantile.

has been shifted several kilometres in upstream direction. In 1998, a significant thinning occurred several kilometres (3 – 10 km) downstream from the grounding line, while in 2018, the steepest gradients were found next to the grounding line. A remarkably similar change in geometry was found at Petermann Gletscher (Münchow et al., 2014). Further downstream, our observations reveal a reduction in ice thickness by only $1.60 \pm 1.25 \text{ m a}^{-1}$ ($32 \pm 25 \text{ m}$ or $11 \pm 9\%$ of the 1998 ice thickness) between 1998 and 2018.

From the analysis of surface elevation changes, strong and localised surface lowering above the central channel is evident (Fig. 7.4). In the central part of the channel (11), we found surface elevation changes of about 50 m between December 2010 and January 2020 corresponding to a linear trend of $-5.9 \pm 0.1 \text{ m a}^{-1}$ (Fig. 7.4a,b). Since the glacier tongue is not in hydrostatic equilibrium at this location, a lowering of the surface can be a result of (1) surface ablation or local accumulation, (2) viscoelastic sink-in and (3) basal melting (Humbert et al., 2015). Here, we speculate that we see the viscoelastic response of a growing subglacial channel at the surface. Outside the channel, surface elevation change rates are in the order of -1 m a^{-1} . This value corresponds well to the findings of Krieger et al. (2020b), who compared TanDEM-X elevations between winter 2010 and winter 2013 at 79NG. Interestingly, Krieger et al. (2020b) found no anomalous surface lowering upstream the grounding line. This also agrees to our findings

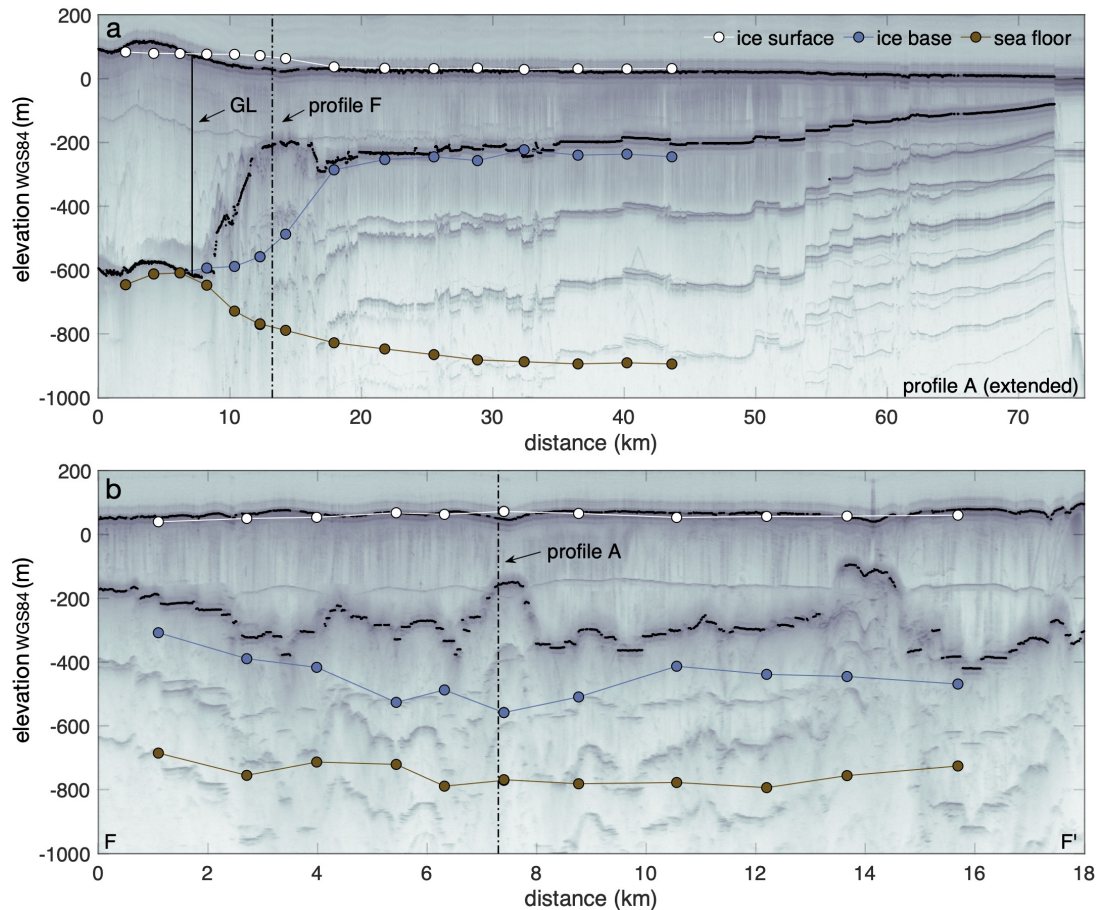


Figure 7.8: Comparison of 79NG geometry between 1998 (reflection seismics) and 2018 (UWB). (a) Along ice-flow profile of 2018 UWB echogram A (extended to the calving front). The 2017 grounding line (GL) and the cross-section with the profile F are marked. (b) Across ice-flow profile of 2018 UWB echogram F. The cross-section with the profile A is marked. The elevation of the ice surface (white), ice base (blue) and the sea floor (brown) were recorded by reflection seismics (dots) in 1998 (Mayer et al., 2000).

in this area. However, while in 2010 the surface at location 11 formed a hill, it transformed to a sink in 2014 and is continuous deepening since. This indicates that the central channel is strongly growing during the time period of observation. Furthermore, TanDEM-X time series suggest that the channel is evolving retrogressive to the ice flow direction. In 2020, the surface elevation at location 11 fell below 30 m above sea level. As we observe a linear trend, we suggest that the lowering in surface elevation will continue in the upcoming years. Without a flattening of the trend, the channel might break through the ice column in 2025.

The distribution of melt rates can be summarised as follows:

- (1) Large basal melting near the grounding line declines to low melt rates towards the calving front. This variation on large spatial scale can have several reasons:
 - (i) As the keel of thick ice near the grounding line is exposed to warmer ocean

water, the heat supply to the ice base is larger (see Appendix 7.6.2). (ii) We assume that increased amplitudes ~ 80 m above the ice base in UWB echograms represent temperate ice (Fig. 7.3a). As all heat supply goes directly into melting, temperate ice at the base supports high basal melt rates. (iii) Subglacial discharge (jet-like) rising along steep basal slopes may drive turbulent mixing with the warm AIW and intensify basal melt (Jenkins and Doake, 1991; Jenkins, 2011; Schaffer et al., 2020). Rising along the sloping ice base, the plume loses heat to the melting of ice and buoyancy by entrainment of ambient water, so that it cools down and eventually detaches from the ice base, leading to a strong decrease in basal melting for the thinner, more gently sloped areas of the floating ice tongue. This concept is consistent with temperatures observed at the calving front, where the outflowing water is 0.9°C cooler than the ingoing AIW (Schaffer et al., 2020).

(2) Variations on medium spatial scale in across-flow direction along the grounding line may be related to the distribution of water column thickness. A water column thickness of 50 to 140 m (Mayer et al., 2000) was found where we observe the highest basal melt rates and where the grounding line reaches farthest downstream. We do not have any information of water column thickness elsewhere. However, further south, the grounding line is situated on a mountainous landform. We hypothesise that only a shallow water column exists here, which prevents the flow of warm ocean currents towards the grounding line, resulting in the observed low basal melt rates.

(3) Small-scale variations in basal melting are evident at several locations near the grounding line. We hypothesise the basal channels to have a major influence on melt rates at this scale. What has forced the channel formation at 79NG is yet unclear. However, basal channels are often linked to the location of subglacial water discharge (Le Brocq et al., 2013; Marsh et al., 2016; Washam et al., 2019). The comparison between our in-situ based melt rates and those derived from satellite measurements (Wilson et al., 2017) indicates large local differences of up to 52 m a^{-1} (Fig. 7.9). Striking differences occur especially within a few kilometres from the grounding line, but are small in the calving front area. The differences are attributed to the different times of investigation and to the hydrostatic assumption in the satellite-derived melt rates, which is not always valid above narrow basal channels (Humbert et al., 2015). However, the average difference is close to zero.

Seasonal variations of basal melt rates have been observed beneath the floating tongue of Petermann Gletscher (Washam et al., 2019). There, summer melt rates are more than four times larger than in winter, likely caused by warmer ocean currents reaching the ice base of Petermann Gletscher (Shroyer et al., 2017; Washam et al., 2019). The absence of a summery increase of basal melt

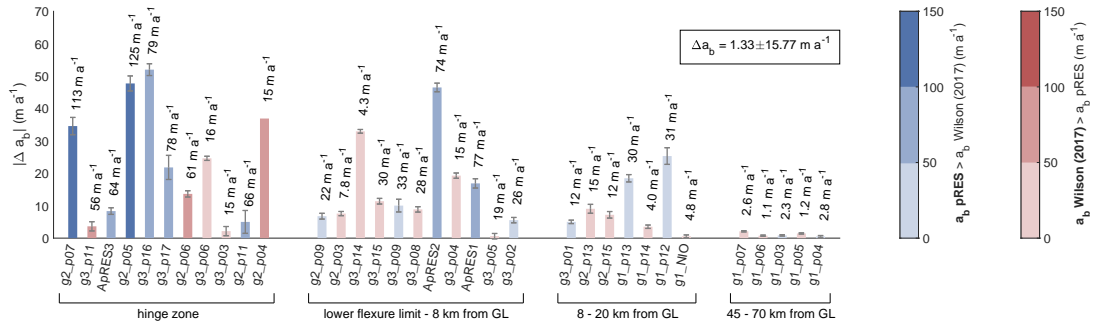


Figure 7.9: Comparison of basal melt rates derived from in-situ and satellite measurements. Blue bars represent the difference in basal melt rates for larger pRES-derived melt rates and red bars for larger satellite-derived melt rates by Wilson et al. (2017). The colour intensity indicates the size of the melt rate. Numbers above bars are pRES-derived melt rates. The bars are allocated based on the distance to the grounding line. Error bars indicate pRES measurement uncertainties. The average difference in basal melt rate is $1.33 \pm 15.77 \text{ m a}^{-1}$.

rates is consistent with in-situ measurements of ocean temperatures and velocities between September 2016 and September 2017 (Schaffer et al., 2020), showing persistent inflow of warm AIW into the cavity and an overlaying outflow of cold modified AIW throughout the year without seasonality. However, the significant decrease of the melt rate in 2018 at all ApRES sites could be caused by lower temperatures or a reduced inflow of AIW into the cavity that remained low in 2019 and in the first half of 2020. The repeat of the ApRES measurements after two years show on which time scales the ice thickness changes – from the perspective of a Lagrangian and Eulerian reference frame. The high melt rates between October 2016 and July 2018 have reduced the ice thickness at the starting location of the ApRES measurement by 50 m (Eulerian frame). Due to the lower melt rates from July 2018 on, the ice thinned less than before (Lagrangian frame). As a result, the ice thickness at the location where the measurement of ApRES2b stopped in December 2019 was even thicker than two years before. A large spread between the median and the 95% quantile – as observed at ApRES1 and ApRES2a within several months – shows a large spatial variability of melt rates and that high melt rates are limited to small areas.

7.5 Conclusion

In this study, we found a large variability of basal melt rates near the grounding line of 79NG ranging from $< 27 \text{ m a}^{-1}$ to extreme melt rates of up to $144 \pm 2 \text{ m a}^{-1}$. These high melt rates led to massive thinning and a steeper ice base near the grounding line in the past decades. Further downstream, melt rates decline and remain low to the calving front. Measured deepening of basal channels near the

grounding line point to the question if these changes are predominantly driven by the ocean or by glacier hydrology. The time series of melt rates over four years show interannual fluctuations that indicate a weakening of the inflow of AIW into the cavity since mid 2018. However, given the vast size of supraglacial lakes (Schröder et al., 2020) and projections suggesting advancing lakes (Leeson et al., 2014; Ignéczi et al., 2016), the role of subglacial discharge is likely to increase in the future.

7.6 Appendix

7.6.1 Basal melt rates from nadir and off-nadir reflections

We have defined different types how nearby basal channels affect the origin of the first recorded basal reflection in repeated pRES echograms (Tab. 7.1 and Fig. 7.10). All have in common that the derived ΔH underestimates the ΔH nadir or ΔH off-nadir.

Table 7.1: Possibilities how basal channels affect recording of nadir and off-nadir reflections. Notation: t_1 : time of first measurement, t_2 : time of repeated measurement, H_1 : ice thickness at t_1 , H_2 : ice thickness at t_2 , ΔH nadir: difference in ice thickness nadir, ΔH off-nadir: difference in ice thickness at off-nadir location, ΔH derived: difference in depth at nadir projection.

Type	t_1	t_2	ΔH
A	nadir	off-nadir	ΔH nadir < ΔH derived < ΔH off-nadir Basal channel did not exist or was too small to be detected at t_1 . At t_2 , growth of channel is significantly larger than ice thickness reduction nadir of measurement device.
B	off-nadir	off-nadir	ΔH derived < ΔH off-nadir Basal channel exists at t_1 . At t_2 , ice thickness reduction nadir of measurement device is not significantly larger than growth of channel.
C	off-nadir	nadir	ΔH off-nadir < ΔH derived < ΔH nadir Basal channel exists at t_1 . At t_2 , ice thickness reduction nadir of measurement device is significantly larger than growth of channel.
D	off-nadir	off-nadir	ΔH derived < ΔH off-nadir Two basal channel exist at t_1 . At t_2 , ice thickness reduction nadir of measurement device is not significantly larger than growth of at least one of both channels. This type can not be distinguished from Type B with simple measurements.

Several pRES echograms indicate the occurrence of numerous strong basal reflections (Fig. 7.11). For steep basal gradients, the off-nadir reflection may occur prior to the nadir reflection. We interpret the first basal reflection as an off-nadir reflection, as long as no further information reveal the true nadir reflection. Herewith, the resulting basal melting in the vicinity of the measurement is always underestimated, although the nadir melt rate might be lower. We have identified two of the different types with pRES measurements:

ApRES1: Type A (Fig. 7.11a)

In 2017, the first basal return occurred nadir to the measuring device. In 2018, the first basal return occurred off-nadir, but the nadir reflection could be identified based on the time series of the ApRES station. Here, ΔH off-nadir was

larger than ΔH nadir. However, this behaviour is interpreted as the formation (or the continued growing) of a basal channel nearby. The nadir basal melt rate is 77 m a^{-1} and the off-nadir $> 95 \text{ m a}^{-1}$, resulting in a difference of $> 18 \text{ m a}^{-1}$.

pRES_g4_p02: Type A (Fig. 7.11b)

In 2017, the first basal return occurred nadir to the measuring device. In 2018, the first basal return occurred off-nadir, but the nadir reflection could be identified. This finding is similar to ApRES1, but nadir melting is significant lower. The nadir basal melt rate is 7 m a^{-1} and the off-nadir $> 79 \text{ m a}^{-1}$, resulting in a difference of $> 19 \text{ m a}^{-1}$.

pRES_g2_p04: Type B (Fig. 7.11c)

The first basal return occurred off-nadir in both echograms, but nadir reflections could be identified in both. Here, ΔH off-nadir was larger than ΔH nadir. We interpret this behaviour as the formation or the continued growing of a basal channel nearby. The nadir basal melt rate is 15 m a^{-1} and the off-nadir $> 54 \text{ m a}^{-1}$, resulting in a difference of $> 39 \text{ m a}^{-1}$.

pRES_g3_p16: Type B / Type C (Fig. 7.11d)

The first basal return occurred off-nadir in both echograms, but nadir reflections could be identified in both. Here, ΔH nadir was larger than ΔH off-nadir. This behaviour indicates a reduction in height of a nearby channel. The nadir basal melt rate is 79 m a^{-1} and the off-nadir $> 28 \text{ m a}^{-1}$, resulting in a difference of $< 51 \text{ m a}^{-1}$.

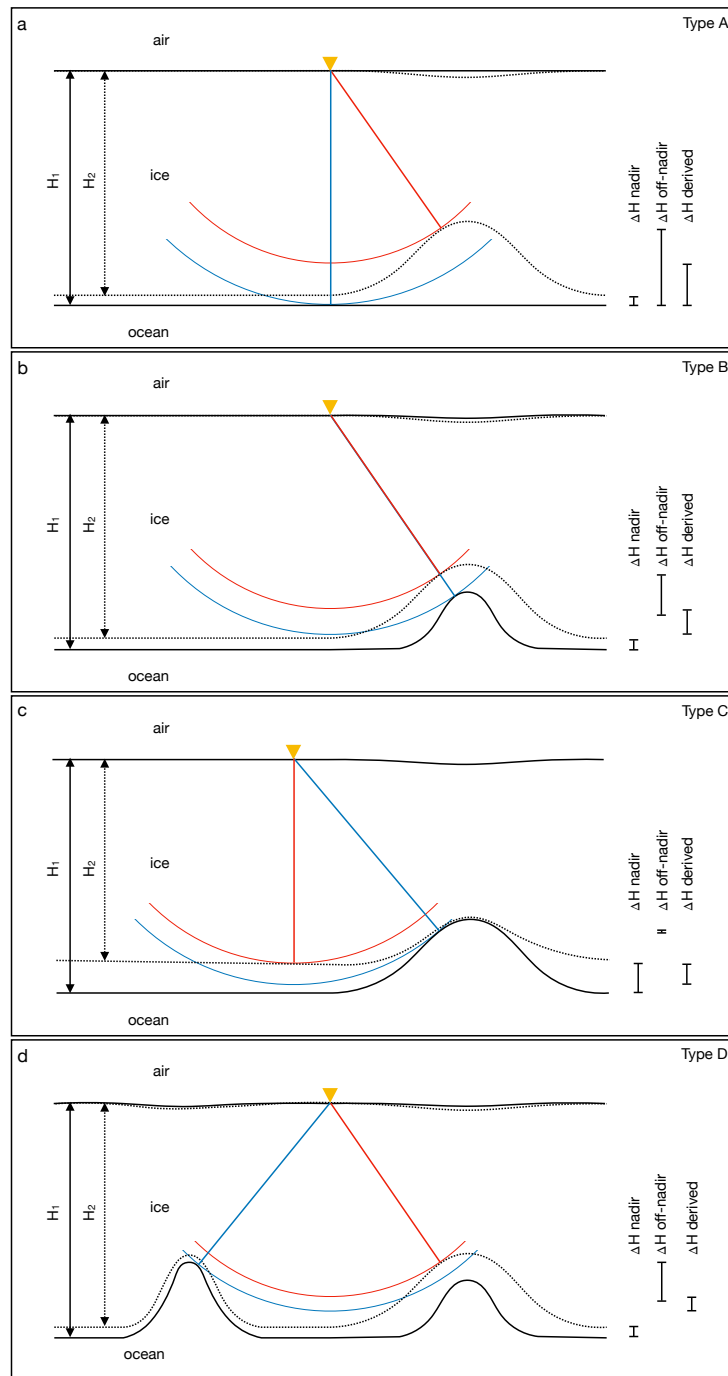
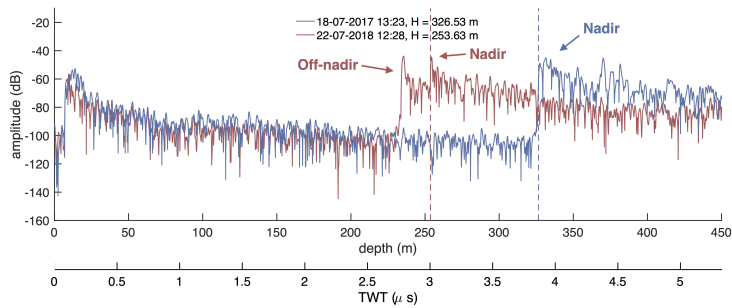
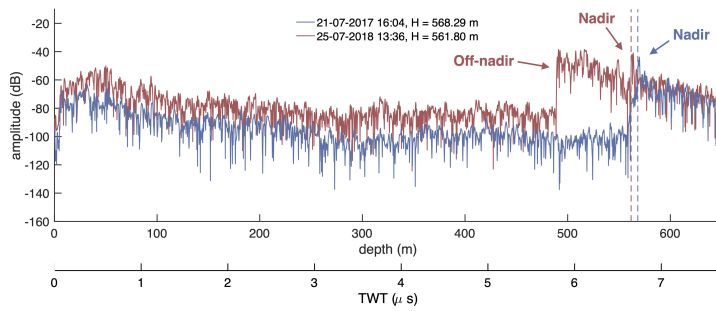


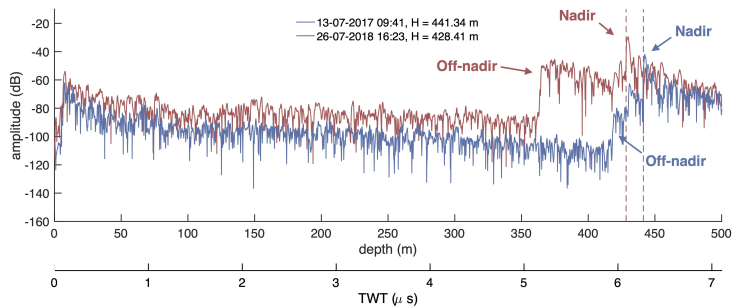
Figure 7.10: Sketch of off-nadir reflections and their influence on basal melt rates. The solid lines and the ice thickness H_1 refer to the time of the first measurement (blue), t_1 , and the dotted line as well as H_2 refer to the time of the repeat measurement (red), t_2 . The yellow triangles mark the measurement positions. The red and blue straight lines mark the closest distance from the measurement to the ice base. The segments of a circle (up to 30° to nadir) correspond to the possible positions of the reflector with the shortest distance. The lengths of the bars on the right reflect the thinning of the ice between t_1 and t_2 for the position of the measurement (ΔH nadir), for the position of the closest reflector at t_2 (ΔH off-nadir), and for the difference in length of the blue and red lines (ΔH derived). Note that at least one of ΔH nadir or ΔH off-nadir is always larger than ΔH derived. The different types A – D are described in Tab. 7.1.



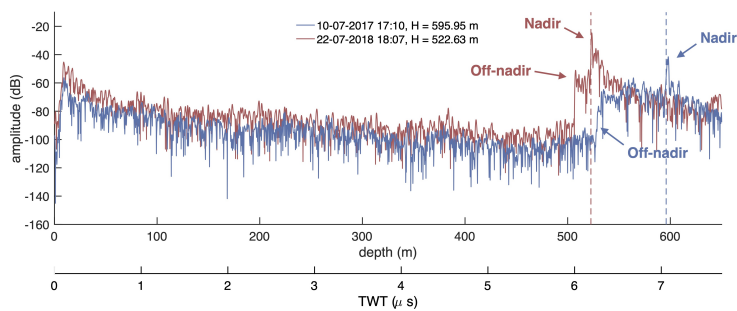
(a) ApRES1



(b) pRES_g4_p02



(c) pRES_g2_p04



(d) pRES_g3_p16

Figure 7.11: ApRES and pRES measurements with identified nadir and off-nadir reflections. Echograms from the first measurement is shown in blue and from the repeated measurement in red. Vertical dashed lines mark the nadir basal return and thus represent the ice thickness.

7.6.2 Oceanic heat flux

In order to estimate the oceanic heat flux q_w required to sustain the basal melt rates a_b [m s^{-1}] derived in this study, we separate the heat flux q_w into two components: the heat flux q_m to melt the ice and the heat flux into the glacier interior q_i that is required for heating the ice by ΔT to the pressure melting point:

$$q_w = \underbrace{\rho_i a_b L}_{q_m} + \underbrace{\rho_i c_i(T) a_b \Delta T}_{q_i} \quad (7.9)$$

The heat fluxes depends on the density of the ice, $\rho_i = 917 \text{ kg m}^{-3}$, the latent heat of fusion, $L = 334000 \text{ J kg}^{-1}$, and the specific heat capacity for ice, $c_i(T) = 146.3 + 7.253 \cdot T[\text{K}] \text{ J kg}^{-1} \text{ K}^{-1}$ with the temperature T in Kelvin (Ritz, 1987). For an assumed range of glacier interior temperatures between 0 K (temperate ice) and 30 K below the pressure melting point, a basal melt rate of 140 m a^{-1} , as it was observed at ApRES1 and ApRES2a, requires a heat flux between 1360 and 1600 W m^{-2} . This heat flux must be provided by the water in the cavity below 79NG.

To obtain an estimate of the oceanic heat flux, we follow the methods implemented in the Finite Element Sea ice Ocean Model (FESOM; Timmermann et al., 2012). Here, a three-equation system is used that determines the temperature and salinity of a thin boundary layer along the ice base from its heat and fresh-water exchange with the ice and the ambient ocean (Hellmer and Olbers, 1989; Holland and Jenkins, 1999). Beside the ocean temperature, the heat flux into this boundary layer is determined by the flow velocity in the ambient ocean, as the latter determines the friction velocity and thus defines the turbulent fluxes of heat and salt (Jenkins and Doake, 1991).

As an example case for the 79NG sub-ice cavity, we assume a salinity of 34.5 psu and an ice draft of 320 m, estimated for the location of ApRES2a, where the highest melt rates of 140 m a^{-1} were determined during winter. Measurements of the inflow temperatures exceed 1.2°C at the calving front (Schaffer et al., 2020), corresponding to 2.9 K above the pressure melting point at the position of the observation. In order to produce a sufficiently high turbulent heat flux into the boundary layer for this given temperature, an ambient velocity of 0.22 m s^{-1} is required for temperate ice and 0.27 m s^{-1} for ice of 30 K below the pressure melting point. Previously simulated velocities of a buoyant plume rising along the ice base of 79NG indicate velocities of up to 0.25 m s^{-1} (Schaffer, 2017). From these numbers, we conclude that the ocean currents underneath 79NG are able to supply a heat flux that is high enough to explain the maximum determined melt rates.

7.6.3 ApRES echograms

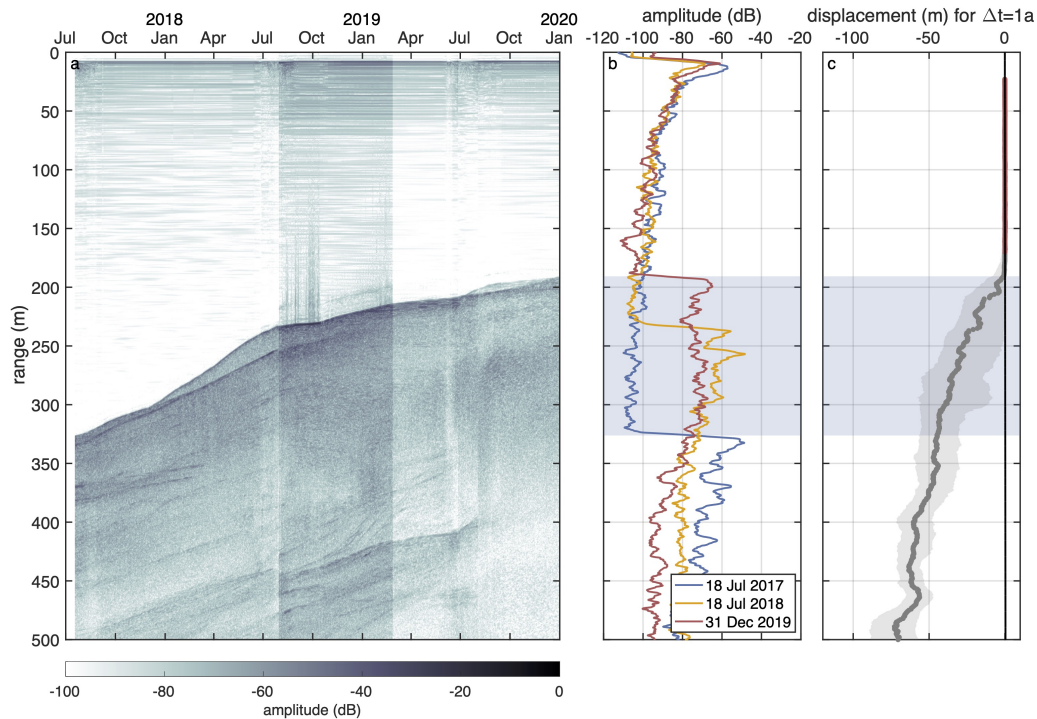


Figure 7.12: ApRES1 echograms. (a) Time-echogram of a Lagrangian measurement at ApRES1 recorded between July 2017 and December 2019. (b) Single echograms from 18 July 2017 (first measurement), 18 July 2018 and 31 December 2019 (last measurement), smoothed with a 5 m moving average filter. The blue shaded range corresponds to the displacement of the first basal return within the measurement period. (b) Mean vertical displacement of internal and basal segments (grey dots). The grey shaded area marks the range between the 25% and 75% quantile. Those displacements from segments between 20 m and 20 m above the first basal return at the end of the measurement period (red dots) were used to derive the change in ice thickness due to vertical strain by fitting a linear function (black line). Displacements of segments within the blue shaded range are partly from internal and partly from basal reflections.

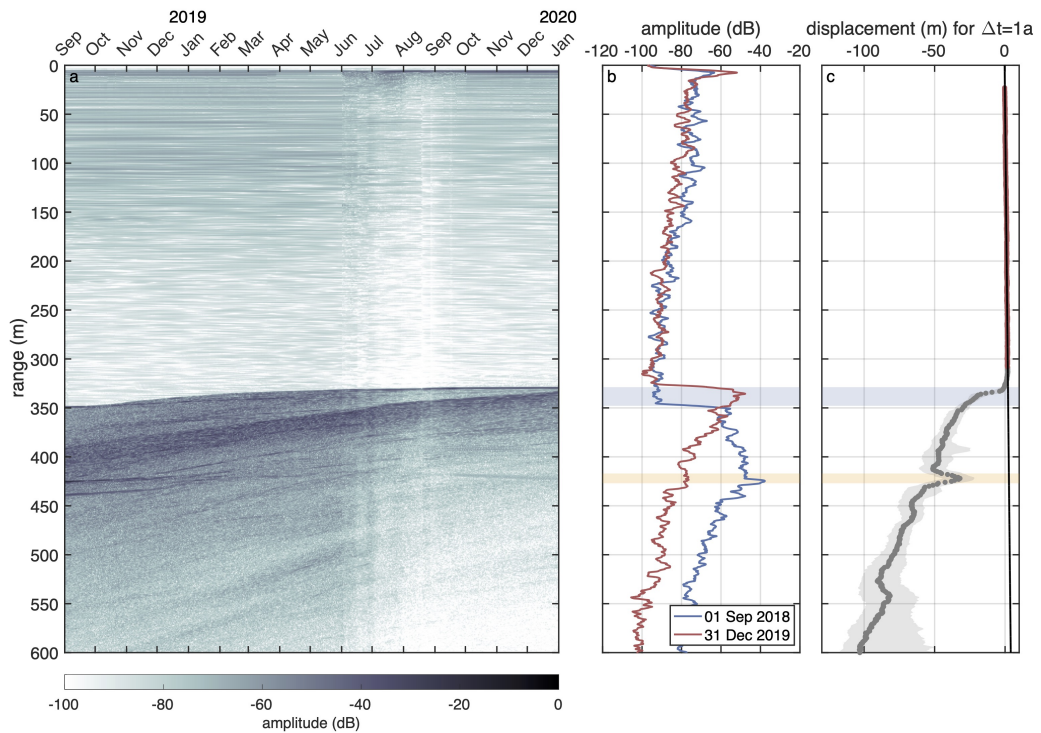


Figure 7.13: ApRES2b echograms. (a) Time-echogram of a Lagrangian measurement at ApRES2b recorded between September 2018 and December 2019. (b) Single echograms from 01 September 2018 (first measurement) and 31 December 2019 (last measurement), smoothed with a 5 m moving average filter. The blue shaded range corresponds to the displacement of the first basal return within the measurement period. (b) Mean vertical displacement of internal and basal segments (grey dots). The grey shaded area marks the range between the 25% and 75% quantile. Yellow shaded ranges mark depth of radar artefacts. Those displacements from segments between 20 m and 20 m above the first basal return at the end of the measurement period (red dots) were used to derive the change in ice thickness due to vertical strain by fitting a linear function (black line). Displacements of segments within the blue shaded range are partly from internal and partly from basal reflections.

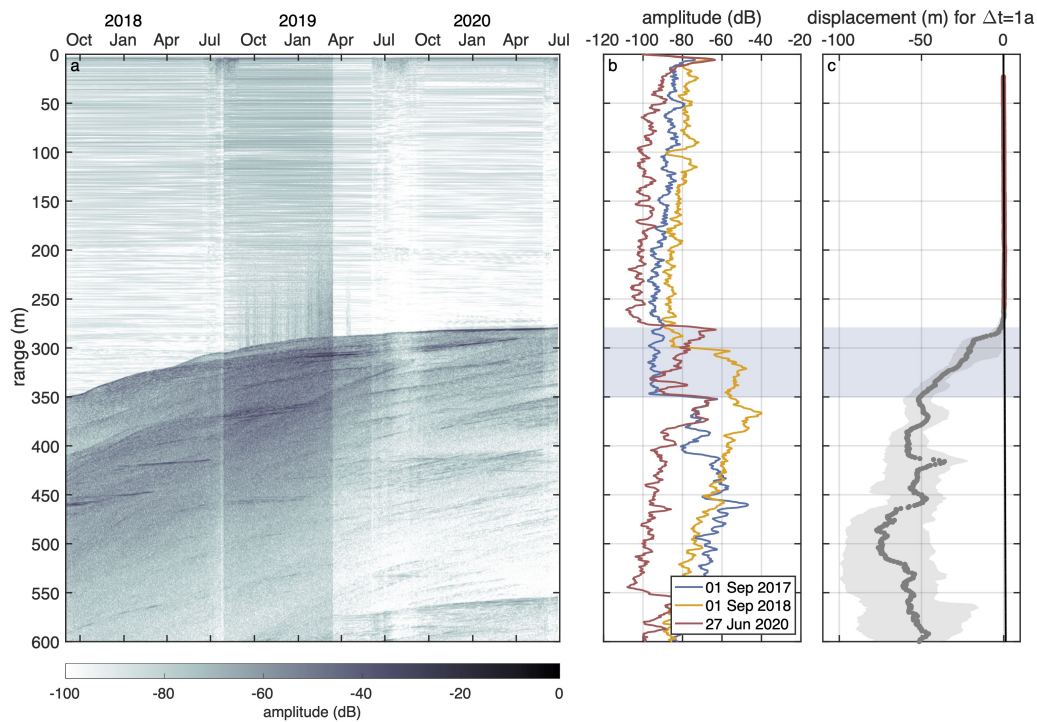


Figure 7.14: ApRES3 echograms. (a) Time-echogram of a Lagrangian measurement at ApRES3 recorded between September 2017 and June 2020. (b) Single echograms from 01 September 2017 (first measurement), 01 September 2018 and 27 June 2020 (last measurement), smoothed with a 5 m moving average filter. The blue shaded range corresponds to the displacement of the first basal return within the measurement period. (c) Mean vertical displacement of internal and basal segments (grey dots). The grey shaded area marks the range between the 25% and 75% quantile. Those displacements from segments between 20 m and 20 m above the first basal return at the end of the measurement period (red dots) were used to derive the change in ice thickness due to vertical strain by fitting a linear function (black line). Displacements of segments within the blue shaded range are partly from internal and partly from basal reflections.

Data Availability

Stake surface ablation/accumulation measurements from 2017 to 2018 (<https://doi.org/10.1594/PANGAEA.922131>; Zeising et al., 2020), time-series of basal melt rates (<https://doi.org/10.1594/PANGAEA.928903>; Zeising et al., 2021d) and basal melt rates derived from single repeated pRES measurements (<https://doi.org/10.1594/PANGAEA.928541>; Zeising et al., 2021e) and are available at the World Data Center PANGAEA.

Acknowledgements

This project is part of the GROCE project and is funded by BMBF under the grant 03F0778A. NN has received funding from the European Union's Horizon 2020 research and innovation programme under grant agreement No 689443 via project iCUPE (Integrative and Comprehensive Understanding on Polar Environments). TanDEM-X and TerraSAR-X data were made available through German Aerospace Center proposals GLAC7208 and HYD2059. We thank the European Space Agency (ESA) for providing the Sentinel-1 and Sentinel-2 data. The authors would like to thank Emerson E&P Software, Emerson Automation Solutions, for providing licenses in the scope of the Emerson Academic Program. We like to thank Steven Franke for support in handling UWB data. We want to thank Jens Köhler and Graham Niven for their support in the field. We acknowledge the effort of Shfaqat Abbas Khan for servicing our ApRES in the lockdown in 2020 and to retrieve our SD cards.

Filchner Ice Shelf, Antarctica

8.1 Introduction

The Antarctic Ice Sheet is surrounded by numerous ice shelves from which the Filchner Ice Shelf (FIS) is one of the largest. Located in the southern Weddell Sea, FIS extends over an area of over 100,000 km² (Rignot et al., 2013). Several East Antarctic glaciers – Bailey Ice Stream, Slessor Glacier, Recovery Glacier and the Support Force Glacier (SFG) – drain into FIS (Fig. 8.1), the basins of which add up to $2.147 \cdot 10^6$ km² (22% of the East Antarctic Ice Sheet (EAIS)), and cause a grounding line ice discharge of 106.3 ± 5.7 Gt a⁻¹ (9.6% of EAIS).

Figure 8.1 shows the surface ice flow velocities of the AIS (Mouginot et al., 2019a,b) with the drainage basins of the Ronne and Filcher ice shelves (Shepherd et al., 2020). Many ice shelves and their feeding ice streams – like those at FIS – are indicated by enhanced flow velocities that often exceed 1000 m a⁻¹ at the calving front.

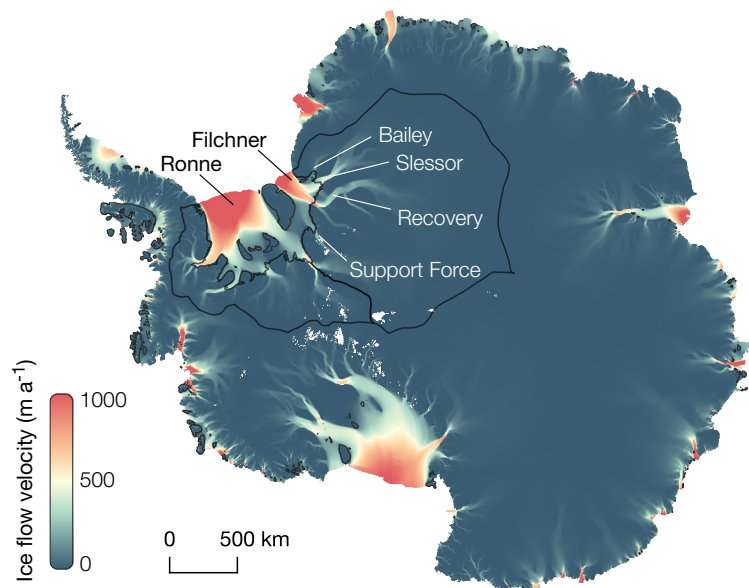


Figure 8.1: Surface ice flow velocity map of AIS (Mouginot et al., 2019a,b). Filchner Ice Shelf and Ronne Ice Shelf are marked with their drainage basins (Shepherd et al., 2020) as well as the Bailey Ice Stream, Slessor Glacier, Recovery Glacier and Support Force Glacier.

8.2 Basal melting

Ice shelves are of particular importance for regulating ice-sheet discharge due to their potential buttressing effect (Dupont and Alley, 2005; Gagliardini et al., 2010; Fürst et al., 2016). A thinning of the ice shelf through basal melting can lead to a reduction in buttressing, which causes an acceleration in glacier flow (Pritchard et al., 2012), and highlights the importance of monitoring the basal melt rates of the Antarctic ice shelves. Satellite remote sensing allows for ice-shelf wide estimations of basal melt rate by solving the ice thickness evolution equation (Rignot et al., 2013; Moholdt et al., 2015; Berger et al., 2017; Adusumilli et al., 2020) with major uncertainties from various factors. The estimated basal melt rates of the FIS by Rignot et al. (2013), Moholdt et al. (2015) and Adusumilli et al. (2020) are all approx. 0.4 m a^{-1} which is relatively small compared to the ice shelves in the Amundsen Sea, whose melt rates are several meters per year (Rignot et al., 2013; Adusumilli et al., 2020).

As part of the FISP in 2015/2016 and 2016/2017, funded by AWI and British Antarctic Survey (BAS), in situ measurement with a pRES were performed for the first time in the southern FIS, which form the basis for deriving a spatial distribution of basal melt rates. A comparison of melt rates from in situ radar measurements with those derived from satellite remote sensing allows to assess the uncertainties of the remote sensing-product and thus to improve the construction of parametrisations of ice sheet–ocean models that are based on remote sensing-derived melt rates. The resulted distribution and the comparison are presented in the research article *Basal melt of the southern Filchner Ice Shelf, Antarctica* (Chapter 9; Zeising et al., 2021f), that is submitted to the journal *The Cryosphere* in 2021.

8.3 Basal channel at Support Force Glacier

Remote sensing measurements, e.g. satellite imagery, laser altimetry and airborne radar, revealed the occurrence of numerous along-flow channels on the surface of Antarctic ice shelves (Alley et al., 2016), which are the surface expression of a basal channel (Le Brocq et al., 2013). With heights of typically up to several hundreds of meters and a width of a few kilometres, basal channels reduce the ice thickness and might contribute to the instability of ice shelves due to fracturing (Alley et al. (2016); Dow et al. (2018)).

The causes of the formation of basal channels remain poorly understood, but based on current knowledge, three causes can be defined (Alley et al. (2016)): (1) ocean currents that cause a channel formation after the grounding line, (2) outflow

of subglacial water that cause a channel formation at the grounding line (Le Brocq et al., 2013) and (3) basal obstacles upstream the grounding line indenting the ice from below (Drews et al., 2017).

A basal channel that already exists upstream the grounding line was found at SFG. DEMs reveal a surface depression over approx. 100 km from the grounding line on until it fades out. Airborne radar and seismic measurements indicate a maximum channel height of 280 m at the grounding line that is reduced to 170 – 205 m further downstream, as shown in the research article *Evidence for a grounding line fan at the onset of a basal channel under the ice shelf of Support Force Glacier, Antarctica, revealed by reflection seismics* by Hofstede et al. (2021a), on which the author of this thesis contributed as co-author.

Although channels like the one at SFG fade out over larger distance from the grounding line, several studies found enhanced basal melting inside the channels from observations and modelling (Le Brocq et al., 2013; Langley et al., 2014; Drews, 2015; Marsh et al., 2016; Dow et al., 2018). Le Brocq et al. (2013) suggests that the decrease in basal melting and thus in channel height, is caused by uprising fresh water that becomes super-cooled due to reduced pressure.

In order to derive the melt rate distribution and quantity at the basal channel at SFG, pRES measurement have been performed in the vicinity of the channel in the course of FISP. Based on these melt rates, ice thicknesses and derived vertical strain rates, used for a viscoelastic model, the channel evolution is investigated. The results are presented in the research article *On the evolution of an ice shelf melt channel at the base of Filchner Ice Shelf, from observations and viscoelastic modelling* (Chapter 10), that is submitted to the journal *The Cryosphere* in 2021.

Basal melt of the southern Filchner Ice Shelf, Antarctica

9

This chapter is submitted as a research article to the journal *The Cryosphere* in 2021 (Zeising et al., 2021f).

Authors and affiliations

Ole Zeising^{1,2}, Daniel Steinhage¹, Keith W. Nicholls³, Hugh F. J. Corr³, Craig L. Stewart^{4,5} and Angelika Humbert^{1,2}

¹Alfred-Wegener-Institut Helmholtz-Zentrum für Polar- und Meeresforschung, Bremerhaven, Germany

²Department of Geosciences, University of Bremen, Bremen, Germany

³British Antarctic Survey, Natural Environment Research Council, Cambridge, UK

⁴Scott Polar Research Institute, University of Cambridge, Cambridge, UK

⁵now at: National Institute of Water and Atmospheric Research, Wellington, New Zealand

Contributions

A.Humbert has designed the study and conducted the field study together with D.Steinhage. K.W.Nicholls supported the field study. **O.Zeising** processed the pRES data and analysed the basal melt rates together with A.Humbert. K.W.Nicholls contributed to melt rate analysis and its discussion together with H.F.J.Corr. C.L.Stewart wrote main parts of the MATLAB routines and supported data analysing. **O.Zeising** carried out a detailed comparison of the pRES-derived results with those from remote sensing. **O.Zeising** wrote Sect. 9.2 ("Materials and methods"), 9.3 ("Results") – with the exception of Sect. 9.3.2 ("Small scale spatial variability") which was written by **O.Zeising** and A.Humbert – and 9.4 ("Comparison with remote sensing basal melt estimates"). To all other sections **O.Zeising**, A.Humbert and K.W.Nicholls contributed to the writing. Figures were created by **O.Zeising**. A.Humbert has supervised the study.

Abstract

Basal melt of ice shelves is a key factor governing discharge of ice from the Antarctic Ice Sheet as a result of its effects on buttressing. Here, we use radio echo sounding to determine the spatial variability of the basal melt rate of the southern Filchner Ice Shelf, Antarctica along the inflow of Support Force Glacier. We find moderate melt rates with a maximum of 1.13 m a^{-1} about 50 km downstream of the grounding line. The variability of the melt rates over distances of a few kilometres is low (all but one $< 0.15 \text{ m a}^{-1}$ at $< 2 \text{ km}$ distance), indicating that measurements on coarse observational grids are able to yield a representative melt rate distribution. A comparison with remote sensing based melt rates revealed that, for the study area, large differences were due to inaccuracies in the estimation of vertical strain rates from remote sensing velocity fields. These inaccuracies can be overcome by using modern velocity fields.

9.1 Introduction

Filchner Ice Shelf (FIS), a West Antarctic ice shelf draining major East Antarctic ice streams (Bailey, Slessor, Recovery and Support Force glaciers) is thought to be vulnerable to a change in its basal mass balance within this century (Hellmer et al., 2012) as a result of the possible penetration of relatively warm, off-shelf waters into the ocean cavity beneath the ice shelf. Subsequent thinning of the ice shelf would reduce its buttressing of inland glaciers, allowing them to speed up and thin, and their grounding lines to retreat landward. If the stress perturbation is sufficiently large then a positive ice-loss feedback may occur as the ice sheet's grounding line retreats across the deepening beds of the tributary ice streams (Schoof, 2012). The current discharge of ice across the grounding line at FIS is $106.3 \pm 5.7 \text{ Gt a}^{-1}$ (Rignot et al., 2019), which is about 9.6 % of the discharge from East Antarctica, underlining the importance of understanding the current state of the ice shelf for assessing future change in basal melt. In addition, precise melt rates serve as validation for models projecting the future contribution of these ice streams to sea level change.

Basal melt rates can be derived from satellite remote sensing data by solving the ice thickness evolution equation (Rignot et al., 2013; Moholdt et al., 2015; Berger et al., 2017; Adusumilli et al., 2020). Although the Lagrangian approach adopted in recent years (Moholdt et al., 2015) has led to improvements, major uncertainties from various factors remain. Hence, in situ observations of basal melt rates are required for assessing the reliability of remote sensing approaches. This is even more urgent, as remote sensing-derived basal melt rates are used

to construct parametrisations that diagnose basal melt rates from modelled sub-ice shelf ocean conditions. These models are used to project the contribution of Antarctica to sea level change. Significant errors in observed distributions of basal melt rate therefore have a profound effect on the outcome of projections of future sea level rise, such as ISMIP6 (Seroussi et al., 2020), as a result of their effect on the calibration of basal melt rate parametrisations (Jourdain et al., 2020).

In recent years, the use of the phase-sensitive radio echo sounder (pRES) opened new possibilities for the precise determination of basal melt rates. Nicholls et al. (2015) and Stewart et al. (2019) presented basal melt rates from near Ross Island, Ross Ice Shelf, Antarctica, which were derived from 10-days of autonomous pRES (ApRES) measurements, and measurements from 78 stations, time-averaged between 2013 and 2014. Stewart et al. (2019) observed strong seasonal melt rate variability, with values up to 53 m a^{-1} within a five day period in January 2013 and an exponentially reducing mean annual basal melt rate with increasing distance from the calving front, with values up to 7.7 m a^{-1} . Vaňková et al. (2020) presented a tidal melt and vertical strain analysis from 17 ApRES records across Filchner-Ronne Ice Shelf. They found the tidal vertical strain to be depth dependent only near the grounding line, with significant tidal melt measurable at some locations. The derived melt rates were used by Bull et al. (2021) to evaluate an ocean model. Marsh et al. (2016) investigated basal melt rates at 25 points at a melt channel near the grounding line of Ross Ice Shelf. They found basal melt rates decreasing from 22 m a^{-1} at the upstream end of the channel to 2.5 m a^{-1} 40 km downstream. A strong seasonal variability in melt rate was recorded by Washam et al. (2019) on Petermann Gletscher, Greenland, using an ApRES recording on the flank of a basal melt channel. In Summer 2016, they found extreme melt rates equivalent to 80 m a^{-1} but most of the year the mean basal melt rate ranged from 0 to 10 m a^{-1} .

Our survey is focused on the more benign southern part of FIS, which might be more susceptible to the potential inflow of warm waters (Hellmer et al., 2012). Recent observations from hot-water drilled boreholes through Filchner-Ronne Ice Shelf have revealed an interannual change in circulation mode starting in 2017, highlighting the variability in conditions within the sub-ice shelf cavity (Hattermann et al., 2021).

Here, we aim at understanding the magnitude and variation of basal melt over an area extending from the grounding line of Support Force Glacier, as far downstream as was feasible. In austral summer 2015/16, under the framework of the Filchner Ice Shelf Project (FISP), pRES measurements were carried out at a total of 94 locations, and then repeated a year later. The stations were distributed along the central flow line of Support Force Glacier's extension on to FIS and

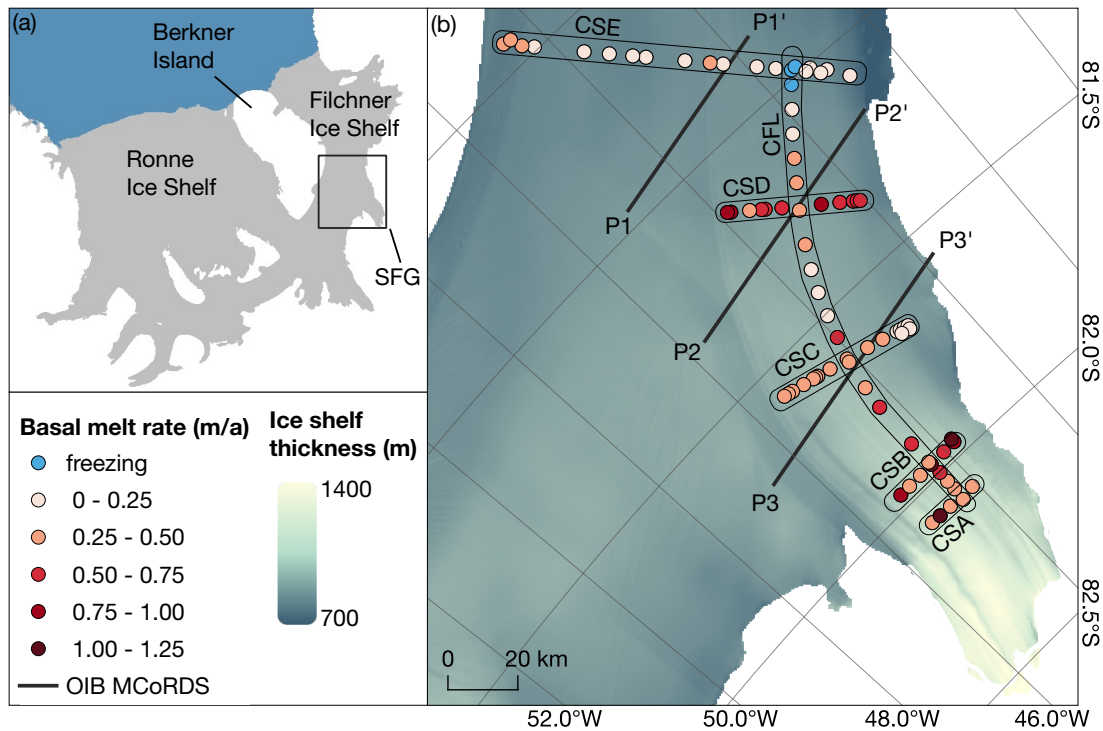


Figure 9.1: (a) Map of the Ronne and Filchner ice shelves (BedMachine Antarctica (Morlighem, 2020; Morlighem et al., 2020)) with the marked study area (black box) near the SFG. (b) Study area with derived basal melt rates (dots), grouped depending on their location on the Central Flow Line (CFL) and five Cross-Sections CSA, CSB, CSC, CSD and CSE. Multi-channel Coherent Radar Depth Sounder (MCoRDS) profiles (P1–P3) flown as part of NASA’s Operation IceBridge (OIB) campaign in 2016 (Paden et al., 2014 updated 2019) are shown by black lines (Echograms are included in the Appendix, Fig. 9.6). Background colour shows the ice-shelf thickness from BedMachine Antarctica (Morlighem, 2020; Morlighem et al., 2020).

along four cross-sections, providing along-flow and across-flow melt rate distributions (Fig. 9.1). A further transect crossed the entire FIS south of Berkner Island. As far as safety allowed, we extended the profiles along the eastern margin towards the inland ice, to capture an area where gradients in the bathymetry were expected, steering the flow of water masses. With this observational design we intended to measure the large scale distribution of melt rates, but in addition we included more closely spaced stations to detect variations on short spatial scales. In the following, we first introduce the methodology and the data basis. We then present and discuss the derived basal melt rates and compare them with remote sensing data.

9.2 Materials and methods

Our estimation of basal melt rates is based on measurements using a pRES that is described in detail in Brennan et al. (2014) and Nicholls et al. (2015). The

pRES transmits a frequency modulated sweep (chirp) from 200 to 400 MHz over a period of one second. After internal processing, only the difference in frequency between the transmitted and received signals, called the deramped frequency, is saved. Details of the internal processing are given by [Brennan et al. \(2014\)](#). By repeating the measurements after a time period, we are able to track changes in depth of internal reflectors within the ice, and of the basal echo, to a precision of millimetres. This allows the study of firn densification, vertical strain due to ice flow, and the (Lagrangian) change in ice-shelf thickness. Being a Lagrangian measurement, no steady state assumption is required, and the basal melt rate can be separated from the overall change in ice thickness.

Our 94 measurement stations are grouped depending on their location on the Central Flow line (CFL) and five Cross-Sections (CS) A–E (for location, see [Fig. 9.1](#)). The time period between repeated measurements varied between 323 and 356 days. To improve the signal-to-noise ratio, we recorded 100 chirps at each site. Low correlation chirps were rejected during preprocessing. Those remaining chirps were averaged and then Fourier transformed to yield a complex (amplitude and phase) profile as a function of two-way-travel time. To convert the profile into a function of range we calculated the velocity profile of the electromagnetic wave for each location by estimating the density-depth profile based on [Herron and Langway \(1980\)](#) with accumulation and mean annual temperature from RACMO 2.3/ANT ([van Wessem et al., 2014](#)).

Using a procedure similar to that described by [Corr et al. \(2002\)](#) and [Jenkins et al. \(2006\)](#), we aligned the two radar profiles using a 50 m window below the firn-ice boundary by cross-correlating the amplitude profiles. This provided a datum within the ice column, removing the effects of instrument temperature change, firn densification and snow accumulation and ablation.

The thickness change (DH_i/Dt) in the solid-ice below the aligned reflector is caused only by the dynamic ice thickness change due to vertical strain ($H_i\dot{\epsilon}_{zz}$) and by the basal melt rate a_b :

$$\frac{DH_i}{Dt} = H_i\dot{\epsilon}_{zz} - a_b, \quad (9.1)$$

with H_i the solid-ice thickness below the aligned reflector and $\dot{\epsilon}_{zz}$ the vertical strain rate. In order to determine the vertical strain, the displacement between visits was calculated with a cross-correlation of the amplitude and phase information for each layer deeper than the aligned reflector. Under the plain-strain assumption the vertical strain is constant with depth; a least-squares method was used to calculate a linear fit of the shift of those layers that exhibited a high correlation value. The gradient of the linear fit is the vertical strain. The change

in ice thickness below the aligned reflector is derived from the shift of the basal reflector, which was calculated in the same way as the shift of the internal layers. The largest error in the calculation comes from the alignment of the data because it is based only on the amplitude correlation. The uncertainty in the calculation of the phase shift is closely related to the signal to noise ratio of the reflectors. An additional uncertainty arises from the assumption of a linear strain-depth relation, although this is generally thought reliable for plug flow.

9.3 Results

9.3.1 Large scale spatial variability

Seventy-nine of the 94 measurements were suitable for retrieval of basal melt rates. The main reasons for excluding the other 15 stations are (1) low correlation values in the depth of the firn-ice transition, which made it impossible to align the measurements, (2) changes in the shape of the basal reflector that prevented the reflections from being unequivocally matched, (3) too few high correlation values for a linear fit to be used to calculate the vertical strain rate.

For the remaining stations, we found a mean basal melt rate of $0.38 \pm 0.26 \text{ m a}^{-1}$ (mean + standard deviation; Fig. 9.2a) with a maximum of 1.13 m a^{-1} at a location about 50 km downstream of the grounding line and freezing in the northernmost part of the central flow line (CFL). Of similar size but with different sign, the mean value of DH_i/Dt is $-0.38 \pm 0.32 \text{ m a}^{-1}$ (Fig. 9.2b), representing a thinning of the solid ice, whereas the mean value of $H_i \dot{\epsilon}_{zz}$ ($-0.01 \pm 0.20 \text{ m a}^{-1}$) is close to zero (Fig. 9.2c).

We present the distribution of a_b in Fig. 9.1b, as well as an along-flow profile (CFL) and five cross-sections (CSA-CSE) in Fig. 9.3. Seventy percent of the estimated basal melt rates range between 0 and 0.50 m a^{-1} . Higher melt rates

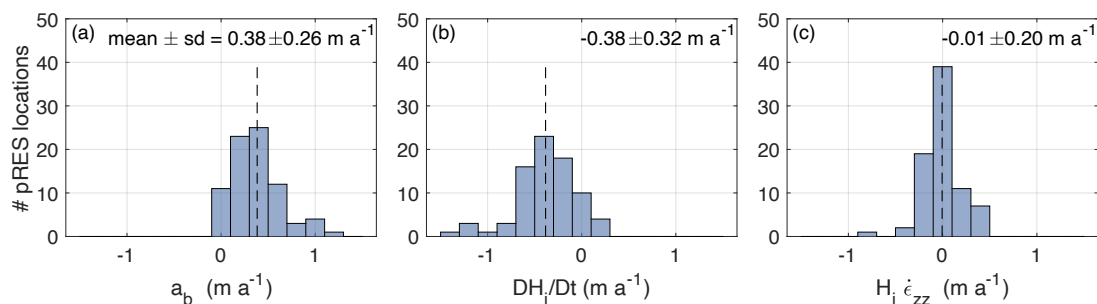


Figure 9.2: Distribution of pRES-derived results of (a) the basal melt rate a_b , (b) the change in solid-ice thickness DH_i/Dt and (c) the dynamic change in solid-ice thickness $H_i \dot{\epsilon}_{zz}$. The numbers in the upper right corner state the mean value and the standard deviation (sd).

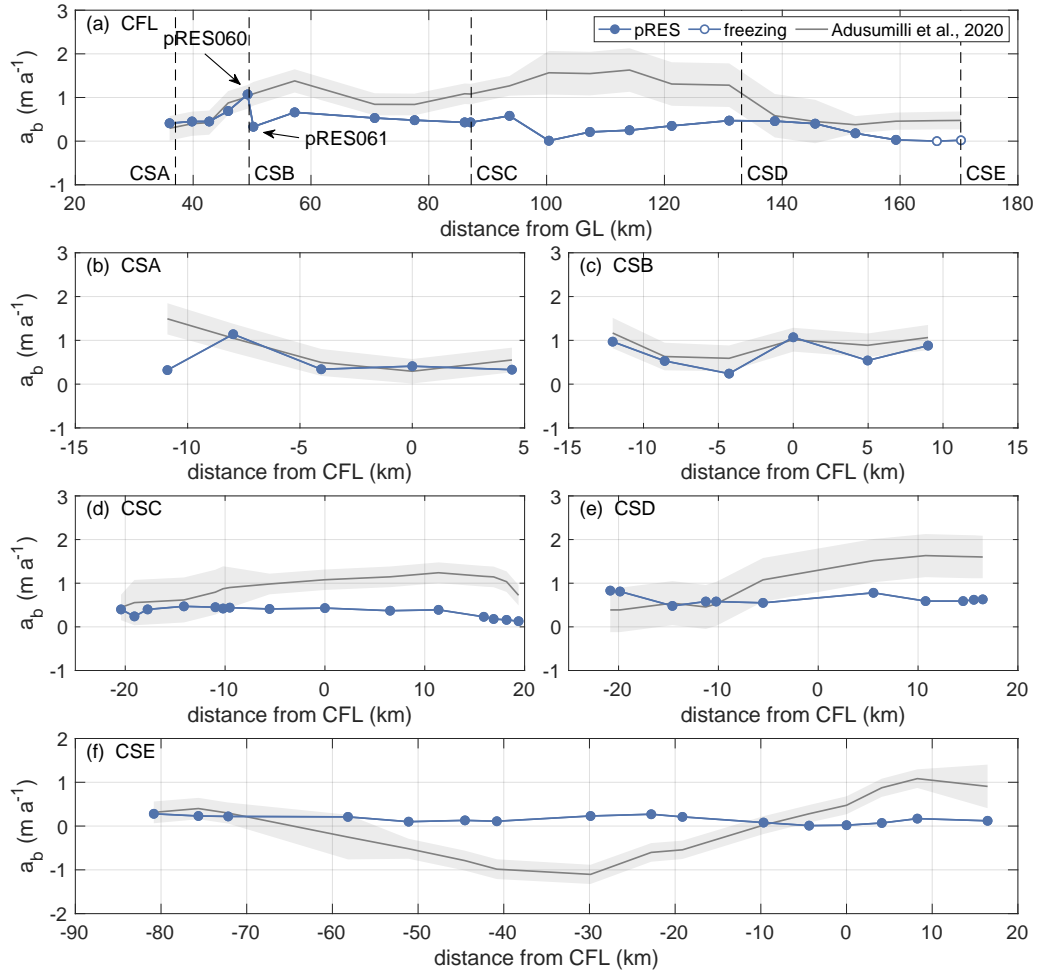


Figure 9.3: Variation of the basal melt rate (a) along the Central Flow Line (CFL) of Support Force Glacier’s extension on the FIS and (b–f) the cross-sections CSA–CSE. Locations are shown in Fig. 9.1. pRES-derived values are shown in blue. The dark grey line represents remote sensing-derived melt rates and the light grey bounds display the uncertainty, both published by Adusumilli et al. (2020). Derived errors of the pRES measurements are too small to visualise. For CFL, the distance refers to the grounding line (GL) of Support Force Glacier and for all cross-sections to the CFL with positive distances on the eastern side.

were found for nine stations within 100 km of the grounding line at the CFL, CSA and CSB. All three stations with $a_b > 1 \text{ m a}^{-1}$ are located in this part of the study area. The variation of a_b along ice flow is weak and shows no clear trend of increasing melt towards the grounding line, despite the increasing ice draft (Fig. 9.3a). In the direction across ice flow (Fig. 9.3b-f) the largest variations in a_b appear in the two southernmost cross-sections (CSA, CSB). The northernmost cross-section, ranging from Berkner Island towards the inland ice (CSE), has a generally low a_b . Three stations, all at the northernmost part of CFL, indicate freezing. Apart from the southern part, higher basal melt rates, of up to 0.82 m a^{-1} , occur only at CSD. A large scale distribution of a_b can also be influenced by changes in vertical gradients of the ice temperature. An

ice shelf fed by a fast glacier typically contains a cold core as a result of ice advection, leading to larger vertical temperature gradients some distance from the grounding line. However, with melting over centuries, the ice temperature is more likely to approach a parabolic profile, with only moderate temperature gradients (Humbert, 2010).

9.3.2 Small scale spatial variability

In order to assess the small scale spatial variability of the basal melt rates and hence the representativeness of measurements over large distances, we carried out 18 pRES measurements located, each within a 2-km of another measurement, at different locations across our survey area. In Fig. 9.4 we display the difference in melt rates $|\Delta a_b|$ between nearby station pairs as a function of the difference in ice-shelf draft $|\Delta h_b|$, derived from the BedMachine surface elevation (Morlighem, 2020; Morlighem et al., 2020), which gives an indication of large scale basal topography for the two locations. The basal melt rate of the higher melt rate station is indicated by colour, and the size of the dot represents the separation. For all but two $|\Delta h_b|$ is below 10 m and $|\Delta a_b|$ below 0.10 m a^{-1} , independent of the magnitude of a_b or the distance between the measurements. The largest $|\Delta a_b|$ of 0.71 m a^{-1} is coincident with $|\Delta h_b|$ of 10.5 m within a distance of $< 1 \text{ km}$ and was observed at locations pRES060 and pRES061 (Fig. 9.3 and Fig. 9.7). At location pRES060, we observed the higher melt rate as well as the larger draft of the two locations, which indicates an increased thermal forcing as a result of the higher basal pressure. Beside, the station with the second largest basal melt rate of $a_b > 1.0 \text{ m a}^{-1}$ indicates a localised change in draft of 15.5 m. Overall, this gives evidence that individual measurements are representative of a large

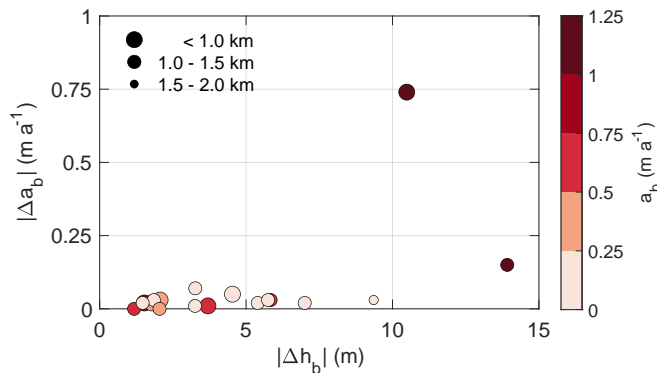


Figure 9.4: Small scale variability of basal melt rates and ice-shelf draft. Difference in basal melt rate $|\Delta a_b|$ in relation to ice-shelf draft $|\Delta h_b|$ for nearby stations (average distance: $1126 \pm 296 \text{ m}$). The colour of each dot represents a_b of the station with the larger basal melt rate and the size indicates the distance between both stations.

area on the scale of many ice thicknesses and only minor variation due to the specific choice of the location of the measurement is to be expected for an ice base with suppressed basal topography. Airborne radar echograms (Fig. 9.6), recorded within NASA’s Operation IceBridge (OIB) with a Center for Remote Sensing of Ice Sheets (CREGIS) Multi-channel Coherent Radar Depth Sounder (MCoRDS) in 2016 (Paden et al., 2014 updated 2019), show that this largely applies to the study area. For the most part, these radargrams show a smooth ice shelf base with some slight variations of a few metres over several hundreds of metres, but without terrace structures. One exception is a basal channel in the west with a height of approx. 50 m (Fig. 9.6e,f). At three locations around this channel, pRES measurements have been performed (western part of CSC in Fig. 9.3d). These show low variability, with a basal melt rate $\sim 0.2 \text{ m a}^{-1}$ lower in the centre of the channel.

9.4 Comparison with remote sensing basal melt estimates

The analysis of remote sensing-derived basal melt rates is based on precisely measured elevation changes of the ice-shelf surface and on the correction of the surface mass balance, firn densification and dynamic change in ice thickness (e.g. Moholdt et al., 2015; Adusumilli et al., 2020). The dynamic change in ice thickness and thus the vertical strain rate is often derived from the divergence of a satellite sensor-derived surface velocity field.

We used the pRES-derived vertical strain rates to assess the reliability of strain rates derived from different remote sensing velocity fields. Satellite-derived melt rates at FIS from Rignot et al. (2013), Moholdt et al. (2015) and Adusumilli et al. (2020) were all based on the strain rates derived from the same early MEaSUREs velocities (Rignot et al., 2011; Scheuchl et al., 2012). However, this velocity field contained some significant data gaps in our study area that were not present in modern velocity fields such as the Landsat Ice Speed of Antarctica (LISA) product from which vertical strain rates were derived by Alley et al. (2018) or the newest MEaSUREs data set (Mouginot et al., 2019b,a). Instead of comparing the vertical strain rate itself, we compared the dynamic ice thickness change ($H_i \dot{\epsilon}_{zz}$) that was derived from the vertical strain rate and the solid-ice thickness. The result reveal a significant improvement over the last decade in the accuracy of the determination of vertical strain rates from remote sensing.

While the average deviation between the pRES-derived product and that from Moholdt et al. (2015) was $0.40 \pm 0.44 \text{ m a}^{-1}$ (mean \pm standard deviation; Fig. 9.5a,b

and Fig. 9.8), there were much smaller deviations ($-0.01 \pm 0.35 \text{ m a}^{-1}$) from the product of Alley et al. (2018) (Fig. 9.5c,d and Fig. 9.8). The comparison with the dynamic ice thickness that we calculated using the latest MEASUREs data set (Mouginot et al., 2019a,b) also showed only minor deviations of $0.04 \pm 0.17 \text{ m a}^{-1}$ (Fig. 9.5e,f and Fig. 9.8). Here, similar to Moholdt et al. (2015), we applied a Gaussian filter with a $27 \times 27 \text{ km}$ window to smooth the velocity data, and calculated the divergence to obtain the vertical strain rate. The comparison highlights the recent improvement in the estimation of velocity fields for more accurate calculation of dynamic ice thickness changes, and demonstrates good agreement between remote sensing-derived strain rates and those from in situ measurements. Remote sensing-derived melt rates published by Rignot et al. (2013), Moholdt et al. (2015) and Adusumilli et al. (2020) suggested a similar pattern of melt rates: southeast of Berkner Island, a freezing regime in the west switches to a melting regime eastwards, with melting persisting towards the south to the Support Force Glacier. However, a data gap in the velocity field meant that no melt rates could be determined by Rignot et al. (2013) for a large part of our study area.

The comparison with the results from Adusumilli et al. (2020) reveals a broader distribution of the remote sensing-derived melt rate ($-1.1 - 1.6 \text{ m a}^{-1}$) at the pRES locations with an average deviation from the pRES-derived values of $0.35 \pm 0.57 \text{ m a}^{-1}$ (Figs. 9.3 and 9.5g,h), which is of size similar to the deviation of the dynamic change in ice thickness. Another reason for the discrepancies can be the different measurement periods over which the basal melt rates were estimated: Adusumilli et al. (2020) shows that basal melt rates can vary at interannual timescales. In order to investigate whether different measurement periods contributed to the discrepancies between the results from the different methods, we compared the change in ice thickness DH_i/Dt (Eq. 9.1) after the correction for the surface mass balance and firn densification (Fig. 9.9). Some of the differences occur because Adusumilli et al. (2020) defines H_i as the ice-shelf thickness in units of m of ice equivalent, which is slightly higher than the solid-ice thickness that we use for the pRES-based estimates. However, the comparison of DH_i/Dt shows a good agreement, with an average difference of only $0.04 \pm 0.24 \text{ m a}^{-1}$ (Fig. 9.5i,j). Since variations in basal melt rate contribute to DH_i/Dt and this only shows slight differences, a temporal variation in basal melting can be excluded as the reason for the significant discrepancies that we find. Furthermore, this indicates that the techniques derive consistent changes in ice thickness from their initial measurements after applying the corrections for the surface mass balance and the firn densification, and that the large differences in basal melt rates result principally from differences in the strain rate, which can be improved by the use of

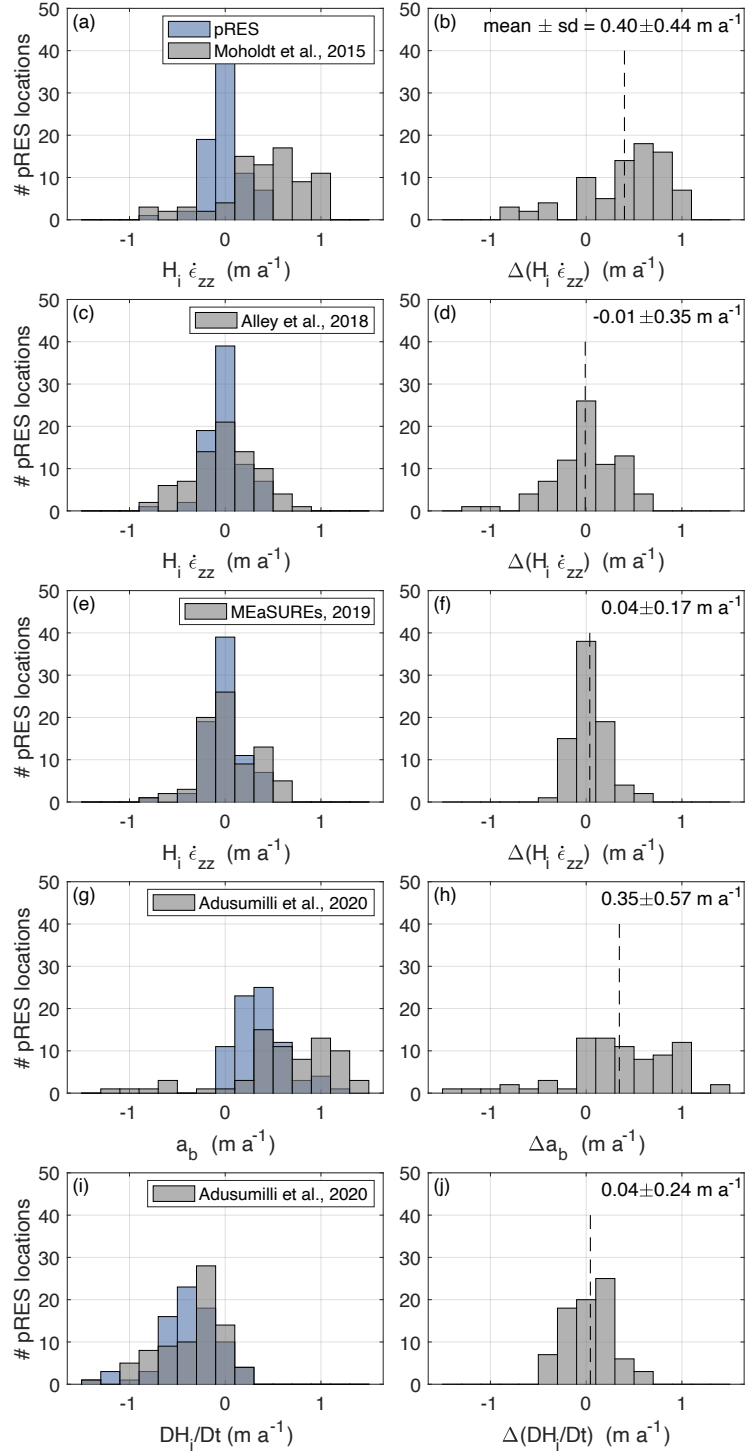


Figure 9.5: Comparison of remote sensing (grey) and pRES-derived (blue) results. The left column shows the distributions (a) of the dynamic change in ice thickness $H_i \dot{\epsilon}_{zz}$ for the results published by Moholdt et al. (2015), (c) Alley et al. (2018) and (e) derived from the MEaSUREs product (Mouginot et al., 2019b,a), (g) of the basal melt rate a_b and (i) of the change in ice thickness DH_i/Dt , both in comparison with those from Adusumilli et al. (2020). The right column (b,d,f,h,j) shows the distribution of the deviation between remote sensing and pRES-derived values according to (a,c,e,g,i). The numbers in the upper right corner state the mean value and the standard deviation (sd). Positive value refer to larger numbers derived from the remote sensing-based method.

modern surface velocity products.

9.5 Conclusion

We have presented the first spatial distribution of basal melt rates in the southern Filchner Ice Shelf derived from repeated phase-sensitive radar measurements. In general the melt rates are moderate with maximum values in the centre of less than 1.13 m a^{-1} . We tested the representativeness of individual measurements by assessing the variability over short distances. Spatial variability in a_b is low, with occasional outliers possibly linked to large basal gradients. This gives us confidence that a small number of widely spaced measurements accurately represent the large scale melt pattern. Temporal variability, however, is not captured. We find freezing at three locations – all in the northern part of the study area – but as yet we are unable to extract a rate from the radar data.

Our in situ measurements reveal that inaccuracies in the estimation of dynamic ice thickness change negatively affected recent remote sensing-derived melt rates at our study area at the Filchner Ice Shelf. A comparison with strain rates published by [Alley et al. \(2018\)](#) and with those derived from the newest MEaSUREs velocity field indicates that these inaccuracies can be overcome by using state-to-the-art velocity fields, in which data gaps could be closed. Our study demonstrates that satellite-derived basal melt rates hold great promise, but care needs to be taken, as modelling of the future contribution of Antarctica to sea level rise is currently calibrated using such products ([Jourdain et al., 2020](#)). This highlights the need to obtain more data sets such as the one presented here, from across different ice shelves, and to conduct repeated field surveys to assess temporal variability.

9.6 Appendix

9.6.1 Airborne radar echograms

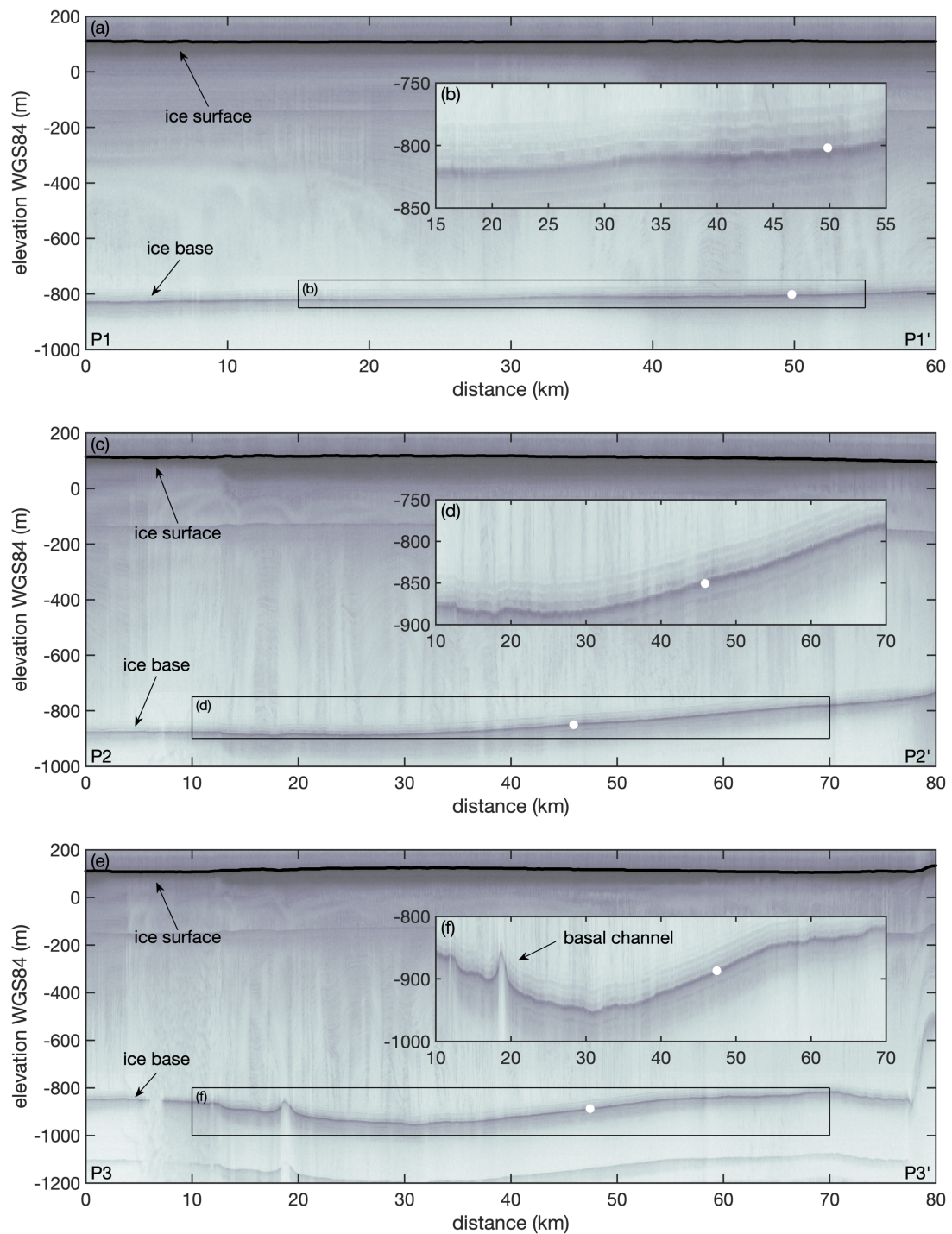


Figure 9.6: Airborne radar echograms (a) P1, (c) P2 and (e) P3 (location in Fig. 9.1), recorded with a Multi-channel Coherent Radar Depth Sounder (MCoRDS) as part of NASA’s Operation IceBridge (OIB) campaign in 2016 (Paden et al., 2014 updated 2019; Arnold et al., 2020). (b,d,f) Insets showing enlarged basal section visualised by black box in (a), (c) and (e). The white dots mark the depth of the ice base derived from a near-by pRES measurement.

9.6.2 pRES echograms

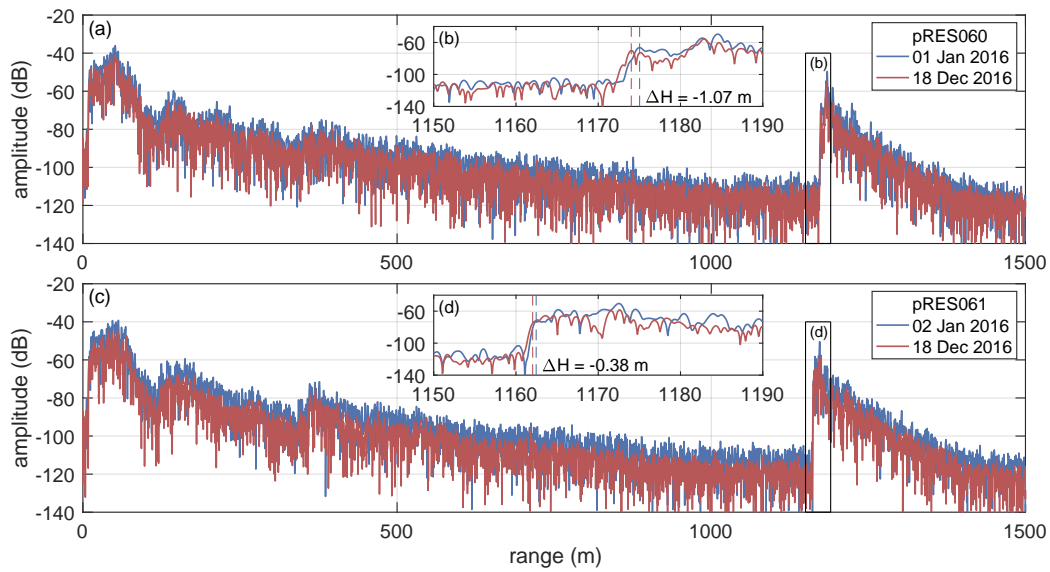


Figure 9.7: Amplitude profiles of first and repeated measurements at locations pRES060 (a,b) and pRES061 (c,d). Insets in (b) and (d) showing enlarged basal section, visualised by black boxes in (a) and (c). (b,d) Vertical dashed lines mark the ice thickness and ΔH the change in ice thickness between both visits.

9.6.3 Comparison with remote sensing

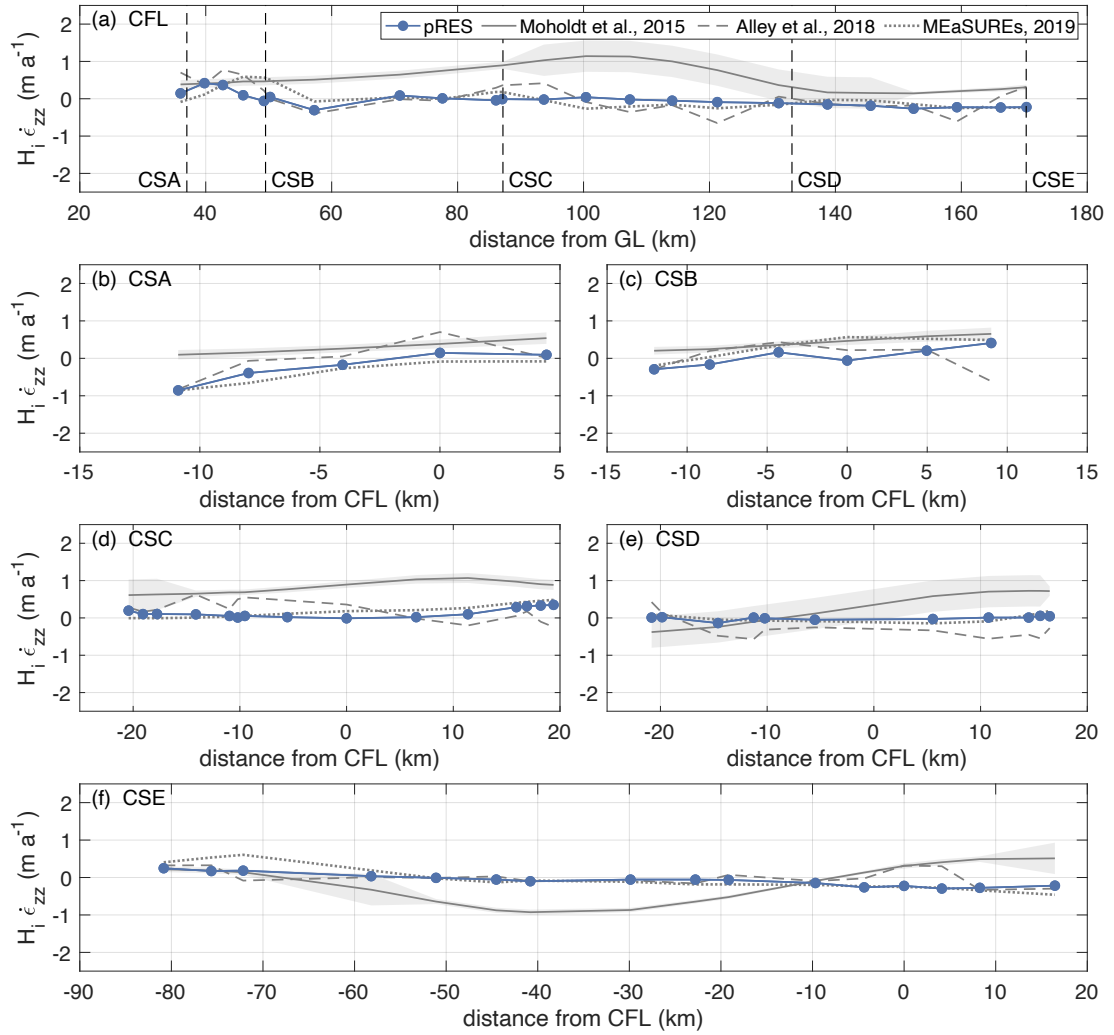


Figure 9.8: Variation of the dynamic ice thickness change $H_i \dot{\epsilon}_{zz}$ (a) along the Central Flow Line (CFL) of Support Force Glacier’s extension on the FIS and (b–f) the cross-sections CSA–CSE. Locations are shown in Fig. 9.1. pRES-derived values are shown in blue. Remote sensing-derived values are represented by the solid grey line for results published by Moholdt et al. (2015), by a dashed line for results published by Alley et al. (2018), and by a dotted line for estimations derived from the MEaSUREs product (Mouginot et al., 2019b,a). The bounds of the results from Moholdt et al. (2015) display the uncertainties. Derived errors of the pRES measurements are too small to visualise. For CFL, the distance refers to the grounding line (GL) of Support Force Glacier and for all cross-sections to the CFL with positive distances on the eastern side.

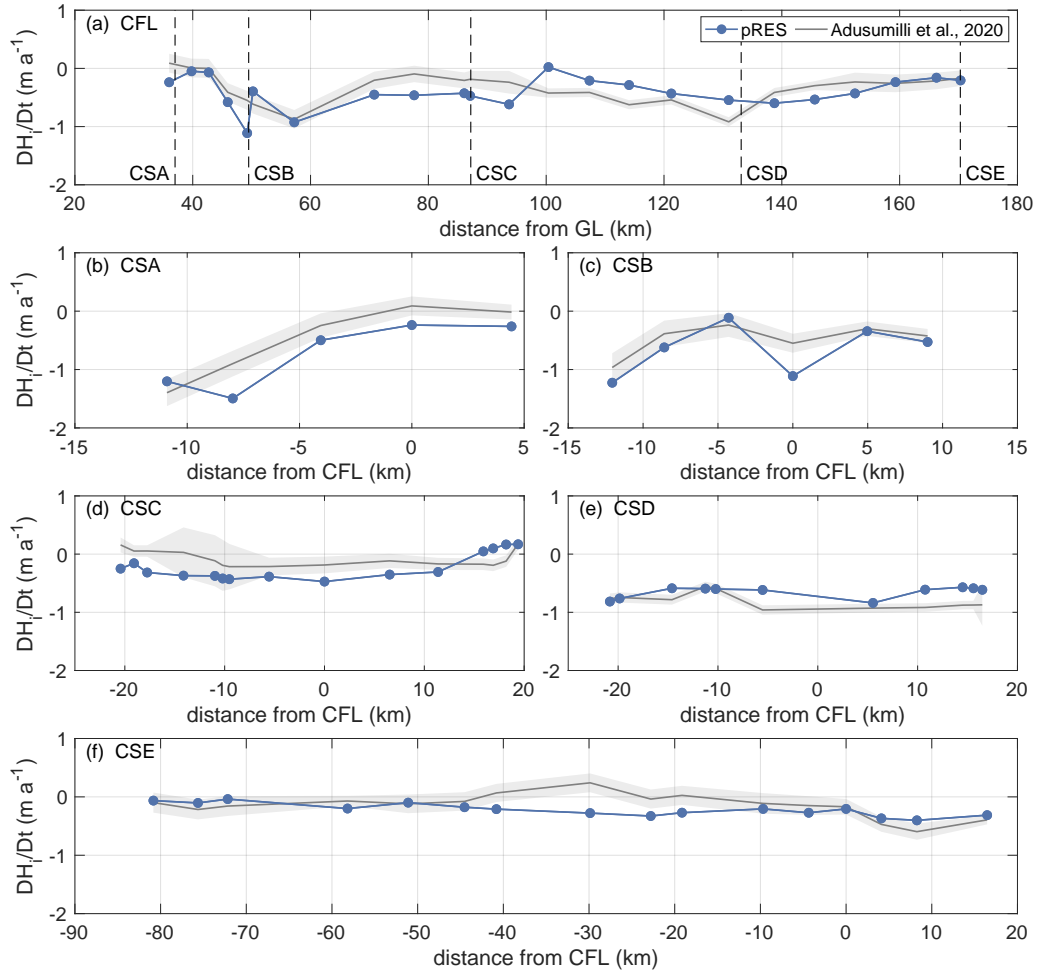


Figure 9.9: Variation of the ice thickness change DH_i/Dt (a) along the Central Flow Line (CFL) of Support Force Glacier’s extension on the FIS and (b–f) the cross-sections CSA–CSE. Locations are shown in Fig. 9.1. pRES-derived values are shown in blue. Remote sensing-derived values are represented by the dark grey line for results published by Adusumilli et al. (2020). The light grey bounds display the uncertainties. Derived errors of the pRES measurements are too small to visualise. For CFL, the distance refers to the grounding line (GL) of Support Force Glacier and for all cross-sections to the CFL with positive distances on the eastern side.

Data availability

Raw data of the pRES measurements and derived melt rates (<https://doi.org/10.1594/PANGAEA.930735>; Zeising et al., 2021c) are available at the World Data Center PANGAEA. Echograms recorded with a Center for Remote Sensing of Ice Sheets (CReSIS) Multi-channel Coherent Radar Depth Sounder (MCoRDS) within NASA’s Operation IceBridge (OIB) campaign in 2016 can be accessed at <https://nsidc.org/data/IRMCR1B/versions/2> (Paden et al., 2014 updated 2019) (last access: 25 April 2021). Basal melt rate data published by Adusumilli et al. (2020) can be accessed at <https://doi.org/10.6075/J04Q7SHT> (last access: 04 March 2021). Ice-shelf divergence and thickness data published by Moholdt et al. (2015) can be accessed at <https://doi.org/10.21334/npolar.2016.cae21585> (last access: 29 April 2021). Strain rate data published by Alley et al. (2018) can be accessed through open ftp by contacting the National Snow and Ice Data Center (NSIDC) (last access: 25 June 2021). MEaSURES velocity product can be accessed at <https://nsidc.org/data/nsidc-0754/versions/1> (Mouginot et al., 2019b) (last access: 13 April 2021). BedMachine Antarctica product can be accessed at <http://nsidc.org/data/nsidc-0756> (Morlighem, 2020) (last access: 12 April 2021).

Acknowledgements













This work was funded by the AWI strategy fund project FISP. Support for this work came from the UK Natural Environment Research Council large grant “Ice shelves in a warming world: Filchner Ice Shelf System” (NE/L013770/1). We acknowledge provision of data products by Susheel Adusumilli (Scripps Institution of Oceanography, University of California San Diego, La Jolla, CA, USA), that have been published in Adusumilli et al. (2020). We want to thank Graham Niven and Bradley Morrell for their support in the field. We are grateful for discussions with Veit Helm and Niklas Neckel (AWI) on remote sensing-derived vertical strain rates and our results.

On the evolution of an ice shelf melt channel at the base of Filchner Ice Shelf, from observations and viscoelastic modeling

10

This chapter is submitted as a research article to the journal *The Cryosphere* in 2021.

Authors and affiliations

Angelika Humbert^{1,2}, Julia Christmann¹, Hugh F. J. Corr³, Veit Helm¹, Lea-Sophie Höyns^{1,4}, Coen Hofstede¹, Ralf Müller^{5,6}, Niklas Neckel¹, Keith W. Nicholls³, Timm Schultz^{5,6}, Daniel Steinhage¹, Michael Wolovick¹, and Ole Zeising^{1,2}

¹Alfred-Wegener-Institut Helmholtz-Zentrum für Polar- und Meeresforschung, Bremerhaven, Germany

²Department of Geosciences, University of Bremen, Bremen, Germany

³British Antarctic Survey, Natural Environment Research Council, Cambridge, UK

⁴Department of Mathematics and Computer Science, University of Bremen, Bremen, Germany

⁵Institute of Applied Mechanics, University of Kaiserslautern, Kaiserslautern, Germany

⁶Technical University of Darmstadt, Darmstadt, Germany

Contributions

A.Humbert has designed the study, conducted the field study together with D.Steinhage. **O.Zeising** processed the pRES/ApRES data and analyzed the melt rates together with A.Humbert. J.Christmann performed the viscoelastic simulations together with T.Schultz and with contributions from **O.Zeising** and A.Humbert. J.Christmann, A.Humbert and **O.Zeising** analyzed the results together with R.Müller. V.Helm and **O.Zeising** processed the GPS data.

L.Höyns and M.Wolovick performed the inverse modeling. C.Hofstede performed the seismic measurements and supported the discussions. N.Neckel calculated the TDX-DEM and flow velocities. K.W.Nicholls supported the field study and contributed to melt rate analysis and its discussion together with H.F.J.Corr. **O.Zeising** wrote Sect. 10.2 ("Observations") with contributions from A.Humbert and with the exception of Sect. 10.2.2 ("Digital Elevation Model (DEM)") which was written by V.Helm. J.Christmann wrote Sect. 10.3 ("Viscoelastic modeling") with contributions from **O.Zeising** and A.Humbert. A.Humbert wrote Sect. 10.4 ("Discussion") with contributions from **O.Zeising**, J.Christmann and K.W.Nicholls. All authors helped to improve writing. Figures were designed by **O.Zeising** – with the exception of Fig. 10.5 created by J.Christmann.

Abstract

Ice shelves play a key role in the stability of the Antarctic Ice Sheet due to their buttressing effect. A loss of buttressing as a result of increased basal melting or ice shelf disintegration will lead to increased ice discharge. Some ice shelves exhibit channels at the base that are not yet fully understood. In this study, we present in-situ melt rates of a channel which is up to 330 m high and located at the southern Filchner Ice Shelf. Maximum observed melt rates are 2.3 m a^{-1} . Melt rates decline inside the channel along flow and turn into freezing 55 km downstream of the grounding line. While closer to the grounding line melt rates are higher within the channel than outside, this reverses further downstream. Comparing the evolution of this channel under present-day climate conditions over 250 years with its present geometry reveals a mismatch. This mismatch indicates melt rates two times higher were necessary over the past 250 years to form today's channel geometry. In contrast, forcing the model with present-day melt rates results in a closure of the channel, which contradicts observations. Time series of melt rate measurements show strong tidally-induced variability in vertical strain-rates. We found no evidence of seasonality, but discrete pulses of increased melting occurred throughout the measurement period. The type of melt channel in this study diminishes with distance from the grounding line and are hence not a destabilizing factor for ice shelves.

10.1 Introduction

Melt channels in ice shelves have been hypothesized to destabilize ice shelves and were often linked to enhanced basal melt. This triggered a variety of observational studies (Le Brocq et al., 2013; Langley et al., 2014; Drews, 2015; Marsh et al., 2016; Dow et al., 2018; Hofstede et al., 2021a). However, such channels diminish with increasing distance from the grounding line at numerous locations. The main questions are thus if such channels are indeed locations of enhanced basal melt and what causes them to diminish. Channels at the base of ice shelves may either be incised by subglacial channels beneath the inland ice transporting water into the ocean (Le Brocq et al., 2013), arise from topographic features or from shear margins developing surface troughs when adjusting to floatation (Alley et al., 2019). Such features like bedrock undulations or eskers imprinted into the ice geometry on the inland ice side create a channel-type geometry on the floating part (Drews et al., 2017; Jeffry et al., 2018). In both cases, the channel at the ice base will be altered by two factors: basal melt arising from oceanic heat and viscoelastic creep. Surface troughs on ice shelves, which are detectable by satellites- and airborne remote sensing, are linked due to buoyancy equilibrium to incisions at the ice base, thus either to melt channels (e.g. Le Brocq et al., 2013; Langley et al., 2014) or to basal crevasses (e.g. Humbert et al., 2015). Channels at the ice base have been surveyed using radio echo sounding (Rignot and Steffen, 2008; Vaughan et al., 2012; Le Brocq et al., 2013; Dutrieux et al., 2014; Langley et al., 2014; Dow et al., 2018). The typical dimensions range from 300 – 500 m wide and up to 50 m high channels (Langley et al., 2014) to 1 – 3 km wide and 200 – 400 m high ones (Rignot and Steffen, 2008). Channel flanks are not necessarily smooth but may form terrace structures in lateral (across ice flow) dimension as shown by Dutrieux et al. (2014) for Pine Island Glacier, Antarctica. These terraces are separated by up to 50 m high walls with steep slopes between 40° and 60°. Hofstede et al. (2021a) found a basal channel on Support Force Glacier at the transition to Filchner Ice Shelf attributed to the outflow of subglacial water. The channel increases in height close to the grounding line and widens afterwards. Between 7 and 14 km from the grounding line, the flanks of the channel became steeper and terraces formed on its sides, which are sustained over 38 km from the grounding line, but decline in height between 14–38 km. Within this distance, the height varied only slightly from 170 to 205 m. This particular channel is the focus of this study.

In-situ observations of melt rates in such channels are often conducted with a phase sensitive Radio Echo Sounder (pRES), which is described in more detail below. Basal melt rates in a channel at Ross Ice Shelf, Antarctica were found

by Marsh et al. (2016) to be up to 22.2 m a^{-1} near the grounding line and only 2.5 m a^{-1} for observations 40 km downstream. In lateral direction, the melt rate is only 0.82 m a^{-1} demonstrating enhanced melt inside the channel. At Pine Island Glacier, Antarctica, Stanton et al. (2013) found basal melt rates of up to 24 m a^{-1} and an across-channel variability that they suggested to be related to channelized flow. The decreasing of melt rates inside the channel in the flow direction is likewise described by Le Brocq et al. (2013). Uprising fresh water enhances basal melting inside the channel. At some point, it becomes super-cooled due to the falling pressure. Thus, the melt rate decreases and could even change to refreezing. Similar to Le Brocq et al. (2013), Marsh et al. (2016) assumed that the channel at Ross Ice Shelf is formed by the outflow of subglacial meltwater. Washam et al. (2019) found high seasonal variability in basal melting within a channel at Petermann Gletscher, Greenland. In summer, melt rates reached a maximum of 80 m a^{-1} , whereas in winter, melt rates were below 5 m a^{-1} . They suggested that increased subglacial discharge during summer strengthens ocean currents under the ice which drives the high melt rates. Besides seasonal variability, melt rates also change within smaller periods. Vaňková et al. (2020) identified melt rate variations at the M_2 tidal constituent at six of 17 locations at Filchner-Ronne Ice Shelf, Antarctica.

Modeling basal melt rates requires coupled ice-ocean models, solving the energy jump condition at the transition of ice to the ocean. While none of the global circulation models deals with ice shelf cavities, there are some coupled ice-sheet-ocean models simulating large scale basal melt rates (Gwyther et al., 2020; Dinniman et al., 2016; Jourdain et al., 2017; Seroussi et al., 2017; Timmermann and Hellmer, 2013; Galton-Fenzi et al., 2012). However, only a few of them incorporate melt channels: Gladish et al. (2012) showed that channels confine the warm water and stabilize the ice shelf by preventing melt on broader spatial scales. This conclusion is affirmed by Millgate et al. (2013) who found that an increasing number of melt channels lead to a decreasing overall mean melt rate. Our study will provide an observational dataset of basal melt rates that allows assessing this type of modeling. The change in geometry due to mechanical deformation is another important contribution to the evolution of basal channels. The gradients in displacement \mathbf{u} lead to strain $\boldsymbol{\varepsilon}$ that causes a change in ice thickness. This component is governed by the viscoelastic nature of a Maxwell fluid for ice. While ice is reacting purely viscous on long time scales, its behavior on short time scales is elastic (Reeh et al., 2000; Gudmundsson, 2011; Sergienko, 2013; Humbert et al., 2015; Christmann et al., 2016; Schultz, 2017; Christmann et al., 2019). The transition from grounded to floating ice and short term geometry changes due to basal melt or accumulation are examples of ice affected

by the elastic response. Over time scales of years, viscous creep becomes more relevant. As a consequence, the geometry of melt channels needs to be modeled using viscoelastic material models, which we will also engage below.

In this study, we present in-situ melt rates of a large melt channel feature of the southern Filchner Ice Shelf at the inflow from Support Force Glacier (SFG). Field measurement and satellite-borne data enable us to investigate how this feature evolves using numerical modeling. In addition to the spatial distribution of basal melt, we are analyzing the temporal evolution of melt rates. We split this manuscript into two main parts, starting with observations followed by a modeling section. We present the methodology and the results in each part separately. A synthesis is then focusing on the evolution of the melt channel.

10.2 Observations

10.2.1 Data acquisition

We acquired data at a melt channel on the southern Filchner Ice Shelf under the framework of the Filchner Ice Shelf Project (FISP). We performed 44 phase-sensitive radar (pRES) measurements (locations are shown in Fig. 10.1) in the season 2015/16, that have been repeated in 2016/17 as Lagrangian-type measurements. These measurements were taken in 13 cross-sections ranging from 14 to 61 km downstream the grounding line (Fig. 10.1). This allows us to investigate the spatial variability of basal melt rates. At each cross-section, up to four measurements were performed at different locations: at the steepest western flank (SW), at the lowest surface elevation (L), at the steepest eastern flank (SE) and outside east of the channel (OE; Fig. 10.1b). In order to achieve an all-year time series, one autonomous pRES (ApRES) station was installed (Fig. 10.1b). This instrument performed autonomous measurements every two hours resulting in 4342 measurements between 10 January 2017 and 6 January 2018. A GPS station was also in operation at this point from December 24, 2015 to May 5, 2016. To distinguish the single-repeated measurements from the autonomous measurements, we refer to them as *pRES* and *ApRES* measurements.

10.2.2 Materials and methods

pRES device and processing

The pRES device is a low-power, ground-based radar that allows for estimating displacement of layers from repeated measurements with a precision of millimeters (Brennan et al., 2014). This accuracy enables investigating even small basal

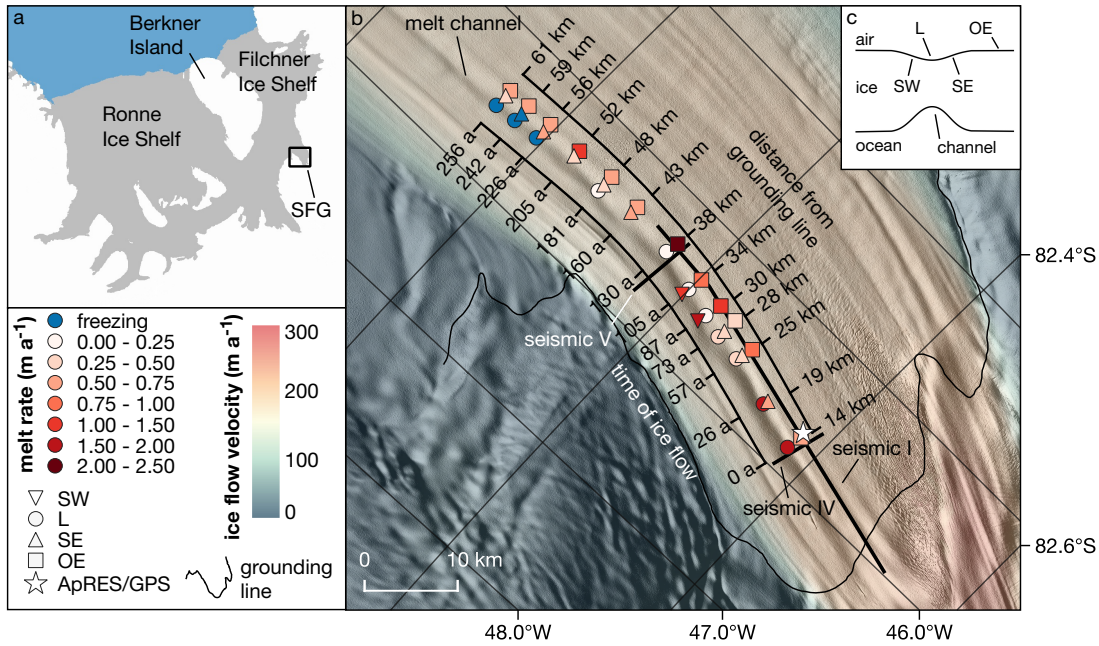


Figure 10.1: (a) Map of the Ronne and Filchner ice shelves (BedMachine Antarctica (Morlighem, 2020; Morlighem et al., 2020)). The study area near the Support Force Glacier (SFG) is marked with a black box. (b) Study area with pRES-derived basal melt rates at 13 cross-sections of the melt channel. The different symbols indicate the position relative to the channel, as shown in (c). For each cross-section, the distance from the grounding line and the duration of ice flow from the location furthest upstream are given. The location of an ApRES/GPS station is shown by a star. The seismic I, IV and V lines mark the location of active seismic profiles (Hofstede et al., 2021a,b). The background is a hillshade of the Reference Elevation Model of Antarctica (Howat et al., 2018, 2019) overlaid by the ice flow velocity (Hofstede et al., 2021a). (c) Sketch of a cross-section of the channel with measurement locations on the steepest western surface flank (SW), at the lowest surface elevation (L), on the steepest eastern surface flank (SE) and outside east of the channel (OE).

melt rates, taking snow accumulation together with firn compaction and strain in vertical direction into account (Corr et al., 2002; Jenkins et al., 2006). The pRES is a frequency modulated continuous wave (FMCW) radar that transmits a sweep, called *chirp*, over a period of one second with a center frequency of 300 MHz and bandwidth of 200 MHz (Nicholls et al., 2015). For a better signal to noise ratio, the single-repeated measurements were performed with 100 chirps per measurement and the measurements of the time series with 20 chirps due to memory and power limitations. After collecting the data, each chirp was correlated with every other chirp in order to reject those which had a low correlation coefficient on average. The remaining chirps were stacked.

We followed Brennan et al. (2014) and Stewart et al. (2019) for data processing to get amplitude- and phase-depth profiles. The final profile that contains the amplitude and phase information as a function of two-way travel time was received from a Fourier transformation. To convert two-way travel time into depth,

the propagation velocity of the radar wave is computed following [Kovacs et al. \(1995\)](#). For this the density is required. Here we use a model described by [Herron and Langway \(1980\)](#). As input parameters, accumulation rate and mean annual temperature is needed, for which we use data from the regional climate model RACMO 2.3/ANT ([van Wessem et al., 2014](#), multi-annual mean 1979 – 2011). Despite the correction of higher propagation velocities in the firn, the uncertainty of the velocity and thus of the depth is 1% ([Fujita et al., 2000](#)).

Basal melt rates from repeated pRES measurements

The method for determining basal melting rates, previously described by e.g. [Nicholls et al. \(2015\)](#) and [Stewart et al. \(2019\)](#), is based on the ice thickness evolution equation. The change in ice thickness over time $\partial H/\partial t$ consists of a component arising from deformation and accumulation/ablation at both interfaces (e.g. [Zeising and Humbert, 2021b](#)). As our observations are discrete in time, the change of ice shelf thickness ΔH within the time period Δt , that is caused by changes at the surface and in the firn ΔH_s (e.g. snow accumulation/ablation and firn compaction), by strain in vertical direction ΔH_ε and by thickness changes due to basal melt ΔH_b is considered:

$$\frac{\Delta H}{\Delta t} = \frac{\Delta H_s}{\Delta t} + \frac{\Delta H_\varepsilon}{\Delta t} + \frac{\Delta H_b}{\Delta t} \quad (10.1)$$

([Vaňková et al., 2020](#); [Zeising and Humbert, 2021b](#)).

In order to obtain the basal melt rate, the change in ice thickness must be adjusted for the other contributions. Snow accumulation/ablation, firn compaction but also changes in radar hardware (and settings) can cause an vertical offset near the surface that cannot be distinguished from one another. Following [Jenkins et al. \(2006\)](#), we aligned both measurements below the firn-ice transition. To this end, we compute the depth of pore closure h_{pc} takes place, i.e. the depth at which a density of 830 kg m^{-3} is reached. To this end, we apply the densification model ([Herron and Langway, 1980](#)) and mean annual accumulation rate and temperature from the multi-year mean RACMO2.3 product ([van Wessem et al., 2014](#)). In our study area, h_{pc} varies between 62 m and 71 m. The actual alignment is based on a correlation of the amplitudes for a window of 6 m around h_{pc} . No reliable alignment could be obtained from the correlation for nine stations, since the correlation values were not unambiguous. As a consequence, these stations were not considered.

After the alignment, the change in the ice thickness H_i below the depth of the pore close h_{pc} is only affected by vertical strain and basal melt. Thus the basal

melt rate a_b (positive for melting, negative for freezing) is

$$a_b = -\frac{\Delta H_b}{\Delta t} = -\left(\frac{\Delta H_i}{\Delta t} - \frac{\Delta H_\varepsilon}{\Delta t}\right) \quad (10.2)$$

with ΔH_ε being the thickness change due to vertical strain ε_{zz} . ΔH_ε is derived from integrating ε_{zz} from the aligned reflector at h_{pc} to the ice base h_b

$$\Delta H_\varepsilon = \int_{\bar{h}_b}^{h_{pc}} \varepsilon_{zz} dz. \quad (10.3)$$

Here, \bar{h}_b denotes the averaged depth of the ice base of the measurements. The vertical strain is defined as

$$\varepsilon_{zz} = \frac{\partial u_z}{\partial z} \quad (10.4)$$

with the displacement in vertical direction u_z .

In order to determine u_z , we followed the method described by [Stewart et al. \(2019\)](#). We divided the first measurement in segments of 6 m width with 3 m overlap from a depth of 20 m below the surface to 20 m above the ice base. To determine vertical displacements, we cross-correlated each segment of the first measurement with the repeated measurement. The lag of the largest amplitude correlation coefficient was used to find the correct minimum phase difference, from which we derived the vertical displacement. Since noise prevents the reliable estimation of the vertical displacement from a certain depth on, we calculated the depth at which the averaged correlation of unstacked chirps undercuts the empirical value of 0.65. We name this the noise-level depth limit h_{nl} , which is 743 m on average in this study area. Only those segments located below h_{pc} and above h_{nl} were used to avoid densification processes and noise to influence the strain estimation. A linear regression was calculated from the shifts of the remaining segments, assuming a constant vertical strain distribution over depth as the overall trend. However, at six stations, all in the hinge zone where the ice is bended by tides, we observed a slight deviation from a linear trend at deeper layers (Fig. 10.9a). The segments that indicate a non-linear distribution are located below h_{nl} and are hence not taken into account for the regression. Nevertheless, we want to provide a lower limit considering other forms of strain-depth relations. For this purpose, we use a strain model that is decreasing linearly from half the ice thickness (approximately h_{nl}) to the depth of at which $\varepsilon_{zz} = 0$ (Fig. 10.9b). This serves as a lower limit of the displacement, whereas a linear $\varepsilon_{zz}(z)$ gives the upper limit. The average of both gives ΔH_ε and the difference the uncertainty.

In order to derive ΔH_i , we used a wider segment of 10 m around the basal return, which was identified by a strong increase in amplitude. Its upper limit is located 9 m above the basal return, while the lower limit is defined 1 m below the basal return. The vertical displacement of the ice base and thus the change in ice thickness was obtained from the cross-correlation of the basal segment.

The uncertainty of the melt rate results mainly from the alignment of the repeated measurement and the uncertainty of ΔH_ε . This leads to uncertainties in the melt rate of more than 0.2 m a^{-1} for locations in the hinge zone, while at other locations the uncertainty is predominantly in the range of $< 0.05 \text{ m a}^{-1}$.

In order to classify how representative the melt rates are for the past, we reconstructed the ice thickness based on the values derived from the pRES measurements. First, we interpolated the a_b , ΔH_ε and ΔH_s along the distance of the channel to get continuous values between the cross-sections and smoothed the results in order to obtain a trend for each process. We converted the distance downstream of the upstream most cross-section to an age beyond this cross-section by assuming the mean flow velocity is constant. Next, we treat the change in ice thickness as a transport equation. To this end, we compute the advection of the ice thickness under present day climate conditions (H_{PDadv}). For this we use interpolated functions of $a_b(t)$, $\Delta H_\varepsilon(t)$ and $\Delta H_s(t)$. The expected ice thickness at H_{PDadv} is then the thickness at $t_0 = 0$ a plus the cumulative change in ice thickness:

$$H_{\text{PDadv}}(t) = H(t_0) + \int_{t_0}^t (\Delta H_s(t') + \Delta H_\varepsilon(t') + a_b(t')) dt'. \quad (10.5)$$

We can turn this around and calculate a synthetic melt rate $a_b^{\text{syn}}(t)$ that reconstructs the ice thickness H :

$$H(t) = H(t_0) + \int_{t_0}^t (\Delta H_s(t') + \Delta H_\varepsilon(t') + a_b^{\text{syn}}(t')) dt'. \quad (10.6)$$

Descriptions of the symbols are given in Tab. 10.1.

Basal melting from ApRES time series

The processing of the autonomous measured time series differs slightly from the single-repeated measurements. For the ApRES time series, the instrument was located below the surface, thus snow accumulation had no influence on the measured ice thickness and an alignment of the measurements is not necessary. This gives the possibility to determine the firn compaction ΔH_f . Without the alignment, thickness change due to strain needs to be considered for the whole ice

thickness H

$$\Delta H_\varepsilon = \int_0^H \varepsilon_{zz} dz. \quad (10.7)$$

For processing, we followed the method described by [Zeising and Humbert \(2021b\)](#), which differs slightly from the processing applied by [Vaňková et al. \(2020\)](#). Similar to processing of the single-repeated measurements, we divided the first measurement into the same segments and calculated the cross-correlation of the first measurement (t_1) with each repeated measurement (t_i). The displacement was obtained by the lag of the minimum phase difference. To avoid half-wavelength ambiguity due to phase wrapping, we limited the range of expected lag based on the displacement derived for the period $t_1 - t_{i-1}$.

The estimation of the vertical strain for the period $t_1 - t_i$ is based on a regression analysis of the vertical displacements for chosen segments. Only those segments located below a depth of 70 m and above the noise-level depth limit of $h \approx 600$ m were used to avoid densification processes and noise to influence the strain estimation. Assuming constant strain over depth (which is a first guess only), the regression analysis gives the vertical strain and the cumulative displacement $u_z(z)$ is

$$u_z(z) = \varepsilon_{zz} z + \Delta H_f \quad (10.8)$$

where the intercept at the surface is the firn compaction ΔH_f . By increasing the time period, the cumulative melt of the ApRES time series is derived.

In order to investigate if the basal melt is affected by tides, we first de-trended the cumulative melt time series and computed the frequency spectrum afterwards. Subsequently, we used frequencies up to the solar annual constituent as input for a harmonic fit of $\Delta H(t)$. We then de-tided $\Delta H(t)$ by subtracting the harmonic fit and calculated the thinning rate. Assuming, that basal melt causes changes on short time scales of several days, we attribute abrupt increases in the thinning rate to basal melt anomalies.

Global Positioning System (GPS) processing

The GPS processing is similar to the method used by [Christmann et al. \(2021\)](#). With the Waypoint GravNav 8.8 processing software, we applied a kinematic precise point positioning (PPP) processing for the GPS data that were stored in daily files. We merged three successive daily solutions to enable full day overlaps avoiding jumps between individual files. Afterwards, we combined the files in the middle of each 1-day overlap using relative point to point distances and removed outliers. The data has been low-pass filtered for frequencies higher than 1/3600 Hz. For tidal analysis, we calculated the power spectrum of the vertical displacement.

Digital Elevation Model (DEM)

We use the TanDEM-X PolarDEM 90m Digital Elevation data product provided by the German Aerospace Center (DLR) as reference elevation model (DLR, 2020). As the elevation values represent ellipsoidal heights relative to the WGS84 ellipsoid we refer the PolarDEM to the EIGEN-6C4 Geoid (Foerste et al., 2014). In the following, we refer the DEM heights above Geoid as observed surface elevation h_{TDX} . The absolute vertical height accuracy of the PolarDEM is validated against ICESat data and given to be < 10 m (Rizzoli et al., 2017). For our region of interest the accuracy is given to be < 5 m as shown in Fig. 16 of Rizzoli et al. (2017).

10.2.3 Results and discussion of observations

Spatial melt rate distribution around basal channel

The estimated basal melt rates derived from single-repeated pRES measurements range from 0 to 2.3 m a^{-1} (Fig. 10.2a). Some stations indicate basal freezing. A trend of decreasing melt rates in along channel direction was found at the thinnest part (L) of the channel. Here, melt rates decrease from 1.8 m a^{-1} to basal freezing, measured at the three most downstream cross-sections. Outside of the channel (OE), basal melt rates are more variable without a trend. Stations at the eastern flank (SE) show a lower range. Here, a_b varies between basal freezing and 0.8 m a^{-1} .

The height of the channel (difference in ice thickness between L and OE; Fig. 10.2b) increases from about 200 m at the southernmost cross-section to a maximum difference of about 330 m over a distance of 20 km in ice flow direction. At this location the melt rates within the channel fall below those outside the channel and the height of the channel decreases, reaching ~ 100 m at the northernmost cross-section.

In Fig. 10.2c we display the melt rates as a function of ice-shelf draft, derived from the TanDEM-X surface elevation and the pRES ice thickness. The melt rates outside the channel (OE) seem to be independent of the ice-shelf draft, while inside the channel (L) the melt rates decrease with reduced draft. However, melt rates at the largest drift inside the channel are approx. three times larger than those outside the channel or at the steepest eastern flank (SE) at similar draft. The distribution of ΔH_ε shows a significant thickening of more than 1 m a^{-1} at the most upstream cross-section at L and OE (Fig. 10.10). In ice flow direction, ΔH_ε declines, reaching about zero above the channel at the cross-section furthest downstream. In contrast, outside the channel, strain-thinning occurred 30 km

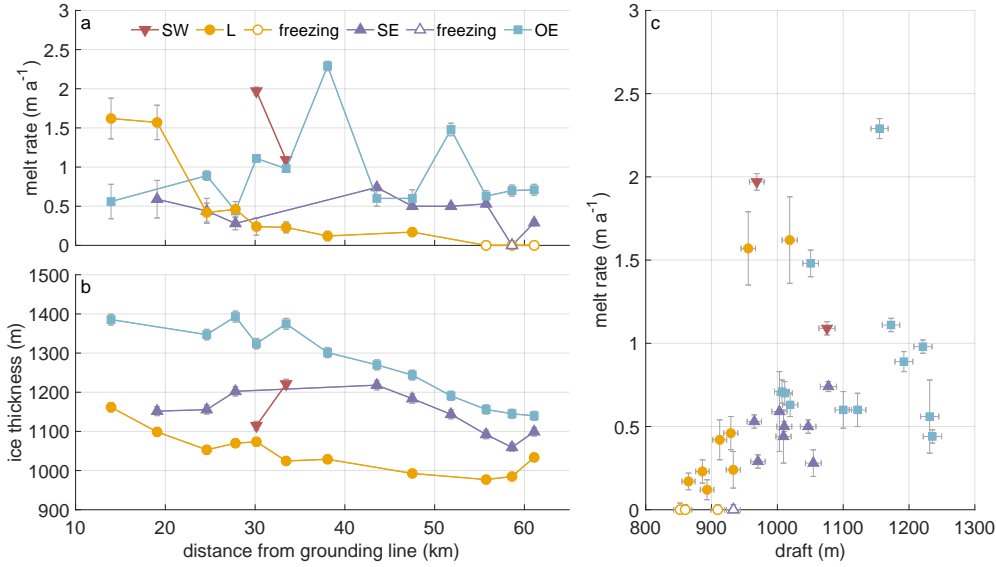


Figure 10.2: Spatial distribution of pRES-derived (a) basal melt rates (positive a_b represents melting) and (b) ice thickness at the locations SW (red), L (yellow), SE (purple) and OE (blue) around the channel as a function of distance from the grounding line. (c) Melt rate as a function of ice draft obtained from pRES-derived ice thickness and h_{TDX} . Uncertainties are shown by gray error bars.

from the grounding line on. The change in ice thickness due to firn compaction and accumulation is close to zero in the entire study area (Fig. 10.10).

However, the measurements only show a snapshot, as the variability on longer time scales is unknown. Based on the interpolated melt rates, ΔH_ε and ΔH_s along the channel (solid lines in Fig. 10.3a and 10.10), we computed the advected ice thickness under present day climate conditions H_{PDadv} (solid lines in Fig. 10.3b). The comparison of H_{PDadv} with the measured ice thickness (dashed lines) shows large differences of up to 185 m above the channel. While the observed ice thickness decreases rapidly above the channel, H_{PDadv} remains almost constant. In contrast, no significant differences between the observed ice thickness and H_{PDadv} can be identified outside the channel. If the present day melt rates were representative for a longer period of time, the channel would be closed within 250 years, as the difference in H_{PDadv} above and outside the channel reaches zero. However, since the channel still exists beyond the northern end of our study area, it can be concluded that the melt rates in the channel must have been higher in the past. How large the melt rates must have been on average can be deduced from the reconstruction of the existing ice thickness. The resulting synthetic average melt rate in the channel is about twice as high as the observed ones, reaching 3.5 m a^{-1} in the upstream area (yellow dashed line in Fig. 10.3a). Assuming a steady state ice thickness upstream of the study area (supported by low elevation change found in (Helm et al., 2014)) and constant vertical strain and accumu-

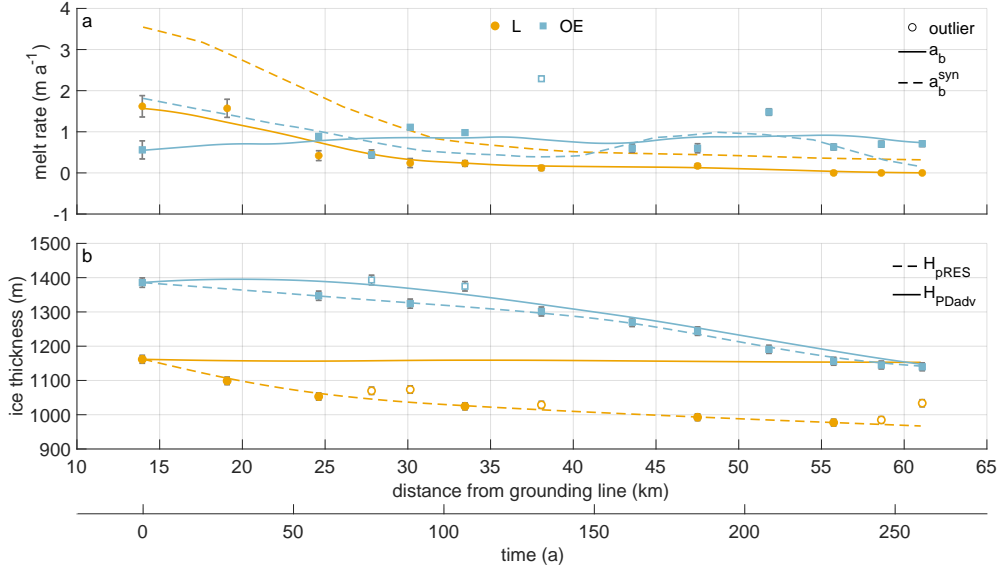


Figure 10.3: (a) Melt rates at locations L (yellow) and OE (blue) are shown by dots (L) and squares (OE). The interpolated melt rates (a_b) are shown by solid lines and synthetic melt rates (a_b^{syn}) that are necessary to reproduce H_{pRES} at L and OE are shown by dashed lines. (b) Ice thickness at locations L (yellow) and OE (blue) are shown by dots (L) and squares (OE). The interpolated ice thicknesses (H_{pRES}) are shown by dashed lines and the advected ice thicknesses under present day climate conditions (H_{pDadv}) from the observed melt rates at L and OE are shown by solid lines. The two x-axes show the distance from the grounding line in kilometers and the duration of ice flow in years from the measurement location furthest upstream. Unconsidered observations were marked as outliers. Error bars mark the uncertainties of the pRES-derived values.

lation in the past, this indicates that melt rates in the last 250 years have been significantly higher than observed now.

In addition to the observations we have presented in this section, we also conducted measurements of the vertical profile of the vertical displacement, that we present below together with simulations.

Time series of basal melting

The ApRES time series outside the melt channel reveals an average melt rate of 0.23 m a^{-1} (Fig. 10.4a). A look at the monthly mean melt rates shows increased melt during the summer months (January, February and November, December) in comparison with the winter season. In these months the melt rates show values from more than 0.3 m a^{-1} up to 0.62 m a^{-1} . The unfiltered time series of the cumulative melt shows a tidal signal with amplitudes of $\sim 1 \text{ cm}$ within 12h around the low-pass filtered cumulative melt. The spectral analysis shows all main diurnal and semi-diurnal constituents, which is in accordance to the frequencies observed from the GPS station (Fig. 10.11). The analysis of melt events from the

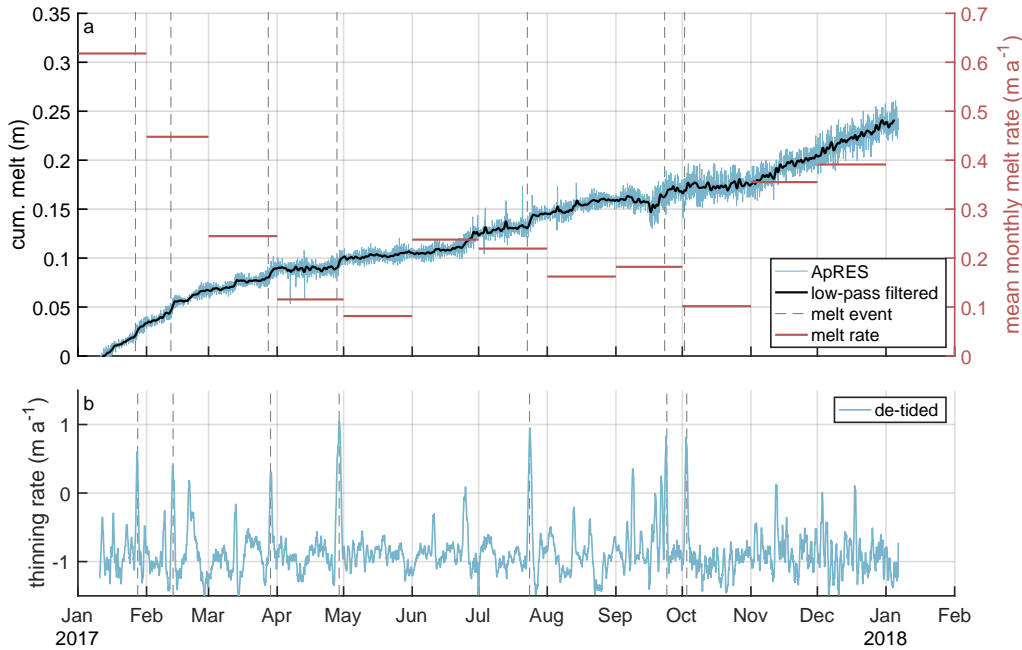


Figure 10.4: Time series of basal melting at ApRES location outside the channel. (a) Cumulative melt (blue line, left y-axis) over measurement period from 10 January 2017 to 6 January 2018 with low-pass filtered time series (black line). Monthly mean melt rates are shown by red lines on the right y-axis. (b) Thinning rate after subtracting of the tidal signal (blue line). The dashed gray lines in (a) and (b) mark stronger melt events.

de-tided thinning rate shows several melt anomalies distributed over the entire measurement period (Fig. 10.4a). These events lasted from a several hours to a few days and melted up to 1.5 cm of ice.

We found evidence for a clear accordance of the strain in the upper ice column with the tidal signal as recorded by GPS measurements. Unfortunately, we are lacking vertical strain in the lower column of the ice due to the noise, which permits to extract the temporal variation of basal melt rates on tidal time scales. As the tidal variation of $\Delta H/\Delta t$ is by far lower than the observed $\Delta H_\epsilon/\Delta t$, either deformation in the upper and lower parts compensates each other or basal melt/freeze takes this role. We can exclude freezing, as we do not find jumps in the amplitude of the basal return in the ApRES signal (Vaňková et al., 2021) over tidal time scales. Consequently, we infer that strain in the lower part compensates the one in the upper part and there is only a small variation of basal melt on tidal time scales.

As our location is close to two hinge zones, upstream and west of the melt channel, only a full three-dimensional model could shade light into the vertical strain in the lower part of the ice column. This is numerically costly for the required non-linear strain theory and not in reach. With melt channels being located (or initiated)

in the hinge zone, any kind of ApRES time series performed at ice columns with a thickness of more than 1000 m is affected by the unclear strain-depth profile in the lower part of the ice column. This may be overcome by a radar device with higher transmission power, that allows to detect the vertical displacement of layers down to the base. The observed tidal dependency of the vertical strain is consistent to the finding from other ApRES locations at the Filchner-Ronne Ice Shelf by [Vaňková et al. \(2020\)](#). They found the strongest dependency, even of the basal melt rate at some stations, on the semidiurnal (M_2) constituent. Beside depth-independent tidal vertical strain, ([Vaňková et al., 2020](#)) found tidal deformation from elastic bending at ApRES stations located near grounded ice.

10.3 Viscoelastic modeling

To obtain a more profound understanding of the evolution of the channel, we conduct transient simulations and analyze the change in geometry of a 2D cross-sections over time, as well as the simulated strain-field. The simulations are forced with the basal melt rates (both interpolated and synthetic) obtained in this study (Fig. 10.3). We transform distance to time in along flow direction of the ice shelf (Fig. 10.1) using present day velocities. This enables us to study under which conditions the channel is stable or vanishes.

Ideally, we would have observations of ice geometry and basal melt rates from the transition from inland onward, but our first cross-section with observations is located 14 km downstream of the grounding line (Fig. 10.1). The initial elastic response of the grounded ice becoming afloat had faded away. Further elastic contributions to the deformation originates from in-situ melt at the base and accumulation at the surface. To initialize our simulations adequately, we therefore conduct a spin-up.

10.3.1 Model

The model comprises non-linear strain theory accounting for finite deformations, as there is no justification to expect a priori the deformation to be small for simulation times of more than 200 a (e.g. [Haupt, 2002](#)). We treat the ice as a viscoelastic fluid and solve the system of equations for displacements using the commercial finite element software COMSOL ([Christmann et al., 2019](#)).

The constitutive relation corresponds to a Maxwell material with an elastic response on short time scales and viscous response on long time scales. For homogeneous, isotropic ice, two elastic material parameters exist (Young's modulus and Poisson's ratio). We conduct all viscoelastic simulations with commonly used val-

ues for ice for Young’s modulus of 1 GPa and Poisson’s ratio of 0.325 (Christmann et al., 2019). Another material parameter of the viscoelastic Maxwell material is the viscosity. It controls the viscous flow of ice. We use a constant viscosity of 5×10^{15} Pa s and discuss the influence of this material parameter later on. This constant viscosity is at the upper limit of the viscosity distribution derived by an inversion of the rate factor in the floating part of Filchner-Ronne Ice Shelf (Appendix Sec. 10.6.2 and Fig. 10.12). This inversion has been conducted using the Ice Sheet and Sea-Level System Model (ISSM) (Larour et al., 2012) in higher-order Blatter-Pattyn approximation (Blatter, 1995; Pattyn, 2003), Bed-Machine geometry (Morlighem et al., 2020) and the velocity field of (Mouginot et al., 2019a,b). It was further supported by a temperature field presented in (Eisen et al., 2020), based on the geothermal heat flux of (Martos et al., 2017).

The model geometry represents a cross-section through the melt channel (Fig. 10.5) with the x -direction being across channel and resembling the seismic IV profile (Fig. 10.1). By assuming plane strain, it is virtually infinite in the y -direction. The computational domain is discretized by an unstructured mesh using prisms with a triangular basis involving a refined resolution near the channel. We use the direct MUMPS solver and backward differentiation formula with automatic time step control and quadratic Lagrange polynomials as shape functions for the displacements. The viscous strain is an additional internal variable in the Maxwell model and we use shape functions of linear discontinuous Lagrange type to save computational effort. In some cases, the geometry evolution leads to degraded mesh elements, which requires automated remeshing from time to time.

In this study, the ice density is 910 kg m^{-3} and the seawater density is 1028 kg m^{-3} . At the upper and lower boundaries, we apply stress boundary conditions: for the ice-ocean interface, a traction boundary condition specifies the water pressure by a Robin-type condition. The ice-atmosphere interface is traction-free. Laterally, we apply displacement boundary conditions. As we take a plane strain approach, we can neglect deformation in the downstream direction. To obtain reasonable lateral boundary conditions, we transfer observed vertical strain and hence, vertical displacements, in horizontal displacements assuming incompressibility

$$\varepsilon_{zz} = -(\varepsilon_{xx} + \varepsilon_{yy}), \quad (10.9)$$

so that u_x becomes

$$u_x = \frac{(\varepsilon_{xx} + \varepsilon_{yy})W}{2}, \quad (10.10)$$

with W the width of the simulated cross-section (Fig. 10.5). We assume that the horizontal displacements are constant in vertical direction at lateral boundaries, resulting in a compression or elongation perpendicular to the channel

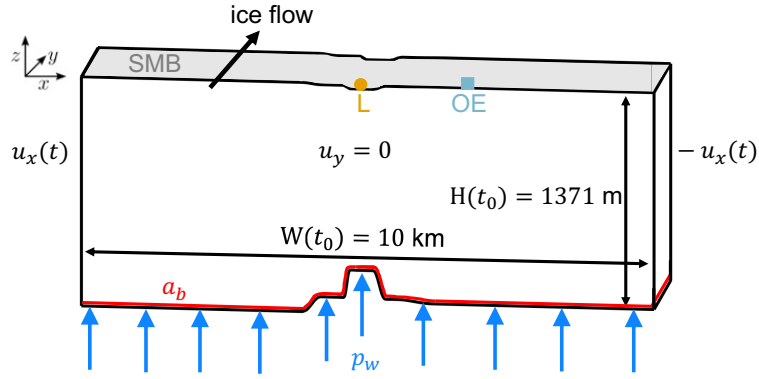


Figure 10.5: The cross-section of the model geometry at the end of the spin-up (t_0) of the first experiment shows its corresponding width and ice thickness outside east. The boundary conditions of the viscoelastic model are the water pressure p_w acting perpendicular to the ice base, the displacement in the flow direction u_y , which is zero due to plane strain assumptions, and the time-dependent displacement $u_x(t)$ acting in the lateral direction derived by pRES observations. The locations of the pRES station at the lowest point (L) of the channel and outside east (OE) are shown at their position on the surface in addition to the SMB (mass increase) and the melt rate a_b (mass decrease) at the base of the geometry.

(Fig. 10.13a).

The climate forcing consists of the SMB and basal melt rate. Technically, both are applied by changing the geometry of the reference configuration with the respective cumulative quantities (Fig. 10.13b,c). For the SMB, we used multi-year mean RACMO2.3 data (van Wessem et al., 2014) ranging from 0.15 to 0.17 m a⁻¹ for a density of 910 kg m⁻³, that we slightly modified to account for the surface depression over the channel: accumulation measurements at the pRES locations indicated higher accumulation in the channel than outside by a factor of roughly 1.5. Thus, we used 50% higher accumulation rates above the basal channel and a smooth cosine-shaped transition in x -direction. A crucial forcing is of course the basal melt rate. Here we conduct individual experiments that are based on our observed melt rates and its variations. As this data is spatially sparse, we need to interpolate those values in across-channel (x) direction. To this end, we assume a smooth cosine-shaped transition.

As we conduct Lagrangian experiments, distance equals time. We define $t_0 = 0$ a at the pRES measurements furthest upstream (Fig. 10.1) that is also the location of the seismic observations by Hofstede et al. (2021a,b). To evaluate our simulations, we compare the simulated surface topography and ice thickness, as well as $u_z(z)$ with the observed one.

We performed a spin-up to avoid model shocks, introduced by the transient behavior of a Maxwell material, that could be falsely interpreted as the response.

The main goal is here is to have the geometry after spin-up fit reasonably to the geometry measured at the seismic IV line (see Fig. 10.1) that we denote as time t_0 . The spin-up covers 75 a, which corresponds to the time from the grounding line to that profile under present day flow speeds. To this end, we take a constant melt rate equal to the melt rate at t_0 and adjust the geometry at the grounding line to match the geometry at t_0 of the seismic IV profile reasonably well. After the spin-up, the width $W(t_0)$ of the simulated geometry is 10 km. With this procedure an initial elastic deformation at the beginning of the transient simulation vanished and the viscoelastic geometry evolution of the melt channel can be evaluated for different melt scenarios.

Short-term forces like the time-varying climate forcing as well as the lateral extension or compression demand the usage of a viscoelastic instead of a viscous model to simulate the temporal evolution of the basal channel. We conduct a series of simulations with different material parameters and identify the best match of observed and simulated ice thickness above (L) and outside east (OE) of the channel. At these two positions most of the pRES measurements were done and the distribution of the melt rates gives an adequate basis to force the model. Due to the sparsity of observations at the western side, we apply a forcing in the model based only on melt rates at L and OE.

In a first experiment, we use an interpolation of the observed melt rates as forcing and compare the results with H_{PDadv} (solid lines in Fig. 10.3). The second experiment aims to derive the best match between simulated and observed geometry. For this experiment, we use synthetic melt rates (dashed lines in Fig. 10.3a).

10.3.2 Results and discussion of simulations

First experiment: pRES-derived melt rate

The spin-up for this experiment is starts with a manually adjusted geometry (including the channel at the base) for $t = -75$ a to fit seismic IV profile for t_0 at the base. We applied a constant melt rate of 1.5 m a^{-1} at L and 0.5 m a^{-1} at OE. This forcing enlarges the melt channel during the spin-up as the ice thickness OE increases due to the prescribed displacement at the lateral boundaries. The general shape of the base matches the seismic profile IV reasonably well (Fig. 10.1 and Fig. 10.14). In the experiment, we force the base with a_b (solid line in Fig. 10.3a).

The results of this experiment are displayed in Fig. 10.6. For both locations, L and OE, the simulated and observed geometry differ significantly. While the simulated ice thickness above the channel only declines by 21 m or 1.7% in 250 a, the observed one is a factor of 9, or 191 m thinner. However, the simulated trend

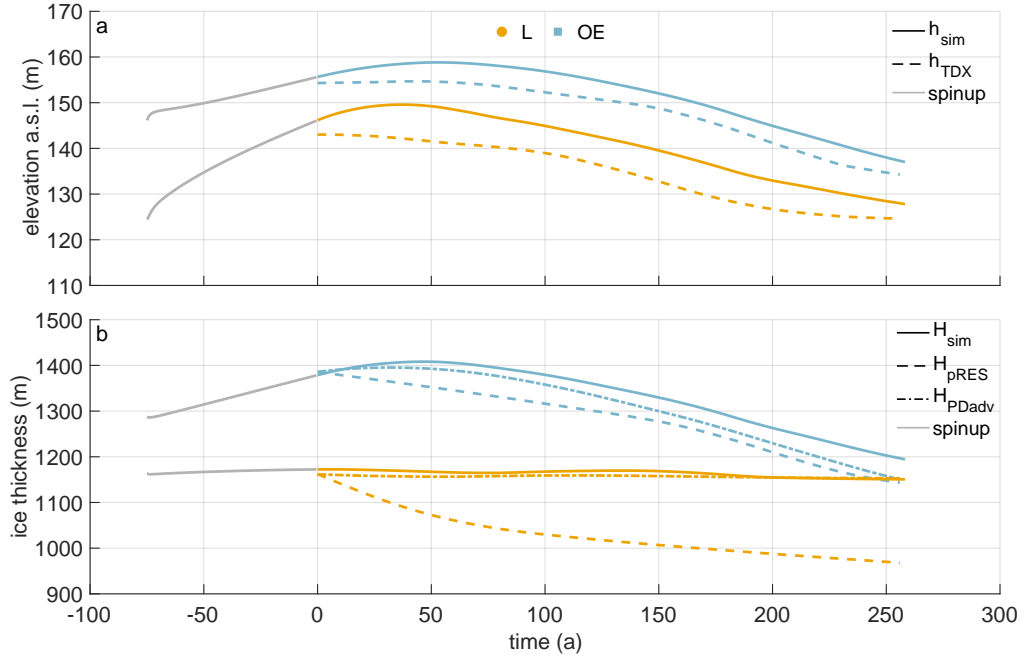


Figure 10.6: First experiment: Simulated surface elevation (a) and ice thickness (b) using the pRES-derived melt rate. Colors denote quantities above the channel (yellow) and outside the channel (blue). (a) Simulated surface elevation h_{sim} (solid lines) and observed h_{TDX} (dashed lines). (b) Simulated ice thickness H_{sim} (solid lines), under present day climate conditions advected H_{PDadv} (dashed-dotted lines) and observed H_{pRES} (dashed lines). Gray lines represent the spin-up.

outside the channel shows thinning. This thinning sets in after 50 a, whereas we find continuous thinning in the observations. This delayed onset of thinning is also represented in the simulated surface topography. Most notably is the match between simulated H_{sim} and advected H_{PDadv} ice thickness under present day climate conditions at L. This match confirms that present day melt rates would not lead to the observed channel evolution over 250 a.

Second experiment: Synthetic melt rate

The spin-up for the second experiment also starts with a geometry that has been manually adjusted for $t = -75$ a to fit seismic IV profile for t_0 at the base. In the second simulation experiment, we force the base with the synthetic melt rate (Fig. 10.3a). Again, the melt rate has been kept constant over the spin-up with $a_b^{\text{syn}}(t_0)$. By disregarding the additional melt of the spin-up, the synthetic melt rate leads to a cumulative melt after 250 a of 290 m (Fig. 10.13a). With that 184 m more ice is melted at L than in the first experiment.

The modeled geometry of this experiment is presented in Fig. 10.7. The simulated ice thickness at L is in very good agreement with H_{pRES} . There is some mismatch at OE, but the simulated trend of thinning is synchronous to the observation.

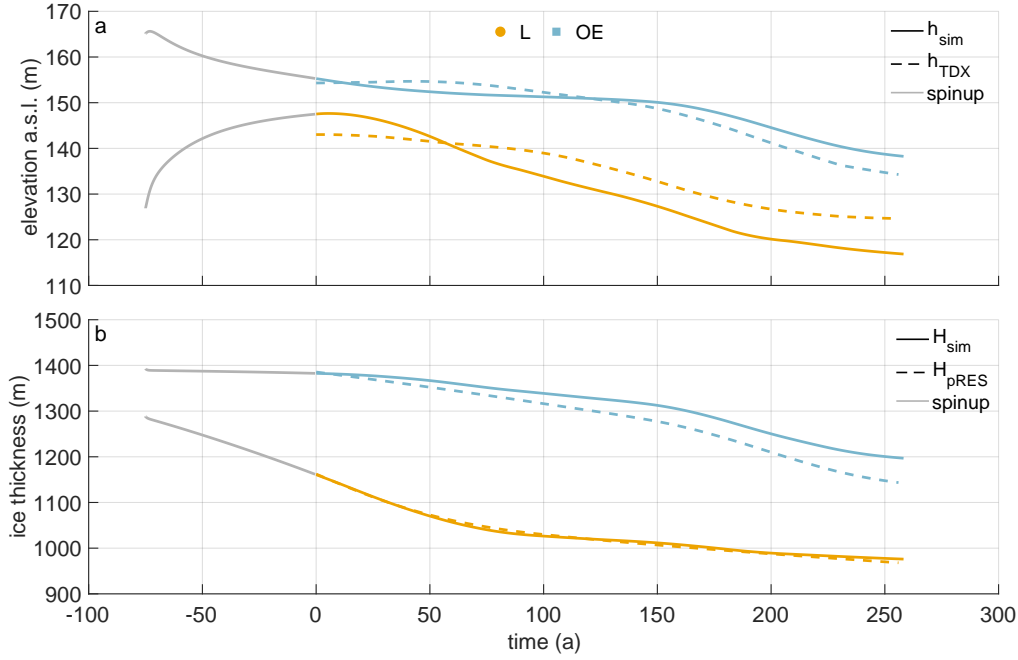


Figure 10.7: Second experiment: simulated surface elevation (a) and ice thickness (b) using the synthetic melt rate. Colors denote quantities above the channel (yellow) and outside the channel (blue). (a) Simulated surface elevation h_{sim} (solid lines) and observed h_{TDX} (dashed lines). (b) Simulated ice thickness H_{sim} (solid lines) and observed H_{pRES} (dashed lines). Gray lines represent the spin-up.

After 250 a the deviation from the observed ice thickness at OE reaches 53 m. The simulated evolution of the base for the second experiment shows a persistent basal channel (Fig. 10.15). The mismatch of the surface elevation at L and OE is reversing over time: while the simulated surface topography at OE is first too low, it is too high in the second half of the transient simulation (Fig. 10.7). However, the trend of the observed h_{TDX} and simulated h_{sim} elevation behave similarly. Above the channel, the surface elevation is first overestimated by 4 m at the end of the spin-up. After 57 a, it turns from an over- to underestimation that results in an 8 m lower h_{sim} than the observed h_{TDX} after 250 a. To assess if the ice is in buoyancy equilibrium, we compute the freeboard at the position L for an ice density of 910 kg m^{-3} . The surface elevation is 133 m at t_0 and decreases to 112 m after 250 a. Although h_{TDX} is larger than this, the ice is approaching flotation in downstream direction. One could take another approach and estimate the mean density under the assumption of buoyancy equilibrium: at t_0 this corresponds to 901 kg m^{-3} and after 250 a to 896 kg m^{-3} . As more ice is melted from below and with higher snow accumulation at L, the density decreases, which is to be expected.

After 250 a, the simulated freeboard at OE is 1 m higher than the surface elevation of 138 m inferred by buoyancy equilibrium using an ice density of 910 kg m^{-3} .

Similar considerations regarding OE lead to a 3 m higher h_{TDX} than 132 m out of buoyancy equilibrium. Overall, we see convergence to equilibrium state at OE and the simulated surface elevation at L. At the end of the simulation, only h_{TDX} above the channel does not reach buoyancy equilibrium, which leads to the justifiable assumption that the mean ice density at L is lower than OE.

At the position of the furthest upstream pRES observations we can see from the seismic IV profile that the influence of the grounding line has not completely vanished. The assumption of buoyant equilibrium is therefore likely to be flawed. At the end of the simulation, the geometry should be close to buoyancy equilibrium despite melting and a 50% higher SMB at L than OE. Hence, simulations carried out using a higher SMB within the channel would result in better agreement with the observed values of h_{TDX} .

Next, we exploit the variation of the vertical displacement over depth. The results are presented in Fig. 10.8. For this purpose, we calculated the cumulative vertical displacement in one year over depth. For comparability, the vertical displacements due to accumulation and snow compaction were removed from the observed distributions.

Most notably, we move from a vertically extensive regime into a compressive by increasing distance to the grounding line. Given the complexity of the problem, the simulations show a reasonable agreement with the observations. The best match is reached at OE, which is not that surprising. The generally good agreement of the simulated displacements outside the channel comes from tuning u_x at the lateral boundary to match u_z from the pRES measurements at OE. Both simulated and observed vertical displacement distributions show that the strain decreases from L to OE. The only exception here is $t = 57$ a, where the vertical strain at SE is larger than the one at L. While at 0 a and 26 a the deviation of the simulated displacements between L and OE is small, it increases afterwards. From 105 a, the simulated vertical displacements agree very well with those of the pRES-measurements, where a displacement distribution was derivable at L and OE. The same comparison for the first experiment (Fig. 10.16) shows similar results, with significantly less pronounced differences between L and OE. Hence, the mismatch to the observed vertical displacements for this experiment using the measured melt rates is higher than for the second experiment with the synthetic melt rates. The simulated strain evolution of the cross-section confirms that the viscoelastic model needs to account for finite deformation as the strain exceeds 10% (Fig. 10.17).

As the last point of this second experiment, we consider the influence of the viscosity on the evolution of the melt channel (Fig. 10.18). To reach the ice

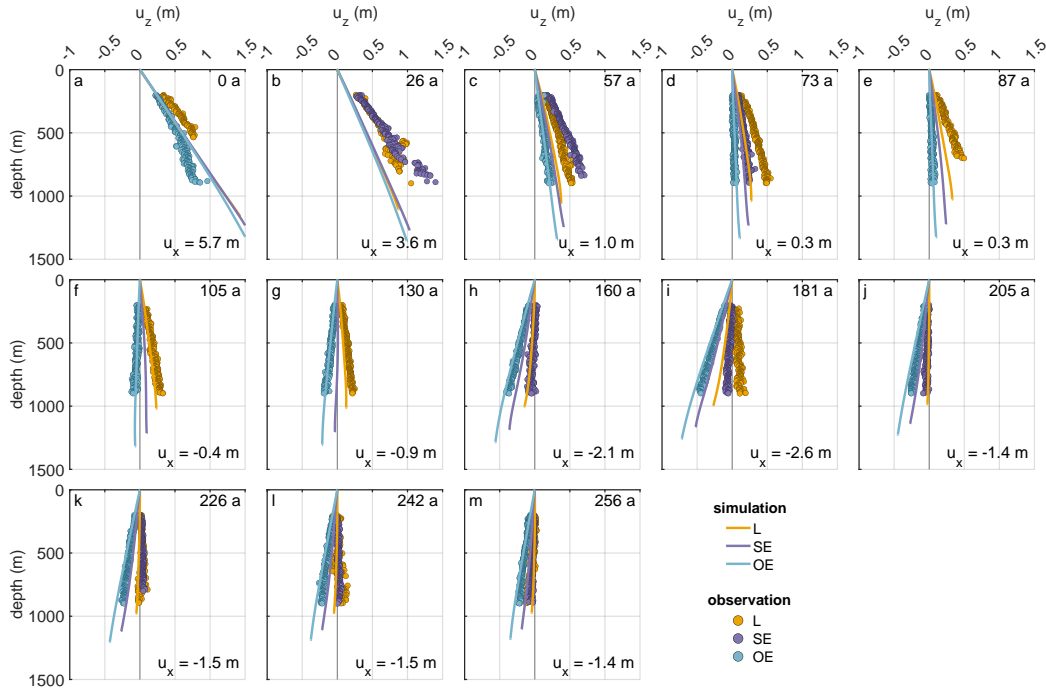


Figure 10.8: Second experiment: comparison of displacements (u_z) derived from observations (dots) and the simulations (lines). The different panels show the displacement for $\Delta t = 1$ a allocated to the simulation time (number in the upper right corner). The numbers in the lower right corners give horizontal displacement u_x derived from ε_{zz} of the pRES measurements outside the channel (OE) with positive values representing compression and negative values extension.

thickness of seismic IV, the simulation applying the smallest viscosity needs a higher initial channel and hence, less ice thickness at L at the beginning of the spin-up (Appendix Sec. 10.6.2). The channel thickness of the pRES-measurement is modeled best using a viscosity of 5×10^{15} Pa s. A two times higher viscosity leads to an ice thickness in the channel that is 42 m smaller after 250 a, while a five times lower viscosity results in 116 m thicker ice above the channel due to more viscous flow into the channel. The simulated ice thickness OE is similar for all three different viscosities.

10.4 Discussion

Melt rates inside the channel are in general rather moderate $< 2 \text{ m a}^{-1}$. For comparison values retrieved at a channel 1.7 km from the grounding line of the Ross Ice Shelf at Mercer Whillans ice streams inflow were 22.2 m a^{-1} (Marsh et al., 2016). At the Ross Ice Shelf, the values dropped to below 4 m a^{-1} over a distance of 10 km and reached 2.5 m a^{-1} after 40 km. We also find a factor of five lower values in the center of the channel over a distance of 11 km, however, this takes

place between 14 and 25 km downstream the grounding line. However, at about the same distance, we find a peak in basal melt rate of 2.3 m a^{-1} (Figs. 10.1 and 10.2) at OE. Interestingly enough, this location corresponds to a steep basal topography in the seismic profiles I and V, indicating that we might have not been entirely outside the channel at this spot, but potentially at a steep flank. At the Ross Ice Shelf, the ratio between inside the channel and 1 km outside is about 27, whereas we find only a factor of 3, with a distance between L and OE being 1.8 km. Zeising et al. (2021f) presented pRES-derived basal melt rates downstream of our study area. Roughly 40 km downstream the northernmost cross-section ($\sim 200 \text{ a}$ of ice flow), these measurements show that the channel still exists, but with a small height of $\sim 16 \text{ m}$. Inside the channel, Zeising et al. (2021f) determined a melt rate of 0.25 m a^{-1} and outside 0.41 m a^{-1} . The larger melt rates outside the channel compared to inside is in agreement with the finding of our study. In general, the channel height declines, so the channel fades out. The channel diminishes by melt rates inside the channel falling below those outside the channel. The trend in vertical strain has only a minor contribution to this evolution. We thus do not find any evidence that such channels are a cause for instabilities of ice shelves as suggested by Dow et al. (2018).

One of the main findings of our study is that the present geometry can only be formed with considerable higher melt rates in the past (see Fig. 10.3). This finding is based on the assumption that the strain-rates were in the past similar to present day. This is justified, as significant changes in strain would require a change in the system that would cause other characteristics to change, like the main flow direction, for which we do not find any indication.

The pRES melt rate observations covered only one year. As the ocean conditions within the sub-ice shelf cavity are known to respond to the ocean forcing from the ice front (e.g. Nicholls, 1997), they would expect to be subject to significant inter-annual variability. Underlying any interannual variability, a long-term reduction in basal melt rates would be the expected response to a reduction in production of dense shelf waters north of the ice front, resulting from a reduction in sea ice formation (Nicholls, 1997), resulting in turn from a reduction in the southerly winds that blow freshly produced sea ice to the north.

A decrease in northward motion of sea ice has been observed in the satellite record (e.g. Holland and Kwok, 2012), and modeling experiments by Naughten et al. (2021) find decreasing basal melt rates. This reduction is therefore consistent with higher basal melt rates in the past. However, our model results suggest that the mismatch between the past melt rates needed to explain the observed channel geometry and those that were observed applies only to the channel, and not to the ambient ice. This could be explained by historically higher levels of

subglacial outflow at the grounding line, or anomalously low levels during the observation period. Subglacial outflow contributes to the buoyant flow up the basal slope and therefore the shear-induced turbulence that raises warm water from deeper in the water column towards the ice base. [Smith et al. \(2009\)](#) found an active subglacial lake at the transition between Academy Glacier and SFG, and also [Humbert et al. \(2018\)](#) suggest in the upstream area of SFG a subglacial lake.

[Hofstede et al. \(2021a\)](#) showed that the subglacial channel appears 7 km upstream of the grounding line increasing its height to 280 m at the grounding line. The location of the channel corresponds with increased subglacial flux found by [Humbert et al. \(2018\)](#) using a simple routing scheme. The channel formed on the grounded part is most likely the source of a grounding line fan and thus carrying sediments, formed at the seabed under the basal channel [Hofstede et al. \(2021a\)](#). Once this topographic feature reaches the ocean, it will focus on the relatively buoyant flow and enhance shear-driven vertical mixing, bringing heat and salt to the ice base leading to higher basal melt rates.

However, with increasing distance along the channel, the basal gradient, and therefore the speed of the buoyant flow, reduces, as does the entrainment of warm water from beneath. Coupled with the increasing pressure freezing point at the ice base this leads to a gradual reduction of the melt rate in the channel. From [Fig. 10.2a](#), the melt rate in the channel reduces below that of the ambient ice base by about 30 km distance from the grounding line, suggesting that the effect of basal melting thereafter is to suppress the channel. The cause of the strong melt anomalies identified in the ApRES measurements remains unclear as no direct ocean observation exists near SFG. However, the time scale of the events is consistent with the passage of warm cored eddies. Such features have been observed in the ocean cavity beneath the neighboring Ronne Ice Shelf ([Nicholls, 2018](#)).

The channel height is found to increase until 30–35 km downstream of the grounding line. Further downstream, the channel begins to close. Our modeling results show that less viscous ice (1×10^{15} Pa s) would tend to shut the channel faster than the rate we observe. For the best match between observed and modeled geometry, we need viscosities around 5×10^{15} Pa s of stiff ice to prevent the closure by deformation. This claim is also confirmed by the inversion of the viscosity to model observed surface velocities in the melt channel region ([Appendix Sec. 10.6.2](#)). With a viscosity of 5×10^{15} Pa s, we can simulate with a viscoelastic model the channel evolution in both experiments matching the observations: (i) pRES-derived melt rates result in an ice thickness fitting the present day advected ice thickness H_{PDadv} , (ii) synthetic melt rates lead to the observed ice thickness

H_{pRES} .

The difference in geometry change, due to different values of the viscosity, manifests stronger inside the channel than outside. This was to be expected because of the load situation resulting from the prescribed geometry (Fig. 10.18). The simulated geometry change is mainly due to the elastic response to thinning by basal melt and ice accumulation. Any purely viscous simulation would overrate the deformation. Higher melt rates were needed to compensate for this. [Wearing et al. \(2021\)](#) presents a full Stokes simulation of a comparable melt channel and indeed needs high melt rates to keep the channel open. It is important to keep this result in mind for (future) inverse modeling of melt rates in melt channels.

We find a difference (-4 m to 8 m) between simulated and observed surface elevation at L. The elevation difference is most likely caused by the constant density that we used for the simulations, as the ice thickness matches well. For the thinner ice above the channel, this could be achieved by an ice density decreasing from outside to inside and from upstream to downstream the channel. However, one has to keep in mind, that the accuracy of the surface elevation product is 5 m.

In general, we benefited highly from having measurements of vertical strain available. This opens new possibilities to identify weaknesses in the modeling and gave us useful insight into the spatial variation of the vertical strain across such a topographic feature. Although the pRES surveys only about half the ice thickness, the slope of $u_z(z)$ in the upper half is distinct for the positions L, SE and OE and greatly varies with distance from the grounding line, also influenced by the embayment of the ice shelf. Simulated u_z at L start to match only after about 100 a well with observations, which could result from the first few cross-sections still being influenced by the hinge zone. Tidal bending was not taken into account here, due to the 2D setting. This could in future be investigated, if repeated pRES measurements would be conducted up to the grounding line covering the entire hinge zone, in which it would also be extremely advantageous to obtain basal melt rates.

Our study demonstrates that viscoelastic simulations can be a useful but complex tool to analyze melt channel evolution. In an inverse approach, viscoelastic models could also give more insights into basal melt rates of channel systems of ice shelves in general, given that satellite-borne surface elevation is available in high resolution. However, the fact that large deformations require non-linear strain theory will make this a challenging endeavor. As changes in basal melt rates will inevitably lead to surface elevation changes of channel systems, systematic monitoring of the surface topography from space can serve as an early warning system and trigger further in-situ observation similar to this study.

10.5 Conclusions

We find basal melt rates in a melt channel and its surroundings on Filchner Ice Shelf to be up to 2.3 m a^{-1} . Basal melt rates inside the channel drop with distance down-flow, even turning into freezing 55 km downstream of the grounding line. Close to the grounding line, melt rates are larger inside the channel than outside, while further downstream this relationship reverses. Over distance along flow, the channel dimension decreases from a maximum height of 330 m to below 100 m. The channel diminishes because the reduced melt rate is unable to maintain the channel geometry against viscoelastic deformation. Analysis of the present day ice thickness advection revealed large differences compared to the observed ice thickness above the channel, which indicates that melt rates have been about twice as large in the last 250 a. The viscoelastic simulation confirms this statement and indicates that basal melt channels need high basal melt rates and relatively cold ice to persist. The deformation of the basal melt channel is mainly driven by the elastic response to the basal melt rate. The observed and simulated evolution of this melt channel demonstrates that melt channels of this kind are not a destabilizing element of ice shelves. The ApRES time series showed brief melt anomalies distributed over the entire measurement period and slightly increased melt rates in summer.

10.6 Appendix

10.6.1 Observations

Additional table

Table 10.1: Description of symbols

Symbol	Description
u_x	horizontal displacement in across flow
u_y	horizontal displacement in along flow
u_z	vertical displacement
ε_{xx}	horizontal strain in across flow
ε_{yy}	horizontal strain in along flow
ε_{zz}	vertical strain
$\overline{h_b}$	averaged depth of the ice base
h_{pc}	depth of the pore closure relative to surface
h_{nl}	noise-level depth limit relative to surface
h_{sim}	simulated surface elevation
h_{TDX}	TanDEM-X surface elevation
H	ice thickness
H_{pRES}	pRES derived ice thickness
H_{sim}	simulated ice thickness
H_{PDadv}	advection of the ice thickness under present day climate conditions
t	time
t_0	$t = 0$ a, defined at the most upstream pRES measurement location
t_1	1st measurement of ApRES time series
t_i	i-th measurement of ApRES time series
Δt	time period between repeated measurements
ΔH	change in ice thickness
ΔH_i	change in ice thickness below the depth of the pore close
ΔH_s	change in ice thickness at the surface and in the firn
ΔH_f	change in ice thickness due to firn compaction
ΔH_ε	change in ice thickness due strain
ΔH_b	change in ice thickness due to basal melt
a_b	basal melt rate
a_b^{syn}	synthetic basal melt rate
W	width of the cross-section in simulations

Additional figures

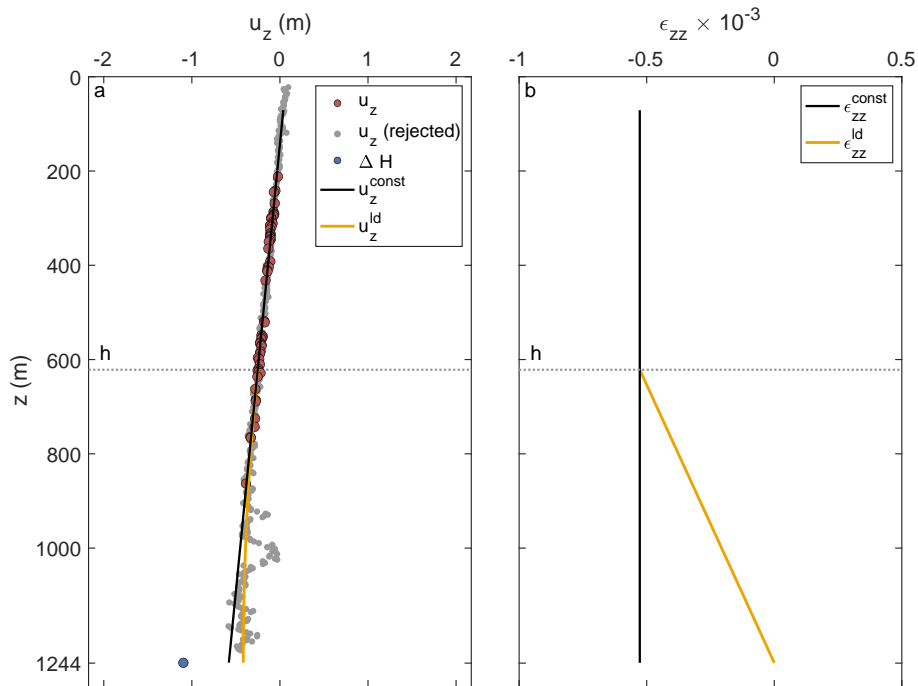


Figure 10.9: Strain analysis of an pRES measurement. (a) Derived vertical displacements u_z for $\Delta t = 1$ a of the ice base (ΔH ; blue dot) and internal layers (red and gray dots). Displacements used for the linear regression u_z^{const} (black line) are colored in red and rejected displacements are shown in gray. The second model u_z^{ld} with a linear decrease (ld) from depth h (dotted line) to zero at the ice base is shown in orange. (b) Vertical strain for $\Delta t = 1$ a of both models whose displacement is shown in (a).

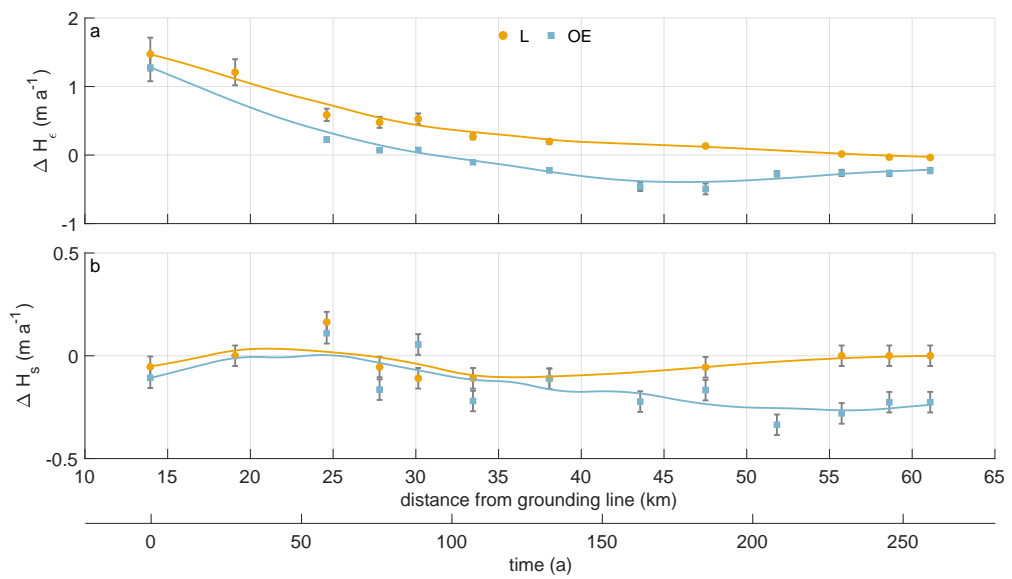


Figure 10.10: Distribution of pRES-derived (a) change in ice thickness due to strain and (b) ice thickness change due to surface process (firn compaction and accumulation) above the channel (yellow dots) and outside east of the channel (blue squares). The solid lines represent a smoothed fit. Error bars mark the uncertainties of the pRES-derived values.

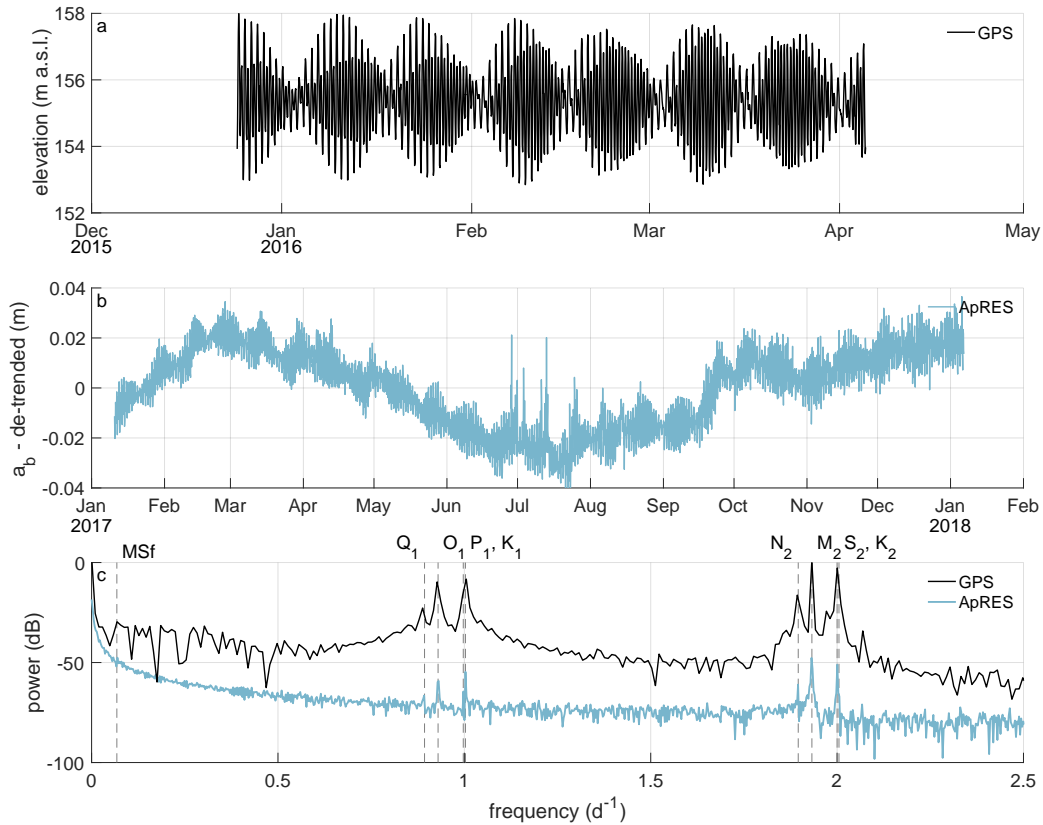


Figure 10.11: (a) Surface elevation recorded by the GPS station from end of December 2015 to early April 2016. (b) Linear de-trended basal melt rate (a_b) from ApRES observations between January 2017 and January 2018. (c) Frequency spectrum from data shown in (a) and (b). Vertical gray dashed lines mark the constituents with half day periods ($N_2 = 12.66$ h, $M_2 = 12.42$ h, $S_2 = 12.00$ h, $K_2 = 11.97$ h), daily periods ($Q_1 = 26.87$ h, $O_1 = 25.82$ h, $P_1 = 24.07$ h, $K_1 = 23.93$ h), and Fortnightly period ($MSf = 14.76$ d). Notice, due to a shorter measuring period of the GPS, the resolution in frequency space is lower than of the ApRES.

10.6.2 Modeling

Viscosity from inverse modeling

For estimating the viscosity distribution in the Filchner-Ronne Ice Shelf, we conduct a control-method inversion for the rheology parameter in the floating part. We use the Ice Sheet and Sea Level System Model (Larour et al., 2012) applied to the Filchner-Ronne Ice Shelf using the Blatter-Pattyn higher-order approximation (Blatter, 1995; Pattyn, 2003). The calculation is done on an unstructured finite element grid with a refined resolution of 2 km at the grounding line, in the shear margins as well as at other regions of faster ice flow. In the melt channel domain we further refine the resolution of the grid to 0.5 km.

To generate the geometry of the ice shelf the BedMachine Antarctica v2 data set is used (Morlighem et al., 2020; Morlighem, 2020). For the ice rigidity in the grounded region, as well as an initial guess of ice rigidity in the floating shelf, we assume the results of a long-term thermal spin-up also used in Eisen et al. (2020) based on the geothermal flux from Martos et al. (2017). We constrain ice surface velocities to fit the MEaSURES data set (Mouginot et al., 2019a,b).

Our optimization approach iteratively infers two parameters – the basal friction parameter in the grounded area and the ice rheology parameter in the floating area. For this purpose two cost functions are built. Each cost function consists of two data misfits, linear and logarithmic, as well as a Tikhonov regularization term:

$$J(\mathbf{v}, k) = \gamma_1 \int_S \frac{(v_x - v_x^{\text{obs}})^2 + (v_y - v_y^{\text{obs}})^2}{2} dS + \gamma_2 \int_S \left(\log \left(\frac{\|\mathbf{v}\| + \varepsilon}{\|\mathbf{v}^{\text{obs}}\| + \varepsilon} \right) \right)^2 dS + \gamma_t J_{\text{reg}} \quad (10.11)$$

The first term will be most sensitive to velocity observations in fast-flowing areas, the second term will be most sensitive to velocity observations in slow-flowing areas, while the third term penalizes oscillations in the optimization parameter. We performed an L-curve analysis to find suitable weights $\gamma_1, \gamma_2, \gamma_t$ for both cost functions. With this trade-off curve, we can make sure that we find a regularization term that fits the data well without overfitting noise. For the basal friction inversion, we found best weights $\gamma_1 = 1, \gamma_2 = 5 \times 10^{-6}$ and $\gamma_t = 1 \times 10^{-8}$, while for the ice rigidity inversion the optimal weights were $\gamma_1 = 1, \gamma_2 = 0.8$ and $\gamma_t = 4 \times 10^{-17}$.

We linearize and solve the optimization problem using the M1QN3 algorithm with an incomplete adjoint (Larour et al., 2012). For this inversion setting we apply a gradient relative convergence criterion $\epsilon_{\text{gttol}} = 10^{-6}$ and two points which are less than $\text{dxmin} = 10^{-4}$ from each other are considered identical. Besides we used a maximum number of iterations and function evaluations of 1000. We show our

best-fit results for ice viscosity in the region around the melt channel in Fig. 10.12. The range of the viscosity is between 5.0563×10^{13} and 2.6656×10^{15} Pa s.

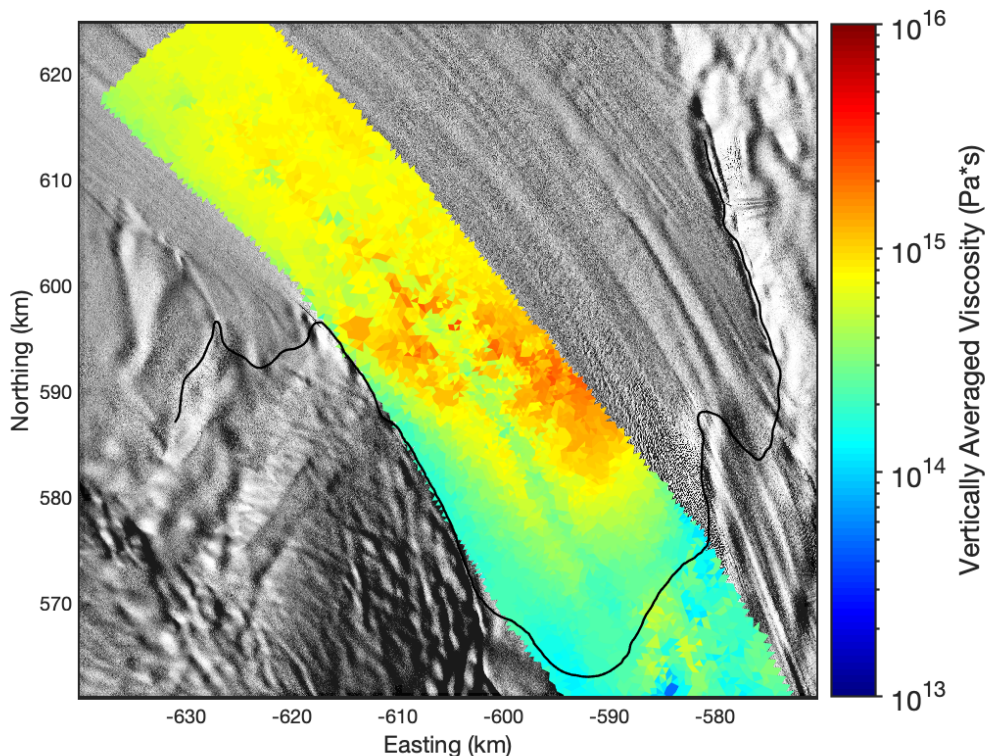


Figure 10.12: Ice viscosity in the melt channel area obtained from inverse modeling. The map extent is the same as in Fig. 10.1. The background image is a hillshade of the Reference Elevation Model of Antarctica (Howat et al., 2018, 2019).

Sensitivity of experiment 2 on viscosity

To capture the influence of the viscosity, different constant values (one smaller and one higher as in the second experiment) are investigated in a further experiment. The spin-up for each viscosity starts at $t = -75$ a with an arbitrary basal geometry that should fit seismic IV profile at the end of the spin-up (t_0). The melt rate $a_b^{\text{syn}}(t_0)$ is again assumed to be constant over the spin-up for all different viscosity values. We force the base with the synthetic melt rate (Fig. 10.3a), the same melt rate we already used in the second experiment. The initial base for the middle and high viscosity is nearly the same as 5×10^{15} Pa s is for ice a rather high value requiring cold ice (Fig. 10.18). For the smallest viscosity, a deeper channel at the beginning of the spin-up is needed.

Additional figures

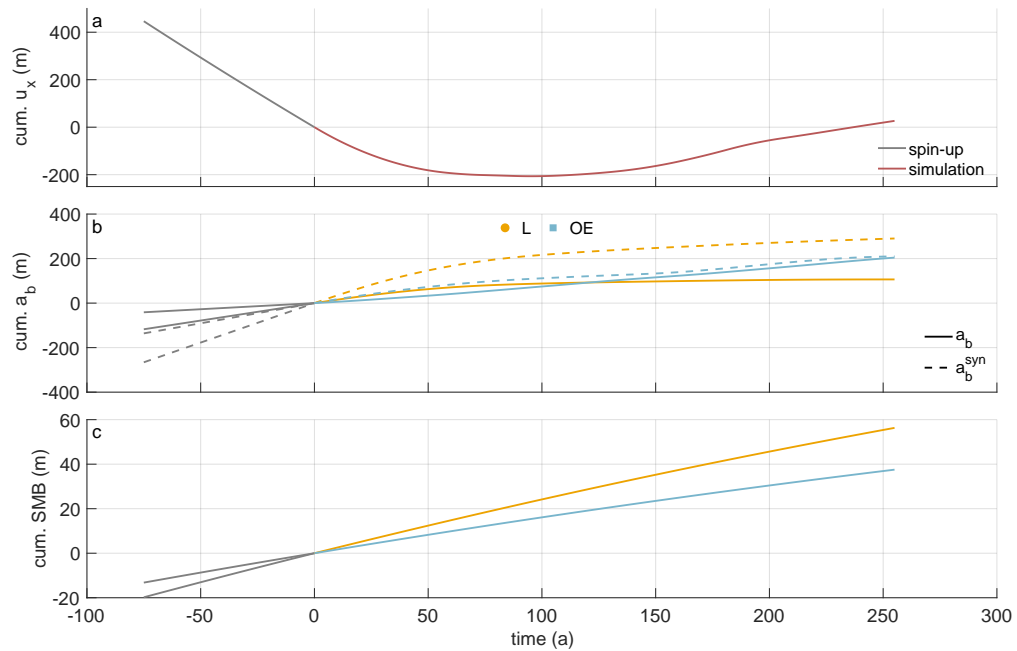


Figure 10.13: Model input derived from pRES measurements and RACMO (van Wessem et al., 2014). (a) Cumulative horizontal displacement calculated from pRES-derived vertical strain rates outside of the channel. (b) Cumulative basal melt rates above (yellow) and outside the channel (blue). Solid lines are derived from the pRES measurements and dashed lines are synthetic melt rates that are necessary to reproduce the measured ice thickness distribution. (c) Cumulative surface mass balance (SMB) derived from multi-year mean RACMO2.3 data (van Wessem et al., 2014) for a density of 910 kg m^{-3} outside the channel (blue) and above the channel (yellow), 50% larger. Gray lines represent values used in the spin-up and colored lines values used in the simulation of the evolution of the channel.

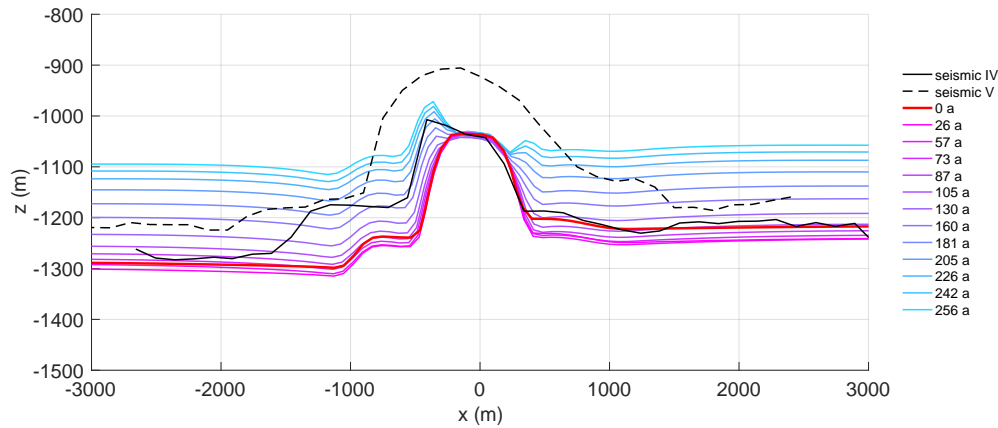


Figure 10.14: Evolution of the base for the first experiment applying pRES-derived melt rates in the viscoelastic simulation. The black curve shows seismic profile IV (Hofstede et al., 2021b) and the red line the simulated base after the spin-up. For each position of pRES observations, the simulated base is shown using a color distribution ranging from red (furthest upstream) to blue (furthest downstream). The dashed black line is the base of seismic profile V (Hofstede et al., 2021b) near the pRES observation fitting to 130 a

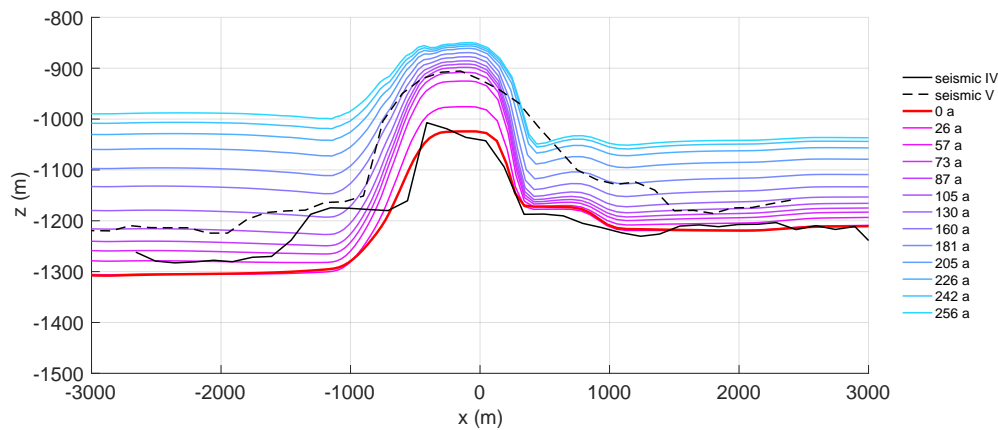


Figure 10.15: Evolution of the base for the second experiment applying synthetic melt rates in the viscoelastic simulation. The black curve shows seismic profile IV (Hofstede et al., 2021b) and the red line is the simulated base after the spin-up. For each position of pRES observations, the simulated base is shown using a color distribution ranging from red (furthest upstream) to blue (furthest downstream). The dashed black line is the base of seismic profile V (Hofstede et al., 2021b) near the pRES observation fitting to 130 a. The opening of the basal channel cannot be rebuilt with the model as the melt rate inside the channel is only applied to constant channel width. The basal channel stays open during the simulation time of 256 a.

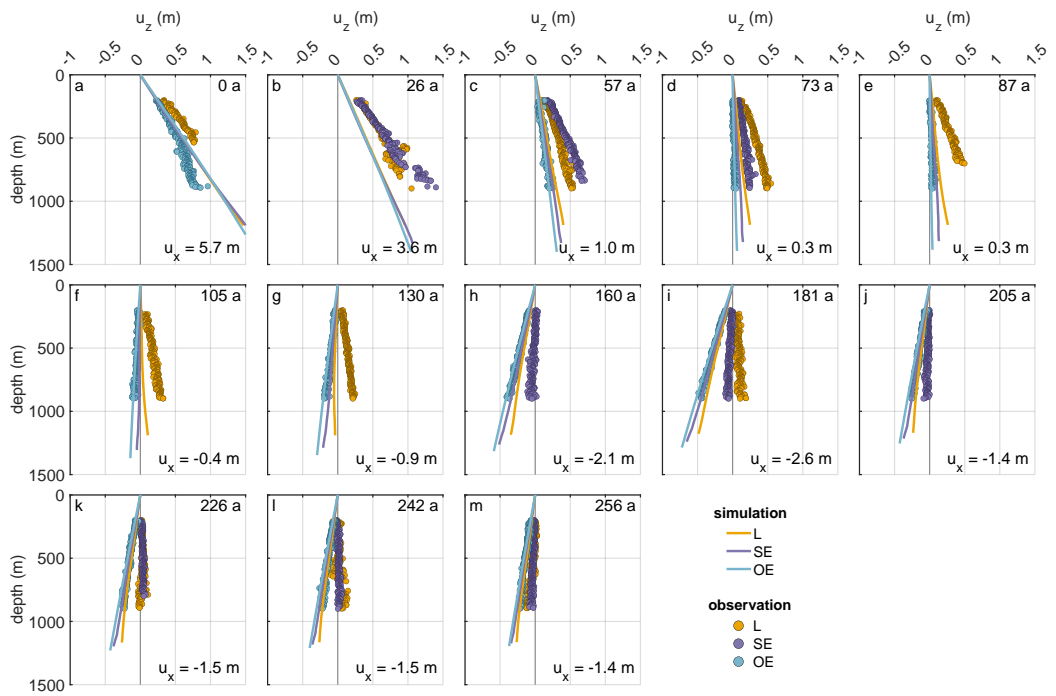


Figure 10.16: First experiment: comparison of displacements (u_z) derived from pRES measurements (dots) and from the simulations (lines). The different panels show the displacement for $\Delta t = 1$ a allocated to the year of the model (number in upper right corner). The numbers in the lower right corners give horizontal displacement u_x derived from ε_{zz} of the pRES measurements outside the channel (OE) with positive values representing compression and negative values extension.

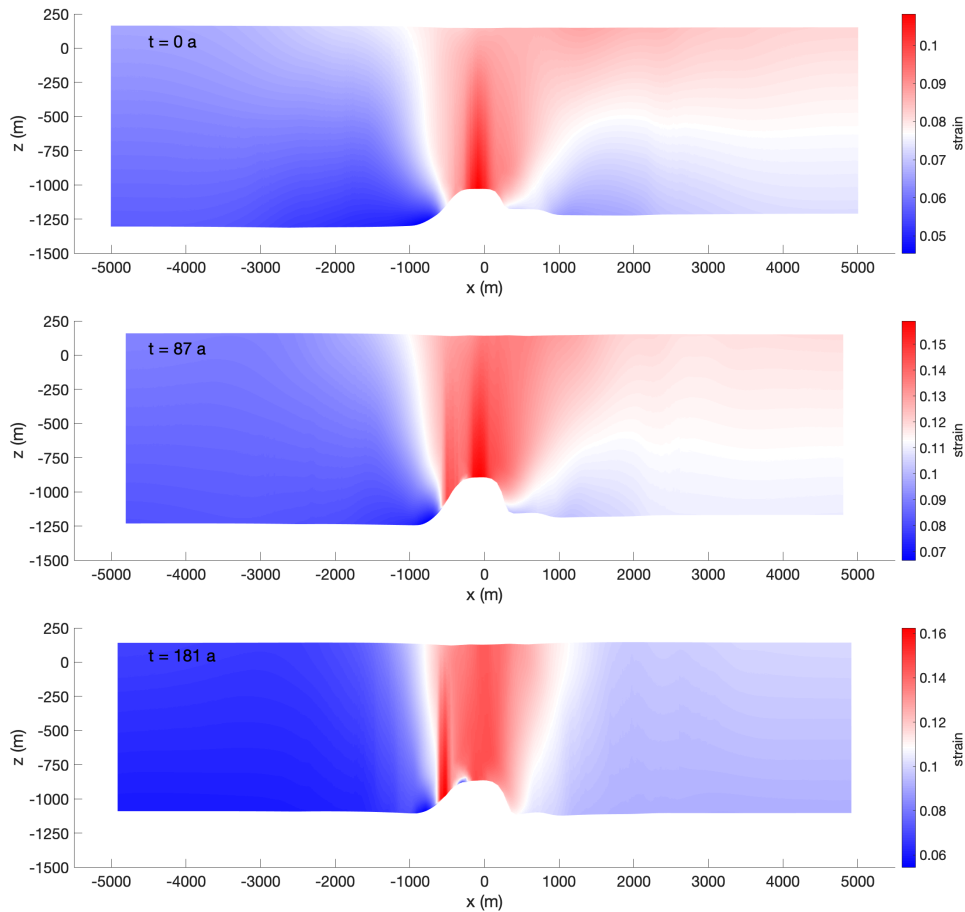


Figure 10.17: Simulated vertical strain of the current configuration of the second experiment using synthetic melt rates for (a) $t = 0$ a (after the spin-up, maximum lateral compression), (b) $t = 87$ a (small lateral displacement), (c) $t = 181$ a (maximum lateral extension). The white color shows the mean strain at each point in time. Bluish colors denote a strain deviation that is smaller than the mean value, while for the reddish areas the strain is higher. The highest strain occurs inside the channel caused by the viscous flow. The geometry variation caused by the melt rate counteract this ice flow and the basal channel persists. The maximum strain value increases from a to c through an increasing simulation time.

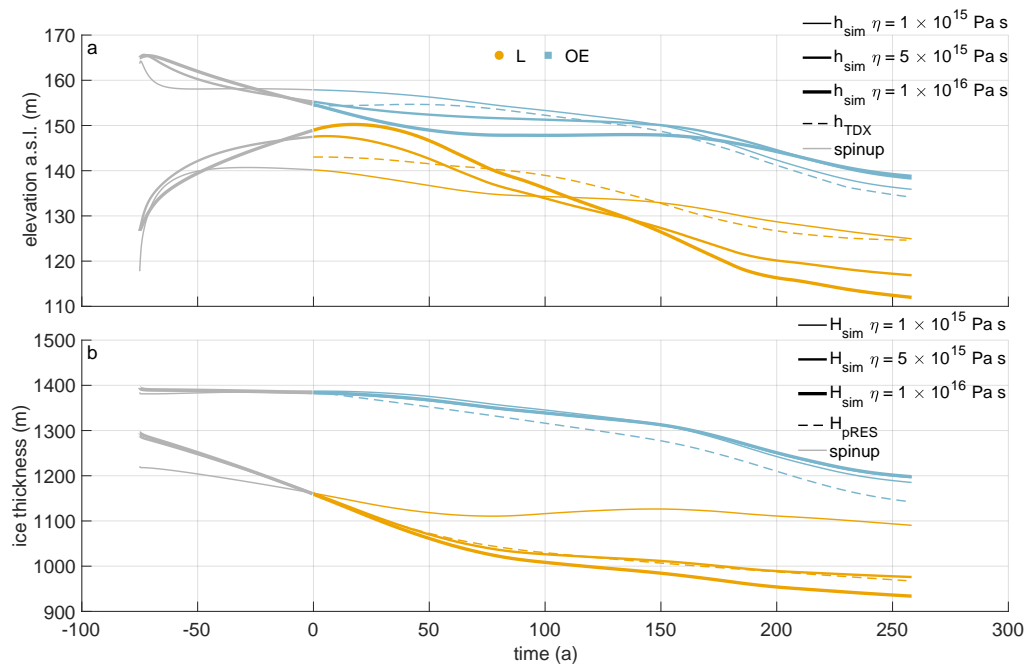


Figure 10.18: (a) Surface elevation above the channel (yellow) and outside the channel (blue) derived from the simulation (solid lines) and from TanDEM-X DLR (2020) (dashed lines). (b) Ice thickness above the channel (yellow) and outside the channel (blue) derived from the simulation (solid lines) and from pRES measurements (dashed lines). The thickness of the solid lines represents the different viscosities: 1×10^{15} Pa s (thin line), 5×10^{15} Pa s (medium line, same value as in the second experiment), 1×10^{16} Pa s (thick line). Gray lines represent values used in the spin-up and colored lines values used in the simulation of the evolution of the channel.

Data availability

Raw data of the ApRES time series (<https://doi.org/10.1594/PANGAEA.932413>; Zeising et al., 2021b) and processed GPS measurements (<https://doi.org/10.1594/PANGAEA.932441>; Zeising et al., 2021a) are available at the World Data Center PANGAEA. Raw data and derived products of the single-repeated pRES measurements and surface accumulation data at pRES locations are submitted to the World Data Center PANGAEA. The seismic data (<https://doi.org/10.1594/PANGAEA.932278>; Hofstede et al., 2021b) are available at the World Data Center PANGAEA. BedMachine Antarctica product can be accessed at <http://nsidc.org/data/nsidc-0756200> (Morlighem, 2020) (last access: 12 April 2021) MEaSURES velocity product can be accessed at <https://nsidc.org/data/nsidc-0754/versions/1> (Mouginot et al., 2019b) (last access: 13 April 2021).

Code availability

The mph file of the finite element software COMSOL Multiphysics (Version 5.6) of the viscoelastic finite deformation simulation used for this study is available via AWI's gitlab (<https://gitlab.awi.de/jchristm/viscoelastic-finite-defos-meltchannel>).

Acknowledgements

This work was funded by the AWI strategy fund project FISP. We acknowledge the support of BAS for the field campaign, in particular the support of the Graham Niven and Bradley Morell, who have been field assistants in the two expeditions. L.H. is funded through the Helmholtz School for Marine Data Science (MarDATA), Grant No. HIDSS-0005. Support for this work came from the UK Natural Environment Research Council large grant “Ice shelves in a warming world: Filchner Ice Shelf System” (NE/L013770/1).

Conclusion and outlook

This theses aims to quantify basal melting in key areas from phase-sensitive radar analysis and to enhance the understanding of processes driving changes in ice sheets and ice shelves by combining these measurements with other methodologies. These key areas are: (1) the Northeast Greenland Ice Stream (NEGIS), the largest ice stream in Greenland and its only remaining outlet glacier with a floating ice tongue, the Nioghalvfjærdsbræ (79°N Glacier, 79NG) and (2) the Filchner Ice Shelf (FIS), one of the largest ice shelves in Antarctica.

The NEGIS drains large parts of the Greenland Ice Sheet (GrIS) and therefore has the potential to contribute significantly to sea-level rise in the future. However, little is known about its formation and its dynamics. From autonomous phase-sensitive radar measurements at the EastGRIP drill site near the onset of the NEGIS, large melt rates of $0.19 \pm 0.04 \text{ m a}^{-1}$ were found. This indicates the presence of subglacial water at the base, which transports heat to the base and causes the high melt rates. Furthermore, it is assumed that subglacial water lubricates the ice base, enabling basal sliding and thus causing the formation of the ice stream far inland. In order to further explore the origin of this unique ice stream, a melt rate distribution at the onset of the NEGIS is required to infer the extent of increased heat fluxes and thus of the subglacial water system.

Measurements of the spatial distribution and temporal variability of basal melting on the 79NG show extremely high melt rates of up to 145 m a^{-1} in the vicinity of the grounding line. Airborne radar measurements and remote sensing-derived surface elevation also show large changes in ice thickness both upstream and downstream of the grounding line. In particular, these measurements reveal the growth of a large channel starting in 2010 and reaching a huge height of 490 m in 2018. The combination of these data indicates major changes in ice thickness caused by high basal melt rates, which can endanger the stability of the glacier in the future, even if it currently appears stable. These results confirm the need to continue monitoring changes occurring at 79NG and to measure melt rates in the future. The loss of the floating ice tongue of 79NG would accelerate the ice flow of the NEGIS, as it was the case after the collapse of the ice tongue of Zachariæ Isstrøm (ZI). This would result in greater mass loss of the GrIS and contribute to future sea-level rise.

In Antarctica, the FIS is threatened to be thinned out by warm ocean currents,

which leads to high basal melt rates (Hellmer et al., 2012). The analysis of an ApRES time series in the southern FIS near the grounding line of the Support Force Glacier (SFG) shows strong tidal fluctuations of the vertical strain and the occurrence of several melt events within the measurement period. However, melt rates in the study area are of moderate size, mostly $< 1 \text{ m a}^{-1}$. Larger melt rates of $> 2 \text{ m a}^{-1}$ were only present in the vicinity of a basal melt channel. A comprehensive analysis of the evolution of the melt channel by means of radar measurements and viscoelastic simulations revealed higher melt rates in the past of up to 3.5 m a^{-1} , which have led to present days geometry.

The in situ measurements outside the area of the channel show partly large differences to melt rates derived from satellite-remote sensing measurements. A detailed analysis shows that the reason for the differences is the ice flow velocity that was used to determine the strain rate for the remote sensing-derived melt rates. However, these differences can be overcome by using more accurate velocity products. Satellite-derived melt rates are of great importance because they allow the determination with good spatial and temporal resolution of all Antarctic ice shelves. Therefore, ice sheet/ocean models that simulate the future contribution of the Antarctic Ice Sheet (AIS) to sea-level rise use these products for the parametrisation of melt rates. An evaluation of the accuracy of remote-derived melt rates by means of in situ measurements at other locations will therefore be necessary in order to further improve the melt rate estimations.

The pRES device itself plays a central role in this thesis. It was designed in order to determine basal melt rates of ice shelves by measuring vertical displacements with high accuracy. A spatial variability could be derived by means of single-repeated measurements at intervals of approximately one year. In addition, the pRES was operated autonomously with the aim of revealing the temporal variability of melt rates or to achieve a higher accuracy, e.g. at the EastGRIP drill site.

However, some disadvantages prevented the evaluation of a few measurements or even more precise results. Noise and weak reflections at larger depths prevented the determination of vertical displacements down to the ice base for thick ice, which contributed to inaccuracies in the basal melt rate. Even low correlation of the repeated measurements in the upper layers prevented the evaluation of the melt rate at some locations, the origin of which is unclear. Due to the simple set up with only one pair of antennas, it is not possible to migrate the data, which makes side reflections difficult to identify. Therefore, the use of the pRES on glaciers with complex basal geometry is more difficult and the evaluation of such data is only possible through further information of the basal geometry, e.g.

through airborne radar measurements. For flat basal geometries, however, it is an ideal measuring device from which melt rates with high accuracy can be determined.

This work focuses on the use for the determination of basal melt rates. However, there are other areas of application of the pRES device. The distribution of vertical displacements in the firn can be used to investigate firn densification, as shown in a study by [Case and Kingslake \(2021\)](#). Another application is the detection of melt water intrusions or water-filled englacial channels, as shown by [Kendrick et al. \(2018\)](#). Here, a modification of the pRES device was used that consisted of an antenna array ([Young et al., 2018](#)).

By means of polarimetric measurements, which are performed with different antenna orientations, conclusions can be drawn about anisotropy and thus about the crystal orientation ([Jordan et al., 2020](#); [Young et al., 2021](#); [Ershadi et al., 2021](#)). Previously, the crystal orientation was mainly derived from ice-core data. However, by performing these polarimetric measurements with the pRES device, the orientation fabric can be determined with a significantly higher spatial distribution. Measurements of this kind have also been taken in the course of projects in which I was involved, the evaluation of which is still in progress.

References

- Adusumilli, S., Fricker, H. A., Medley, B., Padman, L., & Siegfried, M. R. (2020). Interannual variations in meltwater input to the Southern Ocean from Antarctic ice shelves. *Nature Geoscience*, *13*(9), 616–620, <https://doi.org/10.1038/s41561-020-0616-z>.
- Alfred-Wegener-Institut (2016). Polar aircraft Polar5 and Polar6 operated by the Alfred Wegener Institute. *Journal of large-scale research facilities*, *2*(A87), <https://doi.org/10.17815/jlsrf-2-153>. Christine Wesche, Daniel Steinhage and Uwe Nixdorf.
- Alley, K. E., Scambos, T. A., Anderson, R. S., Rajaram, H., Pope, A., & Haran, T. M. (2018). Continent-wide estimates of Antarctic strain rates from Landsat 8-derived velocity grids. *Journal of Glaciology*, *64*(244), 321–332, <https://doi.org/10.1017/jog.2018.23>.
- Alley, K. E., Scambos, T. A., Siegfried, M. R., & Fricker, H. A. (2016). Impacts of warm water on Antarctic ice shelf stability through basal channel formation. *Nature Geoscience*, *9*(4), 290–293, <https://doi.org/10.1038/ngeo2675>.
- Alley, R. B., Pollard, D., Parizek, B. R., Anandakrishnan, S., Pourpoint, M., Stevens, N. T., MacGregor, J. A., Christianson, K., Muto, A., & Holschuh, N. (2019). Possible Role for Tectonics in the Evolving Stability of the Greenland Ice Sheet. *Journal of Geophysical Research: Earth Surface*, *124*(1), 97–115, <https://doi.org/10.1029/2018JF004714>.
- Andryieuski, A., Kuznetsova, S. M., Zhukovsky, S. V., Kivshar, Y. S., & Lavrinenko, A. V. (2015). Water: Promising Opportunities For Tunable All-dielectric Electromagnetic Metamaterials. *Scientific Reports*, *5*(1), 13535, <https://doi.org/10.1038/srep13535>.
- Arnold, E., Leuschen, C., Rodriguez-Morales, F., Li, J., Paden, J., Hale, R., & Keshmiri, S. (2020). CReSIS airborne radars and platforms for ice and snow sounding. *Annals of Glaciology*, *61*(81), 58–67, <https://doi.org/10.1017/aog.2019.37>.
- Bennett, M. R. (2003). Ice streams as the arteries of an ice sheet: their mechanics, stability and significance. *Earth-Science Reviews*, *61*(3), 309–339, [https://doi.org/10.1016/S0012-8252\(02\)00130-7](https://doi.org/10.1016/S0012-8252(02)00130-7).
- Berger, S., Drews, R., Helm, V., Sun, S., & Pattyn, F. (2017). Detecting high spatial variability of ice shelf basal mass balance, Roi Baudouin Ice Shelf, Antarctica. *The Cryosphere*, *11*(6), 2675–2690, <https://doi.org/10.5194/tc-11-2675-2017>.
- Berthier, E., Cabot, V., Vincent, C., & Six, D. (2016). Decadal Region-Wide and Glacier-Wide Mass Balances Derived from Multi-Temporal ASTER Satellite Digital Elevation Models. Validation over the Mont-Blanc Area. *Frontiers in Earth Science*, *4*, 63, <https://doi.org/10.3389/feart.2016.00063>.
- Beyer, S., Kleiner, T., Aizinger, V., Rückamp, M., & Humbert, A. (2018). A confined–unconfined aquifer model for subglacial hydrology and its application to the Northeast Greenland Ice Stream. *The Cryosphere*, *12*(12), 3931–3947, <https://doi.org/10.5194/tc-12-3931-2018>.

- Blatter, H. (1995). Velocity and stress fields in grounded glaciers: a simple algorithm for including deviatoric stress gradients. *Journal of Glaciology*, 41(138), 333–344, <https://doi.org/10.3189/S002214300001621X>.
- Bogorodsky, V. V., Bentley, C. R., & Gudmansen, P. E. (1985). *Radioglaciology*, volume 1. Springer, <https://doi.org/10.1007/978-94-009-5275-1>.
- Brennan, P. V., Lok, L. B., Nicholls, K., & Corr, H. (2014). Phase-sensitive FMCW radar system for high-precision Antarctic ice shelf profile monitoring. *IET Radar, Sonar & Navigation*, 8(7), 776–786, <https://doi.org/10.1049/iet-rsn.2013.0053>.
- Brondex, J., Gillet-Chaulet, F., & Gagliardini, O. (2019). Sensitivity of centennial mass loss projections of the Amundsen basin to the friction law. *The Cryosphere*, 13(1), 177–195, <https://doi.org/10.5194/tc-13-177-2019>.
- Bull, C. Y. S., Jenkins, A., Jourdain, N. C., Vaňková, I., Holland, P. R., Mathiot, P., Hausmann, U., & Sallée, J.-B. (2021). Remote Control of Filchner-Ronne Ice Shelf Melt Rates by the Antarctic Slope Current. *Journal of Geophysical Research: Oceans*, 126(2), e2020JC016550, <https://doi.org/10.1029/2020JC016550>.
- Case, E. & Kingslake, J. (2021). Phase-sensitive radar as a tool for measuring firn compaction. *Journal of Glaciology*, (pp. 1–14)., <https://doi.org/10.1017/jog.2021.83>.
- Christianson, K., Peters, L. E., Alley, R. B., Anandakrishnan, S., Jacobel, R. W., Riverman, K. L., Muto, A., & Keisling, B. A. (2014). Dilatant till facilitates ice-stream flow in northeast Greenland. *Earth and Planetary Science Letters*, 401, 57–69, <https://doi.org/10.1016/j.epsl.2014.05.060>.
- Christmann, J. (2017). *Viscoelastic Modeling of Calving Processes at Antarctic Ice Shelves*. PhD thesis, Technische Universität Kaiserslautern.
- Christmann, J., Helm, V., Khan, S. A., Kleiner, T., Müller, R., Morlighem, M., Neckel, N., Rückamp, M., Steinhage, D., Zeising, O., & Humbert, A. (2021). Elastic deformation plays a non-negligible role in Greenland’s outlet glacier flow. *Communications Earth & Environment*, 2(1), 232, <https://doi.org/10.1038/s43247-021-00296-3>.
- Christmann, J., Mueller, R., & Humbert, A. (2019). On nonlinear strain theory for a viscoelastic material model and its implications for calving of ice shelves. *Journal of Glaciology*, 65(250), 212–224, <https://doi.org/10.1017/jog.2018.107>.
- Christmann, J., Plate, C., Müller, R., & Humbert, A. (2016). Viscous and viscoelastic stress states at the calving front of Antarctic ice shelves. *Annals of Glaciology*, 57(73), 10–18, <https://doi.org/10.1017/aog.2016.18>.
- Corr, H. F., Jenkins, A., Nicholls, K. W., & Doake, C. (2002). Precise measurement of changes in ice-shelf thickness by phase-sensitive radar to determine basal melt rates. *Geophysical Research Letters*, 29(8), 73–1–74–4, <https://doi.org/10.1029/2001GL014618>.
- Cuffey, K. M. & Paterson, W. S. B. (2010). *The Physics of Glaciers - 4th ed.* Elsevier.
- Dahl-Jensen, D., Gundestrup, N., Gogineni, S. P., & Miller, H. (2003). Basal melt at NorthGRIP modeled from borehole, ice-core and radio-echo sounder observations.

- Annals of Glaciology*, 37, 207–212, <https://doi.org/10.3189/172756403781815492>.
- Dansgaard, W. & Johnsen, S. (1969). A flow model and a time scale for the ice core from camp century, greenland. *Journal of Glaciology*, 8(53), 215–223, <https://doi.org/10.3189/S0022143000031208>.
- Dinniman, M. S., Asay-Davis, X. S., Galton-Fenzi, B. K., Holland, P. R., Jenkins, A., & Timmermann, R. (2016). Modeling Ice Shelf/Ocean Interaction in Antarctica: A Review. *Oceanography*, 29(4), 144–153, <https://doi.org/10.5670/oceanog.2016.106>.
- DLR (2020). TanDEM-X - PolarDEM - Antarctica, 90m. <https://doi.org/10.15489/9jhr18jepi65>.
- Dow, C. F., Lee, W. S., Greenbaum, J. S., Greene, C. A., Blankenship, D. D., Poinar, K., Forrest, A. L., Young, D. A., & Zappa, C. J. (2018). Basal channels drive active surface hydrology and transverse ice shelf fracture. *Science Advances*, 4(6), <https://doi.org/10.1126/sciadv.aao7212>.
- Drews, R. (2015). Evolution of ice-shelf channels in Antarctic ice shelves. *The Cryosphere*, 9(3), 1169–1181, <https://doi.org/10.5194/tc-9-1169-2015>.
- Drews, R., Pattyn, F., Hewitt, I. J., Ng, F. S. L., Berger, S., Matsuoka, K., Helm, V., Bergeot, N., Favier, L., & Neckel, N. (2017). Actively evolving subglacial conduits and eskers initiate ice shelf channels at an Antarctic grounding line. *Nature Communications*, 8(1), 15228, <https://doi.org/10.1038/ncomms15228>.
- Dupont, T. K. & Alley, R. B. (2005). Assessment of the importance of ice-shelf buttressing to ice-sheet flow. *Geophysical Research Letters*, 32(4), <https://doi.org/10.1029/2004GL022024>.
- Dutrieux, P., Stewart, C., Jenkins, A., Nicholls, K. W., Corr, H. F., Rignot, E., & Steffen, K. (2014). Basal terraces on melting ice shelves. *Geophysical Research Letters*, 41(15), 5506–5513, <https://doi.org/10.1002/2014GL060618>.
- Eisen, O., Hamann, I., Kipfstuhl, S., Steinhage, D., & Wilhelms, F. (2007). Direct evidence for continuous radar reflector originating from changes in crystal-orientation fabric. *The Cryosphere*, 1(1), 1–10, <https://doi.org/10.5194/tc-1-1-2007>.
- Eisen, O., Winter, A., Steinhage, D., Kleiner, T., & Humbert, A. (2020). Basal roughness of the East Antarctic Ice Sheet in relation to flow speed and basal thermal state. *Annals of Glaciology*, 61(81), 162–175, <https://doi.org/10.1017/aog.2020.47>.
- Ershadi, M. R., Drews, R., Martín, C., Eisen, O., Ritz, C., Corr, H., Christmann, J., Zeising, O., Humbert, A., & Mulvaney, R. (2021). Polarimetric radar reveals the spatial distribution of ice fabric at domes in East Antarctica. *The Cryosphere Discussions [preprint]*, 2021, 1–34, <https://doi.org/10.5194/tc-2020-370>.
- Fahnestock, M. A., Abdalati, W., Joughin, I., Brozena, J., & Gogineni, P. (2001a). High geothermal heat flow, basal melt, and the origin of rapid ice flow in central Greenland. *Science*, 294(5550), 2338–2342, <https://doi.org/10.1126/science.1065370>.
- Fahnestock, M. A., Bindschadler, R., Kwok, R., & Jezek, K. (1993). Greenland ice sheet surface properties and ice dynamics from ers-1 sar imagery. *Science*, 262(5139), 1530–1534, <https://doi.org/10.1126/science.262.5139.1530>.

- Fahnestock, M. A., Joughin, I., Scambos, T. A., Kwok, R., Krabill, W. B., & Gogineni, S. (2001b). Ice-stream-related patterns of ice flow in the interior of northeast Greenland. *Journal of Geophysical Research: Atmospheres*, *106*(D24), 34035–34045, <https://doi.org/10.1029/2001JD900194>.
- Foerste, C., Bruinsma, S., Abrykosov, O., Lemoine, J.-M., Marty, J. C., Flechtner, F., Balmino, G., Barthelmes, F., & Biancale, R. (2014). EIGEN-6C4 The latest combined global gravity field model including GOCE data up to degree and order 2190 of GFZ Potsdam and GRGS Toulouse. <https://doi.org/10.5880/icgem.2015.1>.
- Franke, S., Jansen, D., Beyer, S., Neckel, N., Binder, T., Paden, J., & Eisen, O. (2021). Complex Basal Conditions and Their Influence on Ice Flow at the Onset of the Northeast Greenland Ice Stream. *Journal of Geophysical Research: Earth Surface*, *126*(3), e2020JF005689, <https://doi.org/10.1029/2020JF005689>.
- Fujita, S., Maeno, H., & Matsuoka, K. (2006). Radio-wave depolarization and scattering within ice sheets: a matrix-based model to link radar and ice-core measurements and its application. *Journal of Glaciology*, *52*(178), 407–424, <https://doi.org/10.3189/172756506781828548>.
- Fujita, S., Matsuoka, T., Ishida, T., Matsuoka, K., & Mae, S. (2000). A summary of the complex dielectric permittivity of ice in the megahertz range and its applications for radar sounding of polar ice sheets. In *Physics of ice core records* (pp. 185–212).: Hokkaido University Press.
- Fürst, J. J., Durand, G., Gillet-Chaulet, F., Tavard, L., Rankl, M., Braun, M., & Gagliardini, O. (2016). The safety band of Antarctic ice shelves. *Nature Climate Change*, *6*(5), 479, <https://doi.org/10.1038/nclimate2912>.
- Gagliardini, O., Durand, G., Zwinger, T., Hindmarsh, R. C. A., & Le Meur, E. (2010). Coupling of ice-shelf melting and buttressing is a key process in ice-sheets dynamics. *Geophysical Research Letters*, *37*(14), <https://doi.org/10.1029/2010GL043334>.
- Galton-Fenzi, B. K., Hunter, J. R., Coleman, R., Marsland, S. J., & Warner, R. C. (2012). Modeling the basal melting and marine ice accretion of the Amery Ice Shelf. *Journal of Geophysical Research: Oceans*, *117*(C9), <https://doi.org/10.1029/2012JC008214>.
- Gladish, C. V., Holland, D. M., Holland, P. R., & Price, S. F. (2012). Ice-shelf basal channels in a coupled ice/ocean model. *Journal of Glaciology*, *58*(212), 1227–1244, <https://doi.org/10.3189/2012JoG12J003>.
- Goelzer, H., Nowicki, S., Edwards, T., Beckley, M., Abe-Ouchi, A., Aschwanden, A., Calov, R., Gagliardini, O., Gillet-Chaulet, F., Gollledge, N. R., et al. (2018). Design and results of the ice sheet model initialisation initMIP-Greenland: An IS-MIP6 intercomparison. *The Cryosphere*, *12*(4), 1433–1460, <https://doi.org/10.5194/tc-12-1433-2018>.
- Greve, R. & Blatter, H. (2009). *Dynamics of Ice Sheets and Glaciers*. Springer Science & Business Media, <https://doi.org/10.1007/978-3-642-03415-2>.
- Gudmundsson, G. H. (2011). Ice-stream response to ocean tides and the form of the basal sliding law. *The Cryosphere*, *5*(1), 259–270, <https://doi.org/10.5194/tc-5-259-2011>.

- Gwyther, D. E., Kusahara, K., Asay-Davis, X. S., Dinniman, M. S., & Galton-Fenzi, B. K. (2020). Vertical processes and resolution impact ice shelf basal melting: A multi-model study. *Ocean Modelling*, *147*, 101569, <https://doi.org/10.1016/j.ocemod.2020.101569>.
- Hale, R., Miller, H., Gogineni, S., Yan, J.-B., Rodriguez-Morales, F., Leuschen, C., Paden, J., Li, J., Binder, T., Steinhage, D., et al. (2016). Multi-channel ultra-wideband radar sounder and imager. In *2016 IEEE International Geoscience and Remote Sensing Symposium (IGARSS)* (pp. 2112–2115).: IEEE.
- Hargreaves, N. D. (1978). The radio-frequency birefringence of polar ice. *Journal of Glaciology*, *21*(85), 301–313, <https://doi.org/10.3189/S0022143000033499>.
- Hattermann, T., Nicholls, K. W., Hellmer, H. H., Davis, P. E. D., Janout, M. A., Østerhus, S., Schlosser, E., Rohardt, G., & Kanzow, T. (2021). Observed interannual changes beneath Filchner-Ronne Ice Shelf linked to large-scale atmospheric circulation. *Nature Communications*, *12*(1), 2961, <https://doi.org/10.1038/s41467-021-23131-x>.
- Haupt, P. (2002). *Continuum Mechanics and Theory of Materials*. Springer, Berlin, <https://doi.org/10.1007/978-3-662-04775-0>.
- Hellmer, H. H., Kauker, F., Timmermann, R., Determann, J., & Rae, J. (2012). Twenty-first-century warming of a large antarctic ice-shelf cavity by a redirected coastal current. *Nature*, *485*(7397), 225–228, <https://doi.org/10.1038/nature11064>.
- Hellmer, H. H. & Olbers, D. J. (1989). A two-dimensional model for the thermohaline circulation under an ice shelf. *Antarctic Science*, *1*(4), 325–336, <https://doi.org/10.1017/S0954102089000490>.
- Helm, V., Humbert, A., & Miller, H. (2014). Elevation and elevation change of Greenland and Antarctica derived from CryoSat-2. *The Cryosphere*, *8*(4), 1539–1559, <https://doi.org/10.5194/tc-8-1539-2014>.
- Herron, M. M. & Langway, C. C. (1980). Firn densification: An empirical model. *Journal of Glaciology*, *25*(93), 373–385, <https://doi.org/10.3189/S0022143000015239>.
- Hofstede, C., Beyer, S., Corr, H., Eisen, O., Hattermann, T., Helm, V., Neckel, N., Smith, E. C., Steinhage, D., Zeising, O., & Humbert, A. (2021a). Evidence for a grounding line fan at the onset of a basal channel under the ice shelf of Support Force Glacier, Antarctica, revealed by reflection seismics. *The Cryosphere*, *15*(3), 1517–1535, <https://doi.org/10.5194/tc-15-1517-2021>.
- Hofstede, C., Beyer, S., Corr, H. F. J., Eisen, O., Hattermann, T., Helm, V., Neckel, N., Smith, E. C., Steinhage, D., Zeising, O., & Humbert, A. (2021b). Seismic reflection data of a basal channel and ocean cavity at the ice shelf-grounding line area of Support Force Glacier, Filchner Ice Shelf, Antarctica. <https://doi.org/10.1594/PANGAEA.932278>.
- Holland, D. M. & Jenkins, A. (1999). Modeling thermodynamic ice–ocean interactions at the base of an ice shelf. *Journal of Physical Oceanography*, *29*(8), 1787–1800, [https://doi.org/10.1175/1520-0485\(1999\)029<1787:MTIOIA>2.0.CO;2](https://doi.org/10.1175/1520-0485(1999)029<1787:MTIOIA>2.0.CO;2).
- Holland, D. M., Thomas, R. H., De Young, B., Ribergaard, M. H., & Lyberth, B.

- (2008). Acceleration of Jakobshavn Isbræ triggered by warm subsurface ocean waters. *Nature Geoscience*, 1(10), 659–664, <https://doi.org/10.1038/ngeo316>.
- Holland, P. R. & Kwok, R. (2012). Wind-driven trends in Antarctic sea-ice drift. *Nature Geoscience*, 5(12), 872–875, <https://doi.org/10.1038/ngeo1627>.
- Howat, I. M., Morin, P., Porter, C., & Noh, M.-J. (2018). The Reference Elevation Model of Antarctica. <https://doi.org/10.7910/DVN/SAIK8B>.
- Howat, I. M., Porter, C., Smith, B. E., Noh, M.-J., & Morin, P. (2019). The Reference Elevation Model of Antarctica. *The Cryosphere*, 13(2), 665–674, <https://doi.org/10.5194/tc-13-665-2019>.
- Humbert, A. (2010). The temperature regime of fimbulisen, antarctica. *Annals of Glaciology*, 51(55), 56–64, <https://doi.org/10.3189/172756410791392673>.
- Humbert, A., Steinhage, D., Helm, V., Beyer, S., & Kleiner, T. (2018). Missing evidence of widespread subglacial lakes at Recovery Glacier, Antarctica. *Journal of Geophysical Research: Earth Surface*, 123(11), 2802–2826, <https://doi.org/10.1029/2017JF004591>.
- Humbert, A., Steinhage, D., Helm, V., Hoerz, S., Berendt, J., Leipprand, E., Christmann, J., Plate, C., & Müller, R. (2015). On the link between surface and basal structures of the Jelbart Ice Shelf, Antarctica. *Journal of Glaciology*, 61(229), 975–986, <https://doi.org/10.3189/2015JoG15J023>.
- Hvidberg, C. S., Grinsted, A., Dahl-Jensen, D., Khan, S. A., Kusk, A., Andersen, J. K., Neckel, N., Solgaard, A., Karlsson, N. B., Kjær, H. A., et al. (2020). Surface velocity of the Northeast Greenland Ice Stream (NEGIS): assessment of interior velocities derived from satellite data by GPS. *The Cryosphere*, 14(10), 3487–3502, <https://doi.org/10.5194/tc-14-3487-2020>.
- Ignéczi, A., Sole, A. J., Livingstone, S. J., Leeson, A. A., Fettweis, X., Selmes, N., Gourmelen, N., & Briggs, K. (2016). Northeast sector of the Greenland Ice Sheet to undergo the greatest inland expansion of supraglacial lakes during the 21st century. *Geophysical Research Letters*, 43(18), 9729–9738, <https://doi.org/10.1002/2016GL070338>.
- IPCC (2019). Summary for policymakers. In H.-O. Pörtner, D. Roberts, V. Masson-Delmotte, P. Zhai, M. Tignor, P. E., K. Mintenbeck, A. Alegría, M. Nicolai, A. Okem, J. Petzold, B. Rama, & N. M. Weyer (Eds.), *IPCC Special Report on the Ocean and Cryosphere in a Changing Climate*. In press.
- Jenkins, A. (1991). A one-dimensional model of ice shelf-ocean interaction. *Journal of Geophysical Research: Oceans*, 96(C11), 20671–20677, <https://doi.org/10.1029/91JC01842>.
- Jenkins, A. (2011). Convection-driven melting near the grounding lines of ice shelves and tidewater glaciers. *Journal of Physical Oceanography*, 41(12), 2279–2294, <https://doi.org/10.1175/JPO-D-11-03.1>.
- Jenkins, A., Corr, H. F., Nicholls, K. W., Stewart, C. L., & Doake, C. S. (2006). Interactions between ice and ocean observed with phase-sensitive radar near an Antarctic ice-shelf grounding line. *Journal of Glaciology*, 52(178), 325–346, <https://doi.org/10.3189/172756406791392673>.

[//doi.org/10.3189/172756506781828502](https://doi.org/10.3189/172756506781828502).

- Jenkins, A. & Doake, C. (1991). Ice-ocean interaction on Ronne Ice Shelf, Antarctica. *Journal of Geophysical Research: Oceans*, 96(C1), 791–813, <https://doi.org/10.1029/90JC01952>.
- Jeofry, H., Ross, N., Le Brocq, A., Graham, A. G. C., Li, J., Gogineni, P., Morlighem, M., Jordan, T., & Siegert, M. J. (2018). Hard rock landforms generate 130 km ice shelf channels through water focusing in basal corrugations. *Nature Communications*, 8(1), 4576, <https://doi.org/10.1038/s41467-018-06679-z>.
- Jordan, T. M., Schroeder, D. M., Elsworth, C. W., & Siegfried, M. R. (2020). Estimation of ice fabric within Whillans Ice Stream using polarimetric phase-sensitive radar sounding. *Annals of Glaciology*, 61(81), 74–83, <https://doi.org/10.1017/aog.2020.6>.
- Joughin, I., Abdalati, W., & Fahnestock, M. (2004). Large fluctuations in speed on Greenland’s Jakobshavn Isbræ glacier. *Nature*, 432, 608–610, <https://doi.org/10.1038/nature03130>.
- Joughin, I., Alley, R. B., & Holland, D. M. (2012). Ice-sheet response to oceanic forcing. *Science*, 338(6111), 1172–1176, <https://doi.org/10.1126/science.1226481>.
- Joughin, I., Fahnestock, M., MacAyeal, D., Bamber, J. L., & Gogineni, P. (2001). Observation and analysis of ice flow in the largest greenland ice stream. *Journal of Geophysical Research: Atmospheres*, 106(D24), 34021–34034, <https://doi.org/10.1029/2001JD900087>.
- Joughin, I., Howat, I. M., Fahnestock, M., Smith, B., Krabill, W., Alley, R. B., Stern, H., & Truffer, M. (2008). Continued evolution of Jakobshavn Isbrae following its rapid speedup. *Journal of Geophysical Research: Earth Surface*, 113(F4), <https://doi.org/10.1029/2008JF001023>.
- Joughin, I., Shean, D. E., Smith, B. E., & Floricioiu, D. (2020). A decade of variability on Jakobshavn Isbræ: ocean temperatures pace speed through influence on mélange rigidity. *The Cryosphere*, 14(1), 211–227, <https://doi.org/10.5194/tc-14-211-2020>.
- Joughin, I., Smith, B., Howat, I., & Scambos, T. (2016). MEaSUREs Multi-year Greenland Ice Sheet Velocity Mosaic, Version 1. Boulder, Colorado USA. NASA National Snow and Ice Data Center Distributed Active Archive Center. <https://doi.org/10.5067/QUA5Q9SVMSJG>.
- Joughin, I., Smith, B. E., & Howat, I. M. (2018). A complete map of Greenland ice velocity derived from satellite data collected over 20 years. *Journal of Glaciology*, 64(243), 1–11, <https://doi.org/10.1017/jog.2017.73>.
- Joughin, I., Smith, B. E., Shean, D. E., & Floricioiu, D. (2014). Brief Communication: Further summer speedup of Jakobshavn Isbræ. *The Cryosphere*, 8(1), 209–214, <https://doi.org/10.5194/tc-8-209-2014>.
- Jourdain, N. C., Asay-Davis, X., Hattermann, T., Straneo, F., Seroussi, H., Little, C. M., & Nowicki, S. (2020). A protocol for calculating basal melt rates in the ismip6 antarctic ice sheet projections. *The Cryosphere*, 14(9), 3111–3134, <https://doi.org/10.5194/tc-14-3111-2020>.

[//doi.org/10.5194/tc-14-3111-2020](https://doi.org/10.5194/tc-14-3111-2020).

- Jourdain, N. C., Mathiot, P., Merino, N., Durand, G., Le Sommer, J., Spence, P., Dutrieux, P., & Madec, G. (2017). Ocean circulation and sea-ice thinning induced by melting ice shelves in the Amundsen Sea. *Journal of Geophysical Research: Oceans*, *122*(3), 2550–2573, <https://doi.org/10.1002/2016JC012509>.
- Keisling, B. A., Christianson, K., Alley, R. B., Peters, L. E., Christian, J. E., Anandakrishnan, S., Riverman, K. L., Muto, A., & Jacobel, R. W. (2014). Basal conditions and ice dynamics inferred from radar-derived internal stratigraphy of the northeast Greenland ice stream. *Annals of Glaciology*, *55*(67), 127–137, <https://doi.org/10.3189/2014AoG67A090>.
- Kendrick, A. K., Schroeder, D. M., Chu, W., Young, T. J., Christoffersen, P., Todd, J., Doyle, S. H., Box, J. E., Hubbard, A., Hubbard, B., Brennan, P. V., Nicholls, K. W., & Lok, L. B. (2018). Surface Meltwater Impounded by Seasonal Englacial Storage in West Greenland. *Geophysical Research Letters*, *45*(19), 10,474–10,481, <https://doi.org/10.1029/2018GL079787>.
- Khan, S. A., Kjær, K. H., Bevis, M., Bamber, J. L., Wahr, J., Kjeldsen, K. K., Bjørk, A. A., Korsgaard, N. J., Stearns, L. A., Van Den Broeke, M. R., et al. (2014). Sustained mass loss of the northeast Greenland ice sheet triggered by regional warming. *Nature Climate Change*, *4*(4), 292–299, <https://doi.org/10.1038/nclimate2161>.
- Kjeldsen, K. K., Korsgaard, N. J., Bjørk, A. A., Khan, S. A., Box, J. E., Funder, S., Larsen, N. K., Bamber, J. L., Colgan, W., Van Den Broeke, M., et al. (2015). Spatial and temporal distribution of mass loss from the Greenland Ice Sheet since AD 1900. *Nature*, *528*(7582), 396–400, <https://doi.org/10.1038/nature16183>.
- Kovacs, A., Gow, A. J., & Morey, R. M. (1995). The in-situ dielectric constant of polar firn revisited. *Cold Regions Science and Technology*, *23*(3), 245 – 256, [https://doi.org/10.1016/0165-232X\(94\)00016-Q](https://doi.org/10.1016/0165-232X(94)00016-Q).
- Krieger, L., Floricioiu, D., & Neckel, N. (2020a). Drainage basin delineation for outlet glaciers of Northeast Greenland based on Sentinel-1 ice velocities and TanDEM-X elevations. *Remote Sensing of Environment*, *237*, 111483, <https://doi.org/10.1016/j.rse.2019.111483>.
- Krieger, L., Strößenreuther, U., Helm, V., Floricioiu, D., & Horwath, M. (2020b). Synergistic Use of Single-Pass Interferometry and Radar Altimetry to Measure Mass Loss of NEGIS Outlet Glaciers between 2011 and 2014. *Remote Sensing*, *12*(6), 996, <https://doi.org/10.3390/rs12060996>.
- Kutscher, K., Geier, M., & Krafczyk, M. (2019). Multiscale simulation of turbulent flow interacting with porous media based on a massively parallel implementation of the cumulant lattice Boltzmann method. *Computers & Fluids*, *193*, 103733, <https://doi.org/10.1016/j.compfluid.2018.02.009>.
- Langley, K., von Deschwandten, A., Kohler, J., Sinisalo, A., Matsuoka, K., Hattermann, T., Humbert, A., Nøst, O., & Isaksson, E. (2014). Complex network of channels beneath an Antarctic ice shelf. *Geophysical Research Letters*, *41*(4), 1209–1215, <https://doi.org/10.1002/2013GL058947>.

- Larour, E., Seroussi, H., Morlighem, M., & Rignot, E. (2012). Continental scale, high order, high spatial resolution, ice sheet modeling using the Ice Sheet System Model (ISSM). *Journal of Geophysical Research: Earth Surface*, *117*(F1), F01022, <https://doi.org/10.1029/2011JF002140>.
- Le Brocq, A. M., Ross, N., Griggs, J. A., Bingham, R. G., Corr, H. F., Ferraccioli, F., Jenkins, A., Jordan, T. A., Payne, A. J., Rippin, D. M., et al. (2013). Evidence from ice shelves for channelized meltwater flow beneath the Antarctic Ice Sheet. *Nature Geoscience*, *6*(11), 945–948, <https://doi.org/10.1038/ngeo1977>.
- Leeson, A. A., Shepherd, A., Briggs, K., Howat, I., Fettweis, X., Morlighem, M., & Rignot, E. (2014). Supraglacial lakes on the Greenland ice sheet advance inland under warming climate. *Nature Climate Change*, *5*, 51, <https://doi.org/10.1038/nclimate2463>.
- Lindeman, M. R., Straneo, F., Wilson, N. J., Toole, J. M., Krishfield, R. A., Beaird, N. L., Kanzow, T., & Schaffer, J. (2020). Ocean Circulation and Variability Beneath Nioghalvfjærdsbræ (79 North Glacier) Ice Tongue. *Journal of Geophysical Research: Oceans*, *125*(8), e2020JC016091, <https://doi.org/10.1029/2020JC016091>.
- MacGregor, J. A., Fahnestock, M. A., Catania, G. A., Aschwanden, A., Clow, G. D., Colgan, W. T., Gogineni, S. P., Morlighem, M., Nowicki, S. M., Paden, J. D., Price, S. F., & Seroussi, H. (2016). A synthesis of the basal thermal state of the Greenland Ice Sheet. *Journal of Geophysical Research: Earth Surface*, *121*(7), 1328–1350, <https://doi.org/10.1002/2015JF003803>.
- Marsh, O. J., Fricker, H. A., Siegfried, M. R., Christianson, K., Nicholls, K. W., Corr, H. F., & Catania, G. (2016). High basal melting forming a channel at the grounding line of Ross Ice Shelf, Antarctica. *Geophysical Research Letters*, *43*(1), 250–255, <https://doi.org/10.1002/2015GL066612>.
- Martos, Y. M., Catalán, M., Jordan, T. A., Golynsky, A., Golynsky, D., Eagles, G., & Vaughan, D. G. (2017). Heat Flux Distribution of Antarctica Unveiled. *Geophysical Research Letters*, *44*(22), 11,417–11,426, <https://doi.org/10.1002/2017GL075609>.
- Martos, Y. M., Jordan, T. A., Catalán, M., Jordan, T. M., Bamber, J. L., & Vaughan, D. G. (2018). Geothermal heat flux reveals the Iceland hotspot track underneath Greenland. *Geophysical Research Letters*, *45*(16), 8214–8222, <https://doi.org/10.1029/2018GL078289>.
- Mayer, C., Reeh, N., Jung-Rothenhäusler, F., Huybrechts, P., & Oerter, H. (2000). The subglacial cavity and implied dynamics under Nioghalvfjærdsfjorden Glacier, NE-Greenland. *Geophysical Research Letters*, *27*(15), 2289–2292, <https://doi.org/10.1029/2000GL011514>.
- Mayer, C., Schaffer, J., Hattermann, T., Floricioiu, D., Krieger, L., Dodd, P. A., Kanzow, T., Licciulli, C., & Schannwell, C. (2018). Large ice loss variability at Nioghalvfjærdsfjorden Glacier, Northeast-Greenland. *Nature Communications*, *9*(1), 2768, <https://doi.org/10.1038/s41467-018-05180-x>.
- Menke, W. (2012). Chapter 3 - Solution of the Linear, Gaussian Inverse Problem, Viewpoint 1: The Length Method. In W. Menke (Ed.), *Geophysical Data Analysis:*

- Discrete Inverse Theory (Third Edition)* (pp. 39 – 68). Boston: Academic Press, <https://doi.org/10.1016/B978-0-12-397160-9.00003-5>.
- Millgate, T., Holland, P. R., Jenkins, A., & Johnson, H. L. (2013). The effect of basal channels on oceanic ice-shelf melting. *Journal of Geophysical Research: Oceans*, *118*(12), 6951–6964, <https://doi.org/10.1002/2013JC009402>.
- Moholdt, G., Padman, L., & Fricker, H. A. (2015). Basal mass budget of Ross and Filchner-Ronne ice shelves, Antarctica, derived from Lagrangian analysis of ICE-Sat altimetry. *Journal of Geophysical Research: Earth Surface*, *119*(11), 2361–2380, <https://doi.org/10.1002/2014JF003171>.
- Morlighem, M. (2020). MEaSURES BedMachine Antarctica, Version 2. Boulder, Colorado USA. NASA National Snow and Ice Data Center Distributed Active Archive Center, Accessed 12 April 2021. <https://doi.org/10.5067/E1QL9HFQ7A8M>.
- Morlighem, M., Rignot, E., Binder, T., Blankenship, D., Drews, R., Eagles, G., Eisen, O., Ferraccioli, F., Forsberg, R., Fretwell, P., Goel, V., Greenbaum, J. S., Gudmundsson, H., Guo, J., Helm, V., Hofstede, C., Howat, I., Humbert, A., Jokat, W., Karlsson, N. B., Lee, W. S., Matsuoka, K., Millan, R., Mouginot, J., Paden, J., Pattyn, F., Roberts, J., Rosier, S., Ruppel, A., Seroussi, H., Smith, E. C., Steinhage, D., Sun, B., Broeke, M. R. v. d., Ommen, T. D. v., Wessem, M. v., & Young, D. A. (2020). Deep glacial troughs and stabilizing ridges unveiled beneath the margins of the Antarctic ice sheet. *Nature Geoscience*, *13*(2), 132–137, <https://doi.org/10.1038/s41561-019-0510-8>.
- Morlighem, M., Rignot, E., Seroussi, H., Larour, E., Dhia, H., & Aubry, D. (2010). Spatial patterns of basal drag inferred using control methods from a full-Stokes and simpler models for Pine Island Glacier, West Antarctica. *Geophysical Research Letters*, *37*(14), L14502, <https://doi.org/10.1029/2010GL043853>.
- Motyka, R. J., Truffer, M., Fahnestock, M., Mortensen, J., Rysgaard, S., & Howat, I. (2011). Submarine melting of the 1985 Jakobshavn Isbræ floating tongue and the triggering of the current retreat. *Journal of Geophysical Research: Earth Surface*, *116*(F1), <https://doi.org/10.1029/2009JF001632>.
- Mouginot, J., Rignot, E., & Scheuchl, B. (2019a). Continent-Wide, Interferometric SAR Phase, Mapping of Antarctic Ice Velocity. *Geophysical Research Letters*, *46*(16), 9710–9718, <https://doi.org/10.1029/2019GL083826>.
- Mouginot, J., Rignot, E., & Scheuchl, B. (2019b). MEaSURES Phase-Based Antarctica Ice Velocity Map, Version 1. Boulder, Colorado USA. NASA National Snow and Ice Data Center Distributed Active Archive Center, Accessed 13 April 2021. <https://doi.org/10.5067/PZ3NJ5RXRH10>.
- Mouginot, J., Rignot, E., Scheuchl, B., Fenty, I., Khazendar, A., Morlighem, M., Buzzi, A., & Paden, J. (2015). Fast retreat of Zachariæ Isstrøm, northeast Greenland. *Science*, *350*(6266), 1357–1361, <https://doi.org/10.1126/science.aac7111>.
- Münchow, A., Padman, L., & Fricker, H. A. (2014). Interannual changes of the floating ice shelf of Petermann Gletscher, North Greenland, from 2000 to 2012. *Journal of Glaciology*, *60*(221), 489–499, <https://doi.org/10.3189/2014JoG13J135>.
- Naughten, K. A., De Rydt, J., Rosier, S. H. R., Jenkins, A., Holland, P. R., &

- Ridley, J. K. (2021). Two-timescale response of a large Antarctic ice shelf to climate change. *Nature Communications*, *12*(1), 1991, <https://doi.org/10.1038/s41467-021-22259-0>.
- Neckel, N., Braun, A., Kropáček, J., & Hochschild, V. (2013). Recent mass balance of the Purogangri Ice Cap, central Tibetan Plateau, by means of differential X-band SAR interferometry. *The Cryosphere*, *7*(5), 1623–1633, <https://doi.org/10.5194/tc-7-1623-2013>.
- Neckel, N., Zeising, O., Steinhage, D., Helm, V., & Humbert, A. (2020). Seasonal observations at 79° N Glacier (Greenland) from remote sensing and in-situ measurements. *Frontiers in Earth Science*, *8*, 142, <https://doi.org/10.3389/feart.2020.00142>.
- Nicholls, K. W. (1997). Predicted reduction in basal melt rates of an Antarctic ice shelf in a warmer climate. *Nature*, *388*(6641), 460–462, <https://doi.org/10.1038/41302>.
- Nicholls, K. W. (2018). The study of ice shelf-ocean interaction—techniques and recent results. *Advances in Polar Science*, *3*, 222–230, <https://doi.org/10.13679/j.advps.2018.3.00222>.
- Nicholls, K. W., Corr, H. F., Stewart, C. L., Lok, L. B., Brennan, P. V., & Vaughan, D. G. (2015). A ground-based radar for measuring vertical strain rates and time-varying basal melt rates in ice sheets and shelves. *Journal of Glaciology*, *61*(230), 1079–1087, <https://doi.org/10.3189/2015JoG15J073>.
- Nixdorf, U., Steinhage, D., Meyer, U., Hempel, L., Jenett, M., Wachs, P., & Miller, H. (1999). The newly developed airborne radio-echo sounding system of the AWI as a glaciological tool. *Annals of Glaciology*, *29*, 231–238, <https://doi.org/10.3189/172756499781821346>.
- North Greenland Ice Core Project members (2004). High-resolution record of Northern Hemisphere climate extending into the last interglacial period. *Nature*, *431*(7005), 147–151, <https://doi.org/10.1038/nature02805>.
- Nuth, C. & Kääb, A. (2011). Co-registration and bias corrections of satellite elevation data sets for quantifying glacier thickness change. *The Cryosphere*, *5*(1), 271–290, <https://doi.org/10.5194/tc-5-271-2011>.
- Nye, J., Berry, M., & Walford, M. (1972). Measuring the change in thickness of the antarctic ice sheet. *Nature Physical Science*, *240*(97), 7–9, <https://doi.org/10.1038/physci240007a0>.
- Paden, J., Li, J., Leuschen, C., Rodriguez-Morales, F., & Hale, R. (2014, updated 2019). IceBridge MCoRDS L1B Geolocated Radar Echo Strength Profiles, Version 2. IRMC1B. Boulder, Colorado USA. NASA National Snow and Ice Data Center Distributed Active Archive Center. Accessed 25 April 2021, <https://doi.org/10.5067/90S1XZRBAX5N>.
- Pattyn, F. (2003). A new three-dimensional higher-order thermomechanical ice sheet model: Basic sensitivity, ice stream development, and ice flow across subglacial lakes. *J. Geophys. Res. Solid Earth*, *108*(B8), <https://doi.org/10.1029/2002JB002329>.

- Pattyn, F. & Morlighem, M. (2020). The uncertain future of the antarctic ice sheet. *Science*, 367(6484), 1331–1335, <https://doi.org/10.1126/science.aaz5487>.
- Pritchard, H. D., Ligtenberg, S. R. M., Fricker, H. A., Vaughan, D. G., van den Broeke, M. R., & Padman, L. (2012). Antarctic ice-sheet loss driven by basal melting of ice shelves. *Nature*, 484(7395), 502–505, <https://doi.org/10.1038/nature10968>.
- Rathmann, N., Hvidberg, C., Solgaard, A., Grinsted, A., Gudmundsson, G. H., Langen, P. L., Nielsen, K., & Kusk, A. (2017). Highly temporally resolved response to seasonal surface melt of the Zachariae and 79N outlet glaciers in northeast Greenland. *Geophysical Research Letters*, 44(19), 9805–9814, <https://doi.org/10.1002/2017GL074368>.
- Reeh, N., Mayer, C., Olesen, O. B., Christensen, E. L., & Thomsen, H. H. (2000). Tidal movement of Nioghalvfjærdsfjorden glacier, northeast Greenland: observations and modelling. *Annals of Glaciology*, 31, 111–117, <https://doi.org/10.3189/172756400781820408>.
- Rignot, E., Casassa, G., Gogineni, P., Krabill, W., Rivera, A., & Thomas, R. (2004). Accelerated ice discharge from the Antarctic Peninsula following the collapse of Larsen B ice shelf. *Geophysical Research Letters*, 31(18), <https://doi.org/10.1029/2004GL020697>.
- Rignot, E., Jacobs, S., Mouginot, J., & Scheuchl, B. (2013). Ice-shelf melting around antarctica. *Science*, 341(6143), 266–270, <https://doi.org/10.1126/science.1235798>.
- Rignot, E. & Mouginot, J. (2012). Ice flow in Greenland for the international polar year 2008–2009. *Geophysical Research Letters*, 39(11), L11501, <https://doi.org/10.1029/2012GL051634>.
- Rignot, E., Mouginot, J., & Scheuchl, B. (2011). Ice Flow of the Antarctic Ice Sheet. *Science*, 333(6048), 1427–1430, <https://doi.org/10.1126/science.1208336>.
- Rignot, E., Mouginot, J., Scheuchl, B., van den Broeke, M., van Wessem, M. J., & Morlighem, M. (2019). Four decades of Antarctic Ice Sheet mass balance from 1979 – 2017. *Proceedings of the National Academy of Sciences*, 116(4), 1095–1103, <https://doi.org/10.1073/pnas.1812883116>.
- Rignot, E. & Steffen, K. (2008). Channelized bottom melting and stability of floating ice shelves. *Geophysical Research Letters*, 35(2), <https://doi.org/10.1029/2007GL031765>.
- Ritz, C. (1987). Time dependent boundary conditions for calculation of temperature fields in ice sheets. In E. D. Waddington & J. S. Walder (Eds.), *The Physical Basis of Ice Sheet Modelling*, IAHS Publication No. 170 (pp. 207–216): IAHS Press, Wallingford, UK.
- Rizzoli, P., Martone, M., Gonzalez, C., Wecklich, C., Borla Tridon, D., Bräutigam, B., Bachmann, M., Schulze, D., Fritz, T., Huber, M., Wessel, B., Krieger, G., Zink, M., & Moreira, A. (2017). Generation and performance assessment of the global TanDEM-X digital elevation model. *ISPRS Journal of Photogrammetry and Remote Sensing*, 132, 119–139, <https://doi.org/10.1016/j.isprsjprs.2017.08.008>.
- Rogozhina, I., Petrunin, A. G., Vaughan, A. P., Steinberger, B., Johnson, J. V., Kaban,

- M. K., Calov, R., Rickers, F., Thomas, M., & Koulakov, I. (2016). Melting at the base of the greenland ice sheet explained by iceland hotspot history. *Nature Geoscience*, *9*(5), 366–369, <https://doi.org/10.1038/ngeo2689>.
- Rückamp, M., Goelzer, H., & Humbert, A. (2020). Sensitivity of Greenland ice sheet projections to spatial resolution in higher-order simulations: the Alfred Wegener Institute (AWI) contribution to ISMIP6 Greenland using the Ice-sheet and Sea-level System Model (ISSM). *The Cryosphere*, *14*(10), 3309–3327, <https://doi.org/10.5194/tc-14-3309-2020>.
- Rückamp, M., Neckel, N., Berger, S., Humbert, A., & Helm, V. (2019). Calving Induced Speedup of Petermann Glacier. *Journal of Geophysical Research: Earth Surface*, *124*(1), 216–228, <https://doi.org/10.1029/2018JF004775>.
- Scambos, T. A., Bohlander, J., Shuman, C. A., & Skvarca, P. (2004). Glacier acceleration and thinning after ice shelf collapse in the Larsen B embayment, Antarctica. *Geophysical Research Letters*, *31*(18), <https://doi.org/10.1029/2004GL020670>.
- Schaffer, J. (2017). *Ocean impact on the 79 North Glacier, Northeast Greenland*. PhD thesis, University of Bremen.
- Schaffer, J., Kanzow, T., von Appen, W.-J., von Albedyll, L., Arndt, J. E., & Roberts, D. H. (2020). Bathymetry constrains ocean heat supply to Greenland's largest glacier tongue. *Nature Geoscience*, *13*(3), 227–231, <https://doi.org/10.1038/s41561-019-0529-x>.
- Scheuchl, B., Mouginot, J., & Rignot, E. (2012). Ice velocity changes in the Ross and Ronne sectors observed using satellite radar data from 1997 and 2009. *The Cryosphere*, *6*(5), 1019–1030, <https://doi.org/10.5194/tc-6-1019-2012>.
- Schodlok, M. P., Menemenlis, D., & Rignot, E. J. (2016). Ice shelf basal melt rates around Antarctica from simulations and observations. *Journal of Geophysical Research: Oceans*, *121*(2), 1085–1109, <https://doi.org/10.1002/2015JC011117>.
- Schoof, C. (2012). Marine ice sheet stability. *Journal of Fluid Mechanics*, *698*, 62–72, <https://doi.org/10.1017/jfm.2012.43>.
- Schröder, L., Neckel, N., Zindler, R., & Humbert, A. (2020). Perennial Supraglacial Lakes in Northeast Greenland Observed by Polarimetric SAR. *Remote Sens.*, *12*(17), 2798, <https://doi.org/10.3390/rs12172798>.
- Schroeder, D. M., Bingham, R. G., Blankenship, D. D., Christianson, K., Eisen, O., Flowers, G. E., Karlsson, N. B., Koutnik, M. R., Paden, J. D., & Siegert, M. J. (2020). Five decades of radioglaciology. *Annals of Glaciology*, *61*(81), 1–13, <https://doi.org/10.1017/aog.2020.11>.
- Schultz, T. (2017). Viskoelastische Modellierung der Dynamik eines Gletschers als Antwort auf basales Schmelzen und die Oberflächenmassenbilanz. *Master thesis*.
- Sergienko, O. (2013). Basal channels on ice shelves. *Journal of Geophysical Research: Earth Surface*, *118*(3), 1342–1355, <https://doi.org/10.1002/jgrf.20105>.
- Seroussi, H., Nakayama, Y., Larour, E., Menemenlis, D., Morlighem, M., Rignot, E., & Khazendar, A. (2017). Continued retreat of Thwaites Glacier, West Antarctica, controlled by bed topography and ocean circulation. *Geophysical Research Letters*,

- Seroussi, H., Nowicki, S., Payne, A. J., Goelzer, H., Lipscomb, W. H., Abe-Ouchi, A., Agosta, C., Albrecht, T., Asay-Davis, X., Barthel, A., Calov, R., Cullather, R., Dumas, C., Galton-Fenzi, B. K., Gladstone, R., Golledge, N. R., Gregory, J. M., Greve, R., Hattermann, T., Hoffman, M. J., Humbert, A., Huybrechts, P., Jourdain, N. C., Kleiner, T., Larour, E., Leguy, G. R., Lowry, D. P., Little, C. M., Morlighem, M., Pattyn, F., Pelle, T., Price, S. F., Quiquet, A., Reese, R., Schlegel, N.-J., Shepherd, A., Simon, E., Smith, R. S., Straneo, F., Sun, S., Trusel, L. D., Van Breedam, J., van de Wal, R. S. W., Winkelmann, R., Zhao, C., Zhang, T., & Zwinger, T. (2020). Ismip6 antarctica: a multi-model ensemble of the antarctic ice sheet evolution over the 21st century. *The Cryosphere*, 14(9), 3033–3070, <https://doi.org/10.5194/tc-14-3033-2020>.
- Shean, D. E., Joughin, I. R., Dutrieux, P., Smith, B. E., & Berthier, E. (2019). Ice shelf basal melt rates from a high-resolution digital elevation model (DEM) record for Pine Island Glacier, Antarctica. *The Cryosphere*, 13(10), 2633–2656, <https://doi.org/10.5194/tc-13-2633-2019>.
- Shepherd, A., Ivins, E., Rignot, E., Smith, B., van den Broeke, M., Velicogna, I., Whitehouse, P., Briggs, K., Joughin, I., Krinner, G., Nowicki, S., Payne, T., Scambos, T., Schlegel, N., A. G., Agosta, C., Ahlstrøm, A., Babonis, G., Barletta, V. R., Bjørk, A. A., Blazquez, A., Bonin, J., Colgan, W., Csatho, B., Cullather, R., Engdahl, M. E., Felikson, D., Fettweis, X., Forsberg, R., Hogg, A. E., Gallee, H., Gardner, A., Gilbert, L., Gourmelen, N., Groh, A., Gunter, B., Hanna, E., Harig, C., Helm, V., Horvath, A., Horwath, M., Khan, S., Kjeldsen, K. K., Konrad, H., Langen, P. L., Lecavalier, B., Loomis, B., Luthcke, S., McMillan, M., Melini, D., Mernild, S., Mohajerani, Y., Moore, P., Mottram, R., Mouginot, J., Moyano, G., Muir, A., Nagler, T., Nield, G., Nilsson, J., Noël, B., Otosaka, I., Pattle, M. E., Peltier, W. R., Pie, N., Rietbroek, R., Rott, H., Sandberg Sørensen, L., Sasgen, I., Save, H., Scheuchl, B., Schrama, E., Schröder, L., Seo, K.-W., Simonsen, S. B., Slater, T., Spada, G., Sutterley, T., Talpe, M., Tarasov, L., van de Berg, W. J., van der Wal, W., van Wessem, M., Vishwakarma, B. D., Wiese, D., Wilton, D., Wagner, T., Wouters, B., Wuite, J., & Team, T. I. (2020). Mass balance of the Greenland Ice Sheet from 1992 to 2018. *Nature*, 579(7798), 233–239, <https://doi.org/10.1038/s41586-019-1855-2>.
- Shroyer, E. L., Padman, L., Samelson, R., Münchow, A., & Stearns, L. A. (2017). Seasonal control of Petermann Gletscher ice-shelf melt by the ocean’s response to sea-ice cover in Nares Strait. *Journal of Glaciology*, 63(238), 324–330, <https://doi.org/10.1017/jog.2016.140>.
- Slater, D. A., Felikson, D., Straneo, F., Goelzer, H., Little, C. M., Morlighem, M., Fettweis, X., & Nowicki, S. (2020). Twenty-first century ocean forcing of the Greenland ice sheet for modelling of sea level contribution. *The Cryosphere*, 14(3), 985–1008, <https://doi.org/10.5194/tc-14-985-2020>.
- Smith, B. E., Fricker, H. A., Joughin, I. R., & Tulaczyk, S. (2009). An inventory of active subglacial lakes in Antarctica detected by ICESat (2003–2008). *Journal of Glaciology*, 55(192), 573–595, <https://doi.org/10.3189/002214309789470879>.
- Smith, E. C., Hattermann, T., Kuhn, G., Gaedicke, C., Berger, S., Drews, R., Ehlers, T. A., Franke, D., Gromig, R., Hofstede, C., Lambrecht, A., Läufer, A., Mayer, C.,

- Tiedemann, R., Wilhelms, F., & Eisen, O. (2020). Detailed Seismic Bathymetry Beneath Ekström Ice Shelf, Antarctica: Implications for Glacial History and Ice-Ocean Interaction. *Geophysical Research Letters*, *47*(10), e2019GL086187, <https://doi.org/10.1029/2019GL086187>.
- Smith-Johnsen, S., de Fleurian, B., Schlegel, N., Seroussi, H., & Nisancioglu, K. (2020a). Exceptionally high heat flux needed to sustain the Northeast Greenland Ice Stream. *The Cryosphere*, *14*(3), 841–854, <https://doi.org/10.5194/tc-14-841-2020>.
- Smith-Johnsen, S., Schlegel, N.-J., de Fleurian, B., & Nisancioglu, K. H. (2020b). Sensitivity of the Northeast Greenland Ice Stream to Geothermal Heat. *Journal of Geophysical Research: Earth Surface*, *125*(1), e2019JF005252, <https://doi.org/10.1029/2019JF005252>.
- Stanton, T., Shaw, W., Truffer, M., Corr, H., Peters, L., Riverman, K., Bindschadler, R., Holland, D., & Anandakrishnan, S. (2013). Channelized ice melting in the ocean boundary layer beneath Pine Island Glacier, Antarctica. *Science*, *341*(6151), 1236–1239, <https://doi.org/10.1126/science.1239373>.
- Stewart, C. L. (2018). *Ice-ocean interactions beneath the north-western Ross Ice Shelf, Antarctica*. PhD thesis, University of Cambridge. <https://doi.org/10.17863/CAM.21483>.
- Stewart, C. L., Christoffersen, P., Nicholls, K. W., Williams, M. J., & Dowdeswell, J. A. (2019). Basal melting of Ross Ice Shelf from solar heat absorption in an ice-front polynya. *Nature Geoscience*, *12*(6), 435–440, <https://doi.org/10.1038/s41561-019-0356-0>.
- Straneo, F., Hamilton, G. S., Stearns, L. A., & Sutherland, D. A. (2016). Connecting the greenland ice sheet and the ocean: A case study of helheim glacier and sermilik fjord. *Oceanography*, *29*(4), 34–45, <https://doi.org/10.5670/oceanog.2016.97>.
- Straneo, F., Sutherland, D. A., Holland, D., Gladish, C., Hamilton, G. S., Johnson, H. L., Rignot, E., Xu, Y., & Koppes, M. (2012). Characteristics of ocean waters reaching Greenland's glaciers. *Annals of Glaciology*, *53*(60), 202–210, <https://doi.org/10.3189/2012AoG60A059>.
- Thomsen, H. H., Reeh, N., Olesen, O. B., Bøggilde, C. E., Starzer, W., Weidick, A., & Higgins, A. (1997). The Nioghalvfjærdsfjorden glacier project, North-East Greenland: a study of ice sheet response to climatic change. *Review of Greenland activities*, (pp. 95–103), <https://doi.org/10.34194/ggub.v176.5073>.
- Timmermann, R. & Hellmer, H. (2013). Southern Ocean warming and increased ice shelf basal melting in the twenty-first and twenty-second centuries based on coupled ice-ocean finite-element modelling. *Ocean Dynamics*, *63*, <https://doi.org/10.1007/s10236-013-0642-0>.
- Timmermann, R., Wang, Q., & Hellmer, H. (2012). Ice-shelf basal melting in a global finite-element sea-ice/ice-shelf/ocean model. *Annals of Glaciology*, *53*(60), 303–314, <https://doi.org/10.3189/2012AoG60A156>.
- van Wessem, J. M., Reijmer, C. H., Morlighem, M., Mouginot, J., Rignot, E. and cMedley, B., Joughin, I., Wouters, B., Depoorter, M. A., Bamber, J. L., Lenaerts,

- J. T. M., van de Berg, W. J., van den Broeke, M. R., & van Meijgaard, E. (2014). Improved representation of East Antarctic surface mass balance in a regional atmospheric climate model. *Journal of Glaciology*, *60*(222), 761–770, <https://doi.org/10.3189/2014JoG14J051>.
- Vaňková, I., Nicholls, K. W., Corr, H. F., Makinson, K., & Brennan, P. V. (2020). Observations of tidal melt and vertical strain at the Filchner-Ronne Ice Shelf, Antarctica. *Journal of Geophysical Research: Earth Surface*, *125*(1), e2019JF005280, <https://doi.org/10.1029/2019JF005280>.
- Vaňková, I., Nicholls, K. W., & Corr, H. F. J. (2021). The Nature of Ice Intermittently Accreted at the Base of Ronne Ice Shelf, Antarctica, Assessed Using Phase-Sensitive Radar. *Journal of Geophysical Research: Oceans*, *126*(10), e2021JC017290, <https://doi.org/10.1029/2021JC017290>.
- Vaughan, D. G., Corr, H. F., Bindenschadler, R. A., Dutrieux, P., Gudmundsson, G. H., Jenkins, A., Newman, T., Vornberger, P., & Wingham, D. J. (2012). Subglacial melt channels and fracture in the floating part of Pine Island Glacier, Antarctica. *Journal of Geophysical Research: Earth Surface*, *117*(F3), <https://doi.org/10.1029/2012JF002360>.
- Walford, M. E. R. & Harper, M. F. L. (1981). The detailed study of glacier beds using radio-echo techniques. *Geophysical Journal International*, *67*(2), 487–514, <https://doi.org/10.1111/j.1365-246X.1981.tb02762.x>.
- Washam, P., Nicholls, K. W., Münchow, A., & Padman, L. (2019). Summer surface melt thins Petermann Gletscher Ice Shelf by enhancing channelized basal melt. *Journal of Glaciology*, *65*(252), 662–674, <https://doi.org/10.1017/jog.2019.43>.
- Wearing, M. G., Stevens, L. A., Dutrieux, P., & Kingslake, J. (2021). Ice-Shelf Basal Melt Channels Stabilized by Secondary Flow. *Geophysical Research Letters*, *48*(21), e2021GL094872, <https://doi.org/10.1029/2021GL094872>.
- Weikusat, I., Kipfstuhl, S., Faria, S. H., Azuma, N., & Miyamoto, A. (2009). Subgrain boundaries and related microstructural features in EDML (Antarctica) deep ice core. *Journal of Glaciology*, *55*(191), 461–472, <https://doi.org/10.3189/002214309788816614>.
- Wilson, N. & Straneo, F. (2015). Water exchange between the continental shelf and the cavity beneath Nioghalvfjærdsbræ (79 North Glacier). *Geophysical Research Letters*, *42*(18), 7648–7654, <https://doi.org/10.1002/2015GL064944>.
- Wilson, N., Straneo, F., & Heimbach, P. (2017). Satellite-derived submarine melt rates and mass balance (2011–2015) for Greenland’s largest remaining ice tongues. *The Cryosphere*, *11*(6), 2773–2782, <https://doi.org/10.5194/tc-11-2773-2017>.
- Young, T. J., Martín, C., Christoffersen, P., Schroeder, D. M., Tulaczyk, S. M., & Dawson, E. J. (2021). Rapid and accurate polarimetric radar measurements of ice crystal fabric orientation at the Western Antarctic Ice Sheet (WAIS) Divide ice core site. *The Cryosphere*, *15*(8), 4117–4133, <https://doi.org/10.5194/tc-15-4117-2021>.
- Young, T. J., Schroeder, D. M., Christoffersen, P., Lok, L. B., Nicholls, K. W., Brennan, P. V., Doyle, S. H., Hubbard, B., & Hubbard, A. (2018). Resolving the internal and basal geometry of ice masses using imaging phase-sensitive radar. *Journal of*

Glaciology, 64(246), 649–660, <https://doi.org/10.1017/jog.2018.54>.

- Zeising, O. (2018). Determining of Basal Melt Rate and Anisotropy of Filchner Ice Shelf, Antarctica, from Phase-sensitive Radar Measurements. *Master thesis*.
- Zeising, O., Helm, V., Khan, S. A., Neckel, N., Steinhage, D., & Humbert, A. (2021). GNSS measurements at 79°N Glacier in 2017. PANGAEA. <https://doi.org/10.1594/PANGAEA.928940>.
- Zeising, O., Helm, V., Steinhage, D., & Humbert, A. (2021a). GNSS measurements at a basal melt channel of the southern Filchner Ice Shelf, Antarctica. <https://doi.org/10.1594/PANGAEA.932441>.
- Zeising, O. & Humbert, A. (2021a). Autonomous phase-sensitive radar (ApRES) measurements at EastGRIP drill site, Greenland, PANGAEA. <https://doi.org/10.1594/PANGAEA.931018>.
- Zeising, O. & Humbert, A. (2021b). Indication of high basal melting at the EastGRIP drill site on the Northeast Greenland Ice Stream. *The Cryosphere*, 15(7), 3119–3128, <https://doi.org/10.5194/tc-15-3119-2021>.
- Zeising, O., Neckel, N., Steinhage, D., Scheinert, M., & Humbert, A. (2020). Stake surface ablation/accumulation measurements at 79°N Glacier between 2017 and 2018. <https://doi.org/10.1594/PANGAEA.922131>.
- Zeising, O., Steinhage, D., & Humbert, A. (2021b). Autonomous phase-sensitive radar (ApRES) measurements at a basal melt channel of the southern Filchner Ice Shelf, Antarctica between 2016/17 and 2017/18. <https://doi.org/10.1594/PANGAEA.932413>.
- Zeising, O., Steinhage, D., & Humbert, A. (2021c). Repeated pRES measurements and derived Lagrangian basal melt rates at Filchner Ice Shelf between 2015/16 and 2016/17. <https://doi.org/10.1594/PANGAEA.930735>.
- Zeising, O., Steinhage, D., Neckel, N., & Humbert, A. (2021d). Time series of Lagrangian basal melt rates at 79°N Glacier between 2016 and 2020. <https://doi.org/10.1594/PANGAEA.928903>.
- Zeising, O., Steinhage, D., Neckel, N., Rückamp, M., & Humbert, A. (2021e). Lagrangian basal melt rates at 79°N Glacier between 2017 and 2018. <https://doi.org/10.1594/PANGAEA.928541>.
- Zeising, O., Steinhage, D., Nicholls, K. W., Corr, H. F. J., Stewart, C. L., & Humbert, A. (2021f). Basal melt of the southern Filchner Ice Shelf, Antarctica. *The Cryosphere Discussions [preprint]*, (pp. 1–19)., <https://doi.org/10.5194/tc-2021-230>.

Lists

List of figures

1.1	Ice sheet and ice shelf geometry with physical processes	2
1.2	Radar and other geophysical methods and the investigated processes	4
2.1	Continuum mechanics related material bodies	8
3.1	Temperature curve of ice/water and volumetric water content	16
4.1	Reflection and refraction of an electromagnetic wave	23
4.2	pRES measurement at 79NG	25
4.3	Raw data of pRES measurement	28
4.4	Range imaging of pRES measurement	29
4.5	Setup of an pRES point measurement	31
4.6	Analysis of vertical displacements of internal segments of single-repeated pRES measurement	34
4.7	Analysis of vertical displacement of basal segment	35
4.8	Setup of an ApRES measurement in the accumulation zone	36
4.9	Setup of an ApRES measurement in the ablation zone	36
4.10	Analysis of ApRES time series	38
4.11	Vertical displacement time series of internal segment	39
4.12	Vertical displacement time series of basal segment	39
5.1	Surface ice flow velocity map of GrIS	41
6.1	Surface ice flow velocity map of the Greenland Ice Sheet	47
6.2	Derived vertical displacements from the 2017/18 ApRES time series	53
6.3	Sketch of the energy balance at the ice base	56
6.4	Magnitude of terms in the energy jump condition at the ice base	57
6.5	Vertical strain distributions	59
6.6	Derived vertical displacements from the 2018/19 ApRES time series	60
7.1	Basal melt rate distribution and airborne radar profiles at the floating tongue of 79NG	66
7.2	ApRES2a echograms	69
7.3	Airborne radar echograms along and across ice flow of 79NG	74
7.4	Surface lowering above central channel	75
7.5	Distribution of basal melt rates as a function of distance from the grounding line	76
7.6	Growing basal channel from pRES and UWB echograms	77

7.7	Basal melt rate time series of all ApRES measurements	78
7.8	Comparison of 79NG geometry between 1998 (reflection seismics) and 2018 (UWB)	79
7.9	Comparison of basal melt rates derived from in-situ and satellite measurements	81
7.10	Sketch of off-nadir reflections and their influence on basal melt rates	85
7.11	ApRES and pRES measurements with identified nadir and off-nadir reflections.	86
7.12	ApRES1 echograms	88
7.13	ApRES2b echograms	89
7.14	ApRES3 echograms.	90
8.1	Surface ice flow velocity map of AIS	93
9.1	Map of study area at the southern FIS with derived melt rates	100
9.2	Distribution of pRES-derived results	102
9.3	Variation of the basal melt rate	103
9.4	Small scale variability of basal melt rates and ice-shelf draft	104
9.5	Comparison of remote sensing and pRES-derived results.	107
9.6	Airborne radar echograms.	109
9.7	Amplitude profiles of first and repeated measurements.	110
9.8	Variation of the dynamic ice thickness change.	111
9.9	Variation of the ice thickness change.	112
10.1	Map of the Ronne and Filchner ice shelves with study area near the Support Force Glacier	120
10.2	Spatial distribution of pRES-derived basal melt rates and ice thickness	126
10.3	Observed and synthetic melt rates and observed and present day advected ice thickness	127
10.4	Time series of basal melting at ApRES location outside the channel	128
10.5	Cross-section of the model geometry	131
10.6	Results of first experiment	133
10.7	Results of second experiment	134
10.8	Comparison of observed and simulated displacements of second experiment	136
10.9	Strain analysis of an pRES measurement	142
10.10	Distribution of pRES-derived change in ice thickness due to strain and due to surface process	143
10.11	Surface elevation and basal melt rates with frequency spectrum	144
10.12	Ice viscosity in the melt channel obtained from inverse modeling	146
10.13	Model input derived from pRES measurements and RACMO	147
10.14	Evolution of the base for the first experiment	148
10.15	Evolution of the base for the second experiment	148
10.16	First experiment: comparison of displacements	149

10.17	Simulated vertical strain of the current configuration of the second experiment	150
10.18	Surface elevation and ice thickness from different viscosities	151
A.1	Overview of the study area	V
A.2	Near surface air temperature and ERA5 2 m air temperature reanalysis	VIII
A.3	Relation between near surface air temperature, horizontal surface velocities and surface melt estimates	XI
A.4	Rapid drainage event (< 24 h) of lake 11 in September 2017	XII
A.5	ERA5 reanalysis data for selected dates with high surface melt	XIV
A.6	Increase in summer 2017 surface velocities upstream the hinge line of 79°N Glacier	XV
B.1	Overview of the study area	XXVIII
B.2	Tidal modulation of glacier flow at the GPS stations	XXX
B.3	Tidal effect on basal boundary conditionsXXXII
B.4	Influence of vertical deformation versus sliding in glacier motionXXXV
B.5	Role of sliding and elastic strain of GrIS	XXXVI
B.6	Crevasse fields and stress change of GrIS	XXXIX

List of tables

4.1	pRES specifications	24
6.1	Results ApRES time series	52
7.1	Possibilities how basal channels affect recording of nadir and off-nadir reflections	83
10.1	Description of symbols	141

List of abbreviations

ADC	Analogue-to-Digital Converter
AIW	Atlantic Intermediate Water
AWI	Alfred Wegener Institute
AIS	Antarctic Ice Sheet
ApRES	Autonomous phase-sensitive Radio Echo Sounder
BAS	British Antarctic Survey
CFL	Central Flow Line
EAIS	East Antarctic Ice Sheet
EastGRIP	<i>East Greenland Ice-core Project</i>
FESOM	Finite Element Sea Ice-Ocean Model
FFT	Fast Fourier Transformation
FIS	Filchner Ice Shelf
FISP	<i>Filchner Ice Shelf Project</i>
FMCW	Frequency-Modulated Continuous Wave
GNSS	Global Navigation Satellite System
GrIS	Greenland Ice Sheet
GROCE	<i>Greenland Ice Sheet – Ocean Interaction</i>
HF	High Frequency
79NG	Nioghalvfjærdsbræ (79°N Glacier)
NEGIS	Northeast Greenland Ice Stream
pRES	phase-sensitive Radio Echo Sounder
Radar	radio detection and ranging
SFG	Support Force Glacier
SG	Storstrømmen Glacier
TWT	Two Way Travel Time
UHF	Ultra High Frequency
VHF	Very High Frequency
WAIS	West Antarctic Ice Sheet
ZI	Zachariæ Isstrøm

List of symbols

Symbol	Name	Unit
γ	correlation coefficient	
γ_S	turbulent salt flux	m s^{-1}
γ_T	turbulent heat flux	m s^{-1}
δ_c	coarse-range offset	m
δ_f	fine-range offset	m
δ_t	total offset	m
ΔH	change in ice thickness	m
ΔH_ε	(dynamic) change in ice thickness due to vertical strain	m
ΔH_b	change in ice thickness due to basal melt	m
ΔH_f	change in ice thickness due to firn densification	m
ΔH_s	change in ice thickness due to ablation/accumulation	m
Δt	time period	a
ε	strain tensor	
$\dot{\varepsilon}$	strain rate tensor	s^{-1}
ε_0	permittivity in vacuum	$\text{A m V}^{-1} \text{s}^{-1}$
ε_r	relative permittivity	
η	shear viscosity	Pa s
θ_1	angle of incident of the incident and reflected wave	rad
θ_2	angle of incident of the refracted wave	rad
κ_i	heat conductivity of ice	$\text{W m}^{-1} \text{K}^{-1}$
λ_c	centre wavelength	m
μ_0	permeability in vacuum	$\text{V s A}^{-1} \text{m}^{-1}$
μ_r	relative permeability	
ν	kinematic viscosity of sea water	$\text{m}^2 \text{s}^{-1}$
ρ	density	kg m^{-3}
ρ_i	density of ice	kg m^{-3}
ρ_{oc}	density of ocean	kg m^{-3}
τ_b	basal shear stress	Pa
τ	two way travel time	s
τ	two way travel time	s
Φ_d	deramped phase	rad
Φ_{dc}	centred deramped phase	rad
Φ_r	received phase	rad
Φ_t	transmitted phase	rad
ϕ	energy flux density	W m^2
φ	deformation	

Symbol	Name	Unit
Ω_0	reference configuration	
Ω_t	present configuration	
ω	angular frequency	Hz
ω_c	centre frequency	Hz
ω_d	deramped frequency	Hz
ω_r	received frequency	Hz
ω_t	transmitted frequency	Hz
a_b	basal mass balance	m a^{-1}
a_s	surface mass balance	m a^{-1}
\mathcal{B}	Clausius-Clapeyron constant	K Pa^{-1}
B	bandwidth	Hz
c_i	specific heat capacity of ice	$\text{J kg}^{-1} \text{K}^{-1}$
$c_{p,oc}$	specific heat capacity of ocean	$\text{J kg}^{-1} \text{K}^{-1}$
c	speed of light	m s^{-1}
c_i	propagation velocity in ice	m s^{-1}
$d\mathbf{x}$	line element in present configuration	m
$d\mathbf{X}$	line element in reference configuration	m
\mathbf{d}	strain rate tensor	s^{-1}
\mathbf{E}	electric field	V m^{-1}
E_0	complex amplitude of incident wave	V
E_1	complex amplitude of reflected wave	V
E_2	complex amplitude of refracted wave	V
\mathbf{F}	deformation gradient	
\mathbf{f}	surface force	N m^{-3}
g	energy density	J m^{-3}
H	ice thickness	m
i	complex number	
K	chirp gradient	Hz s^{-1}
k	wavenumber (magnitude of propagation vector)	m^{-1}
k^2	basal friction coefficient	s m^{-1}
\mathcal{L}	characteristic length scale	m
L	latent heat	J kg^{-1}
l_m	lag of maximum correlation value	
l_p	lag of minimum phase difference	
l	lag	
\mathbf{l}	velocity gradient	s^{-1}
M_1	first measurement	
M_2	repeated measurement	

Symbol	Name	Unit
N	effective pressure	Pa
\mathbf{n}	normal vector	
n	refractive index	
n_s	range bin	
p	hydrostatic pressure	Pa
p	pad-factor	
Pr	Prandtl number	
\mathbf{Q}	volume flux	$\text{m}^3 \text{s}^{-1}$
Q_i	energy to heat ice	J
Q_m	energy to melt ice	J
\mathbf{q}	heat flux	W m^{-2}
q_{geo}	geothermal heat flux	W m^{-2}
q_{oc}	oceanic heat flux	W m^{-2}
q_{sw}	heat flux from subglacial water	W m^{-2}
$R_{1,2}$	reflection coefficient	
R	range	m
R_c	coarse range	m
R_f	fine range	m
r	radius footprint	m
r	specific radiation power	$\text{m}^2 \text{s}^{-3}$
S_b	salinity of boundary layer	psu
S_{oc}	salinity of ocean	psu
Sc	Schmidt number	
s	supply density	W m^{-3}
T	temperature	K
T_0	pressure melting temperature for low pressure	K
T_b	temperature of boundary layer	K
T_m	pressure melting temperature	K
T_{oc}	temperature of the ocean	K
$T_{1,2}$	transmission coefficient	
T	pulse duration	s
\mathbf{t}	Cauchy stress tensor	Pa
t	time	s
\mathbf{u}	displacement	m
u	specific internal energy	J kg^{-1}
u_*	friction velocity	m s^{-1}
V	volume	m^3
\mathbf{v}	velocity	m s^{-1}

Symbol	Name	Unit
\mathbf{v}_{oc}	ocean velocity	m s^{-1}
v_b	basal velocity	m s^{-1}
\mathbf{w}	spin tensor	s^{-1}
\mathbf{x}	position vector in present configuration	
\mathbf{X}	position vector in reference configuration	
z	range	m
z_b	ice draft	m

Acknowledgements

First of all, I want to thank my supervisor **Angelika Humbert** for making this PhD possible. You supported me over all the years since my master's thesis which I deeply appreciate. Through your tireless efforts you made it possible for me to go on expeditions and gather field experiences in the unique and beautiful nature of Northeast Greenland. I am extremely grateful for all the knowledge you have passed on to me.

As part of my Thesis Advisory Committee, **Julia Christmann**, **Ralph Timmermann** and **Torsten Kanzow** accompanied my work over the entire period and guided me throughout my studies, for which I want to thank you. In particular, I want to thank **Julia**. You always had an open ear and kept answering my questions, mostly about stress and strain – sometimes with a sponge. It was always a pleasure to meet and discuss my theories with **Ralph** to get his oceanographic expertise. Your very helpful advice has constantly helped me to focus on the essentials. I also want to thank **Torsten** for leading the GROCE project, of which I was very glad to be a part of and contribute with my work.

Special thanks go to **Daniel Steinhage**. No matter what kind of problem I encountered, I always could go to your office and solve it together with you. Without you, this work would not have been possible since you spent weeks and months in the polar regions in order to perform the measurements I analysed in this thesis. In addition, you, **Andreas Frenzel** and **Matthias Hüther** supported me with all of your expertise when I prepared my field expeditions. One of the greatest pleasures during this thesis was the time I spent at the 79°N Glacier in Greenland with **Niklas Neckel**. With your calm manners you led this expedition and made it a unique experience. During the expedition and while I was writing my first manuscript, I was always able to count on your support, which I really appreciate. I would also like to thank the ExNGT-Group of **Maria Hörhold**, **Johannes Freitag** and **Iben Koldtoft**, who were on the Greenland Ice Sheet with **Angelika** and me. It was an adventure to be with you on board the AWI aircraft Polar5 and to perform measurements at many places on the Greenland Ice Sheet.

I extend my gratitude to **Olaf Eisen** for his advice, support and trust in me. I am looking forward to working with you in the future. I also want to express my appreciation for the support by **Ilka Weikusat** who is coordinating the German contribution to EastGRIP and **Frank Wilhelms** who is leading the glaciology

department at AWI.

I want to thank **Veit Helm**, **Thomas Kleiner**, **Martin Rückamp**, **Coen Hofstede** and **Daniela Jansen** for their support whenever I had questions about my research. It was great to work with my PhD colleagues **Steven Franke**, **Nico Stoll** and **Nils Dörr**. Especially, it was a pleasure sharing my office with **Steven** and **Hannah Meyer**.

Without the work of **Keith W. Nicholls** who developed the pRES system and **Craig L. Stewart** who wrote the original MATLAB code for processing the pRES measurements, this thesis would not have been possible.

Finally, I want to thank my parents **Michaela** and **Gunter**, my brother **Arne** and in particular **Saskia** for your unlimited support, trust and encouragement.

Appendix

Seasonal Observations at 79° N Glacier (Greenland) From Remote Sensing and in situ Measurements

A

This chapter is published as a research article at the journal *Frontiers in Earth Science* in 2020 (Neckel et al., 2020).

Authors and affiliations

Niklas Neckel¹, Ole Zeising^{1,2}, Daniel Steinhage¹, Veit Helm¹ and Angelika Humbert^{1,2}

¹Alfred-Wegener-Institut Helmholtz-Zentrum für Polar- und Meeresforschung, Bremerhaven, Germany

²Department of Geosciences, University of Bremen, Bremen, Germany

Contributions

N.Neckel processed and analysed the remote sensing data and wrote the initial draft of the manuscript. N.Neckel, **O.Zeising**, and D.Steinhage conducted field work. **O.Zeising** and V.Helm processed the GPS data. A.Humbert designed the project, lead the field program and supervised the study. All authors continuously discussed the results.

Abstract

This study investigates seasonal ice dynamics of Nioghalvfjærdsfjorden or 79°N Glacier, one of the major outlet glaciers of the North East Greenland Ice Stream. Based on remote sensing data and in-situ GPS measurements we show that surface melt water is quickly routed to the ice-bed interface with a direct response on ice velocities measured at the surface. From the temporally highly resolved GPS time series we found summer peak velocities of up to 22 % faster than their winter baseline. These average out to 9 % above winter velocities when relying on temporally lower resolved velocity estimates from TerraSAR-X intensity offset tracking. From our GPS time series we also found short term ice acceleration after the melt season. By utilizing optical satellite imagery and interferometrically derived digital elevation models we were able to link the post melt season speed-up to a rapid lake drainage event (24 h) with an estimated drainage volume of $28 \times 10^6 \text{ m}^3$. We further highlight that GPS measurements are needed to resolve short term velocity fluctuations with low amplitudes, whereas remote sensing estimates are rather useful for the calculation of general trends in velocity behavior.

A.1 Introduction

Each summer substantial amounts of melt water reach the base of the Greenland Ice Sheet (GrIS) through existing faults such as crevasses and moulines or through hydro-fracturing beneath supraglacial lakes. Once the water reaches the ice-bed interface it can act as a lubricant, seasonally enhancing ice flow in the ablation area (e.g., Zwally et al., 2002; Hoffman et al., 2011; Joughin et al., 2013; Tedesco et al., 2013). Typically, the increase in ice velocity is most pronounced at the beginning of the melt season due to an inefficient subglacial drainage system which is highly sensitive to an increase in water pressure (Bartholomew et al., 2010). During the melt season a more efficient channelized basal drainage system is developed resulting in a deceleration of ice velocities towards the end of the melt season. This general seasonal velocity pattern is particularly observed at glaciers in the south-eastern and western part of Greenland (Bartholomew et al., 2010; Moon et al., 2014; Doyle et al., 2015). In contrast, several glaciers, mostly located in the northern part of Greenland show a direct and strong correspondence between ice velocity and melt water availability suggesting that the development of an efficient basal drainage system is limited or shifted for these glaciers (Moon et al., 2014; Rathmann et al., 2017; Vijay et al., 2019).

So far, most studies investigating seasonal variations of surface velocities are

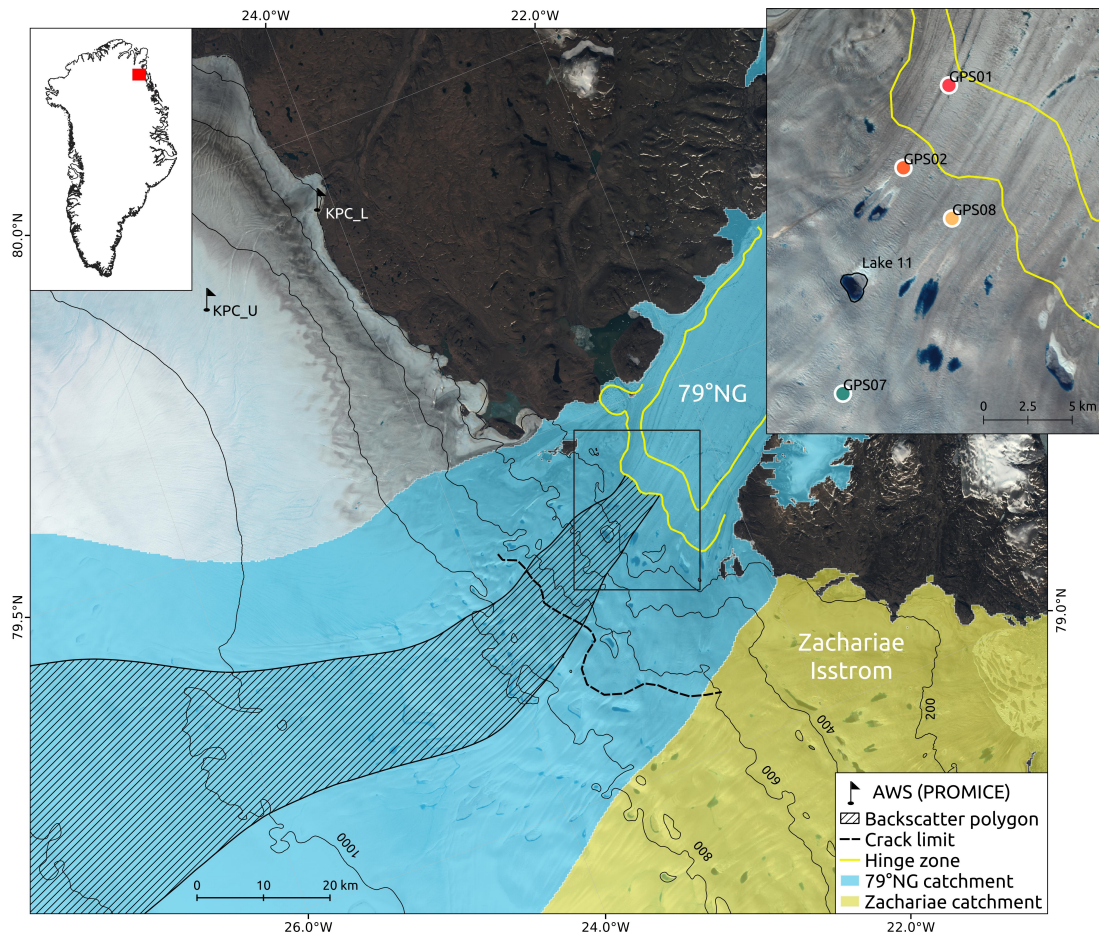


Figure A.1: Overview of the study area. Hatched polygon marks the area used for the backscatter analysis shown in Figure A.2b. Catchment areas are from Krieger et al. (2020a). Inset shows the locations of GPS receivers shown in Figures A.3 and S2. KPC_U and KPC_L are the closest Automatic Weather Stations (AWS) from the PROMICE project (Fausto and van As, 2019). In the background is a Sentinel-2 acquisition from 28 July 2017. Hinge zone is determined from ERS-II SAR interferometry, data were acquired in April/May 2011. Upper limit of major crevasses is shown as dashed black line.

concentrated to the western part of Greenland where supraglacial lakes form and drain frequently and surface velocities show the typical seasonal pattern described above (e.g., Zwally et al., 2002; Bartholomew et al., 2010; Joughin et al., 2013). However, it has been shown previously that the largest increase of supraglacial lakes will likely take place in north-eastern Greenland (Ignéczi et al., 2016). Until now little is known about the influences of supraglacial lakes on ice dynamics in this area.

In this study we focus on Nioghalvfjærdsfjorden or 79°N Glacier, located in north-eastern Greenland (Figure A.1). Draining approximately 6% of the GrIS by area (Krieger et al., 2020a), 79°N Glacier is one of the major outlet glaciers of the North East Greenland Ice Stream, a potentially large contributor to future sea level rise. In order to further investigate the seasonal behavior of 79°N Glacier we

combine remote sensing observations with *in situ* data acquired in 2017. Based on radar backscatter data from the Sentinel-1 satellite mission we link surface melt events to variations in glacier velocities. The latter are derived from *in situ* GPS measurements accompanied by estimates from intensity offset tracking on high resolution TerraSAR-X data. We further investigate the effect of a rapid supraglacial lake drainage event on the velocity dataset and give estimates on the timing and amount of water released during the lake drainage.

A.2 Seasonal melt patterns

To obtain information as to when the melt season starts, for how long it lasts and to what altitude surface melt can be expected we extracted a dense time series of backscatter values from the Sentinel-1 archive. Sentinel-1A was launched on 3 April 2014, followed by its twin satellite Sentinel-1B on 25 April 2016. Both satellites are equipped with a C-band Synthetic Aperture Radar (SAR) sensor with a shifted repeat cycle of 12 days, resulting in a 6 day revisiting time when both satellites are employed. In this study we used numerous Level-1 Single Look Complex (SLC) products obtained in Interferometric Wide swath (IW) mode. The data were acquired between January 2015 and January 2019 in relative orbit 74 over the study area. Following the suggestions of [Winsvold et al. \(2018\)](#) we build our analysis on a time series of the terrain corrected backscatter coefficient gamma nought (γ^0). The processing includes calibrating, mosaicing and multi-looking of the TOPS SAR data followed by a terrain correction and geocoding step. Radiometric calibration was done within the GAMMA[®] software resulting in σ^0 backscatter values using the ellipsoid area as reference area for normalization. Subsequently all bursts of each acquisition were mosaiced into a continuous SLC image. In order to reduce noise, multi-looking was performed with 10 looks in range direction and 2 looks in azimuth direction. To obtain terrain corrected γ^0 values we applied an additional reference area normalization based on the ArcticDEM, gridded to 100 m spatial resolution ([Small, 2011](#); [Porter et al., 2018](#)). Finally, all SAR images were geocoded and linear backscatter values were translated to decibels. Backscatter values returned from glaciers and ice sheets heavily depend on instrument related parameters such as incidence angle and polarization as well as on characteristics of the upper surface layers such as roughness, water content, snow density, grain size and impurities (e.g., [Rau and Braun, 2002](#); [Winsvold et al., 2018](#)). As wet snow absorbs most of the SAR signal, low surface scattering prevails in these areas, allowing to discriminate between wet and frozen zones on a glacier.

In order to estimate the onset and duration of surface melt we employed the

binned backscatter values (γ^0) from the time series shown in Figure A.2b. Following QSCAT scatterometer studies over Greenland (e.g., Wang et al., 2007) we compared all γ^0 values to the mean γ^0 of the respective altitude band for December, January and February of the previous winter ($W\gamma^0$). If γ^0 drops below $W\gamma^0 - 3dB$ the respective bin is treated as surface melt and is marked by a black dot in Figure A.2b. Due to larger data gaps and a 12-day repeat pass in 2015 and 2016 confident interpretations can only be made for 2017 and 2018. In 2017 the onset of surface melt is set to 2 June and lasts until 6 September (96 days) where isolated surface melt is found at low elevations of <250 m. At the other end of the scale surface melt reaches elevations of almost 1750 m on 1 August 2017 (Figure A.2b and Video S1). In 2018 surface melt starts on 15 June and ends on 7 September (84 days). Similar to 2017 the maximum extent of surface melt is found on 2 August, while isolated patches are found at low elevations until September 2018 (Figure A.2b and Video S1). Due to the 6-day repeat pass of Sentinel-1 these estimates might be underestimated by up to 10 days in the most unfavorable case.

As surface melt heavily depends on air temperature, we additionally employed temperature data from nearby Automatic Weather Stations (AWS) as well as from the recently released ERA5 reanalysis dataset (Hersbach and Dee, 2016). Here we used daily averages of near surface air temperature acquired by AWS KPC_L and KPC_U of the Programme for Monitoring the Greenland Ice Sheet (PROMICE) (Fausto and van As, 2019). KPC_L and KPC_U are located at an altitude of 370 and 870 m respectively and their positions are marked in Figure A.1. At the position of KPC_U we also extracted 2 m air temperature data from the ERA5 reanalysis dataset (Figure A.2a). ERA5 reanalysis data are available at a spatial resolution of 0.25° and it is worthwhile noting that PROMICE observations are not assimilated in the reanalysis dataset (Delhasse et al., 2020). Between ERA5 2 m air temperature data and KPC_U near surface air temperature data we found a squared correlation coefficient of 0.98 when investigating the time interval shown in Figure A.2a (Figure S1).

A.3 Surface velocities

Horizontal surface velocities were obtained by GPS measurements and intensity offset tracking on high resolution TerraSAR-X stripmap data. In summer 2017 four autonomous GPS stations were installed near the hinge zone of 79°N Glacier (Figure A.1). All GPS stations included one state-of-the-art Novatel FlexPak6 L-Band GPS receiver, one Novatel choke ring GPS antenna, at least one data logger, two solar panels, one solar charge controller and two 105 Ah batteries. The

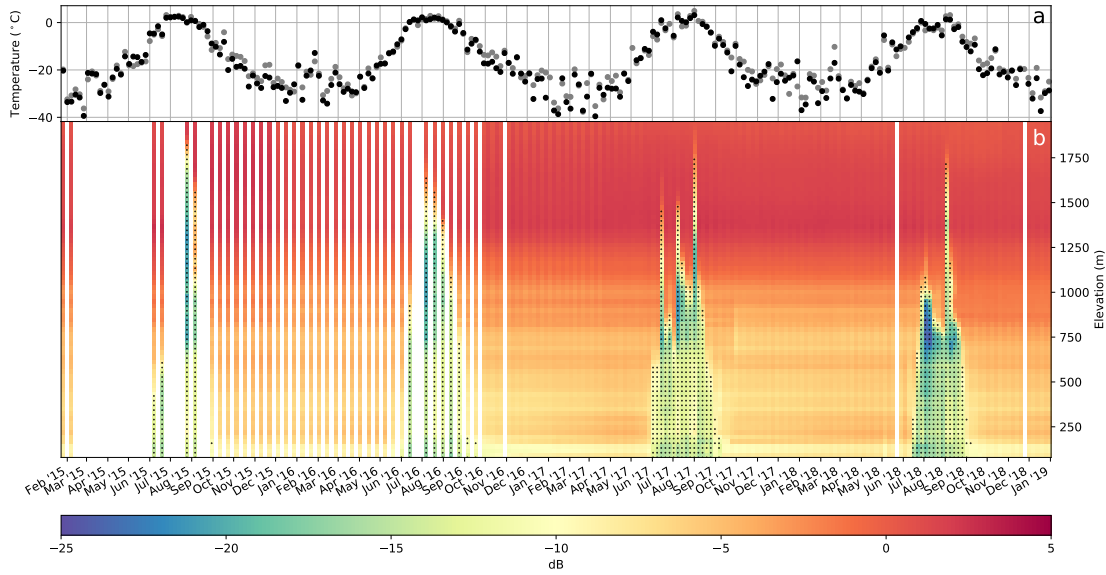


Figure A.2: Near surface air temperature measured at PROMICE AWS KPC_U (Fausto and van As, 2019, Figure A.1, black dots) and ERA5 2 m air temperature reanalysis estimates at the same location (Hersbach and Dee, 2016, grey dots, a). Heat plot of Sentinel-1 backscatter coefficient γ^0 time series (b). Data are extracted from the hatched polygon shown in Figure A.1 and binned to 25 m elevation classes. Bins with surface melt are marked by small black dots.

antennas were mounted on aluminum tripods and fixed to the ice by additional weights and long nails. GPS data were logged every 15 s and were processed using Precise Point Positioning (PPP) processing implemented in the Waypoint[®] software including final precise international GNSS Service ephemerides. Velocities were calculated based on horizontal displacements within a 24 h moving window over all measurements. Each velocity estimate was then allocated to the center time of the moving window. Finally, average velocities were calculated for each day to obtain an overview of the general velocity pattern shown in Figure A.3b-e. In order to detect short term variations in ice velocities (<1 d) related to e.g., lake drainage we produced an additional dataset using a 4 h moving window with no daily averaging (Figure S2). The standard deviation of the horizontal displacement is estimated with <5 mm for all stations. This results in a velocity error of up to 0.06 and 0.01 m d⁻¹ for the 4 and 24 h moving window, respectively. We further obtained velocity fields from TerraSAR-X intensity offset tracking for a similar time period. The processing includes co-registration of SLC data separated by 11 days followed by cross correlating the backscatter intensity of each SLC pair in a predefined moving search window (e.g., Strozzi et al., 2002). Following Rückamp et al. (2019) we chose a window size of 250 m in both range and azimuth direction with a step size of 50 m. Range and azimuth offsets were then projected into a polar stereographic coordinate system assuming surface parallel

ice flow. Surface velocity fields were filtered following the three step filtering approach described by [Lüttig et al. \(2017\)](#). This approach is designed to efficiently detect outliers in surface velocity fields and is based on 1. a segmentation filter which is based on the assumption that velocity fields can be divided into segments of continuous ice flow ([Rosenau et al., 2015](#)), 2. anomalies to a running median and 3. variations of flow directions within a moving search window. Finally, all velocity fields were gridded to 250 m and small data gaps were interpolated with an inverse distance weighting scheme. The latter step was applied since surface velocities were calculated during the melt season where the presence of water strongly modifies the radar backscatter resulting in rather noisy velocity estimates and data gaps. However, as our GPS receivers are located in the central part of the ice stream we expect only small variations in the ice velocities of adjacent flowlines, suggesting a lower sensitivity towards grid resolution when compared to e.g., shear margins ([Joughin et al., 2018](#)). As a measure of confidence we included the weighted standard deviation of the pixel values employed in the inverse distance interpolation of the velocity estimates shown in [Figure A.3b-e](#).

Overall the TerraSAR-X derived velocities are in good agreement with the GPS derived velocities ([Figure A.3b-e](#)). By combining both datasets we found that surface velocities at the four GPS sites start to increase from their winter baseline in early June and are peaking at the end of July / beginning of August 2017 (annotated as summer speed-up in [Figure A.3b](#)). However, velocity estimates derived from GPS data are resolved to a higher temporal resolution than those from intensity offset tracking (1 d versus 11 d). Therefore, a greater amount of detail can be observed in the GPS derived dataset. While all GPS receivers show highest surface velocities on 1 August 2017 this peak is averaged out in the TerraSAR-X estimates leading to slower summer velocities. Depending on the dataset, the location and the winter baseline used as reference, summer acceleration can be up to 22 % for the GPS and 9 % for the TerraSAR-X derived estimates, respectively. Since we lack winter velocities from the GPS stations due to power limitations, all relative velocity changes throughout this study are referenced to the corresponding pixel values of a TerraSAR-X winter velocity field with data acquired on 10 and 21 December 2017 (not shown in [Figure A.3b-e](#)). In order to detect the upper spatial limit of seasonally enhanced flow velocities we calculated differences between all TerraSAR-X velocity fields and the winter 2017 reference field ([Figure A.6](#)). If possible we also computed GPS derived velocity estimates specific to each 11-day time period of the TerraSAR-X estimates. Here we found similar values as from the intensity offset tracking with a summer acceleration of up to 7 % when compared to the December TerraSAR-X velocity field.

After returning to their approximate winter baseline in late August all GPS receivers show a simultaneous speed-up in late September which is significantly lower in the record of GPS 7 (annotated as lake drainage in Figure A.3b, a close-up is shown in Figure S2). Directly after this second velocity peak, velocities remain under their winter baseline for several days, until they slowly start to increase again.

A.4 Lake drainage

To explain the unusual speed-up observed in September 2017, we carefully checked radar and optical satellite acquisitions in this time period. Between 18 and 19 September 2017 we found a sudden drainage of supraglacial lake 11 (name originates from arbitrary indexing of supraglacial lakes in the area, lake position is at -22.978°E , 79.338°N , Figure A.1) on cloud free Sentinel-2 imagery (Figure A.4b, c). In order to obtain an estimate of the drainage volume we further generated two Digital Elevation Models (DEMs) from bistatic TanDEM-X data acquired on 13 and 24 September 2017 following the methods described by Neckel et al. (2013). Both DEMs were vertically adjusted to the same reference DEM by removing a linear trend estimated over stable bedrock. Pixel-by-pixel DEM differences were calculated on the same spatial grid with a resolution of 10 m. The elevation differences are shown in Figure A.4d and show a subsidence of >50 m in the center of the lake. Finally, elevation changes were translated into drainage volume by

$$V_{\text{drain}} = \sum_{i=0}^n (\Delta h^{\text{lake}} p^2)_i, \quad \text{if } \Delta h_i^{\text{lake}} < -1 \quad (\text{A.1})$$

where Δh^{lake} are the elevation changes within manually digitized shorelines, and p is the pixel size which was set to 100 m to reduce noise. In order to solely employ Δh^{lake} values of elevation loss, we introduced a threshold of -1 m in the calculation of V_{drain} . Following Equation 1 we estimated a volume of $28 \times 10^6 \text{ m}^3$ for this drainage event. Almost two month before on 21 July 2017 we installed a data logger at this specific lake with the intention to autonomously record water pressure and temperature. Unfortunately, the data logger could not be recovered in 2018 but was probably lost during the rapid drainage event in September 2017. However, when installing the logger we measured a lake depth of 10.80 m at the location marked by the yellow dot in Figure A.4a (Figure S2). This value fits well to the TanDEM-X derived elevation difference of -11.05 m at the exact location.

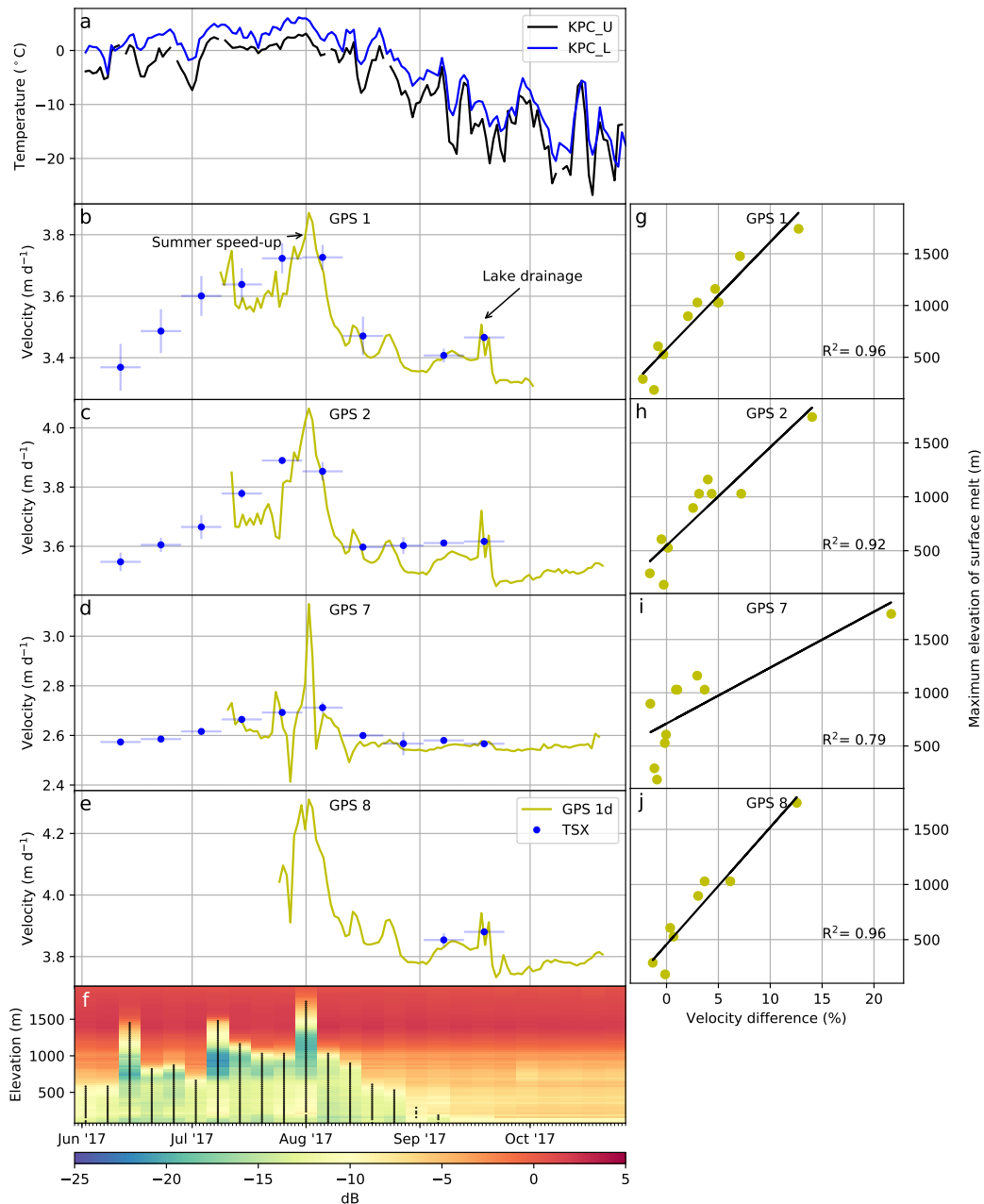


Figure A.3: Relation between near surface air temperature measured at PROMICE AWS KPC_U and KPC_L (a, Fausto and van As, 2019), horizontal surface velocities as measured at the four GPS sites indicated in Figure A.1 (b-e) and surface melt estimates from the Sentinel-1 time series shown in Figure A.2b (f). TerraSAR-X derived surface velocities are centered at the mean date between data acquisitions with light blue bars in x-direction indicating the 11-day period between the dates of data acquisition. Light blue bars in y-direction represent the weighted standard deviation of the pixel values employed in the interpolation of the shown velocity estimates. GPS estimates are averaged over one day. Note the different data ranges in panels b-e. Scatter plots (g-j) show the relation between GPS measured surface velocities relative to a TerraSAR-X derived winter velocity field and the maximum elevation of surface melt from the Sentinel-1 time series shown in Figure A.2b and panel f.

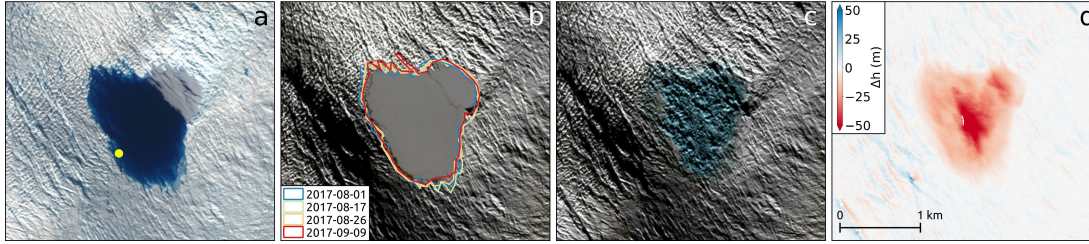


Figure A.4: Rapid drainage event (< 24 h) of lake 11 in September 2017. Sentinel-2 acquisition on 17 August 2017 at 15:09 is shown in **a**, lake is mostly ice free, yellow dot marks the location of lake depth measurement on 21 July 2017 (Figure S2). Sentinel-2 acquisition on 18 September 2017 at 15:49 is shown in **b**, lake is completely covered by lake ice. Additional pre-drainage shorelines are shown. Note the difference in illumination between August and September. Sentinel-2 acquisition on 19 September 2017 at 15:18 is shown in **c**, the lake has drained and is not covered by ice anymore. TanDEM-X derived surface elevation changes between 13 and 24 September 2017 are shown in panel **d**.

A.5 Discussion

By analyzing a dense time series of Sentinel-1 γ^0 backscatter coefficients in relation to surface elevation we obtained a good overview of when the melt season starts and to what altitude surface melt can be expected (Figure A.2b). Also a clear correlation between surface melt and near surface air temperature is found when including additional meteorological datasets in the analysis (Figure A.2a). Focusing on the time with surface velocity measurements, we find that in June, July and August 2017 surface melt is detected generally to elevations between 600 and 1000 m with short term excursions reaching elevations >1250 m. During the melt onset on 2 June 2017 surface melt reaches rather low elevations of 580 m, which is also reflected in the AWS data shown in Figure A.3a. While the higher elevated KPC_U station measured the first positive degree day on 10 June 2017, i.e. 8 days after the detected melt onset, KPC_L recorded the first positive degree day contemporaneous on 1 June 2017. Having in mind that our GPS receivers are located at elevations between 70 and 390 m we conclude that melt water was available during the entire three month period in this region. A general increase in surface velocities is observed at all four GPS stations prior to August 2017 (Figure A.3b-e). Also from our backscatter analysis we detected the largest extent of surface melt at this time reaching elevations of almost 1750 m on 1 August 2017 (Figures A.2b and A.3f). The temporal coexistence of peaks in surface velocities of all GPS receivers to this date is quite striking and suggests a strong and direct reaction of surface velocities to the availability of melt water. At this time also the highest daily mean near-surface air temperatures of $+3.1$ and $+6.1^\circ\text{C}$ were measured at KPC_U and KPC_L respectively, underpinning that surface melt is largely driven by air temperature (Figure A.3a).

This is further supported by ERA5 reanalysis data where a significant anomaly is found when comparing the average 2 m air temperature of 1 August 2017 to the monthly average of July 2017 (Figure A.5a, [Hersbach and Dee, 2016](#)). Also the 0°C isotherm on 1 August 2017 matches quite well with the upper limit of surface melt as detected from the backscatter time series (Figure A.5a). When investigating the scatter plots shown in Figure A.3g-h it is likely that the larger the area affected by surface melt is the stronger the velocity response downstream the glacier. However, the question remains how the melt water is speeding up the glacier. In line with recent work by [Rathmann et al. \(2017\)](#) and [Vijay et al. \(2019\)](#) who also found a direct velocity response of 79°N Glacier to the occurrence of surface melt, we suggest that surface melt water reaches the ice-bed interface quite quickly through predefined pathways such as cracks and crevasses. This is supported when investigating the spatial distribution of seasonal glacier speed-up as shown in Figure A.6. Here the dashed black line marks the upper limit of major crevasses which was delineated with the help of several TerraSAR-X acquisitions. With an average altitude of 680 m this upper crack limit lies at the lower limit of the estimated melt extent shown in Figure A.2b. Even in the time period of the largest melt extent (Figure A.2b) and the highest ice acceleration (Figure A.6d-f) significant changes in surface speed stayed well below this line. This suggests that the melt water from higher elevated regions is routed on the ice surface until it reaches the crevassed zone at lower elevations. Here the water is quickly routed to the ice-bed interface through numerous cracks and crevasses and is acting as a lubricant for the overlaying ice column causing a seasonal acceleration of the ice stream. For the GrIS such mechanisms were first described by [Zwally et al. \(2002\)](#) but were previously known also for mountain glaciers (e.g., [Iken et al., 1983](#)).

After the velocity peak in the beginning of August 2017 velocities started to decrease again accompanied by a decrease in melt extent and air temperature (Figure A.3a-f). Then a second speed-up was recorded by our GPS receivers in September 2017 where no surface melt can be detected from the backscatter time series and near-surface air temperatures measured at KPC_U and KPC_L stayed well below 0°C (Figure A.3a). This second speed-up can clearly be attributed to a rapid drainage event of lake 11 between 18 and 19 September 2017. While the lake was completely covered by lake ice on 18 September 2017 no ice layer was present on 19 September 2017 and the lake area significantly decreased in less than 24 h (Figure A.4b and c). We therefore conclude, that the lake drainage started at some point close to 18 September 2017 and the lake ice broke up due to the drainage event. Considering the short time period of the lake drainage, water-driven fracture propagation seems to be the most likely mechanism to establish

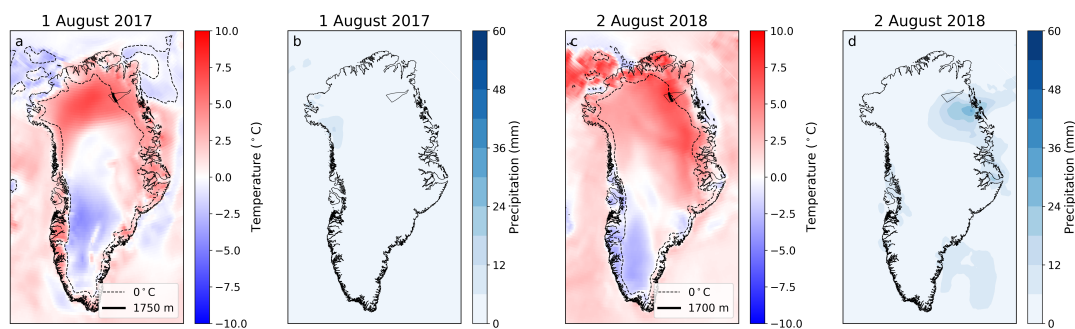


Figure A.5: ERA5 reanalysis data for selected dates with high surface melt. 2 m air temperature anomaly of 1 August 2017 versus the monthly average of July 2017 is shown in **a**, together with the 0°C isotherm and the maximum altitude of surface melt on 1 August 2017 (1750 m). Cumulated hourly precipitation of 1 August 2017 is shown in **b**. Panels **c** and **d** show the same as **a** and **b** but for 2 August 2018. The polygon framed by a black solid line marks the area used for the backscatter analysis shown in Figure A.2b.

a connection to the bed (e.g. [Das et al., 2008](#)). While GPS 1, 2 and 8 received a similar signal on 19 September only a minor speed-up was recorded by GPS 7 which is located upstream of lake 11 (Figures A.1 and A.3b-e). This implies that the water, with an estimated volume of $28 \times 10^6 \text{ m}^3$ was not routed through established channels but overwhelmed the subglacial hydraulic system and spread along the ice-bed interface downstream of lake 11. Here ice velocities increased by up to 24% when compared to pre-drainage velocities (Figure S2). This is in contrast to other studies which report post-drainage ice velocities of 4 to 10 times larger than before a rapid lake drainage event (e.g., [Hoffman et al., 2011](#); [Tedesco et al., 2013](#)). These differences are most likely attributed to the comparatively large distances of our GPS receivers to the lake. While [Tedesco et al. \(2013\)](#) report distances within 2 km of the lake and receiver locations along flowlines through the lake, our GPS receivers are located between 6.5 and 12.5 km from the lake and do not match any flowline through the lake (Figure A.1). Further, it has been shown that changes in water supply are key for driving ice accelerations rather than the absolute amount of water input (e.g., [Schoof, 2010](#); [Bartholomew et al., 2012](#)). This might explain why the relatively large drainage volume has only a limited effect on the ice dynamics in the area.

When focusing our backscatter time series on the melt season 2018 we find indirect evidence for a cold summer with high levels of precipitation as described elsewhere ([Polar Portal Season Report, 2018](#)). Compared to 2017 the melt season started almost two weeks later on 15 June 2018. The largest extent of surface melt is found on 2 August 2018 where it reaches a similar altitude as on 1 August 2017 (Figure A.2b). While compared to 1 August 2017 lower values of daily mean near-surface air temperature of +1.4 and +3.2°C were measured at KPC_U and

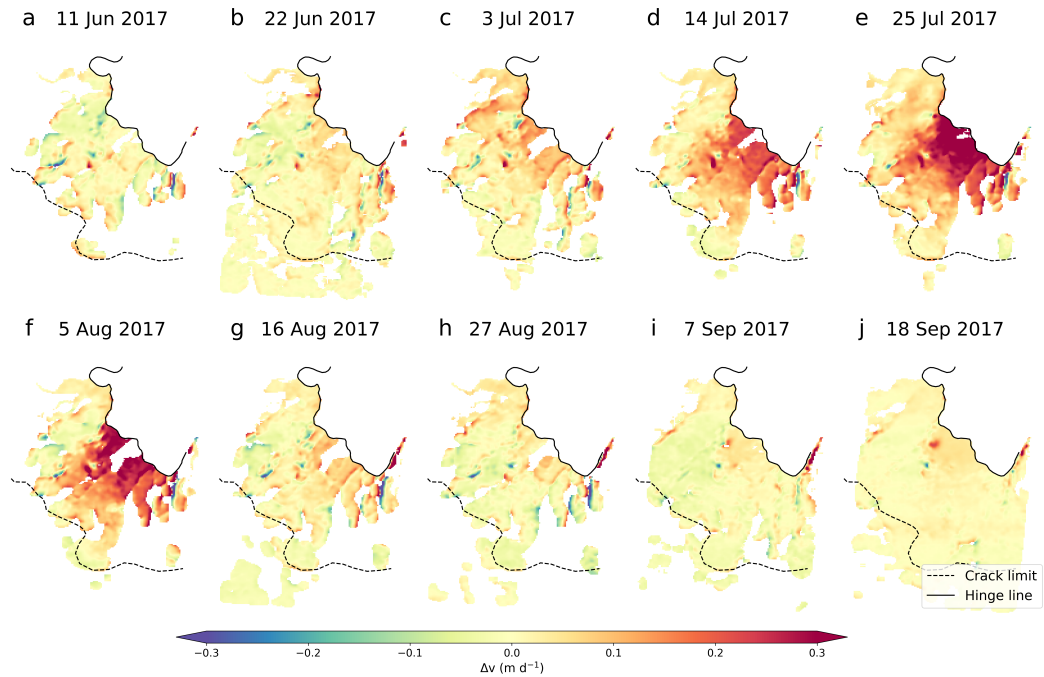


Figure A.6: Increase in summer 2017 surface velocities upstream the hinge line (solid black line) of 79°N Glacier when compared to winter velocities of the same year. Dates are the center dates between the 11-day repeat pass of TerraSAR-X employed in the generation of the summer velocity fields. Winter velocities were derived from TerraSAR-X data acquired between 10 December 2017 and 21 December 2017.

KPC_L respectively, precipitation might have enhanced surface melt and/or accumulated in the upper snow layers. At this day no helicopter supported field work was possible due to rainy conditions with low clouds and also ERA5 re-analysis data suggests precipitation in the area (Figure A.5d). So far no GPS measurements are available for 2018 but it has been shown previously, that precipitation can have a direct influence on glacier velocities (Doyle et al., 2015). The results presented in this study are in general agreement with the findings of Rathmann et al. (2017) who also suggest that the seasonal speed-up of 79°N Glacier is largely driven by surface melt water lubricating the bed. By conducting modeling experiments Rathmann et al. (2017) rule out other potential drivers such as seasonally enhanced sliding along the side walls of the floating tongue. For recent ice flow conditions Mayer et al. (2018) assess a strong buttressing effect of the floating ice tongue, especially within the narrower part of Nioghalvfjerd fjord (i.e. for the first ~30 km downstream the floating part of the ice tongue). This implies a low sensitivity of seasonal ice velocities towards varying sea ice conditions, an assumption which can not be made for the neighboring Zachariæ Isstrom. For the latter Rathmann et al. (2017) find that the break up of the ice mélange coincides with the onset of surface melt upstream the glacier, making a distinction of processes governing the seasonal ice acceleration rather

difficult. When investigating 45 Greenlandic glaciers [Vijay et al. \(2019\)](#) could link the seasonal varying surface velocities of roughly half of them to surface melt induced changes of the subglacial hydrology. For less than a quarter of their study glaciers [Vijay et al. \(2019\)](#) found a correlation between seasonal ice velocities and terminus changes. Even though surface melt water might also play a role in the seasonal velocity evolution of the latter group, [Moon et al. \(2014\)](#) suggest that fluctuations in terminus position are the primary controlling factor for these glaciers. According to the classification scheme introduced by [Moon et al. \(2014\)](#) and [Vijay et al. \(2019\)](#), 79°N Glacier fits well within their type 2 behavior by showing a strong correlation between glacier velocity and runoff. This also implies that a seasonal development of an efficient channelized subglacial drainage system is rather limited for 79°N Glacier.

While the above studies are solely based on remotely sensed surface velocities, we show that by the additional use of GPS measurements short term velocity variations are preserved which would be averaged out if only remote sensing estimates were available. Based on intensity offset tracking on Sentinel-1 data, [Lemos et al. \(2018\)](#) and [Rathmann et al. \(2017\)](#) found a seasonal acceleration of 79°N Glacier by 10 % and 11 % respectively. These estimates match comparably well with our estimate of 9 % based on TerraSAR-X data, even though sampling location, time stamp and reference data were different in all three studies. Such velocity estimates might be sufficient for monthly averaged mass balance estimates or general trends in seasonal velocity behavior, but short term velocity fluctuations with rather low amplitudes are difficult to quantify from the current satellite missions with temporal baselines of several days.

A.6 Conclusions

By combining remote sensing observations with *in situ* GPS measurements we were able to link the occurrence of extensive surface melt to a direct velocity response of 79°N Glacier. While we found a maximum seasonal velocity increase of 22 % from GPS measurements, these average out to 9 % when velocities are calculated over longer time intervals such as the 11-day repeat pass of TerraSAR-X. We therefore conclude, that surface velocities derived by remote sensing give a good overview over entire seasons or major speed-up events, but are not able to fully resolve short term velocity fluctuations triggered by e.g., rapid lake drainage events. For the latter we found an example even after the melt season in mid September when temperatures were well below 0°C. By utilizing digital elevation models from the TanDEM-X satellite mission we were able to estimate a drainage volume of $28 \times 10^6 \text{ m}^3$ which resulted in a minor speed-up of 24 % when compared

to pre-drainage ice velocities estimated from 3 GPS stations downstream the lake. Compared to studies in western Greenland the observed speed up is a magnitude lower. On the one hand this can be attributed to the large distances of our GPS receivers to the lake, on the other hand this could possibly support findings that not the amount of water is decisive for ice acceleration but rather the timing and the changes in water supply in combination with the effectivity of the hydraulic system.

Acknowledgments

TanDEM-X and TerraSAR-X data were made available through German Aerospace Center proposals GLAC7208 and HYD2059. Data from the Programme for Monitoring of the Greenland Ice Sheet (PROMICE) were provided by the Geological Survey of Denmark and Greenland (GEUS) at <http://www.promice.dk>. This project has received funding from the European Union's Horizon 2020 research and innovation programme under grant agreement No 689443 via project iCUPE (Integrative and Comprehensive Understanding on Polar Environments). Ole Zeising received founding through BMBF Project GROCE (03F0778A). We want to thank Jens Köhler and Graham Niven for their help in the field.

References

- Bartholomew, I., Nienow, P., Mair, D., Hubbard, A., King, M. A., & Sole, A. (2010). Seasonal evolution of subglacial drainage and acceleration in a Greenland outlet glacier. *Nature Geoscience*, 3, 408, <https://doi.org/10.1038/ngeo863>.
- Bartholomew, I., Nienow, P., Sole, A., Mair, D., Cowton, T., & King, M. A. (2012). Short-term variability in Greenland Ice Sheet motion forced by time-varying melt-water drainage: Implications for the relationship between subglacial drainage system behavior and ice velocity. *Journal of Geophysical Research: Earth Surface*, 117(F3), <https://doi.org/10.1029/2011JF002220>.
- Das, S. B., Joughin, I., Behn, M. D., Howat, I. M., King, M. A., Lizarralde, D., & Bhatia, M. P. (2008). Fracture propagation to the base of the greenland ice sheet during supraglacial lake drainage. *Science*, 320(5877), 778–781, <https://doi.org/10.1126/science.1153360>.
- Delhasse, A., Kittel, C., Amory, C., Hofer, S., van As, D., S. Fausto, R., & Fettweis, X. (2020). Brief communication: Evaluation of the near-surface climate in era5 over the greenland ice sheet. *The Cryosphere*, 14(3), 957–965, <https://doi.org/10.5194/tc-14-957-2020>.
- Doyle, S. H., Hubbard, A., van de Wal, R. S. W., Box, J. E., van As, D., Scharrer, K., Meierbachtol, T. W., Smeets, P. C. J. P., Harper, J. T., Johansson, E., Mottram, R. H., Mikkelsen, A. B., Wilhelms, F., Patton, H., Christoffersen, P., & Hubbard, B. (2015). Amplified melt and flow of the Greenland ice sheet driven by late-summer cyclonic rainfall. *Nature Geoscience*, 8, 647, <https://doi.org/10.1038/ngeo2482>.
- Fausto, R. S. & van As, D. (2019). Programme for monitoring of the Greenland ice sheet (PROMICE): Automatic weather station data. Version: v03. *Dataset published via Geological Survey of Denmark and Greenland*, <https://doi.org/10.22008/promice/data/aws>.
- Hersbach, H. & Dee, D. (2016). ERA5 reanalysis is in production. *ECMWF Newsletter*, 147(7), <https://doi.org/10.22008/promice/data/aws>.
- Hoffman, M. J., Catania, G. A., Neumann, T. A., Andrews, L. C., & Rumrill, J. A. (2011). Links between acceleration, melting, and supraglacial lake drainage of the western Greenland Ice Sheet. *Journal of Geophysical Research: Earth Surface*, 116(F4), <https://doi.org/10.1029/2010JF001934>.
- Ignéczi, A., Sole, A. J., Livingstone, S. J., Leeson, A. A., Fettweis, X., Selmes, N., Gourmelen, N., & Briggs, K. (2016). Northeast sector of the Greenland Ice Sheet to undergo the greatest inland expansion of supraglacial lakes during the 21st century. *Geophysical Research Letters*, 43(18), 9729–9738, <https://doi.org/10.1002/2016GL070338>.
- Iken, A., Röthlisberger, H., Flotron, A., & Haeberli, W. (1983). The Uplift of Unteraargletscher at the Beginning of the Melt Season - A Consequence of Water Storage at the Bed? *Journal of Glaciology*, 29(101), 28–47, <https://doi.org/10.3189/S0022143000005128>.

- Joughin, I., Das, S. B., Flowers, G. E., Behn, M. D., Alley, R. B., King, M. A., Smith, B. E., Bamber, J. L., van den Broeke, M. R., & van Angelen, J. H. (2013). Influence of ice-sheet geometry and supraglacial lakes on seasonal ice-flow variability. *The Cryosphere*, 7(4), 1185–1192, <https://doi.org/10.5194/tc-7-1185-2013>.
- Joughin, I., Smith, B. E., & Howat, I. M. (2018). A complete map of Greenland ice velocity derived from satellite data collected over 20 years. *Journal of Glaciology*, 64(243), 1–11, <https://doi.org/10.1017/jog.2017.73>.
- Krieger, L., Floricioiu, D., & Neckel, N. (2020). Drainage basin delineation for outlet glaciers of Northeast Greenland based on Sentinel-1 ice velocities and TanDEM-X elevations. *Remote Sensing of Environment*, 237, 111483, <https://doi.org/10.1016/j.rse.2019.111483>.
- Lemos, A., Shepherd, A., McMillan, M., Hogg, A. E., Hatton, E., & Joughin, I. (2018). Ice velocity of Jakobshavn Isbræ, Petermann Glacier, Nioghalvfjærdsfjorden, and Zachariæ Isstrøm, 2015–2017, from Sentinel 1-a/b SAR imagery. *The Cryosphere*, 12(6), 2087–2097, <https://doi.org/10.5194/tc-12-2087-2018>.
- Lüttig, C., Neckel, N., & Humbert, A. (2017). A Combined Approach for Filtering Ice Surface Velocity Fields Derived from Remote Sensing Methods. *Remote Sensing*, 9(10), 23, <https://doi.org/10.3390/rs9101062>.
- Mayer, C., Schaffer, J., Hattermann, T., Floricioiu, D., Krieger, L., Dodd, P. A., Kanzow, T., Licciulli, C., & Schannwell, C. (2018). Large ice loss variability at Nioghalvfjærdsfjorden Glacier, Northeast-Greenland. *Nature Communications*, 9(1), 2768, <https://doi.org/10.1038/s41467-018-05180-x>.
- Moon, T., Joughin, I., Smith, B., van den Broeke, M. R., van de Berg, W. J., Noël, B., & Usher, M. (2014). Distinct patterns of seasonal Greenland glacier velocity. *Geophysical Research Letters*, 41(20), 7209–7216, <https://doi.org/10.1002/2014GL061836>.
- Neckel, N., Braun, A., Kropáček, J., & Hochschild, V. (2013). Recent mass balance of the Purogangri Ice Cap, central Tibetan Plateau, by means of differential X-band SAR interferometry. *The Cryosphere*, 7(5), 1623–1633, <https://doi.org/10.5194/tc-7-1623-2013>.
- Polar Portal Season Report (2018). <http://polarportal.dk/en/news/2018-season-report/>. Technical report, Polar Portal.
- Porter, C., Morin, P., Howat, I., Noh, M.-J., Bates, B., Peterman, K., Keesey, S., Schlenk, M., Gardiner, J., Tomko, K., Willis, M., Kelleher, C., Cloutier, M., Husby, E., Foga, S., Nakamura, H., Platson, M., Wethington, Michael, J., Williamson, C., Bauer, G., Enos, J., Arnold, G., Kramer, W., Becker, P., Doshi, A., D’Souza, C., Cummins, P., Laurier, F., & Bojesen, M. (2018). “ArcticDEM”, Harvard Dataverse, V1. <https://doi.org/10.7910/DVN/OHHUKH>.
- Rathmann, N., Hvidberg, C., Solgaard, A., Grinsted, A., Gudmundsson, G. H., Langen, P. L., Nielsen, K., & Kusk, A. (2017). Highly temporally resolved response to seasonal surface melt of the Zachariæ and 79N outlet glaciers in northeast Greenland. *Geophysical Research Letters*, 44(19), 9805–9814, <https://doi.org/10.1002/2017GL074368>.












- Rau, F. & Braun, M. (2002). The regional distribution of the dry-snow zone on the Antarctic Peninsula north of 70°S. *Annals of Glaciology*, 34, 95–100, <https://doi.org/10.3189/172756402781817914>.
- Rosenau, R., Scheinert, M., & Dietrich, R. (2015). A processing system to monitor Greenland outlet glacier velocity variations at decadal and seasonal time scales utilizing the Landsat imagery. *Remote Sensing of Environment*, 169, 1–19, <https://doi.org/10.1016/j.rse.2015.07.012>.
- Rückamp, M., Neckel, N., Berger, S., Humbert, A., & Helm, V. (2019). Calving Induced Speedup of Petermann Glacier. *Journal of Geophysical Research: Earth Surface*, 124(1), 216–228, <https://doi.org/10.1029/2018JF004775>.
- Schoof, C. (2010). Ice-sheet acceleration driven by melt supply variability. *Nature*, 468, 803, <https://doi.org/10.1038/nature09618>.
- Small, D. (2011). Flattening Gamma: Radiometric Terrain Correction for SAR Imagery. *IEEE Transactions on Geoscience and Remote Sensing*, 49(8), 3081–3093, <https://doi.org/10.1109/TGRS.2011.2120616>.
- Strozzi, T., Luckman, A., Murray, T., Wegmuller, U., & Werner, C. (2002). Glacier motion estimation using SAR offset-tracking procedures. *IEEE Transactions on Geoscience and Remote Sensing*, 40(11), 2384–2391, <https://doi.org/10.1109/tgrs.2002.805079>.
- Tedesco, M., Willis, I. C., Hoffman, M. J., Banwell, A. F., Alexander, P., & Arnold, N. S. (2013). Ice dynamic response to two modes of surface lake drainage on the Greenland ice sheet. *Environmental Research Letters*, 8(3), 034007, <https://doi.org/10.1088/1748-9326/8/3/034007>.
- Vijay, S., Khan, S. A., Kusk, A., Solgaard, A. M., Moon, T., & Bjørk, A. A. (2019). Resolving Seasonal Ice Velocity of 45 Greenlandic Glaciers With Very High Temporal Details. *Geophysical Research Letters*, 46(3), 1485–1495, <https://doi.org/10.1029/2018GL081503>.
- Wang, L., Sharp, M., Rivard, B., & Steffen, K. (2007). Melt season duration and ice layer formation on the Greenland ice sheet, 2000–2004. *Journal of Geophysical Research: Earth Surface*, 112(F4), F04013, <https://doi.org/10.1029/2007JF000760>.
- Winsvold, S. H., Kääb, A., Nuth, C., Andreassen, L. M., van Pelt, W. J. J., & Schellenberger, T. (2018). Using SAR satellite data time series for regional glacier mapping. *The Cryosphere*, 12(3), 867–890, <https://doi.org/10.5194/tc-12-867-2018>.
- Zwally, H. J., Abdalati, W., Herring, T., Larson, K., Saba, J., & Steffen, K. (2002). Surface Melt-Induced Acceleration of Greenland Ice-Sheet Flow. *Science*, 297(5579), 218–222, <https://doi.org/10.1126/science.1072708>.

Elastic deformation plays a non-negligible role in Greenland's outlet glacier flow

B

This chapter is published as a research article at the journal *Communications Earth & Environment* in 2021 (Christmann et al., 2021).

Authors and affiliations

Julia Christmann^{1,2} , Veit Helm¹ , Shfaqat Abbas Khan³ , Thomas Kleiner¹ , Ralf Müller² , Mathieu Morlighem^{4,5} , Niklas Neckel¹ , Martin Rückamp¹ , Daniel Steinhage¹ , Ole Zeising^{1,6} , and Angelika Humbert^{1,6} 

¹Alfred-Wegener-Institut Helmholtz-Zentrum für Polar- und Meeresforschung, Bremerhaven, Germany

²Institute of Applied Mechanics, University of Kaiserslautern, Germany

³DTU Space, National Space Institute, Technical University of Denmark, Department of Geodesy and Earth Observations, Denmark

⁴Department of Earth Sciences, Dartmouth College, Hanover, NH 03755, USA

⁵Department of Earth System Science, University of California, Irvine, California, USA

⁶Department of Geosciences, University of Bremen, Bremen, Germany

Contributions

J.Christmann conducted the viscoelastic simulations. A.Humbert, R.Müller, J.Christmann developed the concept for the viscoelastic simulations and evaluated the results. T.Kleiner conducted the CUAS simulations, A.Humbert and T.Kleiner planned and analysed the CUAS simulations. M.Morlighem developed a new BedMachine dataset. M.Müller conducted ISSM simulations, the ISMIP-HOM experiments with COMice-ve and provided basal friction and buttressing. A.Humbert has designed the study and planned the field expeditions and airborne campaign. D.Steinhage, **O.Zeising**, N.Neckel, V.Helm and S.A.Khan conducted the field study. V.Helm, S.A.Khan and **O.Zeising** processed the GPS data. N.Neckel processed interferograms. V.Helm conducted the airborne campaign and supported the base detection. All authors discussed the results and

contributed to writing.

Abstract

Future projections of global mean sea level change are uncertain, partly because of our limited understanding of the dynamics of Greenland’s outlet glaciers. Here we study Nioghalvfjærdsbræ, an outlet glacier of the Northeast Greenland Ice Stream that holds 1.1 m sea-level equivalent of ice. We use GPS observations and numerical modelling to investigate the role of tides as well as the elastic contribution to glacier flow. We find that ocean tides alter the basal lubrication of the glacier up to 10 km inland of the grounding line, and that their influence is best described by a viscoelastic rather than a viscous model. Further inland, sliding is the dominant mechanism of fast glacier motion, and the ice flow induces persistent elastic strain. We conclude that elastic deformation plays a role in glacier flow, particularly in areas of steep topographic changes and fast ice velocities.

B.1 Introduction

The Greenland Ice Sheet has experienced increased mass loss due to global warming over the past decades (Shepherd et al., 2020). Warmer air and ocean temperatures continue to destabilise outlet glaciers and enhance ice mass loss (Khan et al., 2020). Projecting their future contribution to sea level changes under different climate scenarios has become one of the most fundamental questions for coastal regions (Larour et al., 2017; Goelzer et al., 2020; Seroussi et al., 2020). While much progress has been made in large-scale ice sheet models, the behaviour and accurate modelling of fast-flowing ice streams remain a high priority for simulating future ice mass changes (IPCC, 2013; Oppenheimer et al., 2019). The ice discharge of these fast-flowing outlet glaciers into the ocean is a fundamental process in the ice sheet mass-balance (Mouginot et al., 2019a; Choi et al., 2021). Up to now, little is known on how short-term stress changes control outlet glacier dynamics and hence ice discharge. To model the effect of short-term stress changes, an appropriate material model needs to be employed to represent viscous long-term ice flow and elastic short-term fluctuations of the stress distribution. Current ice flow models discard the elastic part in the underlying material model due to its higher computational demand and complexity (Darby, 1976). The obvious question is to what extent elastic deformation is crucial for glacier motion and in which areas elastic quantities become important.

In fast-flowing ice streams, sliding is a major component that determines the amount of ice discharge (Brondex et al., 2017, 2019) and an improved under-

standing of basal processes is needed to obtain better estimations of the ice outflow (Iverson et al., 2019; Zoet and Iverson, 2020). Our current understanding of basal conditions and their parameterisation in ice sheet models limits the ability to model the evolution of ice sheets over the next century (Franke et al., 2021). The subglacial hydrological system is an important factor controlling the stress at the ice base, as a higher water pressure lubricates the base and enhances sliding speeds (Lliboutry, 1968; Röthlisberger, 1972; Gimbert et al., 2016; Smith et al., 2020). For marine terminating glaciers, a connection between the subglacial hydrological system and the ocean water exists. Ocean tides modulate the water pressure at the grounding line resulting in short-term changes of basal stress. These short-term stress changes are likely transmitted inland and impact the ice dynamics upstream (Anandakrishnan et al., 2003). As direct observations at the base are sparse, numerical models are valuable tools to investigate the variation of stresses.

While it is widely accepted that ocean tides induce non-negligible elastic strains, other potential sources for short-term changes in stresses exist. Most likely steep slopes or steps in bed topography, where ice moving across bed undulations experiences changing stresses, a prerequisite for developing elastic strains. However, it remains unclear whether and where elastic strains exist within the ice for longer times or decline such that the viscous glacier flow prevails. The impact of elastic contributions related to abrupt stress changes on ice dynamics has not been quantified yet, either numerically or through observations. These elastic strains are related to stresses based on the constitutive equation and are commonly used to indicate material failure (e.g., crevasses, damage, cracks). Interestingly, extensive crevasse fields occur in fast-flowing outlet glaciers in Greenland, which exert an important control on ice discharge towards the ocean. Approaches of linear elastic fracture mechanics are promising to represent rapid failure and crevasse formation in large-scale ice sheet models (Colgan et al., 2016). With increasing tensile stresses above a threshold, brittle failure sets in (Benn and Åström, 2018). Based on these considerations, several logical questions arise: Are the crevasse fields located in regions in which elastic strains and stresses do not decline due to stress changes? Could a viscoelastic model provide novel insights into the role of elastic strains and stresses in Greenland's outlet glaciers?

So far, observations of the elastic effects have primarily been focusing on tides: In Antarctica, it has been shown that tides can alter glacier flow up to 80 km upstream of the grounding line of large ice streams (Anandakrishnan et al., 2003; Bindschadler et al., 2003; Gudmundsson, 2007; Walker et al., 2012; Padman et al., 2018; Rosier and Gudmundsson, 2020). The tidally-induced vertical motion of ice shelves and floating ice tongues cause changes in the stress distribution and

contributes to the variability of glacier flow near the grounding line (Padman et al., 2018; Fricker and Padman, 2006). A case study of Rutford Ice Stream showed that only a combination of a viscoelastic material model and a non-linear friction law describes observed fortnightly glacier speed modulation appropriately (Gudmundsson, 2007). The viscoelastic flowline simulation of Bindschadler Ice Stream, West Antarctica, indicated basal motion consistent with flow dominated by basal sliding over a relatively weak till (determined by higher exponents in sliding laws) and not by internal deformation (Walker et al., 2012). These findings suggest a tidal modulation of the glacier motion facilitated by basal sliding. Despite the broad impact of tides on Antarctic ice streams, only a few studies have considered tidally modulated glacier motion on the Greenland Ice Sheet (GrIS) (Lingle et al., 1981; de Juan et al., 2010). Observed bending of the ice tongue at Jakobshavn Glacier (at that time 8 km long) reflected elastic and viscous deformation, while fatigue failure caused by tidal flexure results in deep basal and surface cracks along the grounding line (Lingle et al., 1981). Although tidal stresses only affected the glacier terminus at Helheim Glacier, observations after a calving event showed changes at least 12 km upstream of the grounding line (de Juan et al., 2010). The tidal range around Greenland varies between 0 and 6 m (Padman et al., 2018) with a magnitude that is similar to the tides around the Antarctic Ice Sheet. Observations at a marine-terminating glacier of the Qaanaaq ice cap revealed semi-diurnal speed peaks coinciding with low tides (Sugiyama et al., 2015). Near the calving front of Bowdoin Glacier, tidal forcing and surface speed were in anti-phase. An underprediction of the amplitude of the semi-diurnal variability is presumably related to either inaccuracy in the surface and bedrock topographies or mechanical weakening due to crevassing (Seddik et al., 2019).

We employ a viscoelastic model underpinned by an accurate radar-derived ice geometry to investigate the elastic contribution along the central flowline of Nioghalvfjærdsbræ (79NG), northeast Greenland. The parameters for the simplest homogeneous isotropic viscoelastic material are the viscosity, determining the rate-dependent viscous behaviour, and two elastic constants, namely Young's modulus, affecting the stiffness, and Poisson's ratio, specifying the lateral contraction (see "Methods" section). We rely on observed displacements of GPS stations (see "Methods" section) to assess the accuracy of simulated displacements and validate the material rheology. To model basal sliding we have to know the effective water pressure of the subglacial hydrology and an inferred friction coefficient field (see "Methods" section). The effective pressure is the difference between the ice overburden pressure and the subglacial water pressure and results from the confined-unconfined aquifer system (CUAS) model (Beyer et al., 2018). Inver-

sion of observed surface velocities provides the friction coefficient field. Based on these results, we show that ocean tides change the ice flow only a few kilometres upstream of the grounding line at 79NG. Crevasse fields further upstream thus require another mechanism that sustains elastic deformations. A simulation without tides enables us to evaluate the elastic contribution to the glacier flow at 79NG. We show that sharp bed undulations and glacier motion cause elastic deformations, which do not decline over time. From the gained insights focusing on 79NG, we discuss how this study sheds light on the elastic deformation of other fast-flowing outlet glaciers of the GrIS (viscous model) as the applied viscoelastic Maxwell model demands that elastic and viscous stresses are the same. In the end, we propose ideas for future modelling work.

B.2 Results and discussion

B.2.1 Tidal modulation of glacier flow

For the 79NG, an outlet glacier of the Northeast Greenland Ice Stream (NEGIS), we first analyse the influence of tides on glacier flow (Fig. B.1). In the summer of 2017, we deployed four GPS receivers along a central flowline to measure the tidal influence on glacier flow. The instruments were positioned on the floating part of the ice tongue (GPS-shelf), on the ~ 4 km wide hinge zone (GPS-hinge) that experiences bending with tides (see “Methods” section), and some 14 km (GPS-GL-14) and 45 km (GPS-GL-45) upstream of the grounding line (defined as the upper limit of the hinge zone in 2017, Supplementary Fig. 1). The measured flow velocities of the GPS stations positioned along a flowline (Fig. B.1 and Supplementary Data 1) show an increasing trend towards the grounding line from 290 m a^{-1} at GPS-GL-45 over 950 m a^{-1} at GPS-GL-14 to 1460 m a^{-1} at GPS-hinge and slightly decreases to 1310 m a^{-1} at GPS-shelf (Zeising et al., 2021). These observed velocities are mean values measured over a 14 day period during the summer that are potentially about 10% above winter velocities (Neckel et al., 2020) but fit to the simulated surface velocities of the flowline. We recorded three-dimensional surface movements simultaneously over several tidal cycles. The processed data (see “Methods” section) reveal a tidal signal only in the floating part at GPS-hinge and GPS-shelf (Fig. B.2). At 79NG, we observe no tidal signal at the grounded GPS stations GPS-GL-14 and GPS-GL-45, which indicates rapid attenuation within a few kilometres upstream of the hinge zone. Though it is not directly comparable, this is in contrast to observations on large ice streams in Antarctica (Anandakrishnan et al., 2003; Bindshadler et al., 2003) where the tidal signal is transmitted tens of kilometres upstream of the grounding

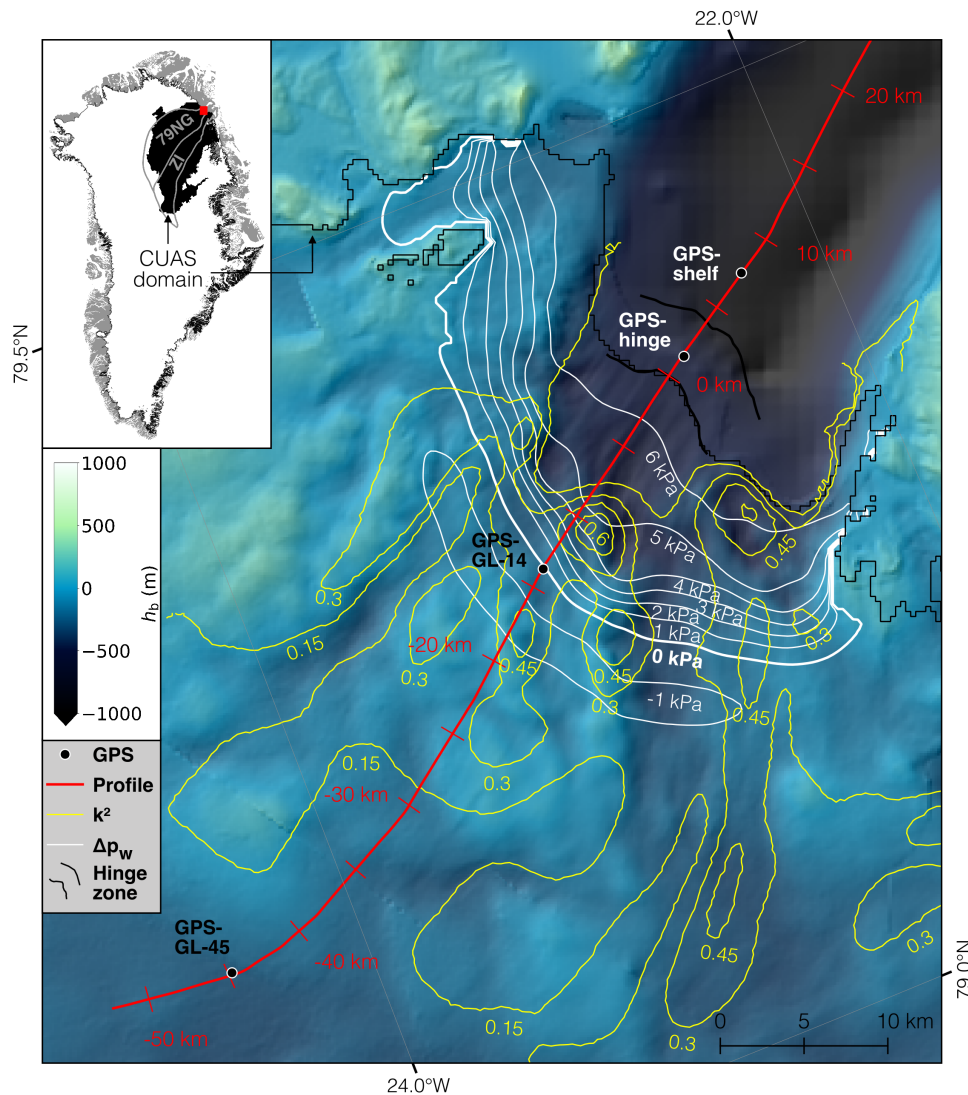


Figure B.1: Overview of the study area, including locations of the GPS stations on the ice flowline profile. The underlying background map shows the bed elevation h_b . Yellow lines represent contours of the basal friction coefficient field k^2 . White lines denote the simulated water pressure difference Δp_w (high tide minus low tide) in the hydrological system. The flowline profile (red line) is used for a flowline model of glacier motion. The grounding line, where the ice becomes afloat is at 0 km. The hinge zone, the zone in which the ice tongue deforms due to bending, is shown by two black lines, one at its upper limit directly at the grounding line and one at the lower limit 4 km downstream the grounding line. The inset shows the CUAS domain that encompasses the NEGIS catchment including the 79NG catchment as a solid black polygon. The red rectangle marks the area close to the grounding line shown in the figure.

line. Inspired by the processes occurring in Antarctica, we deployed the GPS stations and were surprised to see no tidal signal 14 km upstream the grounding line. Besides the tidal signal, a superimposed signal was simultaneously recorded by the GPS receivers (Fig. B.2b, c, d). We link this to supraglacial lake drainage (Neckel et al., 2020).

We set up a numerical model and compare the simulated displacements with observations. The momentum balance of this simulation is solved for a viscoelastic Maxwell rheology (Christmann et al., 2019) (labelled COMice-ve, details see “Methods” section). This viscoelastic model allows us to simulate and distinguish short-term elastic and long-term viscous responses to external loads like ocean tides (Gudmundsson, 2011; Wild et al., 2018; Humbert et al., 2015). For the floating ice tongue of 79NG, we account for observed ocean tides of GPS-shelf in the basal boundary condition. Additionally, we include this tidal signal in the hydrological model CUAS.

The simulated glacier response using a viscoelastic material model reveals an excellent agreement with the observations. We choose elastic constants for Young’s modulus of $E = 1$ GPa and Poisson’s ratio of $\nu = 0.325$, which are consistent with other studies in Antarctica (Gudmundsson, 2011; Humbert et al., 2015). Without further tuning, the correspondence of model results and observations is high with differences less than 1% in the horizontal and vertical direction over large parts of the considered time interval (Fig. B.2 and Supplementary Data 2). The free-floating ice tongue moves up and down caused by ocean tides and the simulated detrended horizontal and vertical displacement coincide with the observations (Fig. B.2d). At both grounded GPS stations GPS-GL-14 and GPS-GL-45 the simulations show no measurable tidal modulation, which agrees with the observations (Fig. B.2a, b). We inferred that the high agreement at GPS-hinge solely arises from the elastic contribution in COMice-ve. Horizontal and vertical displacements computed with purely viscous rheology are not capable of reproducing the observed amplitudes or phase responses (Fig. B.2c). Although we varied viscosity and basal sliding parameters (Supplementary Discussion 1), those simulation results cannot reproduce the displacements accurately. That means that the bending and modulation of flow speeds in the hinge zone are a result of the viscoelastic nature of ice. Hence, at least a viscoelastic Maxwell material model (two parameter fluid) is required on the lower part of the glacier to match the observations.

The question arises of how a viscoelastic material model and tides influence basal sliding. To what extent are these findings (elasticity influences the glacier flow) only applicable to tidally modulated flow? Other numerical studies also discussed the influence of elastic deformations caused by short-term variations. For instance, large calving events in Greenland cause first a reversal of flow and elastically compress the ice front as large icebergs rotate (Murray et al., 2015). The reversal of the ice flow typically lasts for a few minutes and is then followed by a flow acceleration, increased longitudinal strain rates and enhanced responses to tidal forcing (de Juan et al., 2010). Hence, sudden short-term changes like calving

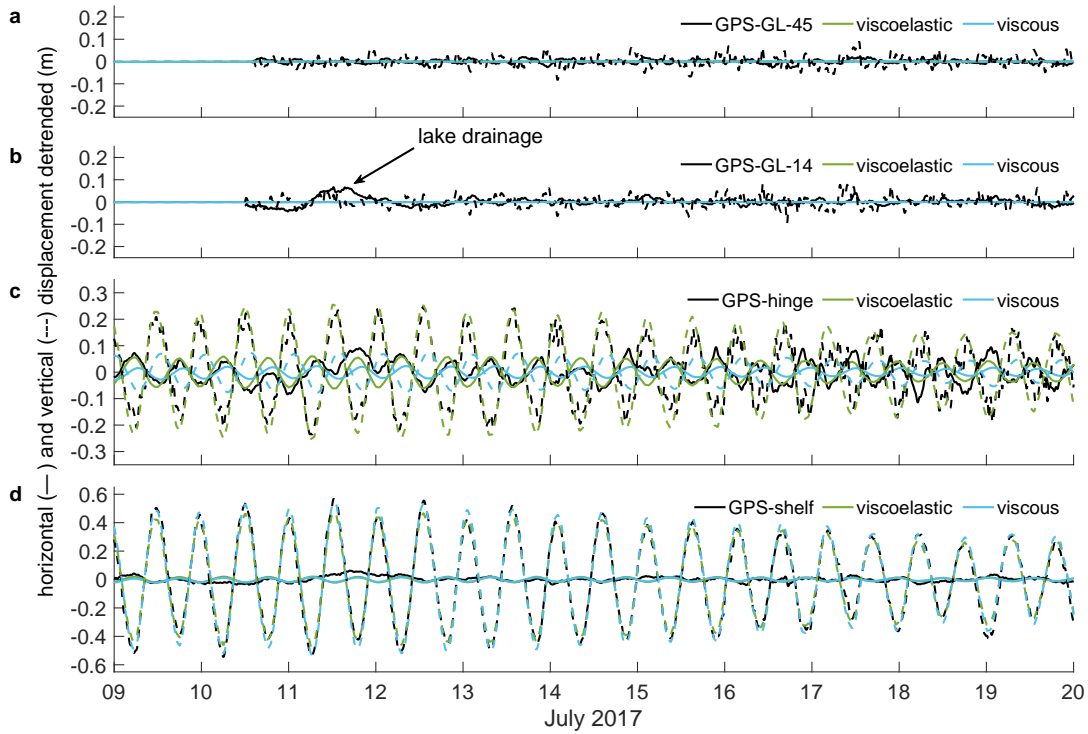


Figure B.2: Tidal modulation of glacier flow at the GPS stations. a–d, Detrended measured and simulated displacements in horizontal (solid lines) and vertical direction (dashed lines) versus time at GPS-GL-45 (a), GPS-GL-14 (b), GPS-hinge (c) and GPS-shelf (d). The locations of the GPS stations are shown in Fig. B.1. Black lines present measured GPS displacements, while green lines show simulated displacements obtained with COMice-ve. Blue lines display displacements for a pure viscous model.

events or lake drainage will induce an additional elastic response, which should be investigated in future work and could be the explanation for flow deceleration and acceleration.

B.2.2 Effect of tides on sliding

We intend to get a complete picture between GPS-GL-14 and the grounding line to estimate how far tides reach inland at 79NG and influence its basal sliding behaviour. Different basal friction laws exist and need to be handled carefully as basal friction is a crucial boundary condition (Brondex et al., 2017; Åkesson et al., 2021). The applied friction law is Budd-like and non-linear (Brondex et al., 2019; Budd et al., 1979) and relates basal shear stress τ_b to basal velocity v_b , the friction coefficient field k^2 and the effective pressure N (see “Methods” section, Eq. 2). As we assume the inferred friction coefficient field to be constant in time for our study (see “Methods” section), changes in the basal shear stress originate from tidal changes in effective pressure and basal velocities. To disentangle the role of each component in the friction law, we analyse the response of the simulated subglacial hydrology to tides resulting in time-dependent effective pressure fields

(see “Methods” section). The simulated vertical movement of the floating base caused by tides result in time-dependent displacement and hence velocity changes. With this tidally modulated setting along the flowline, we show a comprehensive analysis of the glacier system for all quantities included in the basal boundary condition (Fig. B.3 and Supplementary Data 3 and 4). Please note that results are shown point-wise relative to a control run (CTRL) without tidal forcing in the subglacial hydrology system (grounded part) and the water pressure (floating part). The simulated head along the flowline (the corresponding elevation of the water level in a hypothetical borehole connecting glacier surface to bed) is very smooth (Fig. B.3b) and spatial variations of the effective pressure primarily originate from the ice overburden pressure and thus ice thickness variations. In the hinge zone (from 0 to 5 km), the simulation reveals a tidal influence on the basal velocity where the highest differences to the CTRL run occur at the transition between low to high tide. The amplitude in the basal velocity behaves similar to the displacements (Fig. B.2 and Supplementary Fig. 2) where smaller amplitudes appear for the purely viscous or a stiffer material (dashed and dotted lines in Fig. B.3d). Simulated velocities and displacements show a tidal dependency that drops from $\pm 10\%$ at the grounding line to $\pm 0.2\%$ at GPS-GL-14 (Fig. B.3d) to none for GPS-GL-45 (not shown). For the grounded part, the transition from low to high tides and vice versa induces the largest changes compared to the spatial evolution for all other tidal states.

Why occur the lowest or highest basal velocities not at high or low tide but the transition points (Fig. B.3d)? Although we expect the tidal effects on the hydrological system to be relevant for glacier flow, we conduct a further simulation without tidal modulation to disentangle the effect of tides on the friction law and the rheology. Hence, the effective pressure in the subglacial water system is kept constant (CTRL run) and only the basal boundary condition at the floating tongue experiences tidal modulation. The velocity variations induced by the vertical tidal movement of the floating tongue reaches around 10 km upstream the grounding line. The bending of the floating tongue influences the basal velocity and high tide leads to lower velocities at the base of the grounded ice, while low tide causes higher velocities (Supplementary Fig. 3). This scenario highlights that the tidally dependent change of the hydrological system alters the flow behaviour: the envelopes of the velocity changes occur for the transition between low and high tides (Fig. B.3d). If we include tides in the hydrological system, the effective pressure reacts with a decrease in magnitude and a phase shift to tidal forcing depending on the distance to the grounding line (Supplementary Discussion 2). We find the effect of tidal forcing on the hydrological system is limited to a small band up to 20 km upstream the grounding line where the amplitude of the tidal

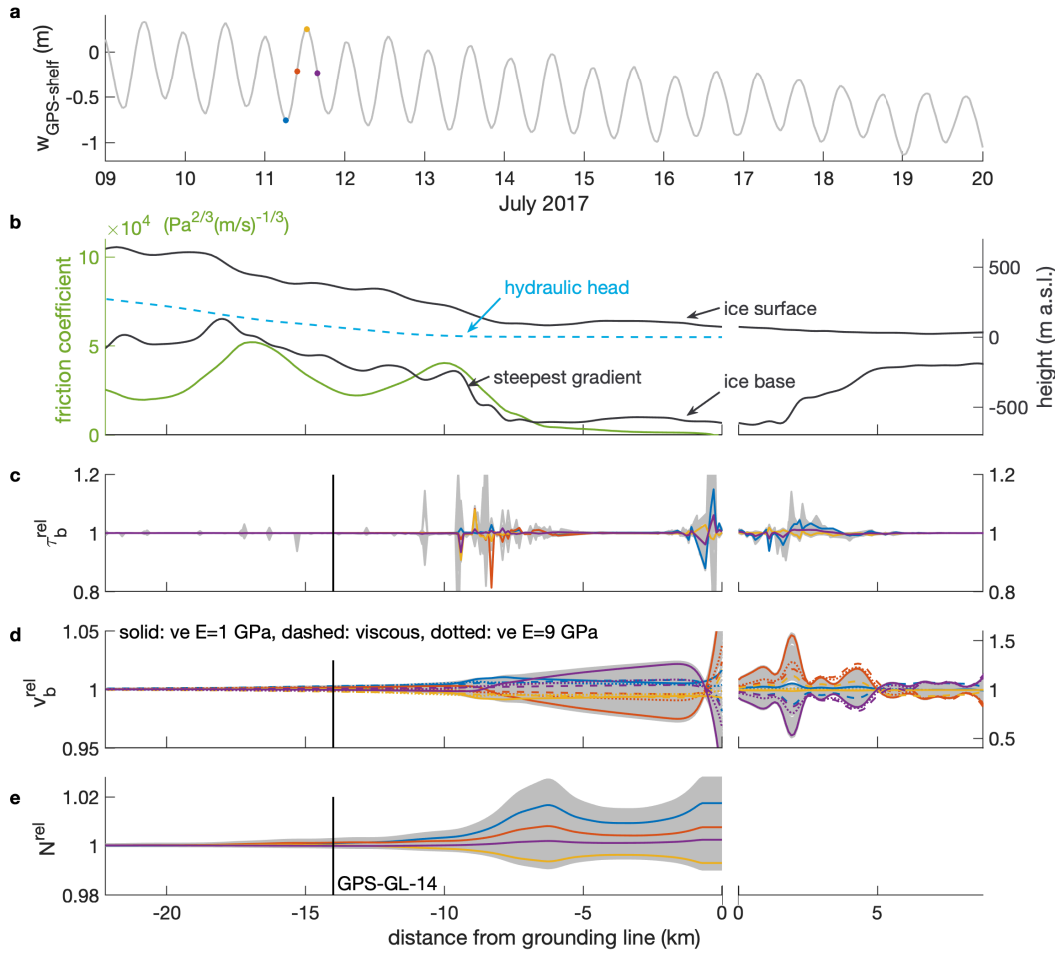


Figure B.3: Tidal effect on basal boundary conditions. **a**, Ocean tidal forcing with four coloured points: blue at low tide, yellow at high tide and red, purple at their transition. The gradual decrease is mainly due to the lunar fortnightly tidal signal. **b**, The green line displays the time-independent friction coefficient k^2 (left axis); the black lines shows the dimensions of the ice domain and the position of the hydraulic head (right axis). **c–e**, Ratio of basal shear stress (**c**), basal flow velocity (**d**), and effective pressure (**e**) relative to the control run without tidal forcing ($(\cdot)^{\text{rel}} = (\cdot)/(\cdot)^{\text{CTRL}}$). The grey lines of the relative values in panel **c–e** depict numerous simulation results computed with changing observed tidal variations (**a**) every 1.5 h. Certain tidal states are highlighted by coloured lines that match the coloured points of panel **a**. Note that the grounded part is shown on the left axis (black vertical line highlights the position of GPS-GL-14) and the floating part on the right axis (different axis scale in **d**). **d** Solid lines show the viscoelastic (ve) simulation with $E = 1$ GPa, dashed lines depict the purely viscous response and dotted lines represent a viscoelastic simulation for a stiffer elastic material with $E = 9$ GPa.

signal decays to only 10% of the signal at the grounding line (Supplementary Figs. 4 and 5). Caused by tidal forcing, relative changes in the effective pressure are small, except at the grounding line (Fig. B.3e and Supplementary Figs. 4 and 6). Additionally, tidal-related changes in the simulated basal velocity are only visible over a distance of less than 14 km upstream the grounding line (Fig. B.3d),

which is consistent with the observations at GPS-GL-14 (Fig. B.2). To validate a non-linear friction law at 79NG similar to the previous work done in Antarctica (Gudmundsson, 2011), we have to consider grounded GPS stations closer to the grounding line that record tidal modulations.

Previous observations of radio-echo sounding data from NEGIS suggested that upstream areas of the ice stream are controlled by variations in basal lubrication while downstream regions are confined by basal topography (Keisling et al., 2014). The observation of the downstream region fits the simulation results of the central flowline model for 79NG shown here. In the basal shear stress, we see impacts of tides with changes up to 40% to the CTRL run near the steep increase in the bed slope at -9 km where also the subglacial hydrology reveals tidal effects (Fig. B.3c, e). In the last ~ 5 km upstream the grounding line, the friction coefficient is small and damps changes in the basal shear stress due to tides (Fig. B.3b). Low friction coefficients facilitate the fast response of glacier speeds to changes in the basal water pressure, which is in line with areas of seasonal speedup and short pulses of acceleration arising from supraglacial meltwater input modulating basal frictional stresses (Neckel et al., 2020). The tidal variation of the hydrology causes a superposed variation in the basal velocity and consequently a larger change in basal shear stress than neglecting ocean tides in the hydrological system. Overall, ocean tides alter the glacier flow in our case not as far inland as in Antarctica (Anandakrishnan et al., 2003). In our simulations, the area of high transmissivity at 79NG (Supplementary Fig. 6b) is confined by the steep basal topography -9 km upstream of the grounding line. Large gradients in the bed or surface topography lead to large gradients in ice overburden and effective pressure. These increase channel wall melt rates (Röthlisberger, 1972) and therefore transmissivity (Beyer et al., 2018). The simulated low aquifer transmissivity at ~ 10 km and further upstream the grounding line hinders the pressure wave to travel further inland at 79NG (Supplementary Discussion 2). This matches very well with our measurements at GPS-GL-14 where no tidal signal was observed.

B.2.3 What governs glacier motion

Ice sheet models typically neglect the elastic deformation and compute ice sheet flow based on a viscous model. To estimate elastic contributions to glacier flow, it is necessary to get better insights into processes influencing glacier motion. We analyse the role of sliding and vertical shear deformation independent of tides for 79NG. Based on this analysis, we aim to derive implications for the entire ice sheet of Greenland. The analysis in this section uses (i) a viscoelastic simulation along the flowline of 79NG and (ii) a continental scale ice sheet simulation. For

the latter, we rely on a viscous model since a viscoelastic simulation is unavailable. The overarching goal is to identify regions where the consideration of elasticity is recommended for a better understanding of outlet glacier dynamics.

We analyse vertical profiles of velocity ratios determined by the velocity $v = |\mathbf{v}|$ at each point relative to its basal velocity $v_b = |\mathbf{v}_b|$ (Fig. B.4a). The simulated velocity field differs from a sliding dominated plug flow (grey area) in regions where the contribution of vertical shear deformation is enhanced. Topographic bed changes seem to induce these higher contributions (e.g., at distances of -18 and -9 km). Slightly before the bed bump peak at -9 km, simulated vertical shear deformation is highest and topographic changes slow down the ice at the base (velocity at the surface is larger than at the base). At this location, we find a maximum of 25% higher velocities at the surface. At some locations, the velocity is even lower at the surface than at the base. Such a feature is known from viscoelastic flow over an undulated bed (Herbert et al., 2015; Pettas et al., 2019). The surface velocity is up to 5% lower than the basal velocity. In general, plug flow is the dominant mechanism and vertical shear deformation is small. The simulation results fit radar and seismic observations indicating deformable subglacial sediment in the far upstream part of NEGIS, which facilitates sliding (Christianson et al., 2014; Bagshaw et al., 2018). At 79NG, the simulation results support that fast-moving outlet glaciers flow mainly by basal sliding (de Juan et al., 2010).

To get better insights into the role of deformation in glacier motion, we first analyse the ratio of vertical shear deformation (d) to sliding (s) and second the amount of viscous to total strain (Fig. B.4b and Supplementary Data 5). We introduce a measure $M_{d/s}^a \in [0, 1]$ representing the absolute contribution of vertical shear deformation to sliding

$$M_{d/s}^a = \frac{1}{H} \int_{h_b}^{h_s} \left(\frac{|v - v_b|}{v} \right) dz$$

with the ice thickness H , the surface and bed elevations h_s, h_b , respectively. This depth-integrated measure is zero for a sliding dominated plug flow and allows us to identify regions in which shear deformation of the vertical ice column is pronounced. Overall, the magnitude of $M_{d/s}^a$ is higher near steeper bed slopes (Fig. B.4b). Vertical shear deformation does not exceed 22% along the entire flow line, although this profile contains a rather steep basal topography. The visualisation of this measure shows a horizontal shift to the downstream side of the slopes (Fig. B.4b). This offset occurs as vertical shear deformation is highest at the end of steep topographic changes indicated by declining slope values. If the friction coefficient reaches low values (near the grounding line or at a distance

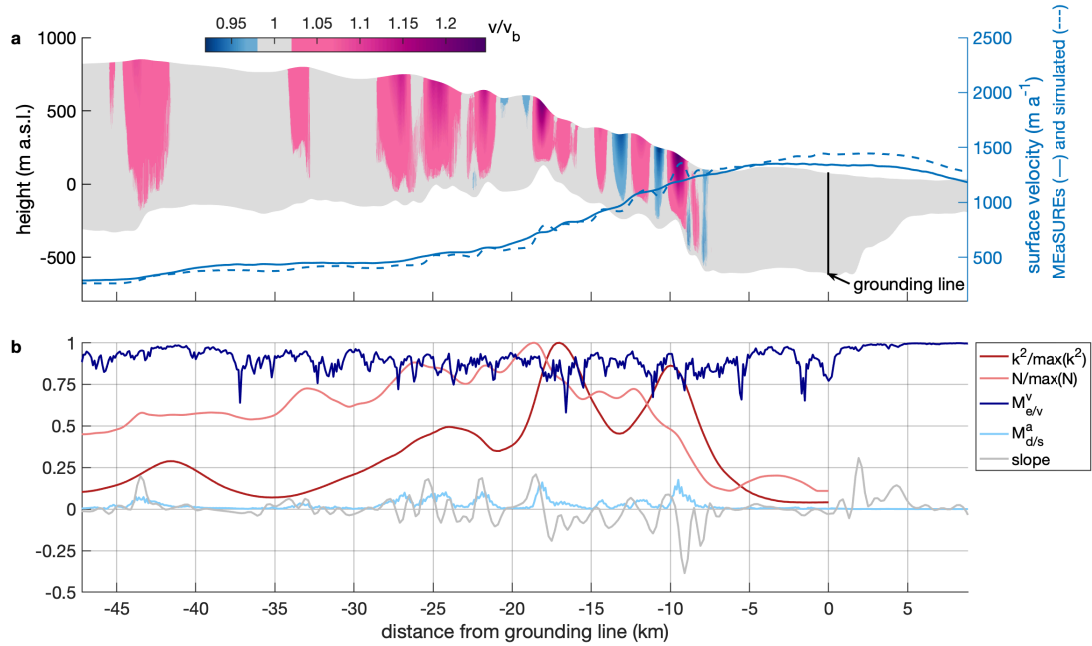


Figure B.4: Influence of vertical deformation versus sliding in glacier motion. **a**, Cross-section of 79NG along ice flow profile (left axis) with the velocity point-wise related to the basal velocity v/v_b (colour bar). Blueish colours depict velocities that are more than 2% smaller than its basal velocities, while reddish colours show domains in which v is at least 2% higher than v_b . The blue lines (right axis) depict the simulated surface velocities compared to MEaSUREs velocity (Joughin et al., 2016, 2018). **b**, The reddish lines show the normalised friction coefficient and effective pressure along the grounded part of the flowline while the blueish curves present the contribution of viscous to total strain $M_{e/v}^v$ and the measure of vertical deformation to sliding $M_{d/s}^a$ that reacts with a slight horizontal delay to the normalised slope of the base shown in grey. All those quantities correspond to one year of simulation time.

of -35 km), vertical shear deformation to sliding $M_{d/s}^a$ is small (Fig. B.4b). The reduction of friction facilitates plug-flow. In the remaining regions, a deformation dependency on slope and friction coefficient is apparent. For a viscous simulation of GrIS motion (Rückamp et al., 2020), we also consider the contribution of vertical shear deformation to sliding (Fig. B.5a). Sliding is dominant in all fast-moving areas but also in the interior of Greenland. Vertical shear deformation occurs up to 35% in the interior or at thin margins where ice is presumably frozen to ground (Rückamp et al., 2019a).

The remaining question is whether bed undulations can induce elastic responses that persist and consequently contribute to glacier motion. The viscoelastic Maxwell model for the flowline of 79NG allows us to distinguish between the viscous and elastic strain contribution as both sum up to the total strain (Christmann et al., 2019). We exploit this property and quantify the ratio of viscous to total strain. We define the number $M_{e/v}^v \in [0, 1]$ based on Euclidean matrix norms of the viscous (ϵ_v) and elastic (ϵ_e) strain

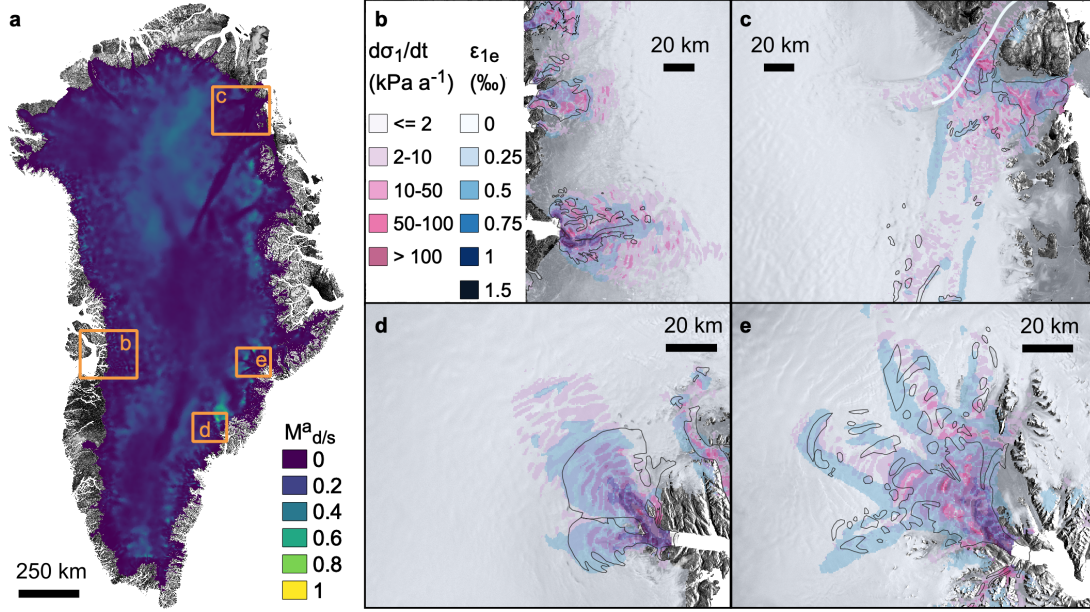


Figure B.5: Role of sliding and elastic strain of GrIS. **a** The contribution of vertical deformation to sliding $M_{d/s}^a$ where the blue colour means that sliding dominates glacier flow. **b–e** Changes in first principal stress $d\sigma_1/dt$ in flow direction (darker red colour means higher stress change) superimposed by elastic first principal strain ε_{1e} (darker blue colour means higher elastic strain) for four glacier basins **b**, Jakobshavn Isbræ, **c**, 79NG and Zacharias Isbræ with the considered flowline in white, **d**, Helheim Glacier, and **e**, Kangerlussuaq Glacier. The black line surround areas of massive crevasse fields.

$$M_{e/v}^v = \frac{\int_{h_b}^{h_s} \|\boldsymbol{\epsilon}_v\|_2 dz}{\int_{h_b}^{h_s} (\|\boldsymbol{\epsilon}_v\|_2 + \|\boldsymbol{\epsilon}_e\|_2) dz}.$$

This measure $M_{e/v}^v$ reaches the value 1 for vanishing elastic strains. Without short-term changes of tides, the amount of viscous relative to total strain consists of 6% elastic strain on average to a maximum above 30% for the grounded part (Fig. B.4b difference of $M_{e/v}^v$ to 1, Supplementary Fig. 7). The ratio of viscous to total strain is close to 1 at the free-floating ice tongue, meaning that the viscous flow dominates as no short-term changes happen. Once elastic strains caused by transient initialisation vanish, the partition of viscous to total strain $M_{e/v}^v$ remains similar for long simulation times (Fig. B.4b for 1 a and Supplementary Fig. 7 for up to 10 a). However, the ice flow over undulated beds induces unexplored time-independent elastic deformations occurring at grounded parts of the fast-flowing 79NG.

So far, large ice sheet models did not consider elastic contributions. The implication to neglect this component is not clear yet. For a glacier motion above undulated beds, the elastic strain increases and kinematics lead to higher displacements (integral of the strain), which enhance the flow velocity of the glacier

(Supplementary Fig. 8). The results of the viscoelastic flowline simulation reveal the existence of elastic strain for changing bed slopes (Fig. B.4b). At 79NG, bed slopes are too fluctuating for the elastic strain to vanish (which is due to fluctuating stresses), except near -4 or -40 km where $M_{e/v}^v$ is almost 1. Consequently, a rougher bed fosters more elastic deformation. For a viscoelastic Maxwell model, the total strain is the sum of elastic and viscous strain (see “Methods” section). The elastic strain is around one order of magnitude smaller than the viscous strain (Supplementary Methods 1 and Supplementary Fig. 9). For instance, a constant elastic strain of 2‰ over 50 km induces an additional elastic elongation of 100 m. In the end, a viscoelastic simulation reveals a higher velocity for a fast-flowing outlet glacier than a viscous one caused by the additional elastic deformation.

We aim to transfer local insights at 79NG to Greenland by determining regions in which elastic deformations may be crucial for understanding outlet glacier dynamics. To deal with the lack of a viscoelastic simulation for entire ice sheets, we leverage the fundamental character of a Maxwell rheology: elastic and viscous stresses are equal. Simulated stresses obtained by a viscous model (initialisation experiment (Rückamp et al., 2020)) can be used to compute principal (i.e., largest) elastic strains (see “Methods” section) on the entire surface of the GrIS (Fig. B.5b–e and Supplementary Fig. 10). Without short-term fluctuations, we would expect that the elastic strain declines with time and vanishes. The largest elastic strain is found in fast-moving outlet glaciers and reaches at most 1.14‰ . As the elastic strain does not vanish for Greenland (Fig. B.5b–e and Supplementary Fig. 10), we analyse the change in first principal stress with respect to time (see “Methods” section). Changing first principal stress over time often coincide with regions of large elastic strains in the fast-moving parts of outlet glaciers (Fig. B.6 and Supplementary Fig. 10). In these areas, elastic strains did not decline as changing stresses prevent this. The estimated occurrence of elastic strains at 79NG (Fig. B.5c) matches with the spatial extent of time-independent elastic strain from the viscoelastic flowline simulation (Fig. B.4b). This agreement indicates that slope change and viscous flow above 250 m a^{-1} cause stress changes inducing elastic strains. For assessing the area of Greenland’s ice affected by an elastic contribution arising from bed undulations, we use the BedMachine bedrock topography (Morlighem et al., 2017) and compute the directional slope (Supplementary Fig. 11). A slope larger than 5% is present in around 10% of the grounded ice of GrIS. For the flowline simulation of 79NG, the mean slope of the last 45 km upstream the grounding line is 4.7% where at least in this region the elastic strain is not negligible (Fig. B.4b).

How does this time-independent elastic strain compare in magnitude to tidal forcing? We first estimate the stress change caused by ocean tides ranging from

0 – 6 m around Greenland (Fig. B.6). For the three floating tongues glaciers, tides span from ~ 0.5 m for Ryder Glacier, ~ 1.0 m for 79NG to ~ 2.2 m for Petermann Glacier. Due to hydrostatic equilibrium, a diurnal tidal range induce $5 - 20 \text{ kPa d}^{-1}$ stress change at the floating tongues. At 79NG, the estimated stress change is $10 \text{ kPa d}^{-1} = 3650 \text{ kPa a}^{-1}$ at the glacier tongue. Independent of tides, we reach one third of this stress change magnitude at the grounded part of outlet glaciers for Jakobshavn Isbræ, 15% at Kangerlussuaq Glacier and 10% at Helheim Glacier (Fig. B.6). We find in other outlet glaciers close to the grounding line about 10% of this value declining to 1% over some tens of kilometres. In the flowline simulation of 79NG, elastic strains occur in sliding dominated flow and in regions with higher vertical deformation (Fig. B.4). In the end, faster flow over rougher beds induces higher elastic strains caused by higher stress changes. Caused by the motion of fast-flowing outlet glaciers over undulated beds, the stress changes are lower of those due to tides. While tides force an elastic elongation and compression on daily time scales, the motion of fast-flowing outlet glaciers induces an elastic elongation independent of time.

As there is no way to conduct in-situ observations of stress, we relate elastic deformation to the occurrence of cracks. Cracks are a representation of the solid nature of a material. Brittle failure is determined by a small process zone in which local elastic quantities causes a fracture, not viscous ones (Gross and Seelig, 2018). The extensive crevasse fields that we observe in outlet glaciers in Greenland are illustrative proofs of this elastic contribution (Supplementary Figs. 10 and 12). Furthermore, crevasse fields in ablation zones facilitate surface meltwater discharge to the ice base. This contributes to seasonal speed-up via lubrication, which increases elastic deformation. Damage in the lower tens kilometres of tidewater glaciers also controls calving dynamics of tidewater glaciers and thus ice discharge rates as feedback (Benn and Åström, 2018). Taking into account that Jakobshavn Isbræ and Kangerlussuaq Glacier contributed to an estimated 8 mm of global sea-level rise over the last century (Khan et al., 2020), understanding their future response is crucial. All ice discharge of the GrIS and in particular Jakobshavn Isbræ and Kangerlussuaq Glacier (Fig. B.5b, d and Supplementary Fig. 13) takes place in a settings where the bed is lubricated (MacGregor et al., 2016), sliding speeds are high (Fig. B.5a) (Lüthi et al., 2002; Ryser et al., 2014; Doyle et al., 2018; Maier et al., 2019, 2021), surfaces are crevassed (Fig. B.5b–e, Supplementary Data 6) (Colgan et al., 2016; Neckel et al., 2020; Nolin and Payne, 2007; Colgan et al., 2011; Chudley et al., 2020). In regions where sliding is dominant, the surface velocity is similar to the basal velocity and areas of high surface velocities fit areas of massive crevasse fields (Supplementary Methods 2 and Supplementary Fig. 12). Crevasses also occur in slow-moving outlet glaciers

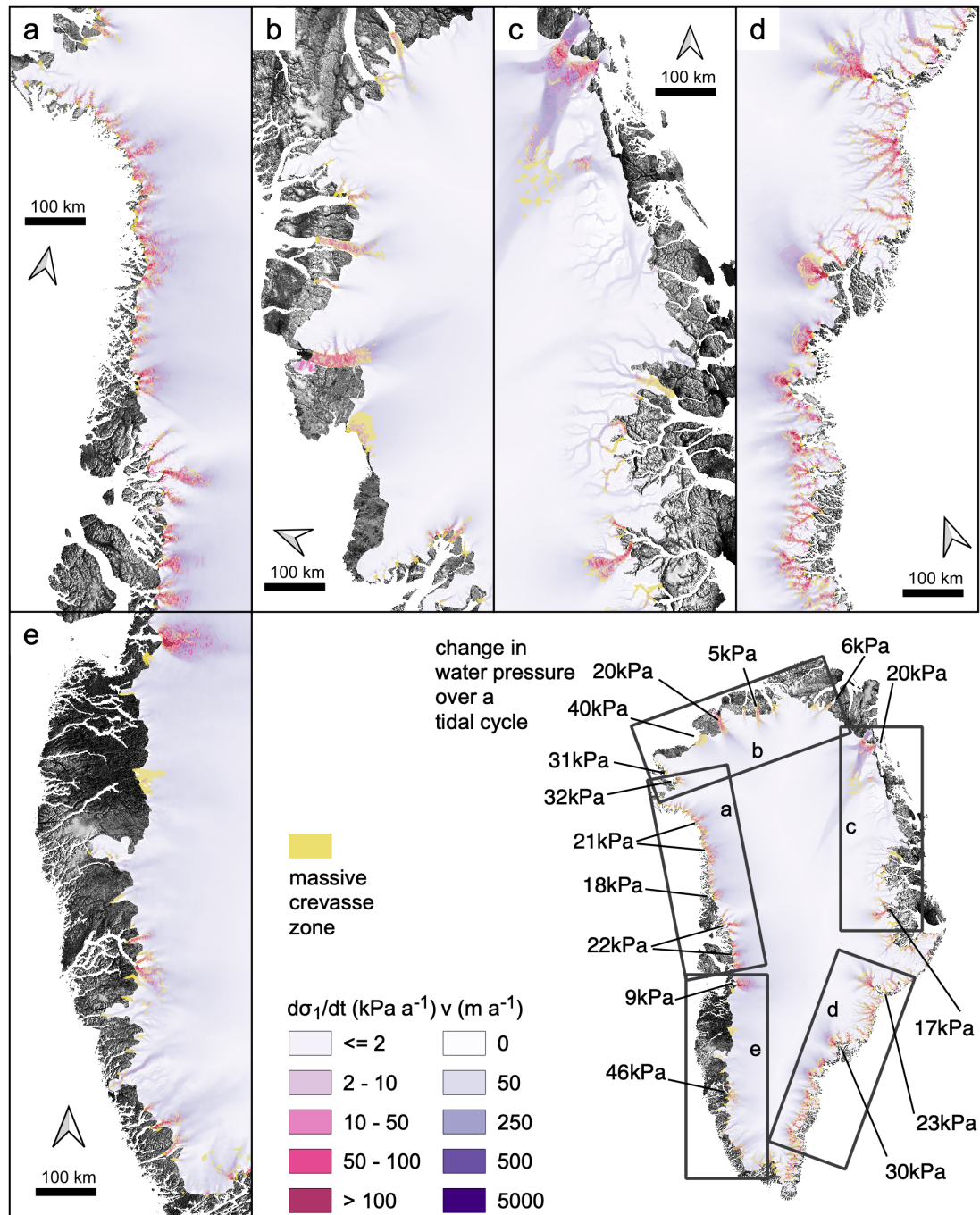


Figure B.6: Crevasse fields and stress change of GrIS. Areas of massive crevasse fields based on the DEM-residual product are displayed in yellow, superimposed on the MEaSUREs velocity field (Joughin et al., 2016, 2018) in purple colour and stress changes due to glacier motion in red colour for **a** the northwestern part, **b** the northern part, **c** the northeastern part, **d** the southeastern part, and **e** the southwestern part of Greenland. The given values in the overview figure denote changes in water pressure caused by a tidal range for some prominent outlet glaciers in Greenland. Areas of crevasses are consistent with areas of high changes in stress.

in which the basal topography will lead to necessary stress changes (Fig. B.6) and to time-independent elastic strains (Supplementary Fig. 10). The extensive match of massive crevasse fields with areas of large stress change supports the

claim that glacier flow over undulated beds induces persistent (time-independent) elastic strains.

B.2.4 Conclusion

By comparing GPS observations with numerical modelling, we demonstrated the need to describe tidal effects on ice by a viscoelastic Maxwell model to reproduce glacier dynamics in the lower part of the 79NG. The tidal influence, not captured by a viscous model, is limited to the hinge (bending) zone downstream the grounding line and up to 10 km upstream the grounding line. For the grounded ice, the subglacial hydrological system is relevant as it causes a phase delay in basal velocities. In the absence of tides, we found sliding to be the dominant mechanism of fast-moving glacier motion, and a absolute contribution of vertical shear deformation to sliding of less than 22% for the viscoelastic simulation of 79NG up to 35% for the viscous simulation of Greenland. Deducing from our viscoelastic modelling, the ice flow induces a persistent elastic to total strain of 6% on average up to a maximum of 30% for the considered flowline of 79NG.

Based on the viscoelastic simulation of 79NG, we developed a new perspective on deformation in outlet glaciers by transferring our findings from the flowline model to a continental scale simulation. We demonstrated that elastic deformation additionally contributes to the motion of outlet glaciers. Independent of tides, elastic deformation plays a role in areas of non-steady stress fields, such as near steep changes in topography or as ice flow speeds up. These new insights are a step forward to better understand the motion of glaciers since the identified regions are currently poorly constrained in ice flow models. In future works, improving the fidelity of ice flow models by considering the elastic contribution may capture the behaviour of fast-moving outlet glaciers. Under the overarching goal of narrowing uncertainties in sea-level projections, it is arguably important to assess how ice discharge to the ocean is affected by including an elastic deformation in the overall ice flow.

B.3 Methods

B.3.1 Viscoelastic modelling

The simulations COMice-ve were conducted with the finite element programme COMSOL applying a viscoelastic Maxwell material model that solves for the unknown displacements (along-flow and in thickness direction) (Christmann et al., 2019). We prescribe the ice geometry along the flowline from a high-resolution basal topography obtained from airborne ultra wide-band radar measurements. All simulation results are obtained using this high-resolution geometry subject to a non-linear Budd-like friction law (Budd et al., 1979). The position of the grounding line is the lowest position of the landward limit of the hinge zone defined from SAR interferometry. We show that this landward limit (upper flexure limit) does not move more than 500 m in the time period of observations. Such small changes make no difference in the simulation results, and for simplicity we assume a fixed grounding line at the lowest position of the upper flexure limit derived by SAR interferometry.

COMice-ve solves the underlying viscoelastic Maxwell equations in a small strain setting that is valid for simulation times up to few years. We discretise the model domain with a triangular mesh with a horizontal resolution of 100 m. This fine spatial resolution is necessary to get rid of the mesh discretisation error (Supplementary Fig. 14). The shape functions for the unknown displacements are quadratic Lagrange polynomials. The viscous strain components are additional internal variables for the Maxwell rheology and we use shape functions of linear discontinuous Lagrange type to save computational effort. The viscous and elastic stress of a Maxwell material are the same while the strain is the sum of elastic and viscous strain. The material relation of the volume-preserving deviatoric stress ($\boldsymbol{\sigma}^D = \boldsymbol{\sigma} - 1/3 \text{tr}(\boldsymbol{\sigma})\mathbf{I}$) to elastic strain $\boldsymbol{\varepsilon}_e^D$ or viscous strain rate $\dot{\boldsymbol{\varepsilon}}_v^D$ is given by the constitutive equation

$$\boldsymbol{\sigma}^D = 2\eta\dot{\boldsymbol{\varepsilon}}_v^D = 2\mu\boldsymbol{\varepsilon}_e^D \quad (\text{B.1})$$

with the elastic material constant $\mu = E/(1+\nu)$ (Darby, 1976). The viscosity η is non-linear and based on Glen's flow law using a temperature field from previous modelling (Rückamp et al., 2019). We choose the same model parameters as used in previous work (Christmann et al., 2019). The major difference to previous applications investigating calving of ice shelves (Christmann et al., 2019, 2016) is the incorporation of a friction law. The general friction power law (Budd-like) relates the basal shear stress ($\boldsymbol{\tau}_b$) to the sliding velocity \boldsymbol{v}_b

$$\boldsymbol{\tau}_b = -N^{1/m}k^2|\boldsymbol{v}_b|^{1/m-1}\boldsymbol{v}_b \quad (\text{B.2})$$

with the stress exponent m . This exponent is positive and unequal to 1 for a non-linear realisation of the friction law. We choose $m = 3$ and adjust the unknown friction coefficient field k^2 (see section “Inversion for basal friction coefficient” in “Methods” section) to result in a modelled flow velocity that best matches the observed surface velocity (Gudmundsson, 2011; Joughin et al., 2019). For the effective pressure $N = p_i - p_w$, the difference of ice overburden pressure p_i and the subglacial water pressure p_w , and the friction coefficient field k^2 we rely on external products. The effective pressure is obtained from a subglacial hydrology model. The output is used to perform a one-way coupling by feeding the resulting spatial and temporal distribution of the effective pressure of the subglacial system along the flowline back into the friction law (basal boundary condition for grounded ice in the viscoelastic model). The friction coefficient field is inferred by solving an inverse problem for the nonlinear friction law. The inferred friction coefficient k_{inv}^2 is related to a simpler effective pressure parameterisation N_{inv} applied for the inversion. Consequently, we adjust the unknown k^2 to include in the friction law of the viscoelastic model by the following rule:

$$k^2 = k_{\text{inv}}^2 \left(\frac{N_{\text{inv}}}{N} \right)^{1/m}. \quad (\text{B.3})$$

This re-scaling ensures that the basal shear stress fed to COMice-ve is comparable to the basal shear stress, which is derived from inversion. The boundary condition at the ice-atmosphere interface is traction-free and at the inflow boundary, we take a constant velocity based on the MEASUREs velocity data-set (Joughin et al., 2016, 2018). Given the observed vertical displacements of the GPS-shelf, we can compute the tidal pressure field perturbation at the base of the ice tongue. The floating ice mass is subject to a hydrostatic water pressure field normal to the submerged ice-ocean boundary line, depending on tide height (e.g., high tide leads to larger water pressure).

We put much effort in reproducing the observed velocities in the grounded part simulated by COMice-ve. However, the 2D flowline model lacks lateral resistance exerted by the fjord side-walls at the floating tongue. As this effect is inherently not covered we rely on a buttressing formulation (Gagliardini et al., 2010). The lateral resistance is accounted for over the whole floating tongue area (i.e., $x > x_{\text{gl}}$) by adding a body force f in the momentum balance equation, such that

$$f = -K|v_x|^{1/m_{lr}-1}v_x \quad (\text{B.4})$$

with v_x the velocity in horizontal direction. In the grounded part, the lateral resistance coefficient K is zero, while on the floating tongue $K > 0$. The exponent

m_{lr} is set equal to m . Here, we tune the lateral resistance coefficient spatially to obtain a reasonable decline of flow velocities downstream from the grounding line.

We conducted the benchmark experiments ISMIP-HOM B and D for verification of the long-term viscous response of the applied viscoelastic model (Supplementary Methods 3 and Supplementary Figs. 8 and 15). The simulated short-term elastic response with the applied model was already verified (Christmann et al., 2016).

B.3.2 Global positioning system (GPS) processing

The Global Positioning System (GPS) data were processed using the GIPSY-OASIS software package including high-precision kinematic data processing methods (Nettles et al., 2008) with ambiguity resolution using Jet Propulsion Laboratory (JPL)'s orbit and clock products, constraint on kinematic position solution. We use the GIPSY-OASIS version 6.4 developed at JPL, and released in January 2020 (Bertiger et al., 2020). We use JPL final orbit products which include satellite orbits, satellite clock parameters and Earth orientation parameters. The orbit products take the satellite antenna phase centre offsets into account. The atmospheric delay parameters are modelled using the Vienna Mapping Function 1 (VMF1) with VMF1grid nominals (Boehm et al., 2006). Corrections are applied to remove the solid Earth tide and ocean tidal loading. The amplitudes and phases of the main ocean tidal loading terms are calculated using the Automatic Loading Provider (<http://holt.oso.chalmers.se/loading/>) applied to the FES2014b (Lyard et al., 2006) ocean tide model including correction for centre of mass motion of the Earth due to the ocean tides. The site coordinates are computed in the IGS14 frame (Altamimi et al., 2016). We convert the Cartesian coordinates at 5 min intervals to local up, north and east for each GPS site monitored at the surface of the 79NG. In addition, we use Waypoint GravNav 8.8 processing software. We applied kinematic precise point positioning (PPP) processing using precise satellite orbits and clocks. The site coordinates are computed in the IGS14 frame and converted to WGS84 during data export at 15 s interval. To avoid jumps between daily solutions of the Waypoint PPP product, as the data is recorded in daily files, we merged three successive files prior to processing to enable full day overlaps. In a second step, the 3-day solutions are combined using relative point to point distances. To avoid edge effects, we combined the files in the middle of each 1-day overlap and removed outliers. To estimate the vertical and horizontal displacements we detrended the vertical, northing and easting components of the data after mapping into a polar-stereographic projec-

tion and alignment in the ice flow direction. Finally, the detrended data was low pass filtered to suppress signal frequencies larger than 1/3600 Hz and re-sampled to 5 min interval to match the GIPSY-OASIS product. A comparison of both processing software products revealed very similar results, with slightly less noise observed in the GIPSY-OASIS product (Supplementary Figs. 16 and 17). The PPP processing with the GIPSY-OASIS software Package of the GPS-shelf data was used as input for the simulation.

B.3.3 Modelling of subglacial hydrology

We applied CUAS to compute the effective pressure $N = p_i - p_w$ at the ice base. The model uses an equivalent porous medium (EPM) approach and accounts for efficient and inefficient drainage. A Darcy-type groundwater flow equation for the EPM is used to evolve the hydraulic head h , where the transmissivity T locally adjusts based on channel and cavity evolution. Areas of high transmissivity represent efficient (channelised) flow, whereas low transmissivity is interpreted as inefficient (distributed) flow.

We used a new version of the BedMachine geometry for Greenland (Morlighem et al., 2017) including the latest AWI airborne data (Franke et al., 2020). In addition to ice sheet basal melt from the Parallel Ice Sheet Model (PISM) output (Aschwanden et al., 2016), we updated and extended the domain outline. We have interpolated the data sets onto a 1.2 km resolution grid (coarse) for the entire NEGIS area and a 300 m resolution grid (fine) covering the area around the 79NG (Supplementary Fig. 18). We manually set the domain outlines guided by the BedMachine ice mask, the pressure-adjusted basal temperature contour of 0.1 °C of the PISM output, digitised ice front and grounding line positions, and ice flow velocities ($\geq 10 \text{ m a}^{-1}$). We used no-flux boundary conditions at lateral margins (homogeneous Neumann boundary conditions for the head) and Dirichlet boundary conditions (zero head) at grounding lines. At the ocean boundary the transmissivity was set to $T_{\text{max}} = 100 \text{ m}^2 \text{ s}^{-1}$ while the initial value was $0.2 \text{ m}^2 \text{ s}^{-1}$ elsewhere. We chose the subglacial water pressure to be equal to the ice overburden pressure as initial condition for the head. We choose the same model parameters as used in previous work (Beyer et al., 2018).

The output of a 50 years long steady-state run on the coarse grid (Supplementary Fig. 18) was used to run a 1 year long simulation on the fine grid in the 79NG nested sub-domain to let the model adjust to the changes in grid resolution. The effective pressure at the end of this spin-up was used to adjust the friction coefficient (Eq. B.3). We run the model for additional 19 days with and without tidal forcing at the grounding line with hourly output to provide time series of N

along the profile shown in Fig. B.1 as input for COMice-ve (Eq. B.2). We applied the tidal forcing as a time dependent Dirichlet boundary condition for the head at the 79NG grounding line.

The simulated subglacial drainage system (Supplementary Fig. 18a, b) shows relatively low effective pressure and transmissivity at the land terminating ice margin, indicating less efficient drainage. Observations indicate that efficient channels can form in the ablation area at the ice sheet margin (Davison et al., 2019). At the margin, the ice is usually thin (decreased creep-closure rates), the surface slope is steep and thus, the gradient of the hydraulic potential is large (enhanced channel wall melt). A sufficient amount of water from surface runoff or lake drainage is available at the glacier base via surface-to-bed hydrological connections (e.g., crevasses or moulins) to allow efficient channel formation. In the model, only ice sheet basal melt is considered as the supply for the hydrological system (Beyer et al., 2018). At the land terminating margin, basal melt from the PISM simulation is low or absent and thus efficient drainage is inhibited in our simulations. The transmissivity is high in the vicinity of the grounding line indicating efficient (channelised) water transport and declines with distance upstream. In this area, N is close to zero and increases towards GPS-GL-14.

B.3.4 Inversion for basal friction coefficient

The viscoelastic NEGIS ice flow model setup makes use of a basal friction coefficient field k_{inv}^2 that is retrieved by an inversion method. For the inversion of the basal friction coefficient, we operate the Ice-Sheet and Sea-level System Model (Morlighem et al., 2010; Larour et al., 2012), an open source finite element flow model appropriate for continental-scale and outlet glacier applications. The modelling domain is the flowline profile (Fig. B.4) and the ice flow is modelled by the full-Stokes equations. Model calculations are performed on a structured finite element grid with a horizontal resolution along-flow of 0.2 km. The domain is vertically extruded with 15 layers refined to the base. A thermo-mechanical coupling is not performed, but a realistic ice rigidity is prescribed based on thermal spin-up (Rückamp et al., 2018). We performed the inversion for the two different bed geometries: (1) BedMachine geometry for Greenland (Morlighem et al., 2017) including the latest AWI airborne data (Franke et al., 2020) and (2) the high-resolution basal topography from airborne ultra wide-band radar measurements.

Within the inverse problem a cost function (J), that measures the misfit between observed, v^{obs} , and modelled horizontal velocities, v_x , is minimised. We use the observed velocities from the MEaSUREs project (Joughin et al., 2016, 2018) as

target within the inversion. This data-set composes a long-term mean (20 a) from several remote sensing products and is independent of our GPS measurements. Please note that v^{obs} is the velocity in the curvilinear coordinate system along the flowline. The cost function is composed of two terms which fit the velocities in fast- and slow-moving areas. A third term is a Tikhonov regularisation to avoid oscillations due to over fitting. The cost function is defined as follows:

$$J(v_x, k_{\text{inv}}) = \gamma_1 \frac{1}{2} \int_{\Gamma_s} (v_x - v^{\text{obs}})^2 dl + \gamma_2 \frac{1}{2} \int_{\Gamma_s} \left(\ln \left(\frac{|v_x| + \varepsilon}{|v^{\text{obs}}| + \varepsilon} \right) \right) dl \quad (\text{B.5})$$

$$+ \gamma_t \frac{1}{2} \int_{\Gamma_b} \nabla k_{\text{inv}} \cdot \nabla k_{\text{inv}} dl,$$

where ε is a minimum velocity used to avoid singularities and Γ_s and Γ_b are the ice surface and ice base, respectively. An L-curve analysis was performed to pick the Tikhonov parameter γ_t (Supplementary Fig. 19a). We obtained a good agreement to the observed velocities by choosing $\gamma_1 = 10$, $\gamma_2 = 1$ and $\gamma_t = 1 \times 10^{-8}$.

The inverse problem is run for the non-linear friction law (Eq. B.2), but uses a simple parameterisation of the effective pressure (Huybrechts, 1990) with $N = \rho_i g h + \min(0, \rho_w g z_b)$, where h is the ice thickness, h_b the glacier base and $\rho_i = 910 \text{ kg m}^{-3}$, $\rho_w = 1000 \text{ kg m}^{-3}$ the densities for ice and fresh water, respectively. The parameterisation accounts for full water-pressure support from the ocean wherever the ice sheet base is below sea-level, even far into its interior where such a drainage system may not exist. With this parameterisation of the effective pressure, the inferred friction coefficient field is independent in time. The obtained results for the inferred friction parameters k_{inv}^2 and simulated surface velocities are shown in Supplementary Fig. 19b, c.

B.3.5 Hinge zone by means of interferometry

We applied Synthetic Aperture Radar Interferometry (InSAR) on Sentinel-1 TOPS SAR data to detect the upper and lower limit of tidal flexure. Interferograms are formed from interferometric wide swath single look complex data acquired at times t_1 and t_2 separated by a temporal baseline of 6 days. Assuming constant horizontal ice flow within a 6 day time period we subtracted another interferogram with data acquired at times t_2 and t_3 to isolate vertical displacements due to ocean tides (Rückamp et al., 2019; Joughin et al., 2016a; Hogg et al., 2016). This way we were able to produce 26 double differential interferograms from which we manually delineated the upper and lower flexure limit (Supplementary Fig. 1). To minimise the effect of inter annual grounding line migration when compared to the model results we focus on the year 2017. Along the profile used for the

viscoelastic modelling we found a maximum variation of 520 m and 880 m for the upper and lower flexure limit, respectively. These variations result from two main reasons (1) the timing between satellite pass and tide level is always different and (2) the horizontal ice flow is not constant within 6 days and hence residua remain in the double differential interferograms (Rack et al., 2017).

B.3.6 Changes of first principal stress for Greenland

The elastic deformation of a Maxwell material is non-negligible when subject to short-term changes in stress, such as those caused by calving events or ocean tides. As a Lagrangian ice parcel passes over an undulating bed, the stress experienced might, however, also change enough to induce non-negligible elastic deformation. Caused by such stress changes (Fig. B.6), we considered areas where time-independent elastic strains might occur caused by the viscous glacier flow (Supplementary Fig. 10). Elastic stresses are proportional to elastic strains and viscous stresses are related to viscous strain rates based on their constitutive equations. The elastic strain exists wherever viscous strain rate is present - hence in any regions of non-zero velocity gradients. To sustain elastic strain, the temporal change of stresses is necessary as the long-term stress response of a Maxwell model corresponds to the one of a viscous fluid (Supplementary Fig. 8). Based on the MEaSURES velocity field (Joughin et al., 2016, 2018) we generate a set of more than 60,000 flowlines with a point to point spacing of 200 m. The seed points of the flowlines were distributed every 5 km across Greenland, where the surface elevation exceeded 500 m. Along each flowline, we estimate the change of first principal stress over time using a raster with 500 m pixel resolution interpolated from the simulated first principal stress data set. We choose the pixel spacing to preserve the finer mesh used in the simulation in areas of fast flow. In total, we interpolate the stress change of more than 100 million points back to the initial input stress field using the same inverse distance weighting interpolation scheme.

To estimate the change in water pressure over a tidal cycle around Greenland, we used the Arctic Ocean Tidal Inverse Model (Padman and Erofeeva, 2004; Padman et al., 2004). We apply the model to a 5 km grid covering Greenland's coastline (including a buffer zone of 50 km towards the ocean) in a temporal resolution of 10 min for a tidal cycle (one month). Finally, the tidal range is given by the difference of the tide level extrema within each Pixel. This allows us to get a rough idea of the change in water pressure and its regional variation around Greenland (Supplementary Fig. 10).

Data availability

Processed GPS data (<https://doi.org/10.1594/PANGAEA.928940>; Zeising et al., 2021) are available at the World Data Center PANGAEA. The new BedMachine data-set is available through NSIDC (<https://nsidc.org/data/IDBMG4>). Source data for Figs. 1 – 5 are provided as Supplementary data.

Code availability

The mph file of the finite element software COMSOL Multiphysics (Version 5.6) of COMice-ve used for this study is available via AWI's gitlab (<https://gitlab.awi.de/jchristm/viscoelastic-79ng-greenland>) and zenodo (<https://doi.org/10.5281/zenodo.5507115>). The hydrology model CUAS is available via zenodo (<https://doi.org/10.5281/zenodo.5506953>).

Acknowledgements

This project is part of the GROCE project and is funded by BMBF under the grant 03F0778A. N.N. has received funding from the European Union's Horizon 2020 research and innovation programme under grant agreement No 689443 via project iCUPE (Integrative and Comprehensive Understanding on Polar Environments). S.A.K. acknowledges support from the INTAROS GA No. 727890 funded by European Union's Horizon 2020 Research and Innovation Programme. The authors would like to thank Emerson E&P Software, Emerson Automation Solutions, for providing licenses in the scope of the Emerson Academic Program. We acknowledge support in the field campaign iGRIFF by Graham Niven, Jens Köhler and Mirko Scheinert. We would also like to thank Malte Thoma and Natalja Rakowsky for maintaining excellent computing facilities at AWI. We thank the chief editor Heike Langenberg, two anonymous reviewers, and Basile de Fleurian for careful reading and very helpful suggestions.

Supplementary information

The online version contains supplementary material available at <https://doi.org/10.1038/s43247-021-00296-3>.

References

- Altamimi, Z., Rebischung, P., Métivier, L., & Collilieux, X. (2016). ITRF2014: A new release of the International Terrestrial Reference Frame modeling nonlinear station motions. *Journal of Geophysical Research: Solid Earth*, *121*(8), 6109–6131, <https://doi.org/10.1002/2016JB013098>.
- Anandakrishnan, S., Voigt, D. E., Alley, R. B., & King, M. A. (2003). Ice stream D flow speed is strongly modulated by the tide beneath the Ross Ice Shelf. *Geophysical Research Letters*, *30*(7), 1361, <https://doi.org/10.1029/2002GL016329>.
- Aschwanden, A., Fahnestock, M. A., & Truffer, M. (2016). Complex Greenland outlet glacier flow captured. *Nature Communications*, *7*(10524), <https://doi.org/10.1038/ncomms10524>.
- Bagshaw, E. A., Karlsson, N. B., Lok, L. B., Lishman, B., Clare, L., Nicholls, K. W., Burrow, S., Wadham, J. L., Eisen, O., Corr, H., Brennan, P., & Dahl-Jensen, D. (2018). Prototype wireless sensors for monitoring subsurface processes in snow and firn. *Journal of Glaciology*, *64*(248), 887–896, <https://doi.org/10.1017/jog.2018.76>.
- Benn, D. I. & Åström, J. A. (2018). Calving glaciers and ice shelves. *Advances in Physics*, *3*(1), 1048–1076, <https://doi.org/10.1080/23746149.2018.1513819>.
- Bertiger, W., Bar-Sever, Y., Dorsey, A., Haines, B., Harvey, N., Hemberger, D., Heflin, M., Lu, W., Miller, M., Moore, A. W., Murphy, D., Ries, P., Romans, L., Sibois, A., Sibthorpe, A., Szilagyi, B., Vallisneri, M., & Willis, P. (2020). GipsyX/RTGx, a new tool set for space geodetic operations and research. *Advances in Space Research*, *66*(3), 469 – 489, <https://doi.org/10.1016/j.asr.2020.04.015>.
- Beyer, S., Kleiner, T., Aizinger, V., Rückamp, M., & Humbert, A. (2018). A confined–unconfined aquifer model for subglacial hydrology and its application to the Northeast Greenland Ice Stream. *The Cryosphere*, *12*(12), 3931–3947, <https://doi.org/10.5194/tc-12-3931-2018>.
- Bindschadler, R. A., Vornberger, P. L., King, M. A., & Padman, L. (2003). Tidally driven stick–slip motion in the mouth of Whillans Ice Stream, Antarctica. *Annals of Glaciology*, *36*, 263–272, <https://doi.org/10.3189/172756403781816284>.
- Boehm, J., Niell, A., Tregoning, P., & Schuh, H. (2006). Global Mapping Function (GMF): A new empirical mapping function based on numerical weather model data. *Geophysical Research Letters*, *33*(7), <https://doi.org/10.1029/2005GL025546>.
- Brondex, J., Gagliardini, O., Gillet-Chaulet, F., & Durand, G. (2017). Sensitivity of grounding line dynamics to the choice of the friction law. *Journal of Glaciology*, *63*(241), 854–866, <https://doi.org/10.1017/jog.2017.51>.
- Brondex, J., Gillet-Chaulet, F., & Gagliardini, O. (2019). Sensitivity of centennial mass loss projections of the Amundsen basin to the friction law. *The Cryosphere*, *13*(1), 177–195, <https://doi.org/10.5194/tc-13-177-2019>.
- Budd, W. F., Keage, P. L., & Blundy, N. A. (1979). Empirical Studies of Ice Sliding. *Journal of Glaciology*, *23*(89), 157–170, <https://doi.org/10.3189/>

S0022143000029804.

- Choi, Y., Morlighem, M., Rignot, E., & Wood, M. (2021). Ice dynamics will remain a primary driver of Greenland ice sheet mass loss over the next century. *Communications Earth & Environment*, 2(1), 26, <https://doi.org/10.1038/s43247-021-00092-z>.
- Christianson, K., Peters, L. E., Alley, R. B., Anandakrishnan, S., Jacobel, R. W., Riverman, K. L., Muto, A., & Keisling, B. A. (2014). Dilatant till facilitates ice-stream flow in northeast Greenland. *Earth and Planetary Science Letters*, 401, 57–69, <https://doi.org/10.1016/j.epsl.2014.05.060>.
- Christmann, J., Mueller, R., & Humbert, A. (2019). On nonlinear strain theory for a viscoelastic material model and its implications for calving of ice shelves. *Journal of Glaciology*, 65(250), 212–224, <https://doi.org/10.1017/jog.2018.107>.
- Christmann, J., Plate, C., Müller, R., & Humbert, A. (2016). Viscous and viscoelastic stress states at the calving front of Antarctic ice shelves. *Annals of Glaciology*, 57(73), 10–18, <https://doi.org/10.1017/aog.2016.18>.
- Chudley, T. R., Christoffersen, P., Doyle, S. H., Dowling, T., Law, R., Schoonman, C., Bougamont, M., & Hubbard, B. (2020). Structural controls on the hydrology of crevasses on the Greenland ice sheet. *Earth and Space Science Open Archive*, (pp.25), <https://doi.org/10.1002/essoar.10502979.1>.
- Colgan, W., Rajaram, H., Abdalati, W., McCutchan, C., Mottram, R., Moussavi, M. S., & Grigsby, S. (2016). Glacier crevasses: Observations, models, and mass balance implications. *Reviews of Geophysics*, 54(1), 119–161, <https://doi.org/10.1002/2015RG000504>.
- Colgan, W., Steffen, K., McLamb, W. S., Abdalati, W., Rajaram, H., Motyka, R., Phillips, T., & Anderson, R. (2011). An increase in crevasse extent, west greenland: Hydrologic implications. *Geophysical Research Letters*, 38(18), <https://doi.org/10.1029/2011GL048491>.
- Darby, R. (1976). *Viscoelastic Fluids: An Introduction to Their Properties and Behavior*. Marcel Dekker, Inc., 9.
- Davison, B. J., Sole, A. J., Livingstone, S. J., Cowton, T. R., & Nienow, P. W. (2019). The Influence of Hydrology on the Dynamics of Land-Terminating Sectors of the Greenland Ice Sheet. *Frontiers in Earth Science*, 7, <https://doi.org/10.3389/feart.2019.00010>.
- de Juan, J., Elósegui, P., Nettles, M., Larsen, T., Davis, J., Hamilton, G., Stearns, L., Andersen, M., Ekström, G., Ahlstrøm, A., Stenseng, L., Khan, S., & Forsberg, R. (2010). Sudden increase in tidal response linked to calving and acceleration at a large Greenland outlet glacier. *Geophysical Research Letters*, 37, <https://doi.org/10.1029/2010GL043289>.
- Doyle, S. H., Hubbard, B., Christoffersen, P., Young, T. J., Hofstede, C., Bougamont, M., Box, J. E., & Hubbard, A. (2018). Physical Conditions of Fast Glacier Flow: 1. Measurements From Boreholes Drilled to the Bed of Store Glacier, West Greenland. *Journal of Geophysical Research: Earth Surface*, 123(2), 324–348, <https://doi.org/10.1002/2017JF004529>.

- Franke, S., Jansen, D., Beyer, S., Neckel, N., Binder, T., Paden, J., & Eisen, O. (2021). Complex Basal Conditions and Their Influence on Ice Flow at the Onset of the Northeast Greenland Ice Stream. *Journal of Geophysical Research: Earth Surface*, *126*(3), e2020JF005689, <https://doi.org/10.1029/2020JF005689>.
- Franke, S., Jansen, D., Binder, T., Dörr, N., Helm, V., Paden, J., Steinhage, D., & Eisen, O. (2020). Bed topography and subglacial landforms in the onset region of the Northeast Greenland Ice Stream. *Annals of Glaciology*, *61*(81), 143–153, <https://doi.org/10.1017/aog.2020.12>.
- Fricker, H. A. & Padman, L. (2006). Ice shelf grounding zone structure from ICESat laser altimetry. *Geophysical Research Letters*, *33*(15), <https://doi.org/10.1029/2006GL026907>.
- Gagliardini, O., Durand, G., Zwinger, T., Hindmarsh, R. C. A., & Le Meur, E. (2010). Coupling of ice-shelf melting and buttressing is a key process in ice-sheets dynamics. *Geophysical Research Letters*, *37*(14), <https://doi.org/10.1029/2010GL043334>.
- Gimbert, F., Tsai, V. C., Amundson, J. M., Bartholomaus, T. C., & Walter, J. I. (2016). Subseasonal changes observed in subglacial channel pressure, size, and sediment transport. *Geophysical Research Letters*, *43*(8), 3786–3794, <https://doi.org/10.1002/2016GL068337>.
- Goelzer, H., Nowicki, S., Payne, A., Larour, E., Seroussi, H., Lipscomb, W. H., Gregory, J., Abe-Ouchi, A., Shepherd, A., Simon, E., et al. (2020). The future sea-level contribution of the Greenland ice sheet: a multi-model ensemble study of ISMIP6. *The Cryosphere*, *14*(9), 3071–3096, <https://doi.org/10.5194/tc-14-3071-2020>.
- Gross, D. & Seelig, T. (2018). Fracture Mechanics with an Introduction to Micromechanics. *Springer International Publishing*, *3*, <https://doi.org/10.1007/978-3-642-19240-1>.
- Gudmundsson, G. H. (2007). Tides and the flow of Rutford Ice Stream, West Antarctica. *112*(F4), <https://doi.org/10.1029/2006JF000731>.
- Gudmundsson, G. H. (2011). Ice-stream response to ocean tides and the form of the basal sliding law. *The Cryosphere*, *5*(1), 259–270, <https://doi.org/10.5194/tc-5-259-2011>.
- Herbert, C. M., Alexander, J., & Martínez de Álvaro, M. J. (2015). Back-flow ripples in troughs downstream of unit bars: Formation, preservation and value for interpreting flow conditions. *Sedimentology*, *62*(7), 1814–1836, <https://doi.org/10.1111/sed.12203>.
- Hogg, A. E., Shepherd, A., Gourmelen, N., & Engdahl, M. (2016). Grounding line migration from 1992 to 2011 on Petermann Glacier, North-West Greenland. *Journal of Glaciology*, *62*(236), 1104–1114, <https://doi.org/10.1017/jog.2016.83>.
- Humbert, A., Steinhage, D., Helm, V., Hoerz, S., Berendt, J., Leipprand, E., Christmann, J., Plate, C., & Müller, R. (2015). On the link between surface and basal structures of the Jelbart Ice Shelf, Antarctica. *Journal of Glaciology*, *61*(229), 975–986, <https://doi.org/10.3189/2015JoG15J023>.
- Huybrechts, P. (1990). A 3-D model for the Antarctic ice sheet: a sensitivity study on

- the glacial-interglacial contrast. *Climate Dynamics*, 5(2), 79–92, <https://doi.org/10.1007/bf00207423>.
- IPCC (2013). *Climate Change 2013: The Physical Science Basis. Contribution of Working Group I to the Fifth Assessment Report of the Intergovernmental Panel on Climate Change* [Stocker, T.F., D. Qin, G.-K. Plattner, M. Tignor, S.K. Allen, J. Boschung, A. Nauels, Y. Xia, V. Bex and P.M. Midgley (eds.)]. Cambridge University Press, Cambridge, United Kingdom and New York, NY, USA, <https://doi.org/10.1017/CBO9781107415324>.
- Iverson, N. R., Helanow, C., & Zoet, L. K. (2019). Debris-bed friction during glacier sliding with ice–bed separation. *Annals of Glaciology*, 60(80), 30–36, <https://doi.org/10.1017/aog.2019.46>.
- Joughin, I., Shean, D. E., Smith, B. E., & Dutrieux, P. (2016a). Grounding line variability and subglacial lake drainage on Pine Island Glacier, Antarctica. *Geophysical Research Letters*, 43(17), 9093–9102, <https://doi.org/10.1002/2016gl070259>.
- Joughin, I., Smith, B., Howat, I., & Scambos, T. (2016b). MEaSUREs Multi-year Greenland Ice Sheet Velocity Mosaic, Version 1. Boulder, Colorado USA. NASA National Snow and Ice Data Center Distributed Active Archive Center. <https://doi.org/10.5067/QUA5Q9SVMSJG>.
- Joughin, I., Smith, B. E., & Howat, I. M. (2018). A complete map of Greenland ice velocity derived from satellite data collected over 20 years. *Journal of Glaciology*, 64(243), 1–11, <https://doi.org/10.1017/jog.2017.73>.
- Joughin, I., Smith, B. E., & Schoof, C. G. (2019). Regularized Coulomb Friction Laws for Ice Sheet Sliding: Application to Pine Island Glacier, Antarctica. *Geophysical Research Letters*, 46(9), 4764–4771, <https://doi.org/10.1029/2019GL082526>.
- Keisling, B. A., Christianson, K., Alley, R. B., Peters, L. E., Christian, J. E., Anandakrishnan, S., Riverman, K. L., Muto, A., & Jacobel, R. W. (2014). Basal conditions and ice dynamics inferred from radar-derived internal stratigraphy of the northeast Greenland ice stream. *Annals of Glaciology*, 55(67), 127–137, <https://doi.org/10.3189/2014AoG67A090>.
- Khan, S. A., Bjørk, A. A., Bamber, J. L., Morlighem, M., Bevis, M., Kjær, K. H., Mouginot, J., Løkkegaard, A., Holland, D. M., Ashwanden, A., Zhang, B., Helm, V., Korsgaard, N. J., Colgan, W., K., L. N., Liu, L., Hansen, K., Barletta, V., Dahl-Jensen, T. S., Søndergaard, A. S., Csatho, B. M., Sasgen, I., Box, J., & Schenk, T. (2020). Centennial response of Greenland’s three largest outlet glaciers. *Nature Communications*, 11(5718), <https://doi.org/10.1038/s41467-020-19580-5>.
- Larour, E., Ivins, E. R., & Adhikari, S. (2017). Should coastal planners have concern over where land ice is melting? *Science Advances*, 3(11), <https://doi.org/10.1126/sciadv.1700537>.
- Larour, E., Seroussi, H., Morlighem, M., & Rignot, E. (2012). Continental scale, high order, high spatial resolution, ice sheet modeling using the Ice Sheet System Model (ISSM). *Journal of Geophysical Research: Earth Surface*, 117(F1), F01022, <https://doi.org/10.1029/2011JF002140>.
- Lingle, C., Hughes, T., & Kollmeyer, R. (1981). Tidal Flexure of Jakobshavns Glacier,

- West Greenland. *Journal of Geophysical Research*, 86, 3960–3968, <https://doi.org/10.1029/JB086iB05p03960>.
- Lliboutry, L. (1968). General Theory of Subglacial Cavitation and Sliding of Temperate Glaciers. *Journal of Glaciology*, 7(49), 21–58, <https://doi.org/10.3189/S0022143000020396>.
- Lüthi, M., Funk, M., Iken, A., Gogineni, S., & Truffer, M. (2002). Mechanisms of fast flow in Jakobshavn Isbræ, West Greenland: Part III. Measurements of ice deformation, temperature and cross-borehole conductivity in boreholes to the bedrock. *Journal of Glaciology*, 48(162), 369–385, <https://doi.org/10.3189/172756502781831322>.
- Lyard, F., Lefevre, F., Letellier, T., & Francis, O. (2006). Modelling the global ocean tides: modern insights from FES2004. *Ocean Dynamics*, 56(5), 394–415, <https://doi.org/10.1007/s10236-006-0086-x>.
- MacGregor, J. A., Fahnestock, M. A., Catania, G. A., Aschwanden, A., Clow, G. D., Colgan, W. T., Gogineni, S. P., Morlighem, M., Nowicki, S. M., Paden, J. D., Price, S. F., & Seroussi, H. (2016). A synthesis of the basal thermal state of the Greenland Ice Sheet. *Journal of Geophysical Research: Earth Surface*, 121(7), 1328–1350, <https://doi.org/10.1002/2015JF003803>.
- Maier, N., Gimbert, F., Gillet-Chaulet, F., & Gilbert, A. (2021). Basal traction mainly dictated by hard-bed physics over grounded regions of Greenland. *The Cryosphere*, 15(3), 1435–1451, <https://doi.org/10.5194/tc-15-1435-2021>.
- Maier, N., Humphrey, N., Harper, J., & Meierbachtol, T. (2019). Sliding dominates slow-flowing margin regions, Greenland Ice Sheet. *Science Advances*, 5(7), <https://doi.org/10.1126/sciadv.aaw5406>.
- Morlighem, M., Rignot, E., Seroussi, H., Larour, E., Dhia, H., & Aubry, D. (2010). Spatial patterns of basal drag inferred using control methods from a full-Stokes and simpler models for Pine Island Glacier, West Antarctica. *Geophysical Research Letters*, 37(14), L14502, <https://doi.org/10.1029/2010GL043853>.
- Morlighem, M., Williams, C. N., Rignot, E., An, L., Arndt, J. E., Bamber, J. L., Catania, G., Chauché, N., Dowdeswell, J. A., Dorschel, B., Fenty, I., Hogan, K., Howat, I., Hubbard, A., Jakobsson, M., Jordan, T. M., Kjeldsen, K. K., Millan, R., Mayer, L., Mouginot, J., Noël, B. P. Y., O’Cofaigh, C., Palmer, S., Rysgaard, S., Seroussi, H., Siegert, M. J., Slabon, P., Straneo, F., van den Broeke, M. R., Weinrebe, W., Wood, M., & Zinglensen, K. B. (2017). BedMachine v3: Complete bed topography and ocean bathymetry mapping of Greenland from multibeam echo sounding combined with mass conservation. *Geophysical Research Letters*, 44(21), 11051–11061, <https://doi.org/10.1002/2017GL074954>.
- Mouginot, J., Rignot, E., & Scheuchl, B. (2019). Continent-Wide, Interferometric SAR Phase, Mapping of Antarctic Ice Velocity. *Geophysical Research Letters*, 46(16), 9710–9718, <https://doi.org/10.1029/2019GL083826>.
- Murray, T., Nettles, M., Selmes, N., Cathles, L. M., Burton, J. C., James, T. D., Edwards, S., Martin, I., O’Farrell, T., Aspey, R., Rutt, I., & Baugé, T. (2015). Reverse glacier motion during iceberg calving and the cause of glacial earthquakes. *Science*, 349(6245), 305–308, <https://doi.org/10.1126/science.aab0460>.

- Neckel, N., Zeising, O., Steinhage, D., Helm, V., & Humbert, A. (2020). Seasonal observations at 79° N Glacier (Greenland) from remote sensing and in-situ measurements. *Frontiers in Earth Science*, 8, 142, <https://doi.org/10.3389/feart.2020.00142>.
- Nettles, M., Larsen, T. B., Elósegui, P., Hamilton, G. S., Stearns, L. A., Ahlstrøm, A. P., Davis, J. L., Andersen, M. L., de Juan, J., Khan, S. A., Stenseng, L., Ekström, G., & Forsberg, R. (2008). Step-wise changes in glacier flow speed coincide with calving and glacial earthquakes at Helheim Glacier, Greenland. *Geophysical Research Letters*, 35(24), <https://doi.org/10.1029/2008GL036127>.
- Nolin, A. W. & Payne, M. C. (2007). Classification of glacier zones in western Greenland using albedo and surface roughness from the Multi-angle Imaging SpectroRadiometer (MISR). *Remote Sensing of Environment*, 107(1), 264–275, <https://doi.org/10.1016/j.rse.2006.11.004>.
- Oppenheimer, M., Glavovic, B., Hinkel, J., van de Wal, R., Magnan, A., Abd-Elgawad, A., Cai, R., Cifuentes-Jara, M., Deconto, R., Ghosh, T., et al. (2019). Sea level rise and implications for low-lying islands, coasts and communities. In H.-O. Pörtner, D. Roberts, V. Masson-Delmotte, P. Zhai, M. Tignor, P. E., K. Mintenbeck, A. Alegría, M. Nicolai, A. Okem, J. Petzold, B. Rama, & N. M. Weyer (Eds.), *IPCC Special Report on the Ocean and Cryosphere in a Changing Climate*. In press.
- Padman, L. & Erofeeva, S. (2004). A barotropic inverse tidal model for the Arctic Ocean. *Geophysical Research Letters*, 31(2), <https://doi.org/10.1029/2003GL019003>.
- Padman, L., Erofeeva, S., & Howard, S. (2004). AOTIM5: Arctic Ocean Inverse Tide Model, on 5 kilometer grid, developed in 2004. <https://doi.org/10.18739/A2S17SS80>.
- Padman, L., Siegfried, M. R., & Fricker, H. A. (2018). Ocean Tide Influences on the Antarctic and Greenland Ice Sheets. *Reviews of Geophysics*, 56(1), 142–184, <https://doi.org/10.1002/2016RG000546>.
- Pettas, D., Karapetsas, G., Dimakopoulos, Y., & Tsamopoulos, J. (2019). Viscoelastic film flows over an inclined substrate with sinusoidal topography. i. Steady state. *Physical Review Fluids*, 4, 083303, <https://doi.org/10.1103/PhysRevFluids.4.083303>.
- Rack, W., King, M. A., Marsh, O. J., Wild, C. T., & Floricioiu, D. (2017). Analysis of ice shelf flexure and its InSAR representation in the grounding zone of the southern McMurdo Ice Shelf. *The Cryosphere*, 11(6), 2481–2490, <https://doi.org/10.5194/tc-11-2481-2017>.
- Rosier, S. H. R. & Gudmundsson, G. H. (2020). Exploring mechanisms responsible for tidal modulation in flow of the Filchner–Ronne Ice Shelf. *The Cryosphere*, 14(1), 17–37, <https://doi.org/10.5194/tc-14-17-2020>.
- Röthlisberger, H. (1972). Water Pressure in Intra- and Subglacial Channels. *Journal of Glaciology*, 11(62), 177–203, <https://doi.org/10.3189/S0022143000022188>.
- Rückamp, M., Falk, U., Frieler, K., Lange, S., & Humbert, A. (2018). The effect of overshooting 1.5 °C global warming on the mass loss of the Greenland ice sheet. *Earth*

System Dynamics, 9(4), 1169–1189, <https://doi.org/10.5194/esd-9-1169-2018>.

- Rückamp, M., Goelzer, H., & Humbert, A. (2020). Sensitivity of Greenland ice sheet projections to spatial resolution in higher-order simulations: the Alfred Wegener Institute (AWI) contribution to ISMIP6 Greenland using the Ice-sheet and Sea-level System Model (ISSM). *The Cryosphere*, 14(10), 3309–3327, <https://doi.org/10.5194/tc-14-3309-2020>.
- Rückamp, M., Greve, R., & Humbert, A. (2019a). Comparative simulations of the evolution of the Greenland ice sheet under simplified Paris Agreement scenarios with the models SICOPOLIS and ISSM. *Polar Science*, 21, 14–25, <https://doi.org/10.1016/j.polar.2018.12.003>.
- Rückamp, M., Neckel, N., Berger, S., Humbert, A., & Helm, V. (2019b). Calving Induced Speedup of Petermann Glacier. *Journal of Geophysical Research: Earth Surface*, 124(1), 216–228, <https://doi.org/10.1029/2018JF004775>.
- Ryser, C., Lüthi, M. P., Andrews, L. C., Hoffman, M. J., Catania, G. A., Hawley, R. L., Neumann, T. A., & Kristensen, S. S. (2014). Sustained high basal motion of the Greenland ice sheet revealed by borehole deformation. *Journal of Glaciology*, 60(222), 647–660, <https://doi.org/10.3189/2014JoG13J196>.
- Seddik, H., Greve, R., Sakakibara, D., Tsutaki, S., Minowa, M., & Sugiyama, S. (2019). Response of the flow dynamics of Bowdoin Glacier, northwestern Greenland, to basal lubrication and tidal forcing. *Journal of Glaciology*, 65(250), 225–238, <https://doi.org/10.1017/jog.2018.106>.
- Seroussi, H., Nowicki, S., Payne, A. J., Goelzer, H., Lipscomb, W. H., Abe-Ouchi, A., Agosta, C., Albrecht, T., Asay-Davis, X., Barthel, A., Calov, R., Cullather, R., Dumas, C., Galton-Fenzi, B. K., Gladstone, R., Golledge, N. R., Gregory, J. M., Greve, R., Hattermann, T., Hoffman, M. J., Humbert, A., Huybrechts, P., Jourdain, N. C., Kleiner, T., Larour, E., Leguy, G. R., Lowry, D. P., Little, C. M., Morlighem, M., Pattyn, F., Pelle, T., Price, S. F., Quiquet, A., Reese, R., Schlegel, N.-J., Shepherd, A., Simon, E., Smith, R. S., Straneo, F., Sun, S., Trusel, L. D., Van Breedam, J., van de Wal, R. S. W., Winkelmann, R., Zhao, C., Zhang, T., & Zwinger, T. (2020). Ismip6 antarctica: a multi-model ensemble of the antarctic ice sheet evolution over the 21st century. *The Cryosphere*, 14(9), 3033–3070, <https://doi.org/10.5194/tc-14-3033-2020>.
- Shepherd, A., Ivins, E., Rignot, E., Smith, B., van den Broeke, M., Velicogna, I., Whitehouse, P., Briggs, K., Joughin, I., Krinner, G., Nowicki, S., Payne, T., Scambos, T., Schlegel, N., A. G., Agosta, C., Ahlstrøm, A., Babonis, G., Barletta, V. R., Bjørk, A. A., Blazquez, A., Bonin, J., Colgan, W., Csatho, B., Cullather, R., Engdahl, M. E., Felikson, D., Fettweis, X., Forsberg, R., Hogg, A. E., Gallee, H., Gardner, A., Gilbert, L., Gourmelen, N., Groh, A., Gunter, B., Hanna, E., Harig, C., Helm, V., Horvath, A., Horwath, M., Khan, S., Kjeldsen, K. K., Konrad, H., Langen, P. L., Lecavalier, B., Loomis, B., Luthcke, S., McMillan, M., Melini, D., Mernild, S., Mohajerani, Y., Moore, P., Mottram, R., Mouginit, J., Moyano, G., Muir, A., Nagler, T., Nield, G., Nilsson, J., Noël, B., Otosaka, I., Pattle, M. E., Peltier, W. R., Pie, N., Rietbroek, R., Rott, H., Sandberg Sørensen, L., Sasgen, I., Save, H., Scheuchl, B., Schrama, E., Schröder, L., Seo, K.-W., Simonsen, S. B., Slater, T., Spada, G., Sutterley, T., Talpe, M., Tarasov, L., van de Berg, W. J., van der Wal, W., van Wessel, M., Vishwakarma, B. D., Wiese, D., Wilton, D.,

- Wagner, T., Wouters, B., Wuite, J., & Team, T. I. (2020). Mass balance of the Greenland Ice Sheet from 1992 to 2018. *Nature*, 579(7798), 233–239, <https://doi.org/10.1038/s41586-019-1855-2>.
- Smith, E. C., Hattermann, T., Kuhn, G., Gaedicke, C., Berger, S., Drews, R., Ehlers, T. A., Franke, D., Gromig, R., Hofstede, C., Lambrecht, A., Läufer, A., Mayer, C., Tiedemann, R., Wilhelms, F., & Eisen, O. (2020). Detailed Seismic Bathymetry Beneath Ekström Ice Shelf, Antarctica: Implications for Glacial History and Ice-Ocean Interaction. *Geophysical Research Letters*, 47(10), e2019GL086187, <https://doi.org/10.1029/2019GL086187>.
- Sugiyama, S., Sakakibara, D., Tsutaki, S., Maruyama, M., & Sawagaki, T. (2015). Glacier dynamics near the calving front of Bowdoin Glacier, northwestern Greenland. *Journal of Glaciology*, 61(226), 223–232, <https://doi.org/10.3189/2015JoG14J127>.
- Walker, R. T., Christianson, K., Parizek, B. R., Anandakrishnan, S., & Alley, R. B. (2012). A viscoelastic flowline model applied to tidal forcing of Bindschadler Ice Stream, West Antarctica. *Earth and Planetary Science Letters*, 319–320, 128 – 132, <https://doi.org/10.1016/j.epsl.2011.12.019>.
- Wild, C. T., Marsh, O. J., & Rack, W. (2018). Unraveling InSAR Observed Antarctic Ice-Shelf Flexure Using 2-D Elastic and Viscoelastic Modeling. *Frontiers in Earth Science*, 6, 28, <https://doi.org/10.3389/feart.2018.00028>.
- Zeising, O., Helm, V., Khan, S. A., Neckel, N., Steinhage, D., & Humbert, A. (2021). GNSS measurements at 79°N Glacier in 2017. PANGAEA. <https://doi.org/10.1594/PANGAEA.928940>.
- Zoet, L. K. & Iverson, N. R. (2020). A slip law for glaciers on deformable beds. *Science*, 368(6486), 76–78, <https://doi.org/10.1126/science.aaz1183>.
- Åkesson, H., Morlighem, M., O'Regan, M., & Jakobsson, M. (2021). Future Projections of Petermann Glacier Under Ocean Warming Depend Strongly on Friction Law. *Journal of Geophysical Research: Earth Surface*, 126(6), e2020JF005921, <https://doi.org/10.1029/2020JF005921>.

Versicherung an Eides Statt / *Affirmation in lieu of an oath*

**gem. § 5 Abs. 5 der Promotionsordnung vom 18.06.2018 /
*according to § 5 (5) of the Doctoral Degree Rules and Regulations of 18 June, 2018***

Ich / I, Ole Zeising

(Vorname / *First Name*, Name / *Name*, Anschrift / *Address*, ggf. Matr.-Nr. / *student ID no.*, if applicable)

versichere an Eides Statt durch meine Unterschrift, dass ich die vorliegende Dissertation selbständig und ohne fremde Hilfe angefertigt und alle Stellen, die ich wörtlich dem Sinne nach aus Veröffentlichungen entnommen habe, als solche kenntlich gemacht habe, mich auch keiner anderen als der angegebenen Literatur oder sonstiger Hilfsmittel bedient habe und die zu Prüfungszwecken beigelegte elektronische Version (PDF) der Dissertation mit der abgegebenen gedruckten Version identisch ist. / *With my signature I affirm in lieu of an oath that I prepared the submitted dissertation independently and without illicit assistance from third parties, that I appropriately referenced any text or content from other sources, that I used only literature and resources listed in the dissertation, and that the electronic (PDF) and printed versions of the dissertation are identical.*

Ich versichere an Eides Statt, dass ich die vorgenannten Angaben nach bestem Wissen und Gewissen gemacht habe und dass die Angaben der Wahrheit entsprechen und ich nichts verschwiegen habe. / *I affirm in lieu of an oath that the information provided herein to the best of my knowledge is true and complete.*

Die Strafbarkeit einer falschen eidesstattlichen Versicherung ist mir bekannt, namentlich die Strafandrohung gemäß § 156 StGB bis zu drei Jahren Freiheitsstrafe oder Geldstrafe bei vorsätzlicher Begehung der Tat bzw. gemäß § 161 Abs. 1 StGB bis zu einem Jahr Freiheitsstrafe oder Geldstrafe bei fahrlässiger Begehung. / *I am aware that a false affidavit is a criminal offence which is punishable by law in accordance with § 156 of the German Criminal Code (StGB) with up to three years imprisonment or a fine in case of intention, or in accordance with § 161 (1) of the German Criminal Code with up to one year imprisonment or a fine in case of negligence.*

Ort / *Place*, Datum / *Date*

Unterschrift / *Signature*